The Ab Initio Calculation of the Chemical Shift Tensor and its Application for the Structure Determination in Ordered and Disordered Phases by Means of Solid-State Nuclear Magnetic Resonance

Dissertation
zur Erlangung des Grades

“Doktor der Naturwissenschaften“

am Fachbereich Chemie der
Universität Bayreuth

Jan Sehnert

geboren in Essen

Bayreuth 2007

Für meinen ganz persönlichen plappernden Affen.

Die vorliegende Arbeit wurde unter der Betreuung von Prof. Dr. J. Senker in der Zeit vom Januar bis zum Dezember 2004 an der Ludwigs-Maximilians-Universität in München und vom Januar 2005 bis zum Juni 2007 an der Universität Bayreuth angefertigt.

Vollständiger Abdruck der von der Fakultät Biologie, Chemie und Geowissenschaften der Universität Bayreuth genehmigten Dissertation zur Erlangung des akademischen Grades Doktor der Naturwissenschaften (Dr. rer. nat.).

Erster Prüfer:	Prof. Dr. J. Senker
Zweiter Prüfer:	Prof. Dr. G. M. Ullmann
Dritter Prüfer:	Prof. Dr. A. Böker
Prüfungsvorsitz:	Prof. Dr. H.-W. Schmidt
Tag der Einreichung:	3. Juli 2007
Tag der mündlichen Prüfung:	9. November 2007

Danksagung

An allererster Stelle möchte ich meinem Doktorvater Prof. Dr. Jürgen Senker meinen tiefempfundenen Dank aussprechen. Dafür, dass die in langen Sitzungen vorgelebte Akribie korrekten wissenschaftlichen Arbeitens letzten Endes doch durch die Nebel meiner Lernresistenz dringen konnte. Für die Offenheit und Freiheit was die Wahl des Themas meiner Dissertation betrifft, und vor allem dafür, dass er sowohl in fachlich als auch in privat bedingungslos zu mir gehalten hat.

Für die gute Zusammenarbeit in gemeinsamen Projekten möchte ich Prof. Dr. W. Schnick, Dr. B. Lotsch und Dr. M. Döblinger von der Ludwig-Maximilians-Universität in München sowie PD Dr. C. Näther von der Christian-Albrechts-Universität zu Kiel und Prof. Dr. E. Kroke von der TU Bergakademie Freiberg danken. Prof. Dr. J. Breu von der Universität Bayreuth gebührt spezieller Dank für seine offene Art der Kritik, die mir sehr geholfen hat mich auf fachlicher Ebene weiter zu entwickeln.

Meinen Laborkollegen Jürgen Thun und Marko Schmidt danke ich für die gute Stimmung und die vielen fruchtbaren Dialoge. Meinen wissenschaftlichen Hilfskräften Kilian Bärwinkel, Christopher Synatschke und Andreas Zapf für die Unterstützung bei meiner Arbeit und dem Aufbau des Labors in Bayreuth. Einen ganz besonderer Dank geht an unsere ersten Hauptpraktikanten Andreas Wagner und Phillipp von den Hoff, mit denen alles begann und die den langen Weg aus München auf sich nahmen, um in Bayreuth eine intensive Zeit zu erleben.

Meinen Eltern will ich dafür danken, dass sie mir das Studium ermöglicht und damit alle Perspektiven für meine Zukunft offen gehalten haben. Meinem Mitstreiter und Freund Björn danke ich, mit dem zusammen ich das Fundament dieser Ausbildung gegossen habe. Meinen Sihings Alexander und Michael danke ich für eine gänzlich andere Art der Ausbildung, die das notwendige Gegengewicht zur fachlichen Welt bildet.

An letzter und für mich wichtigster Stelle aber möchte ich meiner Verlobten Lena Seyfarth danken. Sie vereint alle Facetten, die hier aufgeführt sind in einer Person. Ob im Studium, als gemeinsamer Wachstumskeim für den Arbeitskreis Senker oder als Zuhörerin für Fachliches, Wing Chun, Persönliches und jede Menge blöder Witze, ich möchte keinen anderen Menschen an meiner Seite wissen und freue mich auf unsere gemeinsame Zukunft!

List of abbreviations

1D	One-dimensional
2D	Two-dimensional
3D	Three-dimensional
α, β, γ	Angles of the Euler transformation
γ	Magnetogyric ratio
δ	Chemical shift tensor (Herzfeld-Berger)
δ_{iso}	Isotropic chemical shift (Herzfeld-Berger)
δ_{aniso}	Reduced chemical shift anisotropy
Δ_{aniso}	Shielding anisotropy
δ_{DIP}	Dipolar coupling constant
η	Asymmetry parameter
κ	Skew
μ	Magnetic moment
ρ	Electron density
σ	Chemical shift tensor (Haeberlen-Mehring-Spiess)
σ_{iso}	Isotropic chemical shift (Haeberlen-Mehring-Spiess)
τ_m, t_m	Mixing time
χ_{11}, χ_{22}, χ_{33}	Eigenvalues of tensor χ
χ_{ij}	Components of tensor χ
χ_μ	Atomic orbital
ψ	Wave function
ω	Resonance frequency
Ω	Span
$\mathbf{A}$	Vector potential
A_l^m	Components of the spherical tensor
$\mathbf{B}$	Magnetic field
$\mathbf{B_0}$	External magnetic field
BSSE	Basis set superposition error
c	Velocity of light
CAS	Crystal axis system
CS	Chemical shift

DFT	Density functional theory
E	Energy
GIAO	Gauge-including atomic orbitals
GUI	Graphical user interface
HB	Hydrogen bond
HF	Hartree Fock
$\mathbf{H}_\lambda$	Hamiltonian of the interaction λ
$\mathbf{I}$	Nuclear spin
$I(\omega)$	Spectral density
IGLO	Individualized gauges for localized orbitals
LAS	Laboratory axis system
m	Mass
MAS	Magic angle spinning
NMR	Nuclear magnetic resonance
$\mathbf{p}$	Momentum
PAS	Principle axis system
PBC	Periodic boundary conditions
$\mathbf{r}$	Radius
$\mathbf{R}$	Gauge origin
$\mathbf{R}(\alpha, \beta, \gamma)$	Matrix of the Euler transformation
RAS	Reference axis system
rf	Radio frequency
SW	Sweep width
$T(AS)$	Tensor in a specified axis system
TPP	Triphenyl phosphite
V	Nuclear potential

Table of contents

Chapter 1

Introduction

Solid-state chemistry attends the persistent need for compounds with highly specific properties. In materials research it is for example aspired to tune the mechanical, the optical or the electrical properties of new phases.[1,2,3,4] Another example of high importance is the manipulation of the dissolution and precipitation of active ingredients in drug design.[5] These and many other solid-state properties have their seeds in the atomistic structure of the involved phases which can span from completely disordered to fully ordered condensed systems. A control over the desired property therefore implies exerting influence on the way the atomistic arrangement is formed.[4,6]

In ordered phases this is closely coupled to the phenomenon of polymorphism which denotes the fact that one substance can exhibit several different crystal forms or modifications.[4,5,6,7,8,9,10,11] Whereas this effect is well known and has been studied for over a century, in today's crystal engineering the selective synthesis of different crystalline phases by the active manipulation of the reaction parameters is aspired.[4,9,10,12,13,14,15,16] Besides the control of the crystallization conditions this involves techniques such as co-crystallization, the application of additives or the targeted crystallization on templates.[9,16]

In disordered phases the phenomenon equivalent to polymorphism is known as polyamorphism.[17,18,19,20,21] The appearance of different amorphous phases for one chemical compound is tightly interconnected with an understanding of the structure of glasses.[22,23,24] Apart from the fact that the disordered phases promise interesting new pro-

perties by themselves amorphous materials frequently occur in the synthesis of crystalline materials via precursor compounds.[25] In this process the structure of the amorphous state greatly influences the formation of the crystalline phase.

A key question to all of these phenomena is therefore the structure-property relationship in the desired system.[4,9,10,11,22,23] The control over the process of phase formation requires an understanding of self-assembly, nucleation and growth mechanisms as well as crystal packing in the solid state.[4,6,15,22,23,26] For this the local structure of the phase has to be known as much as the long-range order of the system. A successful solution of the X-ray structure is very valuable in this context as it contains the full information about the solid phase. However, such a structure solution is only easy for single crystals whereas most frequently only microcrystalline powders or mixtures of amorphous and crystalline materials are obtained from the synthesis.[24,25,27,28,29,30] In such cases structural investigations are much more demanding and require the application of a whole spectrum of complimentary techniques.

In this context powder X-ray diffraction has gained increasing interest.[27,28,29] Another important method is solid-state NMR spectroscopy which advanced to a most powerful tool during the past 20 years.[26,30,31,32,33,34,35,36,37] In particular interesting is the fact that NMR can address versatile structural features such as the local arrangement, the symmetry or even the space group in the investigated sample.[32,33,34,35] A third and modern source for information finally are theoretical calculations.[38,39,40,41] Even though each is applicable to the problem of structure solution the true power unfolds upon the combination of these techniques as was most recently shown by combining X-ray and computational methods, X-ray and NMR techniques as well as NMR with computational approaches.[33,35,36,37,40,41]

The here presented work deals with the latter combination and fathoms the potential for structure determination which results from the linkage of solid-state NMR measurements with theoretical structure models via the ab initio computation of the chemical shift tensor. The solution of the gauge origin problem in the 1980s meant a breakthrough to the computation of the NMR chemical shift.[42,43,44,45,46,47] With IGLO (*individual gauge for localized orbitals*) molecular systems could be treated on a large scale and ten years later with GIAO (*gauge including atomic orbitals*) the second important solution to the gauge origin problem was efficiently be implemented.[48] The slightly better performance for small basis sets today makes the latter the most commonly used method.[43]

Due to the much increased computational ressources in theoretical chemistry the calculation of the NMR chemical shift tensor nowadays is a routine task and available in two different implementations. The traditional approach describes the structure as an independent super-molecule in vacuo.[49] For systems such as molecules with an isolated electronic environment this cluster approach poses a good approximation to the real system. However, in condensed phases this approach might lack an accurate description and therefore the band structure of solid-state networks is treated with a different ansatz which includes the definition of a unit cell under periodic boundary conditions.[50,51]

The quality of the computed NMR tensor in principle depends on two factors. One is the quality of description of the structure and with this the position of the atoms themselves. The other is the quality of the wave function which is directly related to the electron density and with this to the shielding of nuclei in the system. Therefore both, structure and electronic environment are closely connected to the NMR property of the chemical shift.[52,53,54,55,56,57] In the last decade the combination of solid state NMR and ab initio calculations of the chemical shift tensor was used to investigate structural features like for example configuration,[58,59,60,61,62] hydrogen bonding[63,64] or even intermolecular arrangement[65]. The non-localized environment of the condensed phases was taken into account using various approaches among them the polarizable continuum model,[66,67] the embedded cluster method[64,66] and the computation of structure and shielding under full periodic boundary conditions.[68,69,70,71] Most of these fundamental studies dealt with well known systems and could therefore unequivocally demonstrate that the interplay of solid-state NMR and ab initio calculations yield accurate structural information on a nanoscopic scale.[72]

Such derived information can be used for structure verification as it was done within most of the abovementioned studies. However, in a further step the ab initio results can as well serve for the purpose of structure prediction. In this case an ab initio structure model has to replace the experimental input for the computation of the chemical shielding.[68,72,73,74,75,76] Furthermore, the ab initio calculated tensor can serve as a base for the simulation of purely theoretical NMR spectra which then can directly be compared to the experiment for the verification of such an ab initio model. This approach requires to couple two different types of calculations, the quantum chemical computation of the atomistic system on the one hand and the calculation of NMR spectra from a spin system on the other hand.[49,50,51,77,78,79]

For this reason as a foundation of this work the Gau2Sim program library was developed. It is capable of converting atomistic information from various quantum chemical calculations into spin systems which can further be treated with classical NMR simulation tools. Large parts of the analysis of the ab initio data with this library were automated which makes difficult procedures as for example the treatment of large systems or the investigation of whole NMR hypersurfaces a routine task. Furthermore, Gau2Sim provides the conversion of the raw tensors into all currently used NMR parameters. Whereas the most common NMR parameter in the comparison with experimental spectra nowadays is the isotropic chemical shift, solid-state NMR furthermore offers the anisotropic part of the chemical shift tensor as a source for information. This includes values like the anisotropy and asymmetry parameter as well as the orientation of the tensor in a local structure segment. Compared to a suitable NMR experiment in principle all of these parameters can be taken for the extraction of structural data. However, little is known about such an approach.

This work therefore comprises a systematic analysis of the application and usability of all of parts of the chemical shift tensor for the purpose of structure verification and prediction in a broad range of systems. These systems differ in their structural assembly and intrinsic interactions. Phases built up by isolated molecules, hydrogen bonded aliphatic and aromatic molecules are as well represented as phases with hydrogen bonded polymeric strings and 2D layers of organic networks. Due to the different strengths of the binding interactions the macroscopic samples cover a whole range of systems starting from completely disordered over partially ordered to fully crystalline phases. Dependent from the type of system different theoretical treatments of the structure were combined with DFT shielding calculations in the cluster approach as well as under periodic boundary conditions. The individual modeling strategy was chosen for the most efficient way of describing the structure of the condensed phase. The hereby used methods varied from force field calculations over semiempirical methods to DFT calculations on homogeneous as well as embedded clusters and under full periodic boundary conditions.

Chapter 2

Theory

The here presented topics aim at the general presentation of a theoretical basis as it is necessary for the understanding of the self-written programs outlined in chapter B and practical applications summarized in chapter 3. All formulas are taken from standard textbooks as well as selected review articles on the topics of NMR theory and ab initio calculations of the NMR chemical shift.[43,80,81,82,83,84,85,86,87] They are expressed as close as possible to IUPAC nomenclature.[84,88] Furthermore, the formulations appear as implemented in the here developed program library Gau2Sim (see chapter B). To follow the consistency with commonly used NMR simulation programs the conventions as found in SIMPSON and GAMMA were used.[78,79]

2.1 The NMR Hamiltonian

In NMR spectroscopy the nuclear spin interacts with a magnetic field. For I=$\frac{1}{2}$ this interaction can either arise from the external magnetic field (Zeemann interaction) or an internal magnetic field as either induced by the surrounding electrons (chemical shift interaction) or neighboring spins (dipole interaction). The full system of interacting nuclei is called a spin system and a macroscopic bulk sample contains an ensemble of these spin systems. The theoretical treatment starts with the expression of a spin Hamiltonian which includes all the occurring interactions:

$$\mathbf{H} = \sum_{\lambda} \mathbf{H}_{\lambda} = \mathbf{H_Z} + \mathbf{H_{CS}} + \mathbf{H_{DIP}} \tag{2.1}$$

The Zeemann Hamiltonian $\mathbf{H_Z}$ leads to a splitting of the energetic levels for $m_l = \pm\frac{1}{2}$ and does not bear any structural information of the system. Therefore it is excluded from the further analysis.

2.2 The chemical shift interaction

For isolated, non-interacting spins the chemical shift Hamiltonian can be broken down into a sum over single spins:

$$\mathbf{H_{CS}} = \sum_{i}^{spins} \mathbf{H_{CS}(i)} \tag{2.2}$$

Each spin interacts with the magnetic field induced by the surrounding electron cloud. As the electron density usually varies in its spatial distribution the chemical shift constitutes an anisotropic property which is be expressed via the interaction tensor $\sigma_{\mathbf{CS}}$. This tensor quantifies the chemical shift which can be formulated as the shielding from the external magnetic field via a single expression combining the Zeeman and chemical shift Hamiltonians:

$$\mathbf{B_{CS}^{ext.}(i)} = (\mathbf{1} - \sigma_{\mathbf{CS}}(i)) \cdot \mathbf{B_0} \tag{2.3}$$

It is practical, however, to isolate the term for the chemical shift interaction for a closer inspection as it will further be done in this work:

$$\mathbf{B_{CS}(i)} = -\sigma_{\mathbf{CS}}(i) \cdot \mathbf{B_0} \tag{2.4}$$

With this the chemical shift is treated as an independent interaction with the magnetic field of the surrounding electrons. The Hamiltonian of the interaction is expressed via the product of the spin $\mathbf{I}$, the interaction tensor σ_{CS} and the external magnetic field $\mathbf{B_0}$:

$$\begin{aligned} \mathbf{H_{CS}} &= \hbar\gamma \left[\mathbf{I_x}\ \mathbf{I_y}\ \mathbf{I_z}\right] \bullet \begin{bmatrix} \sigma_{xx} & \sigma_{xy} & \sigma_{xz} \\ \sigma_{yx} & \sigma_{yy} & \sigma_{yz} \\ \sigma_{zx} & \sigma_{zy} & \sigma_{zz} \end{bmatrix} \bullet \begin{bmatrix} 0 \\ 0 \\ B_z \end{bmatrix} \\ &= C\ \mathbf{I} \bullet \sigma_{\mathbf{CS}} \bullet \mathbf{B_0} \end{aligned} \tag{2.5}$$

The introduction of the dyadic product between $\mathbf{I}$ and $\mathbf{B_0}$ results in a second tensor $\mathbf{X}$:

$$\mathbf{X} = \mathbf{I} \otimes \mathbf{B_0} \tag{2.6}$$

Equation 2.5 can now be written in an overall tensorial form where the matrix multiplication is expressed over the scalar product between the second rank tensors $\sigma_{\mathbf{CS}}$ and $\mathbf{X}$:

$$\mathbf{H_{CS}} = C\ \sigma_{\mathbf{CS}} \circ \mathbf{X} \tag{2.7}$$

This exclusive description of the Hamiltonian via tensors has the advantage of simple transferability between different reference frames, an important property for the theoretical description of NMR experiments (section 2.3.1).
It is convenient to further reduce a second rank tensors into irreducible Cartesian tensors of rank 0 through 2:

$$\begin{aligned} \sigma_{\mathbf{CS}} &= \sigma_{\mathbf{0}} + \sigma_{\mathbf{1}} + \sigma_{\mathbf{2}} \\ &= \sigma_{iso} \begin{bmatrix} 1 & 0 & 0 \\ 0 & 1 & 0 \\ 0 & 0 & 1 \end{bmatrix} + \begin{bmatrix} 0 & \alpha_{xy} & \alpha_{xz} \\ \alpha_{yx} & 0 & \alpha_{yz} \\ \alpha_{zx} & \alpha_{zy} & 0 \end{bmatrix} + \begin{bmatrix} \delta_{xx} & \delta_{xy} & \delta_{xz} \\ \delta_{yx} & \delta_{yy} & \delta_{yz} \\ \delta_{zx} & \delta_{zy} & \delta_{zz} \end{bmatrix} \end{aligned} \tag{2.8}$$

The respective components of $\sigma_{\mathbf{0}}$, $\sigma_{\mathbf{1}}$ and $\sigma_{\mathbf{2}}$ are:

$$\begin{aligned} \sigma_{iso} &= \frac{1}{3}(\sigma_{xx}+\sigma_{yy}+\sigma_{zz}) = \frac{1}{3}Tr\{\sigma_{\mathbf{CS}}\} \\ \alpha_{uv} &= \frac{1}{2}(\sigma_{uv}-\sigma_{vu}) \\ \delta_{uv} &= \frac{1}{2}(\sigma_{uv}+\sigma_{vu}-2\sigma_{iso}) \end{aligned} \tag{2.9}$$

Due to α_{uv}=-α_{vu} and α_{uu}=0 tensor $\sigma_{\mathbf{1}}$ is traceless antisymmetric and contains three distinct components. $\sigma_{\mathbf{2}}$ is traceless symmetric and thus expressed by five distinct components. In first order perturbation theory the first rank tensor $\sigma_{\mathbf{1}}$ exclusively contributes to relaxation mechanisms and does not alter the energy levels of the static Hamiltonian. Therefore it can be ignored for the simulations of NMR spectra which leaves only the symmetric part of the shielding tensor. Upon the representation of $\sigma_{\mathbf{CS}}$ in its principle axis system (PAS) the expression further simplifies to:

$$\begin{aligned} \sigma_{\mathbf{CS}}(PAS) &= \begin{bmatrix} \sigma_{xx} & 0 & 0 \\ 0 & \sigma_{yy} & 0 \\ 0 & 0 & \sigma_{zz} \end{bmatrix} \\ &= \sigma_{iso}\underbrace{\begin{bmatrix} 1 & 0 & 0 \\ 0 & 1 & 0 \\ 0 & 0 & 1 \end{bmatrix}}_{(\sigma_{\mathbf{0}})} + \underbrace{\begin{bmatrix} \delta_{xx} & 0 & 0 \\ 0 & \delta_{yy} & 0 \\ 0 & 0 & \delta_{zz} \end{bmatrix}}_{(\sigma_{\mathbf{2}})} \end{aligned} \tag{2.10}$$

σ is now given in terms of its irreducible Cartesian components with $\sigma_{iso} = \frac{1}{3}Tr\{\sigma_{\mathbf{CS}}\}$ and $\delta_{uu}(PAS) = (\sigma_{uu} - \sigma_{iso})$. This is the source for two different descriptions of the anisotropy of chemical shielding.

In the Haeberlen-Mehring-Spiess convention the chemical shift tensor is expressed as:

$$\sigma_{\mathbf{CS}}(PAS) = \sigma_{iso}\begin{bmatrix} 1 & 0 & 0 \\ 0 & 1 & 0 \\ 0 & 0 & 1 \end{bmatrix} + \delta_{aniso}\begin{bmatrix} -\frac{1}{2}(1+\eta) & 0 & 0 \\ 0 & -\frac{1}{2}(1-\eta) & 0 \\ 0 & 0 & 1 \end{bmatrix} \tag{2.11}$$

$\sigma_{\mathbf{CS}}(PAS)$ is characterized by the isotropic chemical shift σ_{iso}, the reduced anisotropy δ_{aniso} or the shielding anisotropy Δ_{aniso} and the asymmetry parameter η. All values can directly be calculated from the tensor in its representation in the PAS (compare to equation 2.10):

$$\begin{aligned} \sigma_{iso} &= \frac{1}{3}(\sigma_{xx} + \sigma_{yy} + \sigma_{zz}) \\ \delta_{aniso} &= \sigma_{zz} - \sigma_{iso} \\ \Delta_{aniso} &= \frac{3\delta_{aniso}}{2} = \sigma_{zz} - \frac{\sigma_{xx} + \sigma_{yy}}{2} \\ \eta &= \frac{\sigma_{yy} - \sigma_{xx}}{\sigma_{zz} - \sigma_{iso}} \end{aligned} \tag{2.12}$$

In the Haeberlen-Mehring-Spiess convention it is necessary to comply with the axis definition $|\sigma_{zz} - \sigma_{iso}| \geq |\sigma_{xx} - \sigma_{iso}| \geq |\sigma_{yy} - \sigma_{iso}|$.

The Herzfeld-Berger convention aims at a practical description of the chemical shift spectrum rather than the tensor itself. Therefore the axes are sorted according to the eigenvalues of the chemical shift tensor in its PAS as appearing in the spectrum resulting in $\sigma_{zz} \geq \sigma_{yy} \geq \sigma_{xx}$ (compare to equation 2.10). The mathematical expression for the isotropic chemical shift is the same as above and the anisotropy of the chemical shift tensor is expressed via the span Ω and the skew κ. In the Herzfeld-Berger convention $\sigma_{\mathbf{CS}}(PAS)$ is thus described via the following parameters:

$$\begin{aligned} \sigma_{iso} &= \frac{1}{3}(\sigma_{xx} + \sigma_{yy} + \sigma_{zz}) \\ \Omega &= \sigma_{zz} - \sigma_{xx} \\ \kappa &= \frac{3(\sigma_{iso} - \sigma_{yy})}{\sigma_{zz} - \sigma_{xx}} \end{aligned} \tag{2.13}$$

From these values the full chemical shift tensor can be calculated and expressed analogous to equation 2.11:

$$\sigma_{\mathbf{CS}}(PAS) = \sigma_{iso} \begin{bmatrix} 1 & 0 & 0 \\ 0 & 1 & 0 \\ 0 & 0 & 1 \end{bmatrix} + \begin{bmatrix} \left(\frac{\Omega\kappa}{6} - \frac{\Omega}{2}\right) & 0 & 0 \\ 0 & -\frac{\Omega\kappa}{3} & 0 \\ 0 & 0 & \left(\frac{\Omega\kappa}{6} + \frac{\Omega}{2}\right) \end{bmatrix} \tag{2.14}$$

However, due to the axis definition via absolute values in the Haeberlen-Mehring-Spiess convention care has to be taken when comparing the anisotropic parts of $\sigma_{\mathbf{CS}}(PAS)$ in equations 2.11 and 2.14. Two principle cases occur, namely $|\sigma_{xx} - \sigma_{iso}| \leq |\sigma_{zz} - \sigma_{iso}|$ and $|\sigma_{xx} - \sigma_{iso}| \geq |\sigma_{zz} - \sigma_{iso}|$, which is why the parameters δ_{aniso}, η, Ω and κ are not directly convertable into one another.

2.3 Chemical shift spectra

2.3.1 Powder patterns

For one-dimensional chemical shift spectra of non-interacting spins the principle values of $\sigma_{\mathbf{CS}}(PAS)$ pose the observables of the CS tensor. However, the measured resonance frequencies for σ_{xx}, σ_{yy} and σ_{zz} depend on the individual orientation of the tensor towards the external magnetic field $\mathbf{B_0}$. For a calculation of the frequencies it is therefore necessary to transform the tensor from its principle axis system (PAS) into the laboratory axis system (LAS). Such a transformation can be thought of as a rotation of the three tensorial axes of the PAS to match the axes of an arbitrary axis system (AAS). Mathematically this rotation is carried out via a transformation matrix $\mathbf{R}$:

$$T(AAS) = \mathbf{R}\, T(PAS)\, \mathbf{R^{-1}} \tag{2.15}$$

In Cartesian space the transformation is carried out via the Euler matrix $\mathbf{R}(\alpha, \beta, \gamma)$. As this type of rotation was implemented in the Gau2Sim program it is described in more detail in the following. Equation 2.15 is valid for the rotation of a whole coordinate system and can be reduced to an expression where a single vector (the respective axis of the coordinate system) is rotated in a reference frame:

$$\begin{aligned} \mathbf{r'} &= \mathbf{R} \cdot \mathbf{r} \\ \mathbf{r'} &= \mathbf{R^{-1}} \cdot \mathbf{r} \end{aligned} \tag{2.16}$$

$\mathbf{R}$ and $\mathbf{R^{-1}}$ are the transformation matrices of an active and a passive rotation of vector $\mathbf{r}$, respectively, with $\mathbf{R^{-1}} = \mathbf{R^T}$. In NMR spectroscopy usually active rotations are treated which means the vector itself is taken and rotated in the reference frame. However, mathematically the rotation about for example the z axis of is expressed as

$$\mathbf{R_z}(\phi) = \begin{bmatrix} cos(\phi) & -sin(\phi) & 0 \\ sin(\phi) & cos(\phi) & 0 \\ 0 & 0 & 1 \end{bmatrix} \tag{2.17}$$

From this expression it becomes obvious that the transformation matrix is fixed to the axes x, y and z of the standard Cartesian coordinate system. In other words, mathematically the transformation is confined to rotations about the vectors [1 0 0], [0 1 0] and [0 0 1]. Therefore another transformation is introduced, the passive Euler rotation. A passive rotation of $\mathbf{r}$ corresponds to an active rotation of the reference axis system. Usually the rotation is defined as right-handed, but because of the active rotation of the reference frame the passive rotation of the vector $\mathbf{r}$ about an angle ϕ becomes left-handed. Thus a positive passive rotation of $\mathbf{r}$ has to be carried out with $-\phi$. From this difference it is clear that for the specific cases extreme care has to be taken upon the definition of the Euler angles themselves.

In figure 2.1 the single steps of the Euler transformation between two coordinate systems (PAS and RAS) are shown. The PAS (blue) is rotated about its z axis until y(PAS) hits the nodal line defined by the intersection of the xy planes of the RAS and the PAS (compare

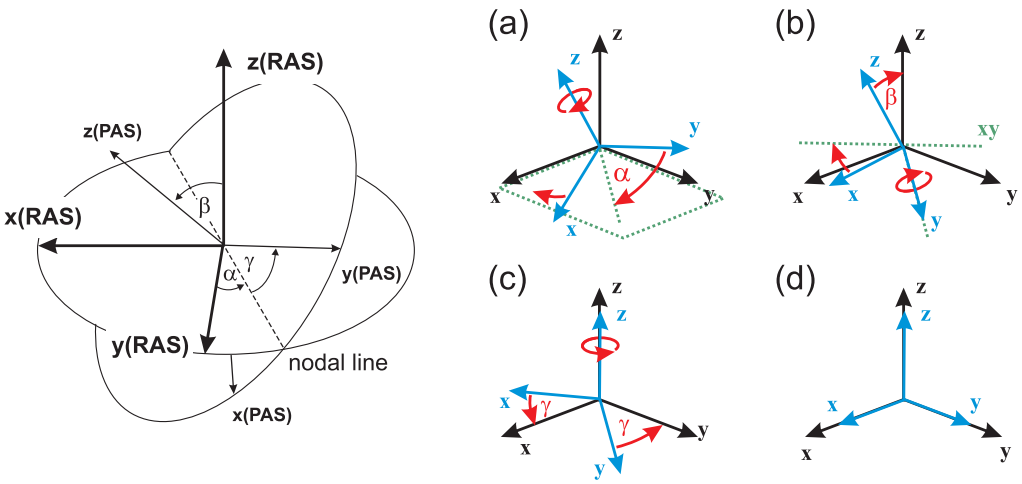

Figure 2.1: Single steps of an Euler transformation between two coordinate systems: the PAS (blue) is rotated into the RAS (black); (a) rotation about the z axis of the PAS until y(PAS) hits the nodal line defined by the intersection of the xy planes of the RAS and the PAS (see also left side of the figure); (b) rotation about the y(PAS) until both z axes match; (c) second rotation about z(PAS).

to the left side of figure 2.1). A rotation about y(PAS) follows until the z axes of both coordinate systems match. The final step is a second rotation about z(PAS) until all axes match. As usual the transformation is described in terms of an *active* rotation of the PAS:

$$\mathbf{R}(\alpha,\beta,\gamma) = \mathbf{R_z}(\alpha)\cdot\mathbf{R_y}(\beta)\cdot\mathbf{R_z}(\gamma) \tag{2.18}$$

As from a mathematical point of view the PAS itself can not be rotated actively and the transformation is expressed via three subsequent *passive* rotations:

$$\mathbf{R^{-1}}(\alpha,\beta,\gamma) = \mathbf{R_z^{-1}}(\gamma)\cdot\mathbf{R_y^{-1}}(\beta)\cdot\mathbf{R_z^{-1}}(\alpha) \tag{2.19}$$

However, to treat the transformation in the commonly used active picture a *pseudo-active* convention is introduced as follows:

$$\begin{aligned}\tilde{\mathbf{R}}(\alpha,\beta,\gamma) &= \mathbf{R^{-1}}(\alpha,\beta,\gamma) = \mathbf{R_z^T}(\gamma)\cdot\mathbf{R_y^T}(\beta)\cdot\mathbf{R_z^T}(\alpha) \\ &= \begin{bmatrix} c_\gamma & -s_\gamma & 0 \\ s_\gamma & c_\gamma & 0 \\ 0 & 0 & 1 \end{bmatrix}\begin{bmatrix} c_\beta & 0 & -s_\beta \\ 0 & 1 & 0 \\ s_\beta & 0 & c_\beta \end{bmatrix}\begin{bmatrix} c_\alpha & -s_\alpha & 0 \\ s_\alpha & c_\alpha & 0 \\ 0 & 0 & 1 \end{bmatrix}\end{aligned} \tag{2.20}$$

s_ϕ and c_ϕ denote the sine and cosine of the respective Euler angle α, β or γ. The pseudo-active, passive and active rotations are connected by:

$$\tilde{\mathbf{R}}(\alpha,\beta,\gamma) = \mathbf{R^{-1}}(\alpha,\beta,\gamma) = \mathbf{R}(-\gamma,-\beta,-\alpha) \tag{2.21}$$

For the transformations of a tensor σ the active rotation is written as

$$\sigma' = \mathbf{R}\,\sigma\,\mathbf{R^{-1}} \tag{2.22}$$

Changing the representation of the tensor between two reference systems A and B, where for example A is the PAS of the tensor and B an arbitrary reference system, the following expressions can be written:

$$(\sigma_A)_B = \mathbf{R^{-1}}\,\sigma_A\,\mathbf{R} = \tilde{\mathbf{R}}\,\sigma_A\,\tilde{\mathbf{R}}^{-1} \qquad (2.23)$$
$$(\sigma_B)_A = \mathbf{R}\,\sigma_A\,\mathbf{R^{-1}} = \tilde{\mathbf{R}}^{-1}\,\sigma_A\,\tilde{\mathbf{R}}$$

The representation $(\sigma_A)_B$ of the tensor σ in system B (transformation form A to B) corresponds to a passive rotation whereas the representation $(\sigma_B)_A$ of the tensor σ in B as seen from A is like an active rotation (transformation form B to A). Hence, if either of the transformations is known its inverse is given as well.
An alternative to the Cartesian expressions is to represent the irreducible tensor in its spherical components (compare to equations 2.5, 2.8 and 2.10):

$$\begin{aligned}
\sigma_0^0 &= -\frac{1}{\sqrt{3}}(\sigma_{xx}+\sigma_{yy}+\sigma_{zz}) \qquad (2.24)\\
\sigma_1^0 &= -\frac{i}{\sqrt{2}}(\sigma_{xy}-\sigma_{yx})\\
\sigma_1^{\pm1} &= -\frac{1}{2}[\sigma_{zx}-\sigma_{xz}\pm i(\sigma_{zy}-\sigma_{yz})]\\
\sigma_2^0 &= \frac{1}{\sqrt{6}}[3\sigma_{zz}-(\sigma_{xx}+\sigma_{yy}+\sigma_{zz})]\\
\sigma_2^{\pm1} &= \pm\frac{1}{2}[\sigma_{xz}+\sigma_{zx}\pm i(\sigma_{yz}+\sigma_{zy})]\\
\sigma_2^{\pm2} &= \frac{1}{2}[\sigma_{xx}-\sigma_{yy}\pm i(\sigma_{xy}+\sigma_{yx})]
\end{aligned}$$

In this notation the transformation of the tensor between the coordinate systems can be performed with Wigner matrices and therefore takes a simpler mathematical form:

$$A_l^m(AAS) = \sum_{m'=-l}^{l} D^{l*}_{m,m'}[\alpha,\beta,\gamma]A_l^{m'}(PAS) \qquad (2.25)$$

It is noteworthy that through the change in description the summation now runs over the angular momentum l rather than Cartesian coordinates.
In the simplest case of the calculation of the spectrum of a single crystal the resonance frequencies result from the direct transformation of the chemical shift tensor from the PAS into the laboratory axis system (LAS). The external magnetic field exhibits cylindrical symmetry which is why it is sufficient to describe the rotation into the LAS by only

two angles, θ and ϕ. The last step of the Euler rotation is not accounted for (compare to (c) in figure 2.1). The resulting Hamiltonian is:

$$\mathbf{H_{CS}} = \{\sigma_{iso}\gamma B_0 + \frac{1}{2}\,\delta_{aniso}\,[3cos^2\theta - 1 - \eta sin^2\theta cos(2\phi)]\}\,\mathbf{I_z} \tag{2.26}$$

In the special case of a single crystal not only the eigenvalues are measurable quantities, but also the orientation and with this the Euler angles α, β and γ can be extracted. However, usually the sample consists of a powder of small crystallites with arbitrary orientation towards the external magnetic field. In this case the tensor orientation is lost as information and all the possible alignments towards $\mathbf{B_0}$ have to be included for the calculation of the spectrum. Furthermore, the treatment of multi-spin systems or multi angle spinning (MAS) in the theoretical description each requires the subsequent introduction of intermediate reference axis systems.

For the simulation of the NMR spectrum therefore subsequent steps are carried out. First the single spins are expressed in terms of their irreducible Cartesian components in the principle axis system (PAS) and rewritten in terms of their spherical components. In the next step for each spin the transformation into the crystal axis system (CAS) is carried out leading to one uniform spin system which in the following is transformed as a whole. For MAS spectra it is required to transform the CAS into the rotor axis system RAS. The final step is the rotation into the laboratory axis system (LAS), the frame in which the FID of the experiment is recorded. The solution of the Schrödinger equation or, in the case of a magic angle spinning experiment, the time-dependent Liouville-von Neumann equation yields the energy levels and with this the transition frequencies of the spins.

In this procedure the powder sample is accounted for via the introduction of an average in the last transformation into the LAS. This powder average poses a finite but dense distribution of crystallite orientations expressed via the angles θ and ϕ with respect to $\mathbf{B_0}$. Through this step the lineshape of the spectral density $I(\omega)$ and with this the lineshape of the chemical shift spectrum becomes a function of the average:

$$\int_{\omega_a}^{\omega_b} I(\omega)\,d\omega \;=\; N \int_{\omega=\omega_a}\int_{\omega=\omega_b} P(\theta,\phi)\,d\theta\,d\phi \tag{2.27}$$

N denotes the number of spins and $P(\theta,\phi)$ is the powder average. The calculation of the spectrum requires the solution of equation 2.27. Even though it is possible to find

an analytical expression for the solution in modern simulation programs the integral is solved numerically.

2.3.2 Lineshape analysis

In the practical application two different conventions exist for the description of chemical shift spectra. The *shielding* convention emanates from the physical picture of a shielded nucleus as outlined above. The *deshielding* picture, however, results from the classical development of NMR spectroscopy. Both notations differ in the definition of the shielding tensor:

$$\begin{aligned} \omega_0 &= \omega_0^{ref}(1-\sigma) \\ \omega_0 &= \omega_0^{ref}(1+\delta) \end{aligned} \tag{2.28}$$

It is common to express the chemical shift tensor via σ in the *shielding* convention whereas δ is taken for the notation in the *deshielding* picture (this δ is not to be confused with δ_{uv} as used in the previous section). From theoretical calculations usually σ is gained whereas simulation programs like SIMPSON work with the deshielding convention of δ (despite this differentiation it is also common to use σ_{iso} when describing absolute values of the isotropic shielding as for example resulting from ab initio tensor calculations whereas δ_{iso} denotes a referenced chemical shift, theoretical as well as experimental).
As a consequence of this variety of definitions care has to be taken when using an ab initio calculated tensor for the depiction of simulated NMR spectra or in the calculation of NMR parameters. Whereas the anisotropy δ_{aniso} and the asymmetry parameter η are usually calculated within the shielding convention, the span Ω and the skew κ are in common use with both conventions. In its representation in the PAS the Cartesian chemical shift tensor is given by the three tensor axes σ_{xx}, σ_{yy} and σ_{zz} (see equation 2.10). To distinguish between this general diagonal matrix and the two specific conventions the notation can be changed to σ_{11}, σ_{22} and σ_{33} for shielding and δ_{11}, δ_{22} and δ_{33} for deshielding. In the shielding convention the axes are sorted according to $\sigma_{11} \leq \sigma_{22} \leq \sigma_{33}$ whereas the deshielding convention uses $\delta_{11} \geq \delta_{22} \geq \delta_{33}$.
Figure 2.2 exemplarily shows a wide-line NMR spectrum as depicted for shielding and

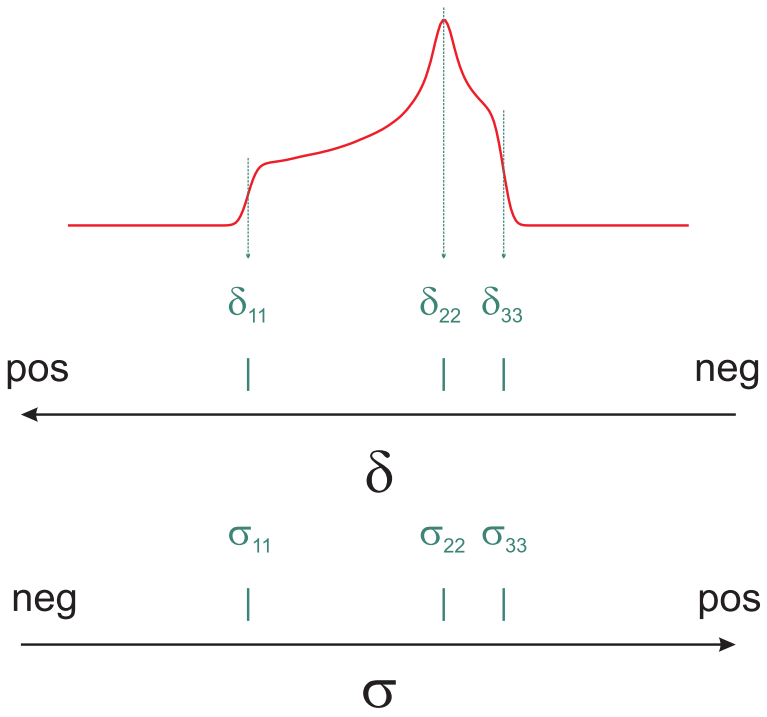

Figure 2.2: Example for the depiction of a wide-line spectrum in the shielding (σ) and the deshielding convention (δ).[84]

deshielding. In the deshielding picture the frequency axis scales from positive to negative values when seen from left to right. With the usual mathematical development from negative to positive values the shielding axis takes the opposite scaling. The principle values δ_{11}, δ_{22}, δ_{33} and accordingly σ_{11}, σ_{22} and σ_{33} can directly be derived from the lineshape of the spectrum. They define the distinct points in the powder pattern which are the foot (left side), the shoulder (right side) and the maximum (middle) of the spectrum. In a real experiment the spectrum usually is broadened (for example due to to inhomogeneities of the magnetic fields) which can be included in the theoretical spectrum by applying a convolution with a Gaussian or Lorentzian function. As a result the foot and the shoulder of the spectrum are defined by the inflection points of the left and right side of the spectrum, respectively (compare to figure 2.2).

It is instructive to compare the development of the Haeberlen-Mehring-Spiess and the Herzfeld-Berger NMR parameters upon a change in the spectral lineshape.[80,84,89] Figure 2.3 shows wide-line spectra with the same anisotropy (or span) and therefore constant values for δ_{11} and δ_{33}. It is convenient to compare the development of the NMR parameters for a continuous shift of the δ_{22} component towards higher field. This development

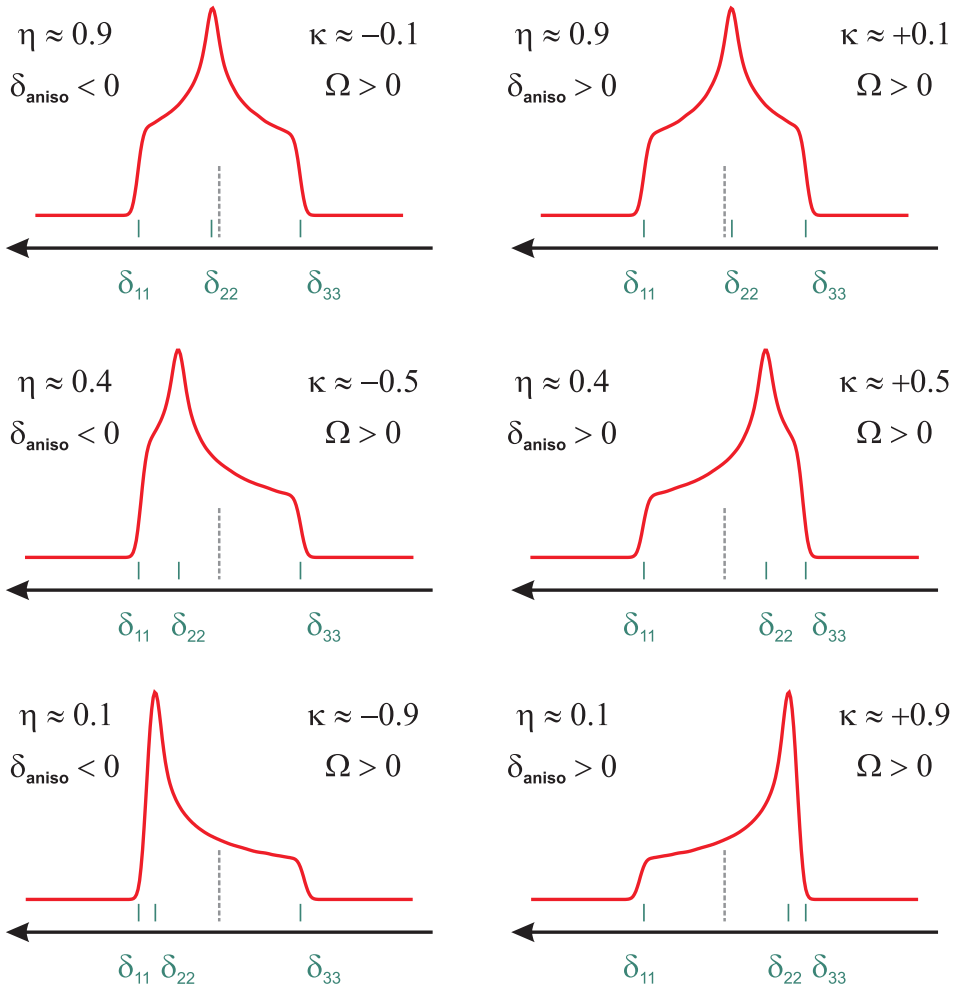

Figure 2.3: Description of wide-line NMR spectra in the Haeberlen-Mehring-Spiess (δ and η) and Herzfeld-Berger (Ω and κ) conventions upon a continuous shift of δ_{22} to higher field; for Haeberlen-Mehring-Spiess the orientation of the spectrum is given in the sign of the anisotropy δ_{aniso} whereas in the Herzfeld-Berger parameters the sign of the skew κ changes.

can be seen when going from the spectrum on the bottom left side via the top spectra to the spectrum on the bottom right side of figure 2.3. With Haeberlen-Mehring-Spiess the overall lineshape is described by the asymmetry parameter η which takes identical values for the different spectra on the left and right side of figure 2.3. The values for η varies between 0 and 1. With $\eta = 1$ the maximum of the spectrum is found in the middle (compare to spectra in the top of figure 2.3). For values below 1 the maximum can either shift to the left or the right side of the spectrum. The direction of this shift is indicated by the

sign of the anisotropy δ_{aniso}.

In contrary to that the span Ω can only take positive values in the Herzfeld-Berger convention and exclusively describes the width of the spectrum. The skew κ varies from -1 to 1 bearing information both about the lineshape itself and the orientation of the maximum in the spectrum.

2.4 Influence of dipole interactions on chemical shift spectra

The tensor of the direct dipolar interaction between two spins i and j is strictly determined by their Cartesian coordinates and can be expressed in a tensor formalism analogous to the chemical shift. The first step again is the definition of the interaction in its PAS (see equation 2.10). The z-axis of the dipole tensor points along the interconnecting line between the spins. In contrary to the chemical shift the dipolar interaction exhibits rotational symmetry with respect to this z-axis. As a result in the dipole interaction η always takes a value of zero. Furthermore, the direction of the x and y axes is arbitrary and only restricted through the demand for an orthonormal coordinate system. Another specialty is that the tensor is purely second rank and therefore exhibits no isotropic part. The coupling constant δ_{DIP} for a spin pair is strictly determined by the distance between and, via the magnetogyric ratio γ, the species of the coupling nuclei i and j:

$$\delta_{DIP} = -\left(\frac{\mu_0}{4\pi}\right)\frac{\gamma_i\gamma_j\hbar}{r_{ij}^3} \tag{2.29}$$

Due to η=0 the angular dependency of the Hamiltonian of two homonuclear dipolar coupling spins reduces to a dependency from only one angle θ when expressed via the powder average:

$$\hat{\mathbf{H}}_{\mathbf{DIP}}^{\mathbf{homo}} = -\left(\frac{\mu_0}{4\pi}\right)\frac{\gamma_i\gamma_j\hbar}{r_{ij}^3}\frac{1}{2}(3cos^2\theta - 1)(3I_zJ_z - \hat{\mathbf{I}}\hat{\mathbf{J}}) \tag{2.30}$$

The lineshape of a system of two exclusively dipolar coupled spins is called a Pake spectrum (see spectrum with two maxima on the left side of figure 2.4).

In a system of *interacting* spins the lineshape of a chemical shift spectrum can be altered by the influence of dipolar coupling. In figure 2.4 the chemical shift anisotropy and the

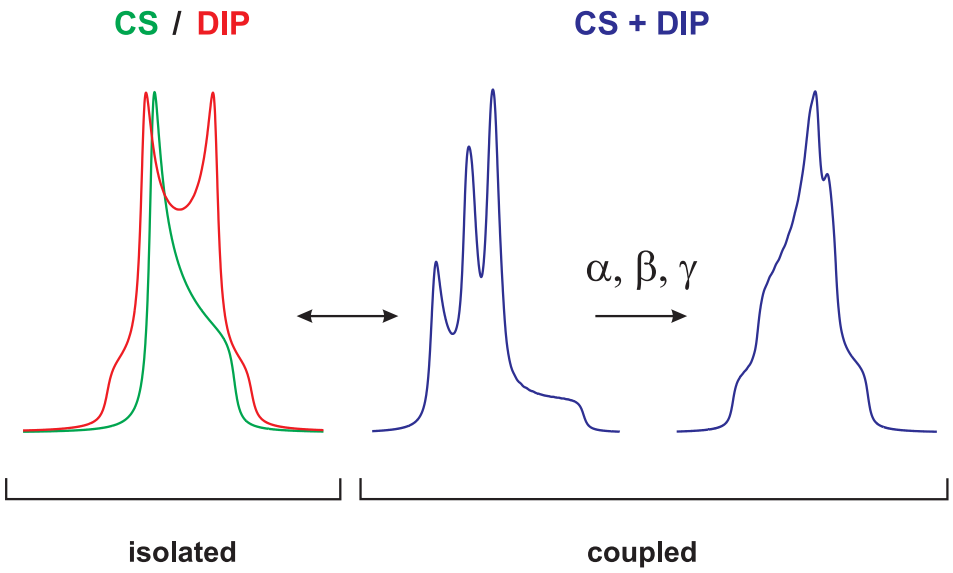

Figure 2.4: Simulated wide-line spectra for uncoupled and coupled spin systems; the influence of the CS tensor orientation in the coupled system becomes obvious.

dipolar coupling constant are of comparable size. The results quite impressively show the influence of a change in the Euler angles of the spin system on the lineshape of the coupled spectrum. For each tensor α, β and γ define the orientation towards the CAS leading to a relative alignment of the CS tensors with respect to the dipole tensor. This alignment markedly influences the strength of the coupling and with this the lineshape. Via a simulation of the spectrum and a fit to the experimental data a lineshape analysis can be carried out indirectly yielding the tensor orientations in the spin system. These orientations are closely related to the local structure of the observed nuclei and therefore bear structural information which are most interesting to extract.

In the general cases though one interaction dominates the other thereby diminishing the influence of coupling to an extent where a lineshape analysis can not yield the tensor orientations anymore. For example a chemical shift spectrum with minor dipolar coupling would receive some broadening but still look like one of the spectra depicted in figure 2.3. In such a situation it is still possible to investigate the tensor orientations. However, more sophisticated strategies have to be chosen to yield this information.

2.5 Two-dimensional rf-driven spin-diffusion spectroscopy

For systems with a dominant chemical shift interaction and weak dipolar coupling the orientation of the chemical shift tensors can indirectly be measured with rf-driven spin-diffusion spectroscopy.[34,90] In principle again the dipole interaction is used to mediate between the single chemical shift tensors as described above. However, the approach follows the strategy of a multidimensional correlation experiment rather than a lineshape analysis.

Figure 2.5 (a) shows the pulse sequence used to correlate the chemical shift tensors. It consists of four distinct periods of time, the preparation, the evolution, the mixing and the detection phase. The experiment starts with the preparation of the spin system of nuclei S (arbitrary $I = \frac{1}{2}$ nuclei) via the transfer of the polarization from the spin system of nuclei I (usually ^{1}H) using cross polarization (CP). In the following evolution period the S polarization is allowed to freely develop. During the evolution and the detection phases the influence of the I spins is switched off by applying a decoupling sequence on the I channel. During the mixing time this is not necessary as the spin lock on S automatically cancels out weak heteronuclear dipolar interactions. After the first evolution time mixing is introduced to the system via a spin lock on the S channel.

Figure 2.5 (b) illustrates the influence of the spin lock on the coupled system of two spins i and j. Without the spin lock all levels of the spins system exhibit different energies and under the constraint of constant energy of the system therefore no exchange between the single states is possible. In contrast to that in the spin lock the mixed states become degenerate allowing for an isoenergetic polarization exchange mechanism called spin flip-flop. Mediated through dipolar coupling one spin changes from m_l=+$\frac{1}{2}$ to m_l=-$\frac{1}{2}$ whereas the other simultaneously changes from m_l=-$\frac{1}{2}$ to m_l=+$\frac{1}{2}$ or visa verse. From the point of view where the whole chemical shift spectrum of a multi-spin system comes into play the spin lock turns the inhomogeneous chemical shift spectrum into a homogeneous spectrum of a dipolar coupled system (see (c) in figure 2.5). The reason for this is that the spin lock scales both the chemical shift as well as the dipole interaction to different extends. The chemical shift interaction is diminished by a factor of about 1000 and thereby vanishes whereas the homonuclear dipolar coupling only scales with the factor s=$\frac{1}{2}$. During the mixing time t_m the spin system therefore freely develops under the

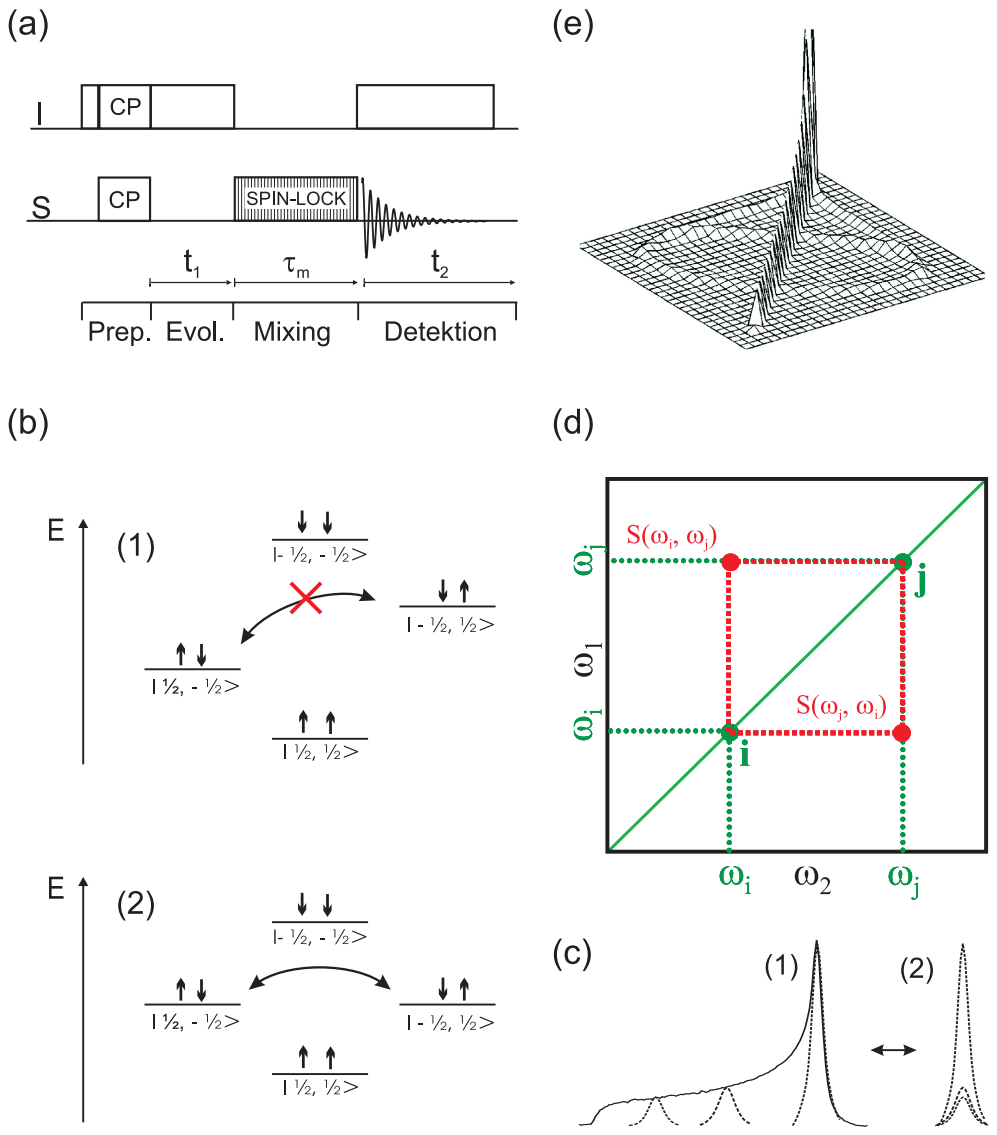

Figure 2.5: 2D rf-driven spin-diffusion spectroscopy: (a) pulse sequence including preparation, evolution, mixing and detection of the spin system; (b) two spin system without and with dipolar coupling; (c) development of an inhomogeneous spectrum in the spin lock; (d) 2D exchange during the mixing time; (e) example of a 2D spectrum for a two spin system with $\eta = 1$.

the influence of homonuclear dipolar coupling.

After the mixing time the spin lock is switched off and the spectrum of the S nuclei is that of a non-interacting system and thus inhomogeneous again. In the detection period the time development of the uncoupled system yields the FID. Through the overall pro-

cedure it is possible to compare the polarization of two spin systems, that is the S nuclei before and after the polarization exchange. This is reflected in the two-dimensional plot as it is exemplarily depicted in figure 2.5 (d) for nuclei with $\eta = 1$. The two axes ω_1 and ω_2 each bear the information of the one-dimensional chemical shift spectrum as depicted on the left side of figure 2.5, (c). The spectral intensity S(ω_i, ω_j) represents the probability of a polarization transfer between two nuclei i and j after the mixing time τ_m. The nuclei are picked out via their resonance frequencies ω_i and ω_j. The signals of two non-interacting spins can be found on the diagonal of the spectrum whereas interacting spins appear off-diagonal. For $\tau_m \mapsto \infty$ all nuclei of the investigated spin system are involved in the polarization transfer and only signals of nuclei with $\omega_i = \omega_j$ (tensors with the same orientation towards $\mathbf{B_0}$) are left on the diagonal.

In simple words the 2D NMR experiment compares the nuclei i and j via their resonances ω_i and ω_j. Through the powder averaging in static samples these frequencies are dependent from the orientation of the respective spins towards the external field $\mathbf{B_0}$ via θ and ϕ, or, in the simple case of $\eta = 1$, only θ. Therefore in principle the 2D spectrum should contain all possible angular orientations as introduced via the powder average and the off-diagonal intensity should spread homogeneously over the 2D plane. However, the experimentally finite mixing time τ_m does not allow for this scenario. It restricts the polarization transfer to local areas. The probability of finding polarization transfer between two nuclei i and j after some mixing time τ_m is proportional to the diffusion rate R_{ij} which again is dependent from the coupling frequency b_{ij} of the dipolar interaction:[91]

$$\begin{aligned} R_{ij} &\propto b_{ij}^2 \\ with \qquad & b_{ij} = -\frac{\mu_0}{4\pi}\frac{\gamma^2\hbar}{r_{ij}^3}\frac{1}{2}(3cos^2\theta_{ij} - 1) \end{aligned} \tag{2.31}$$

Due to the distance dependency of $\frac{1}{r^3}$ in b_{ij} the polarization exchange is restricted to nuclei within a close neighborhood. The polarization transfer during τ_m happens via a rate process which obeys a Markow master equation. Important for an understanding of the 2D spectra is that with this kind of process a limitation in τ_m as well limits the exchange radius, the distance which the polarization transfer is allowed to spread from a given nucleus i during the mixing time. Furthermore, due to the restriction to local transfer via equation 2.31 it is not possible to exchange polarization between different phases as for example different crystallites in a powder sample.

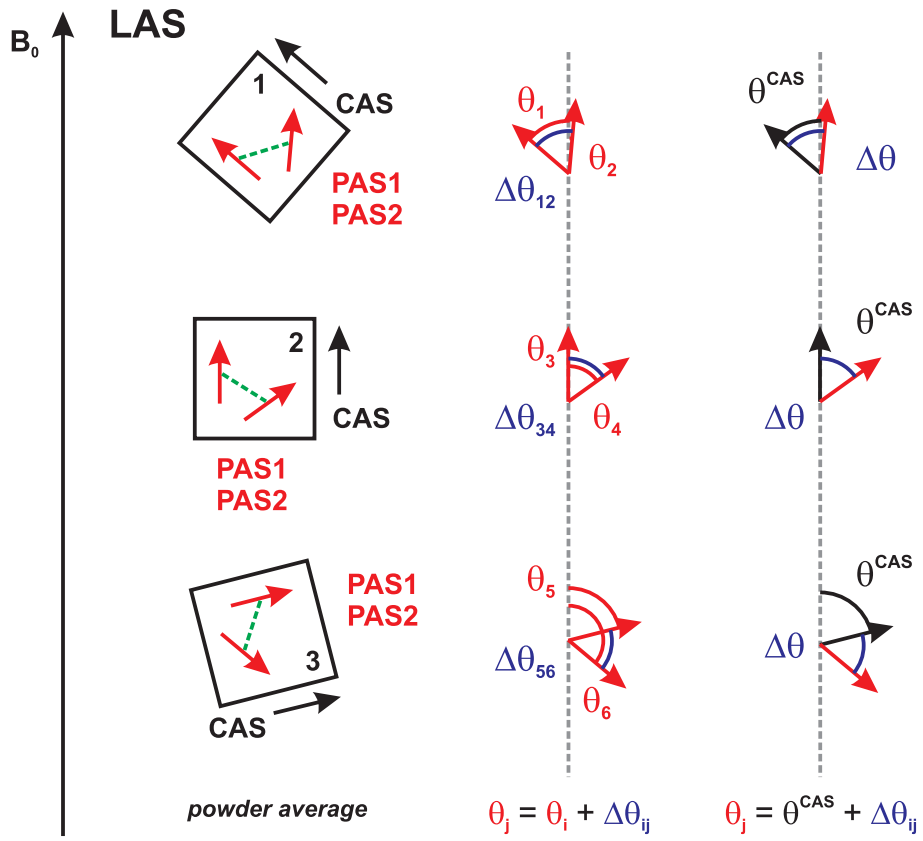

Figure 2.6: Orientations of the laboratory axis system (LAS), crystal axis system (CAS) and principle axis systems (PAS) in a powder sample; the CAS fixes the orientation of a spin i towards the LAS and therewith its resonance frequency ω_i; the resonance ω_j of the second spin j is then given through the fixed orientation $\Delta\theta$ between PAS1 and PAS2, at which point the Euler angles of the spin systems are introduced into the 2D exchange spectrum.

Figure 2.6 shows the projection of an ensemble of spin systems into two dimensions. The external magnetic field B_0 defines the laboratory axis system (LAS). In the sample single crystallites are arranged resulting in a powder average of the crystal axis system (CAS) with respect to the LAS. Finally each crystalline phase consist of a spin system given by the principle axis systems (PAS) of the single spins. During the mixing time polarization exchange takes place in each separate crystallite (in the given example this means exchange between two spins i and j). One fixed orientation of the CAS with respect to the magnetic field defines a special resonance frequency ω_i for spin i. In the

case of polarization exchange with a neighboring spin j the resonance frequency ω_j can not take arbitrary values anymore as it is predefined by the fixed orientation between the principle axis systems of the tensors of the spins i and j. In a simplified term the frequency of spin j is given by $\omega(\theta_j) = \omega(\theta_i + \Delta\theta)$ or, if the CAS is fixed to the orientation of spin i, $\omega(\theta_j) = \omega(\theta^{CAS} + \Delta\theta)$ (compare to figure 2.6). For this reason the 2D exchange spectra directly correlate the orientation of different chemical shift tensors as given by the Euler angles α, β and γ.

The result is a spectrum with typical ridges which represent the individual spin systems. Figure 2.5 (e) shows an example of a 2D spectrum for $\eta = 1$. For $\eta \neq 1$ the powder distribution additionally introduces the angle ϕ and so the resonance frequency becomes a function $\omega(\theta, \phi)$ leading to a more complex form of the ridges. In multi-spin systems these ridges create patterns that are highly characteristic for the local environment and can be used in a fingerprint-like manner to distinguish between different structure models.

However, for such a procedure it is essential to know about the orientation of the chemical shift tensor towards the local structural building block. This information is readily available through a quantum chemical calculation of the NMR tensor. Naturally the ab initio calculated tensor can also be used for a full characterization of the spin system via the NMR parameters described above. Therefore the computation of the NMR chemical shift is a crucial step for the connection of a measured spin system to a structure model.

2.6 The ab initio calculation of the chemical shift tensor

The quantum mechanical derivation of nuclear shielding starts with the Hamiltonian which describes the energy of electrons in a magnetic field. In non-relativistic closed-shell systems the interaction of the electron spin with the magnetic field as well as spin-orbit interactions can be neglected. Then the Hamiltonian of a single electron in a magnetic field defined by the vector potential $\mathbf{A}$ is given by:

$$
\begin{aligned}
H &= \frac{1}{2m}\left(\mathbf{p}+\frac{e}{c}\mathbf{A}\right)^2 + V = H_0 + H_{10} + H_{20} \qquad (2.32)\\
H_0 &= \frac{1}{2m}\mathbf{p}^2 + V\\
H_{10} &= \frac{e}{mc}\mathbf{A}\cdot\mathbf{p}\\
H_{20} &= \frac{e^2}{2mc^2}\mathbf{A}^2
\end{aligned}
$$

$\mathbf{p}$ is the momentum of the electron, V the nuclear potential, e and m are the charge and the mass of the electron and c is the velocity of light. H_0 denotes the Hamiltonian of the electron without the influence of a magnetic field. The field strength $\mathbf{B}$ of a homogeneous magnetic field is related to the vector potential as:

$$\mathbf{A}(\mathbf{r}) = \frac{1}{2}\mathbf{B}\times(\mathbf{r}-\mathbf{R}) \qquad (2.33)$$

$\mathbf{R}$ is a fixed point in space, called the 'gauge origin'. The vector potential is well defined except for the arbitrary choice of the gauge origin.

Equation 2.32 takes the form of an expansion as known from perturbation theory which can be further applied to get the eigenvalue E and eigenfunction ψ as a function of the external magnetic field. H_{10} is the linear perturbation term of H_0 whereas H_{20} is the second quadratic. Through equation 2.33 both contributions to the Hamiltonian become gauge dependent.

All measureable quantities must be independent from the choice of the gauge origin. This means that in an exact solution of the Schrödinger equation E as well as its derivatives with respect to the field strength $\mathbf{B}$ must be gauge independent, too. However, the wave function ψ will depend on $\mathbf{R}$ and therefore the contributions to the perturbation expansion. The energy and wave function can be expressed as

$$
\begin{aligned}
E &= E_0 + E_{10} + E_{20} + ... \qquad (2.34)\\
\psi &= \psi_0 + \psi_{10} + \psi_{20} + ...
\end{aligned}
$$

Through perturbational treatment one gets

$$E_{10} = \langle\psi_0|H_{10}|\psi_0\rangle \tag{2.35}$$

$$\begin{aligned} E_{20} &= E_{20}^d + E_{20}^p \\ &= \langle\psi_0|H_{20}|\psi_0\rangle + Re\langle\psi_0|H_{10}|\psi_{10}\rangle \end{aligned}$$

where ψ_{10} is the solution of

$$(H_0 - E_0)\psi_{10} = (H_{10} - E_{10})\psi_0 \tag{2.36}$$

Usually no permanent magnetic moment is present in the system and E_{10} is zero. The second order perturbation then yields the tensor of the magnetic susceptibility with the diamagnetic and paramagnetic contributions E_{20}^d and E_{20}^p (compare to equations 2.35):

$$E_{20} = E_{20}^d + E_{20}^p = -\frac{1}{2}\sum_{\alpha,\beta} B_\alpha \chi_{\alpha\beta} B_\beta \quad ; \quad \alpha,\ \beta = x,\ y,\ z \tag{2.37}$$

Both E_{20}^d and E_{20}^p are strongly gauge dependent. In the summation this dependency cancels if equation 2.36 is solved exactly. If this is not the case the diamagnetic contribution which is expressed via ψ_0 is obtained quite accurately whereas the paramagnetic contributions can exhibit large errors due to its dependency from ψ_{10}. In an isolated atom the natural choice of the gauge origin would be the center of the nucleus where E_{20}^p=0 and E_{20}^d can be evaluated easily. However, in molecules no natural choice for $\mathbf{R}$ exists and the gauge origin is chosen such that the error with respect to the exact solution of equation 2.36 is as small as possible even for a small basis of the wavefunction.

In the calculation of chemical shifts altogether two interactions of the electron have to be taken into account. The first one is the interaction with an external magnetic field $\mathbf{B}$ as described above, the second is the interaction of the electron with the magnetic field $\mathbf{B_N}$ created by the magnetic moment of the nucleus. Therefore the vector potential $\mathbf{A}$ in

equation 2.32 has to be expanded to $\mathbf{A} + \mathbf{A_N}$. Now the first label of the Hamiltonians is taken to count the order of $\mathbf{A}$ whereas the second is taken for the order of $\mathbf{A_N}$:

$$H = H_0 + H_{10} + H_{01} + H_{11} + H_{20} + H_{02} \tag{2.38}$$

$$\begin{aligned} H_{01} &= \frac{e}{mc}\mathbf{A_N} \cdot \mathbf{p} \\ H_{11} &= \frac{e^2}{2mc^2}\mathbf{A} \cdot \mathbf{A_N} \end{aligned}$$

In the interaction with the atomic magnetic moment of the center of the nucleus ρ can be taken as a natural choice for the gauge origin in the expression for $\mathbf{A_N}$:

$$\mathbf{A_N} = \frac{\mu \times (\mathbf{r} - \rho)}{|\mathbf{r} - \rho|^3} \tag{2.39}$$

With this choice again only the gauge of the external magnetic field remains arbitrary. An analogous expansion of the energy as shown above leads to

$$E_{11} = E_{11}^d + E_{11}^p \tag{2.40}$$

$$\begin{aligned} E_{11}^d &= \langle \psi_0 | H_{11} | \psi_0 \rangle \\ E_{11}^p &= 2Re\langle \psi_0 | H_{01} | \psi_{10} \rangle \end{aligned}$$

E_{11} is related to the chemical shielding tensor via

$$E_{11} = \sum_{\alpha,\beta} \mu_\alpha \sigma_{\alpha\beta} B_\beta \quad ; \quad \alpha,\ \beta = x,\ y,\ z \tag{2.41}$$

Alternatively this expression can be written in terms of a second-order response property via the second derivative of the energy

$$\sigma_{\alpha,\beta} = \left[\frac{\partial^2 E}{\partial B_\alpha \partial \mu_\beta} \right]_{B=0,\mu=0} \quad ; \quad \alpha,\ \beta = x,\ y,\ z \tag{2.42}$$

Apart from the mathematical formulas the interactions of the electrons can be understood in an atomistic picture. The external field induces a current density in the molecule which again induces a magnetic field by itself. The interplay of this induced field with the external magnetic field arises diamagnetism whereas the interaction with the nuclear moment causes the chemical shielding.

Both second order terms E_{20} and E_{11} are derived equally and the discussion about the gauge dependency of E_{20}^{d} and E_{20}^{p} is fully transferable to E_{11}^{d} and E_{11}^{p}. The solution to the gauge problem nowadays is carried out by using distributed gauge origin methods like IGLO (*individualized gauges for localized orbitals*) or GIAO (*gauge-including atomic orbitals*). The difference between both methods is that IGLO uses a formalism where the individual gauge is build into localized molecular orbitals whereas in GIAO the gauge origin is set for the atomic orbitals. In this latter approach the orbitals are written as

$$\chi_{\mu}(\mathbf{r},\mathbf{B}) = exp\left\{\frac{ie}{2c\hbar}(\mathbf{B}\times(\mathbf{R}_{\mu}-\mathbf{R})\cdot\mathbf{r})\right\}\chi_{\mu}^{(0)}(\mathbf{r}) \tag{2.43}$$

$\chi_{\mu}^{(0)}(\mathbf{r})$ is the zero-field wave function at the location $\mathbf{R}_{\mu}$. Upon the evaluation of the Hamiltonian with the field-dependent basis functions $\chi_{\mu}(\mathbf{r},\mathbf{B})$ neither $\mathbf{R}$ nor $\mathbf{R}_{\mu}$ enter the final expressions but only the difference vectors $\mathbf{R}_{\mu}$ - $\mathbf{R}_{\nu}$. Additionally each matrix element carries its individual gauge origin at the center of the basis function associated with this matrix element. All this significantly reduces the error which occurs due to the choice of the gauge origin.

Both IGLO and GIAO base on a Slater determinant as approximation for the many electron wave function and therefore are of the Hartree Fock type of theory. As a consequence single electron equations are solved in the ansatz and electron correlation is not taken into account. However, GIAO and IGLO usually perform well and the inclusion of correlation is only necessary if very high accuracy of the results is aspired. One possibility is to use MP2-GIAO, that is second order Møller-Plesset perturbation theory in a GIAO basis. Another way is the use of density functional theory where electron correlation is partly recovered in the exchange correlation functional E_{XC} on an empirical base. In practical applications DFT is a preferred choice as it is capable of calculating large systems in an adequate time frame. Nevertheless care has to be taken as a special problem arises with DFT in the presence of a magnetic field. Here the unequivocal assignment of an electron density to the potential of the ground state of a system as proposed by the Hohenberg-

Kohn theorem is not valid anymore. Beside the dependency from the electron density $\rho(\mathbf{r})$ the correct expression for E_{XC} should include the current density $j(\mathbf{r})$ which is induced by the magnetic field:

$$E_{XC}[\rho(\mathbf{r})] \Longrightarrow E_{XC}[\rho(\mathbf{r}), j(\mathbf{r})] \tag{2.44}$$

Proposals for $E_{XC}[\rho(\mathbf{r}), j(\mathbf{r})]$ are called current density functionals. Even though implementations of these functionals exist they are still in a phase of early development. Fortunately it could be shown that the general shortcomings of exchange correlation functionals surpass the influence of the current density on the results.[86] Therefore from a pragmatical point of view all standard implementations of DFT/GIAO which are available use the exchange correlation functional in its classical form of $E_{XC}[\rho(\mathbf{r})]$. This is taken as a well working approximation to the correct theoretical description.

Chapter 3

Results and Discussion

3.1 Modeling strategies

The comprehensive task of the here presented work was to develop strategies for the structure determination in ordered and disordered solids using theoretical calculations as a modeling tool. The aim was to extract structural information from the comparison of ab initio chemical shift data with results from solid-state NMR experiments.

To accomplish such a task in a first step a theoretical structure model has to be developed. This model should contain as many information about the investigated system as possible. In the easiest case this means that an already solved X-ray structure needs to be confirmed and can directly be taken as a base for the structure model. A successful geometry optimization of this model which leads to a stable arrangement comparable to the experiment then poses a verification of the structure by itself. However, in the more difficult cases no atomistic details of the system are known and therefore a purely theoretical structure has to be modeled ab initio.

In the next step the such derived structure models can be taken as a base for the computation of the NMR chemical shift tensors. To yield as accurate results as possible the structures are turned into minimal models which comprise all atomistic interactions exerting influence on the local site of interest and therefore can describe the NMR properties close to reality. During this process it is important to consider the two major influences on the NMR tensors. One is the structure of the system itself which on the one hand should

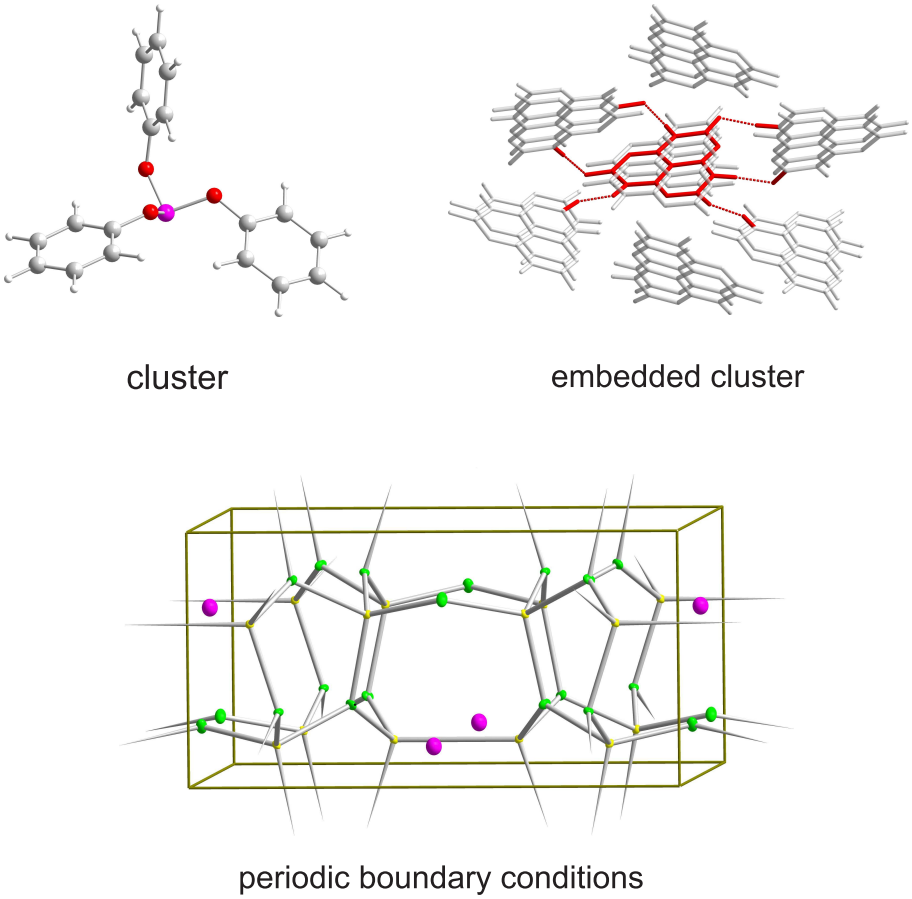

Figure 3.1: Different implementations of theoretical calculations on the atomistic level: molecular systems can be described by an isolated cluster of nuclei and electrons (top left); in the embedded cluster approach large molecular systems are subdivided in separate regions (dark gray central region and gray coordination sphere) which then can be treated with different levels of theory (top right); extended networks require the description via a unit cell with fractional coordinates for the atom positions (bottom).

resemble the real system but on the other hand has to be described on a theoretical level close to the method used for the calculation of the NMR data. The second important factor is the quality of the wavefunction which describes the electronic environment in the model and thereby can have a large impact on the NMR values. Both factors are interconnected because the smaller the model becomes the better the wavefunction can be described.

A rich diversity of techniques is available for modeling purposes. They can be applied depending on the nature and size of the investigated system as well as the accuracy nee-

ded in the description of the structure or desired property. The basic theories are implemented following two principle strategies. In the cluster ansatz the calculated structure is described as an independent system of nuclei and electrons in vacuo. This method is well suited for a description of isolated non-interacting molecules ('cluster' in figure 3.1). The opposite extreme is the case of an extended covalently bonded 3D network. Such a case is best described under periodic boundary conditions (bottom of figure 3.1). The model then comprises a unit cell and atomic positions expressed as fractional coordinates both of which can be relaxed in a geometry optimization. For the computation of large non-periodic systems which are too big to fully be treated on a high level of theory the embedded cluster ansatz can be chosen. Here the central region of interest can be tackled with high level methods whereas the surrounding environment is still included in the model but treated on a lower level of theory ('embedded cluster' in figure 3.1). An advantage of this method is that the different levels of theory can be combined in an arbitrary fashion. Table 3.1 gives an overview over the methods and their implementation as available in the program packages Gaussian03 and MS Modeling4.0 which were used in this work.

With force field methods large systems up to 30000 atoms can easily be tackled. Such methods are well suited for the calculation of large systems or the quick screening of a large number of smaller systems. The structural optimization can be carried out either in molecular clusters or under periodic boundary conditions. As within force field theory all interactions are treated via empirically fitted potentials one of their advantages is that van

Tabelle 3.1: Overview over modeling techniques as implemented in the packages gaussian03 and MS Modeling 4.0 which were used in this work; the maximum system sizes which can be tackled with the respective method are given with the approximate number of atoms.

method	size	implementation	application
force field	30.000	cluster/PBC	structure†
semiempirical	1.000	cluster	structure
HF	∼200	cluster	structure/NMR
DFT	∼200	cluster/PBC	structure/NMR
MP2	30-50	cluster	structure††/NMR

† includes a good description of van der Waals interactions
†† only single point calculations available in practical application

der Waals interactions are explicitly included in the theory. However, a disadvantage is that without the customization of the force field itself only systems can be tackled which are well specified by the given potentials. Furthermore, force fields pose a classical way of treating the system and do not include a description the electrons. In the here presented context this method can thus only be used to calculate the structure of a model but not its NMR property. In general an optimized force field structure has to be further relaxed with for example DFT methods to serve as a base for the computation of the chemical shift on this higher level of theory.

Semiempirical methods allow for sizes of about 1000 atoms. These methods were exclusively available in the cluster implementation. They allow for a quick computation of relatively large systems and bear the advantage that the structural description is close enough to higher level methods to directly serve as a base for the computation of the chemical shift tensors with DFT and moderate basis set sizes.

Hartree Fock and DFT methods can be used in systems with a maximum size of about 200 atoms. Whereas historically HF is the base for a whole group of high level methods, among them MP2, the workhorse in practical applications nowadays is density functional theory. This method was available both in the cluster and the periodic implementation and allows for the accurate computation of the structure as well as the NMR properties of a system.

In the context of practical applicability the highest precision can be gained from the perturbational MP2 method thereby decreasing the number of atoms to about 50 in its maximum. Due to its high demand for computer ressources and time this last method is seldom used for geometry optimizations but rather in single point calculations for rather small molecular clusters. The MP2 method recovers about 80% of the electron correlation in the system and therefore gives a highly accurate description of electronic properties as for example the chemical shift tensor.

Nowadays computation clusters offering ressources of up to four CPUs and large main storage are publicly available without any restriction of the user time. These ressources are sufficient to treat most systems which is why within the scope of this work no sophisticated hardware such as supercomputers was used. Necessarily this restricted the available system sizes and the level of theory in the treatment of the solid state. For this reason the modeling strategy itself was emphasized and the abovementioned methods were applied individually dependent from the question at hand.

3.2 The practical application of modeling to condensed solid-state systems

The investigated solid-state phases covered a broad area of possible organic systems. This included completely and partially disordered phases as well as semi- and fully crystalline structures. The variation ranged from phases built up by non-interacting molecules and aliphatic as well as aromatic hydrogen bonded molecular systems to layered compounds comprising of 1D linked polymeric strings in a hydrogen bonded system and covalently bonded 2D networks (compare to figure 3.2). This is the order in which the following text leads through the publications given in the appendix of this work (publications A - F). For each example an introduction into the system is given followed by a short explanation of the modeling strategies applied for the structure and the NMR properties. The

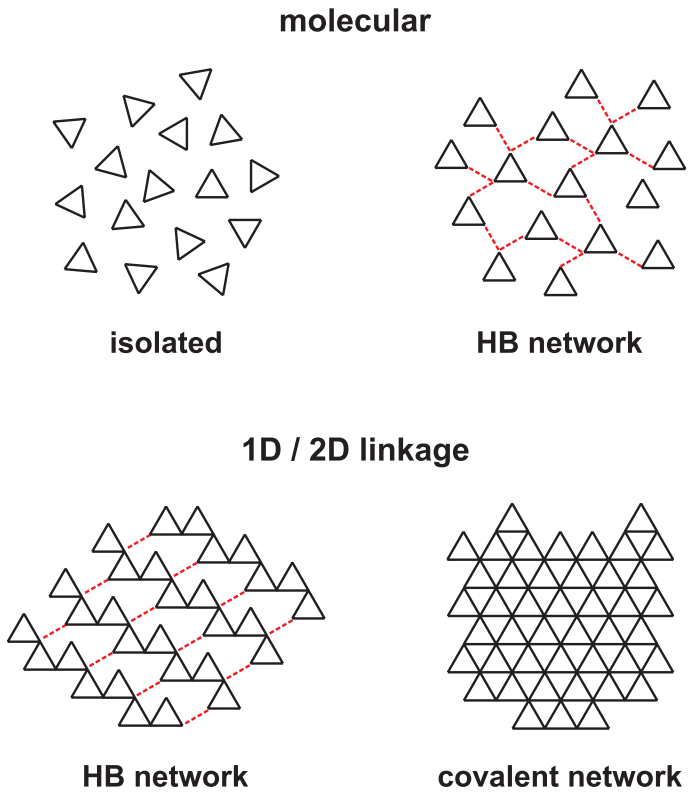

Figure 3.2: The solid-state systems treated within the scope of this work ranged from disordered over partially ordered to fully crystalline phases. These phases comprised of isolated molecules, molecular systems with hydrogen bond interactions, polymeric strings interconnected via hydrogen bonds and covalently bonded 2D networks.

most important accomplishments in the context of structure determination via theoretical modeling are summarized.

3.2.1 Molecular structure - isolated

Starting with a system of non-interacting molecules triphenylphosphite (TPP) shows a most interesting phase behavior which is why it was chosen for a deeper investigation (publication A). Four distinct solid-state phases of TPP are known and it shows both the phenomena polymorphism and its equivalent counterpart in disordered phases, polyamorphism. Upon cooling molten TPP develops a supercooled liquid prior to the formation of a molecular glass (phase aI). Furthermore, two different polymorphs, c1 and c2, are known to exist. c1 crystallizes from the supercooled liquid aI whereas c2 is obtained from solutions of TPP in ionic liquids. However, the challenging task was the determination of the unknown structure of the second amorphous phase aII. Provided the appropriate heating conditions this outstanding phase of TPP can as well be prepared from the supercooled liquid aI. Even though aII is overall disordered it was suspected to comprise of small clusters with the same conformational order and intermolecular arrangement as found in the crystalline phase c1.
The task included a direct measurement of these conformers and clusters via NMR. The key method in this context was rf-driven 2D spin-diffusion spectroscopy. For the measurements it was necessary to introduce selectively isotope labeled sites into the TPP molecule which was carried out in a seven step synthesis starting from 1-[^{13}C]-sodium acetate. The ab initio simulation of 1D and 2D spectra on the base of theoretical models posed the interconnection between the NMR experiments and the proposed TPP structure. The such combined methods resulted in a self-contained concerted approach which was successfully applied in a conformational analysis for tri-(1-[^{13}C]phenyl)-phosphite.
In all of the investigated phases aI, aII and c1 the binding interaction between the molecules is restricted to weakly attractive van der Waals forces. Thus the influence of the condensed phase on the structural distortion of the individual molecule mainly results from packing effects which indirectly change the conformation of the molecules. This situation could well be modeled with the use of DFT for isolated TPP molecules. The level of theory was calibrated to the best match with the X-ray solution of the crystalline phase c1 leading to highly accurate structures with only small deviations from the experiment. On this base a conformational analysis of TPP was performed which resul-

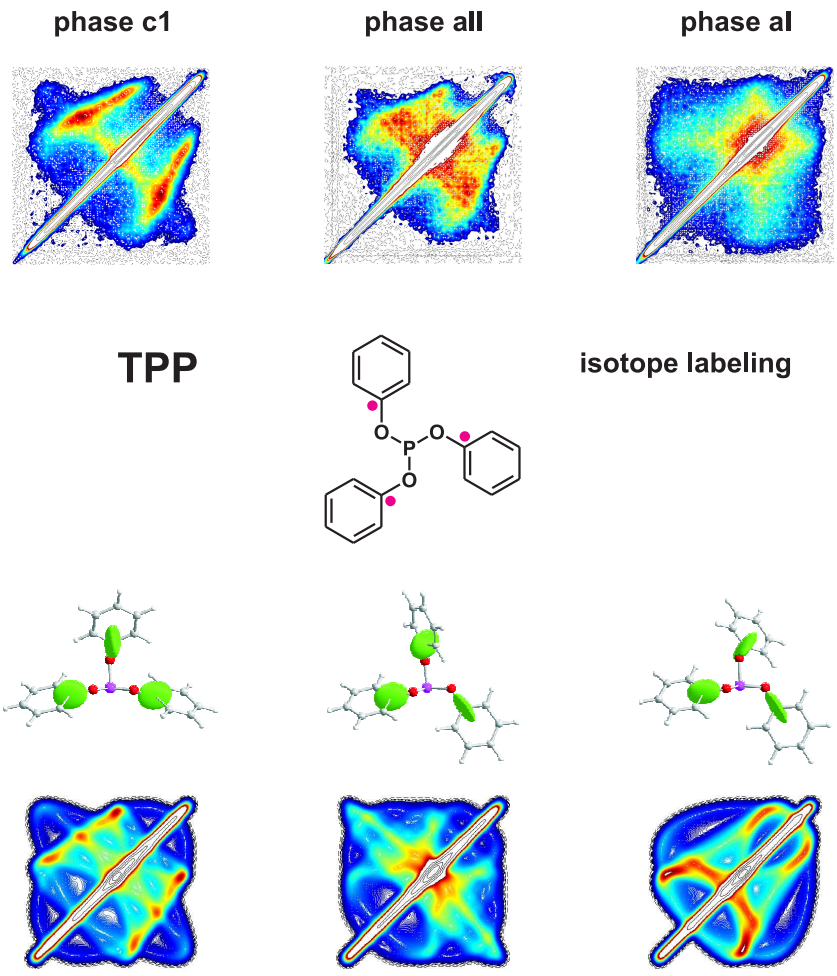

Figure 3.3: The three phases aI, aII and c1 of TPP could clearly be distinguished by rf-driven spin-diffusion spectroscopy measurements on tri-(1-[^{13}C]phenyl)-phosphite (top and middle, the spectra are given for a chosen mixing time of t_m = 10 ms); simulations on three spin systems for $t_m \rightarrow \infty$ showed that this method is highly sensitive to the orientation of the CS tensors (green ellipsoids) of the three labeled sites and directly reflect the arrangement of the phenyl moieties in the single molecules.

ted in seven distinct arrangements of the molecule. These structures posed the base for the calculation of the chemical shift tensor and the ab initio simulation of NMR spectra. Furthermore, the occurrence of small TPP clusters was tested on a model comprising of two molecules. The perturbational calculation of the pair formation energies of different arrangements including the correction of the basis set superposition error revealed that the more a TPP pair seek a parallel arrangement of the molecules the better such a cluster is stabilized. This result strongly supported the assumption of small clusters with an

arrangement as found in c1 as in this phase as well the molecules are parallel aligned.
1D MAS measurements of the well known phase c1 were taken for a comparison with the ab initio calculated NMR parameters δ_{iso}, δ_{aniso} and η of the seven theoretical TPP models to investigate the potential for a conformational analysis in such a crystalline phase. It was found that a structural assignment in c1 can not be carried out by an interpretation of the chemical shift δ_{iso} alone but becomes unequivocal upon using a combination of both the isotropic chemical shift δ_{iso} and the asymmetry parameter η. However, phases aI and aII could not be investigated by MAS spectroscopy which is why the same analysis was carried out for 1D wide-line spectra. In contrary to the high resolution MAS technique it turned out that the resolution of the wide-line spectra is far too low to allow for a conformational analysis in either of these phases.
The only chance for the investigation of the conformers in the disordered TPP phases aI and aII was therefore given with advanced two-dimensionally resolved NMR experiments like the here used rf-driven spin-diffusion spectroscopy. With this technique the local order in phase aII could for the first time unequivocally be shown (compare to the clearly distinct 2D spectra of the overall disordered phase aI and phases aII and c1 in figure 3.3). The similar shape of the 2D patterns in phase aII and the fully crystalline phase c1 implied similar conformational arrangements. To further investigate the influence of the conformational arrangement on the spectral pattern for all of the seven model structures simulations of the 2D experiment were carried out. Figure 3.3 exemplarily shows the 2D patterns of three chosen conformers, only one of them comprising of a wing-like pattern similar to the one found in phase c1. In fact the conformer associated with this pattern resembles the molecular arrangement as found in the crystalline phase. Furthermore, upon the comparison of simulations for highly similar conformers vastly distinct 2D patterns were found clearly revealing the large sensitivity of the here used method to the molecular arrangement (compare middle and right conformer in figure 3.3).
However, even though in principle it could be stated that aII and c1 must comprise of the same TPP conformer the difference in the spectral patterns of both phases, namely the intense bridge rectangular to the diagonal of the spectrum occurring for aII but not for c1, could not be explained. For this reason the structure model of a static conformational arrangement was expanded to include variations of the two distinct phenyl moieties in the molecule (see 'C1' and 'C2' in figure 3.4). It was found that especially variations about the middle phenyl moiety exert a strong influence on the 2D pattern and leads to a bridge

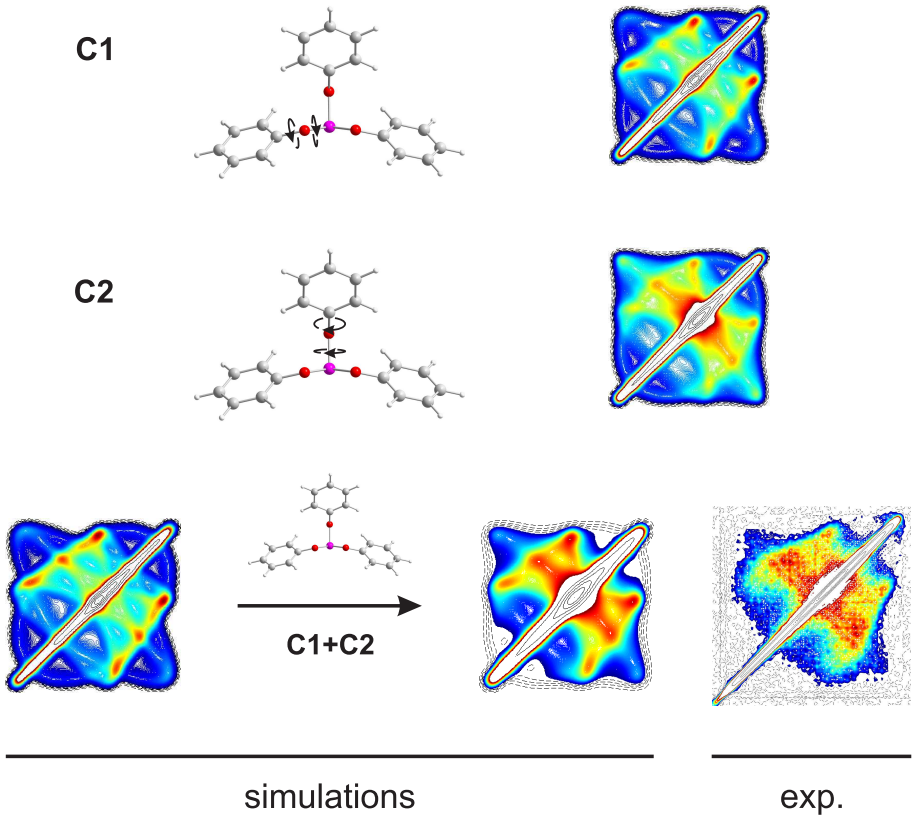

Figure 3.4: The static structure model (bottom left) was extended to include distortions of the phenyl moieties about the P-O and the O-C bonds ('C1' and 'C2'); whereas small variations about the 'C1' moiety does not lead to pronounced changes in the spectral pattern changes in 'C2' exert a strong influence; the experimental pattern of phase aII could be explained by a distortional distribution of the phenyl moieties about one preferential conformer (bottom right).

exactly as observed in the spectrum of phase aII. With distortions about the P-O and O-C bonds of 'C1' and 'C2' of 30 - 40° it was possible to propose a structure model which reflected all important spectral features of the pattern observed for phase aII (bottom of figure 3.4).

These findings reveal the methodological power of the combination of ab initio calculations with rf-driven spin-diffusion spectroscopy measurements. Even in the difficult case of the disordered phase aII experimentally the local order could unequivocally be proven. The simulations allowed to connect this order to a structure model of a preferential conformer. Furthermore, a structural distribution about the preferential conformer was

revealed. An examination in such a high detail is hardly possible with any other analytical method which probably is the reason why the structure of phase aII remained the topic of a heated and controversial debate for such a long time.[21,90] The results emerged from this work very much helped to get a clearer picture of the structural features of phase aII.

However, even though 2D rf-driven spin diffusion spectroscopy prove to be an especially sensitive probe to the local structure this method requires large signal intensities for a sufficient resolution of the 2D patterns. It is restricted to nuclei which occur in high abundance such as ^{31}P or demands isotope labeling as in the case of ^{13}C. Thus it can not be used in a standard analysis of structural features by NMR but is only applied in cases where simpler methods fail to succeed. The next topic focuses exactly on such simpler methods, namely the analysis of ^{13}C 1D MAS measurements on different polymorphs of Prednisolone in natural abundance.

3.2.2 Molecular structure - aliphatic with hydrogen bonding

The work about the (pseudo-)polymorphism of Prednisolone arose from a collaboration with PD Dr. C. Näther in Kiel (publication B and figure 3.5). Two pure phases, form **I** and **II**, and one sesquihydrate were crystallized and investigated with X-ray diffraction, DSC and thermomicroscopy. In the further structural analysis by solid-state NMR and theoretical modeling the confirmation of the X-ray structure by the full assignment of the ^{13}C NMR spectrum was aimed at. In addition, the question of the thermodynamical stability of **I** and **II** was raised.

Prednisolone comprises of a 3D network of hydrogen bonds. Because the X-ray structures of **I** and **II** were already solved from single crystals they could directly be taken as a base for the calculation of the structure and evaluation of the thermodynamic stability. These computations were carried out with force field methods under periodic boundary conditions. The results showed a maximum deviation from the experimental lattice of about 3% and even though the optimization was carried out in $P1$ symmetry and therefore no constraints were applied the exact crystal symmetry of both phases was conserved. The calculated polymorphs nearly perfectly matched with the experimental structures and it was revealed that form **II** is the thermodynamic stable phase. This finding agrees with the results from solvent mediated conversion experiments between the two polymorphs and the outcome of DSC experiments.

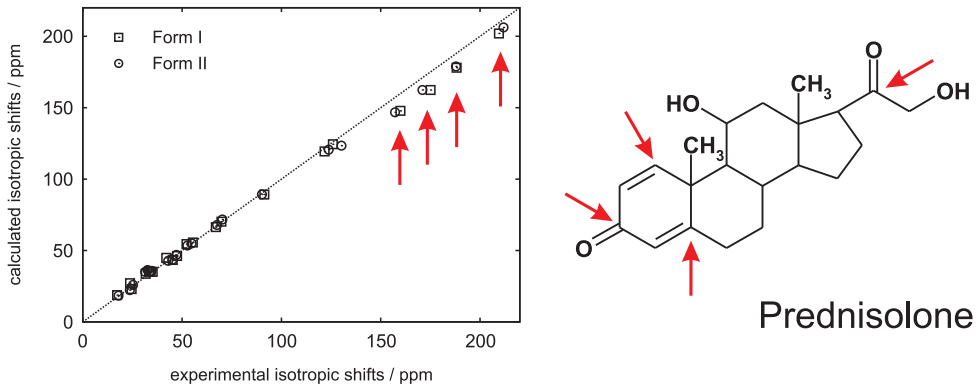

Figure 3.5: Correlation between ab initio calculated and experimental values of the isotropic chemical shift (a guide for the eye which represents perfect correlation is added); above 120 ppm deviations of up to 12 ppm occurred due to the lacking description of hydrogen bonding in the model; the electronic environment of the π systems in prednisolon proofed to be particularly sensitive to the surrounding environment (arrows).

The computation of the ^{13}C NMR chemical shifts was carried out on isolated Prednisolone molecules cut from the respective X-ray structure. To account for the generally poor description of the hydrogen positions in the X-ray structure a geometry optimization of the H atoms was carried out with the semiempirical PM3 method. During this process the dihedral angles of the H atoms were constrained to anticipate a rotation of the OH groups. The ^{13}C chemical shift tensors were further calculated with DFT in the cluster approach. Through this procedure the structural influence of the hydrogen bonding environment of the condensed phase was explicitly included in the models whereas the electronic effect was excluded.

In general the calculated isotropic chemical shifts showed a good agreement with the experimental values (see figure 3.5). Above 120 ppm deviations of up to 13 ppm occurred which could exclusively be assigned to nuclei involved in π bonding. The systematically lower theoretical values revealed a deshielding of these nuclei caused by the hydrogen bonding in the real structure. The neighboring carbon atoms of the OH groups involved in hydrogen bonding did not show such a sensitivity towards the lacking electronic environment. Here the structural arrangement, namely the distortion of the OH group, was sufficient to model the isotropic chemical shifts with good accuracy.

In the context of the work the isotropic chemical shifts could be used for a complete assignment of the experimental spectra. However, form **I** and **II** could not be distinguished

on the base of the structure model of isolated molecules. The models therefore were extended to include the full first coordination sphere of hydrogen bonding. Even though the match of the isotropic shifts with the experiment improved still no unequivocal distinction was possible with their values alone. However, similar to the investigations in the crystalline phase c1 of TPP a distinction of the polymorphs **I** and **II** using the anisotropy δ_{aniso} and the asymmetry parameter η was tried. It showed that the π bonded nuclei not only exhibit a value of δ_{aniso} large enough to be measured in a MAS experiment at low rotational frequencies, but also the parameter η of three of them are sensitive to the hydrogen bonding environment to an extend that η can be taken for a distinction of the different polymorphs by NMR spectroscopy. This is especially true for the C=O carbon of the carboxyl group (compare to figure 3.5). Even though an interesting result in the context of structure determination with NMR no further attempt was made to try such an analysis as the structures of form **I** and **II** were already known from single crystal measurements and the phases only needed to be characterized.

All the calculations performed within this work were quick and computationally undemanding. Therefore these techniques can serve as a standard analysis in the investigation of polymorphism and for the verification of a proposed X-ray structure. In cases where the X-ray structure is not unequivocally known the development of a theoretical model is more demanding. The next example deals with exactly this situation in the structure solution of microcrystalline cyameluric acid. Again a hydrogen bonded environment was investigated and because cyameluric acid comprises of an extended π system the sensitivity of the parameters of the anisotropy of the carbonyl group towards their environment could be brought to practical use.

3.2.3 Molecular structure - aromatic with hydrogen bonding

The X-ray structure solution of cyameluric acid from powder diffraction data proved a challenging task which demanded for the combined analysis of X-ray data, solid-state NMR spectra and computational results alike (publication C). Instead of complicated 2D spectra the NMR analysis based on simple 1D chemical shift patterns which were elucidated for the isotropic chemical shift δ_{iso} in the case of ^{15}N and δ_{iso} as well as the anisotropy δ_{aniso} and asymmetry parameter η for ^{13}C.

Little was known about the cyameluric acid molecule itself. From the literature a broad range of tautomeric forms posed possible candidates for the structure solution. Some but

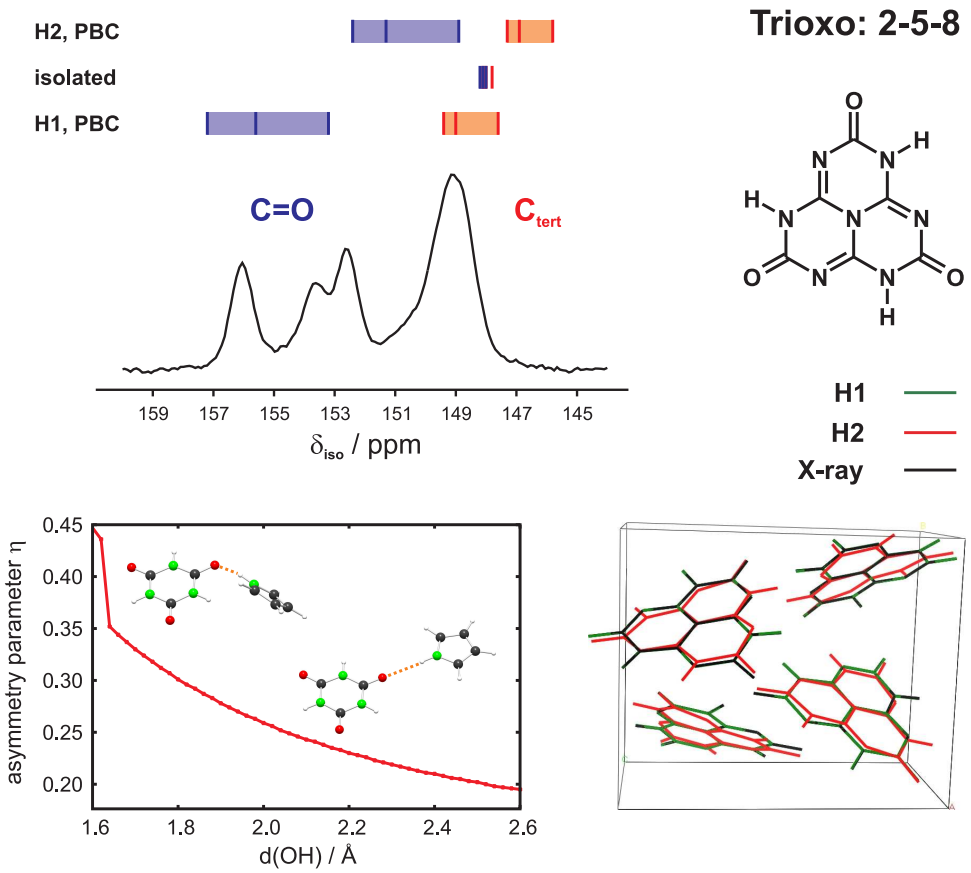

Figure 3.6: The X-ray structure of cyameluric acid could be solved with the 2-5-8 tautomer (top right); the ^{13}C spectrum showed a shift of the C=O signals which could not be explained by calculations of the isolated molecule (top left); the dependency of the carbonyl ^{13}C tensor with respect to its environment was investigated for a small model system and the sensitivity of the asymmetry parameter η towards hydrogen bonding shown (bottom left); from the two possible HB networks H1 and H2 in cyameluric acid H1 could unequivocally be chosen on the base of a comparison of the NMR data of H1 and H2 calculated with DFT under PBC and the experimental ^{13}C and ^{15}N CS parameters (bottom right and top left).

not all of them could be excluded on the base of the ^{1}H NMR spectrum. For the remaining systems a DFT geometry optimization of the isolated molecule with the subsequent calculation of the ^{13}C and ^{15}N NMR tensors was carried out. It showed that the combined chemical shift data from both nuclei was well suited for an assignment to the experimental spectrum and the choice could be narrowed down to the 2-5-8 tautomer of cyameluric acid (see figure 3.6, top right).

The ^{13}C data, however, were largely influenced by the effect of deshielding of the C=O groups by hydrogen bonding to the surrounding environment (see figure 3.6, top left). This sensitivity of the carbonyl ^{13}C tensor was further investigated in a chemically similar model system of cyanuric acid and pyroll. The environment was varied via a scan of the OH distance in the system in which the intermolecular arrangement of the molecules were allowed to freely relax. This resulted in a couple of test structures with linear and distorted arrangements of pyroll with respect to the cyanuric acid and for each structure the ^{13}C tensor was evaluated. The results showed a pronounced sensitivity of the isotropic shift δ_{iso} but as well of the parameters δ_{aniso} and η of the anisotropic part of the tensor (see figure 3.6, bottom left). This structural dependency applied to the intermolecular distance d(OH) as well as to the distortion of the hydrogen bond.

After the successful application of direct space methods still two possible X-ray structure solutions remained. Due to the uncertain localization of the hydrogen atoms the two hydrogen bonding networks H1 and H2 were still possible (compare to figure 3.6, bottom right). We distinguished between these models on the base of DFT structure optimizations and NMR chemical shift calculation in both the cluster as well as the PBC approach. Due to the large system size in the cluster approach an embedded cluster calculation based on a central molecule together with the complete first coordination sphere cut out from the crystal structure proposal was set up (compare to 'embedded cluster' in figure 3.1). The central region was fully optimized on DFT level whereas the remaining structure was described with the semiempirical PM3 method and held rigid during the optimization. This large model therefore included a full electronic description of the hydrogen bonded molecule and the structural relaxation took place within the potential of the rigid environment of the first coordination sphere. The resulting minimum was taken as a base for a DFT calculation of the ^{13}C and ^{15}N NMR parameters. In this calculation the model was further reduced to one central cyameluric molecule with six hydrogen bonded aromatic ligands (see publication C for more details). In the PBC approach the two X-ray structure solutions H1 and H2 could directly be taken as an input for the DFT optimization and subsequent CS tensor calculations.

For both types of calculations the optimized structure of model H1 deviated least from the X-ray solution. The comparison of the theoretical and experimental NMR data as well preferred H1 over H2. As only relative values were taken for a comparison the decision for the final structure could not be met on the base of the ^{13}C chemical shift alone as it

was highly similar between H1 and H2 (compare to the relative ^{13}C shifts in figure 3.6). The match between the calculated and experimental ^{15}N shifts is better for H1. However, the unequivocal assignment came from a comparison of the anisotropic parameters of the ^{13}C tensors. The average anisotropy δ_{aniso} differs significantly between H1 and H2 with the value of H1 resembling the experiment. In addition to that the asymmetry η of H1 perfectly matches with the experiment whereas the values of H2 largely deviate.

From both the calculations in the cyanuric acid - pyrrole model system as well as in the cyameluric acid the impact of an analysis of the anisotropic part of the chemical shift tensor for structure determination became obvious. In the context of cyameluric acid it was used for the verification and falsification of the hydrogen bonding networks H1 and H2 which resulted from X-ray structure proposals. However, the sensitivity of the carbonyl ^{13}C tensor towards its environment seemed large enough to try to even take a further step and use it for the ab initio prediction of hydrogen bond arrangements. For this reason cyameluric acid was taken as a test case for the prediction of the C=O$\cdots$H-N environment via the comparison of NMR data with theoretical values from the cyanuric acid - pyrrole model system.

An in depth study of the dependencies of the anisotropic part of the carbonyl ^{13}C chemical shift tensor from the intermolecular arrangement of the model system was carried out (see publication D). For this a maximum of six intermolecular parameters, all closely connected to structural changes about the hydrogen bond, was taken into account leading to NMR hypersurfaces for the isotropic shift δ_{iso}, the anisotropy δ_{aniso} and the asymmetry parameter η (see figure 3.7). These hypersurfaces were stepwise investigated via the subsystems $\chi\{\tau_1, \tau_2\}^{\tau_3=fix,\ldots\tau_n=fix}$ (χ denotes the investigated NMR parameter and τ the chosen structural parameters two of them being varied whereas all remaining are kept fixed to a set value).

The creation of such surfaces required a quick and effective way of producing whole sets of arrangements which was done with the semiempirical PM3 method. The DFT optimized rigid bodies of the pyroll and the cyanuric acid molecule were combined to form a hydrogen bonded model. In this system the intermolecular variables as occurring in figure 3.7 were permuted and for each of the test structures the ^{13}C tensor calculated with DFT. The extraction of the NMR parameters then yielded the hypersurfaces. As such large systems could not be treated by hand anymore all tasks, from the generation of the different arrangements and calculation of the NMR tensors via the extraction and

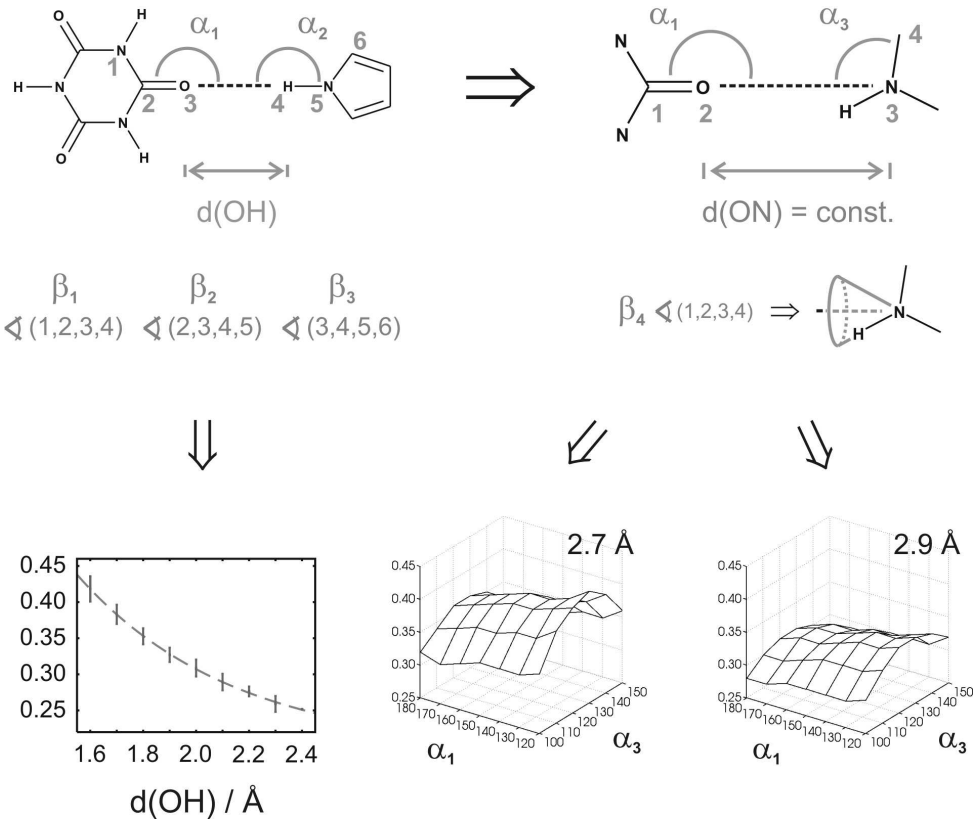

Figure 3.7: For the purpose of predicting the C=O$\cdots$H-N environment in cyameluric acid two models were build, each comprising of cyanuric acid and pyroll (top left to right: reduction of the variables in the models); on the base of these systems hypersurfaces dependent from all of the depicted variables were calculated - as examples the mean value of η as a function of d(OH) and the subsurfaces $\eta\{\alpha_1,\alpha_3\}^{d(NO)=2.7\text{Å},\beta_4=250^\circ}$ and $\eta\{\alpha_1,\alpha_3\}^{d(NO)=2.9\text{Å},\beta_4=250^\circ}$ are shown (bottom left to right); the curvatures of the α_1/α_3 surfaces are very similar, therefore it is possible to convert them into one another by the application of a shift and a mean factor.

investigation of the hypersurfaces and finally the structure prediction from given NMR parameters, were automated via self-written scripts.

The first structure model (top left of figure 3.7) comprises of six structural parameters. The analysis showed that only one of them, β_1, has no pronounced influence on δ_{aniso} and η whereas all others have to be included in a good HB model. The O$\cdots$H distance has the largest impact on the NMR parameters with the mean values following an exponential behavior (see bottom left in figure 3.7). However, the hypersurfaces $\chi\{\tau_1,\tau_2\}^{\tau_3=fix,\tau_4=fix}$ of the angular dependencies show an individual curvature thus

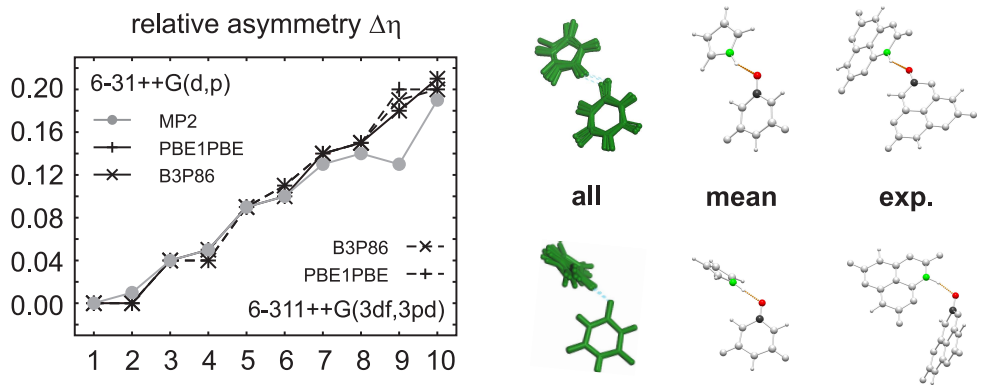

Figure 3.8: With a medium sized basis set DFT describes the relative change of η upon structural changes of the HB as good as on the high MP2 level of theory; on the base of the relative η values of the reduced model system two of the three C=O$\cdots$H-N environments in cyameluric acid could be predicted with high accuracy.

making it impossible to find a similar universal function. These findings were problematic in the sense that the number of variables in the system could not markedly be reduced and the dependency of the NMR parameters from the HB structure remained quite complicated.

In a second model system therefore a reduction of the structural variables was carried out via the coupling of the parameters of the first model in a new description (top right in figure 3.7). The N$\cdots$O distance was fixed to two different values known from the crystal structure solution of cyameluric acid. Such only three structural variables, two angles and one distortion remained in the model. The choice prove fortunate as it could be shown that the η surfaces take a much simpler shape and for the two distances can mathematically be transformed into one another by the subsequent application of a simple shift and factor (see subsurfaces bottom left in figure 3.7).

This second model was further used for the C=O$\cdots$H-N structure prediction in cyameluric acid through an evaluation of the hypersurfaces on the base of the relative values of δ_{aniso} and η derived from ^{13}C measurements. The relative values were taken because they appeared to be highly robust against changes in the theoretical description. The here used combination of DFT with a moderate sized basis set gives results equal to calculations with a very large basis set and even to a perturbational treatment of the system (figure 3.8, left side). It could be proven that a given combination of the anisotropic NMR parameters δ_{aniso} and η unequivocally chooses a set of highly similar HB arrangements from the hypersurfaces. This is an important result as it poses the necessary condition for

the use of these parameters for structure prediction. Furthermore, a mean structure was calculated from the extracted ensembles and compared to the X-ray structure of cyameluric acid (compare to the right side of figure 3.8). For two of the three hydrogen bond environments the overall C=O$\cdots$H-N arrangement could be predicted with high accuracy. For the third bond at least the N$\cdots$O distance could correctly be determined. These results clearly show the possible application of the anisotropic part of the carbonyl ^{13}C chemical shift tensor in the structure prediction of hydrogen bonding environments.
In the last examples it became obvious that the NMR parameters of extended π bonded systems are extremely sensitive to the description of the electronic environment. For a realistic modeling of the hydrogen bonding either large molecular clusters which at least included all molecules of the interacting first coordination sphere or calculations under periodic boundary conditions had to be used. In the systems which are presented next the degree of linkage is increased by covalent bonding introduced in one as well as two dimensions of layered systems. This leads to an even higher sensitivity of the calculated NMR parameters to the modeling technique, especially because these layers consist of aromatic systems. In crystals then the most accurate description is given with PBC. However, for such a calculation a unit cell has to be given and the question arose how to practically build such cells from sketch.

3.2.4 Polymeric system - 1D linkage with hydrogen bonding

On the search for graphitical C_3N_4 in the workgroup of Prof. Dr. W. Schnick at the LMU in Munich a C/N/H sample was prepared through the pyrolysis of melamine resulting in a semicrystalline phase. During the difficult task of structure elucidation which was carried out in a collaboration project a broad analytical repertoire was applied (see publication E). X-ray powder diffraction revealed a layered substance with a high state of disorder between the layers. IR and NMR measurements consistently proved the presence of NH and NH_2 groups and it could be shown that the sample consists of a homogeneous phase. However, the final breakthrough towards a structure proposal could be managed by TEM measurements which showed strings of bridged syndiotactically arranged melem units matching the picture of polymeric melon (compare to '2D' in figure 3.9). Whereas the two-dimensional structure of the single layers could safely be extracted from the TEM data the interlayer arrangement remained a topic of debate. Therefore a combination of structural modeling, the calculation of the ^{13}C and ^{15}N tensors and the comparison to

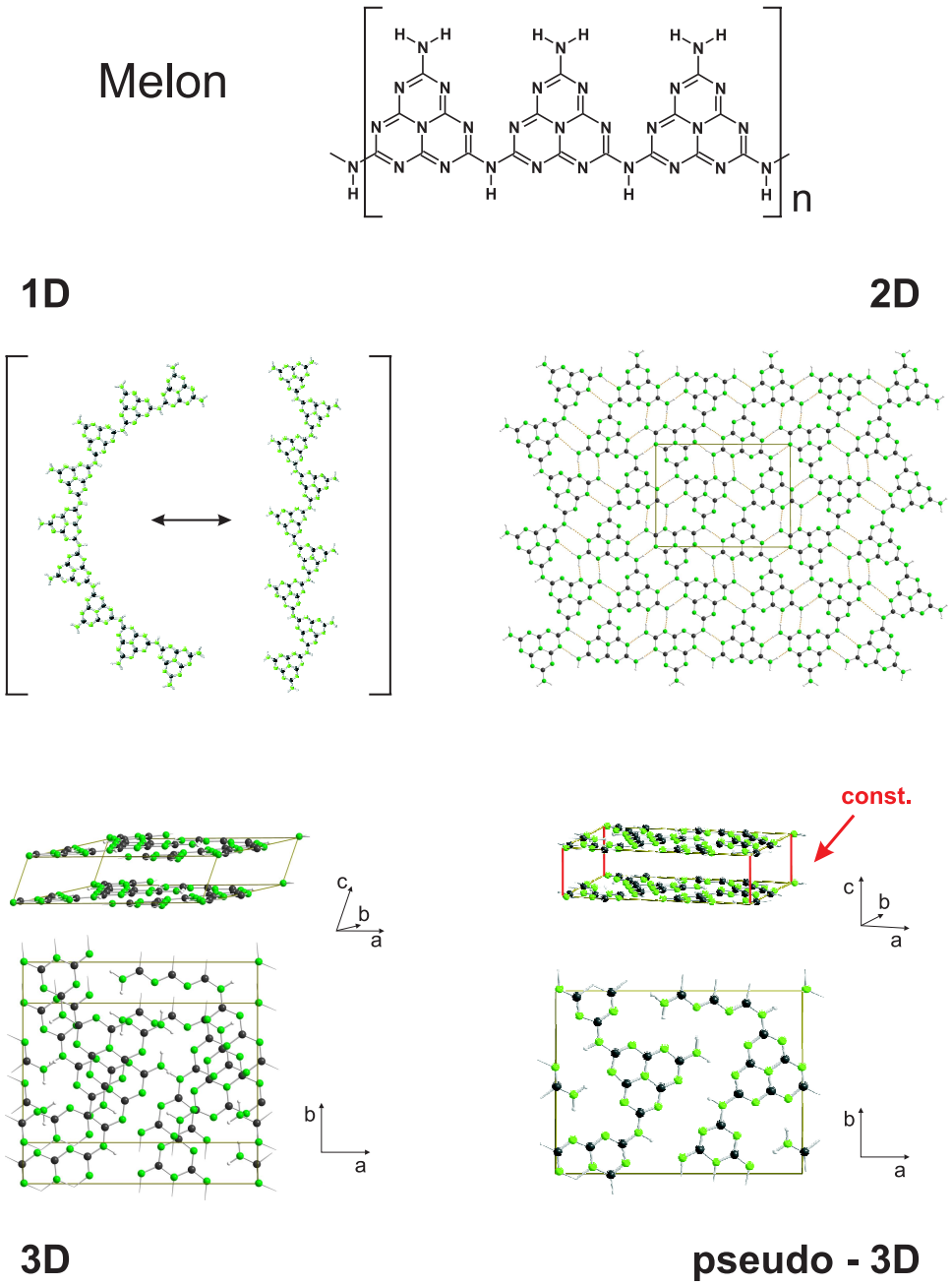

Figure 3.9: Structure determination in a semicrystalline sample of polymeric melon (top); the structure model was systematically increased: starting from one-dimensional strings over a 2D linked HB network to a pseudo-3D description via an orthorhombic unit cell with a constraint slab between the layers; a full 3D model allowed for proposals for the interlayer arrangement and the interlayer distance as found from X-ray diffraction could be confirmed.

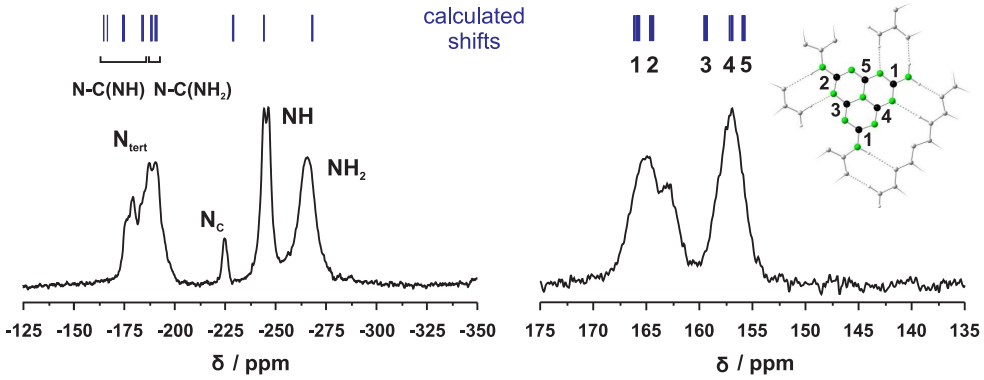

Figure 3.10: DFT calculated ^{13}C and ^{15}N isotropic chemical shifts for the pseudo-3D model (see also figure 3.9); all experimental signals could be assigned thereby confirming the 2D structure solution from TEM measurements.

measured chemical shift spectra was employed for the necessary verification of the TEM structure on the one hand and the creation of proposals for the three-dimensional arrangement on the other hand.

In this context 3D unit cells were modeled from sketch by the stepwise application of a broad variety of different techniques. The approach started with the geometry optimizations on melon clusters. A single 1D linked melon string was relaxed in the two possible periodic arrangements, one isotactic the other one syndiotactic ('1D' in figure 3.9). The isotactic string relaxed into a significantly bent structure and thus the syndiotactic variant clearly is preferred for the formation of periodic structures. In a next step a 2D layer was built from such syndiotactic melon strings. The optimized structure revealed a tightly bonded network with a maximum of possible HB interactions (figure 3.9, '2D'). This structure therefore posed a stable model for a single layer and could serve as a base for the DFT calculation of NMR tensors under PBC. For this purpose from the middle of the PM3 cluster a periodic region was cut out and used for the construction of an orthorhombic pseudo-3D cell with a constrained interlayer slab of 4.43 Å (compare to figure 3.9, 'pseudo-3D'). The such created unit cell was optimized under the contraint of the fixed interlayer distance which resulted in a system of DFT optimized layers in an AAA... stacking. Both the PM3 cluster calculation as well as DFT under PBC matched well with the TEM structure within the margin of the experimental error.

The ^{13}C and ^{15}N isotropic chemical shifts from the pseudo-3D DFT model were compared to the experimental NMR spectra (see figure 3.10). Through the fixed distance of

4.43 Å only minor influence of the van der Waals interactions occur between the layers and the calculated NMR data therefore represent the 2D model of single sheets rather than a full 3D model of the phase. Both the ^{13}C and ^{15}N chemical shifts match well with the NMR spectra. The CPPI assignment of the ^{15}N spectrum could be confirmed from the calculations and an assignment of the ^{13}C signals be carried out (figure 3.10).

Furthermore, a full 3D description of the unit cell was sought. The AAA... stacking as comprised in the pseudo-3D model does not pose a logical structure because the repulsive interactions between the layers are maximized. The search for a more suitable interlayer arrangement was carried out in small steps introducing an interlayer shift in the a/b plane starting from the pseudo-3D cell. This approach required the optimization of many different input structures which is far too costly when carried out by DFT. Additionally, the binding dispersion interaction between the layers is only badly described in density functional theory. Therefore the screening was done by with force field methods.

Releasing the constraint slab the orthorhombic pseudo-3D model retained its AAA... stacking and relaxed into a structure with an interlayer distance of 3.4 Å. From X-ray diffraction, however, the distance was estimated to about 3.2 Å therefore excluding this structure model as a possible choice. Additionally the eclipsed arrangement was highest in energy of all calculated variants. Two other stable arrangements were found with an offset stacking along a and b, both lower in energy than the eclipsed structure ('3D' in figure 3.9 shows the cell shifted along b as an example). They exhibit an interlayer distance of 3.2 Å which is well in accordance with the X-ray data. However, from powder diffraction a disordered state of interlayered arrangement was proposed which still is a topic of investigation in the ongoing research on the melon phase.

In this work semiempirical and force field methods were successfully used for building and screening model systems. Due to the low computational cost this process not only bore the advantage of quick calculations but also the results agreed well with the experimental data. Atomic positions as extracted from cluster calculations could be used to build periodic cells from sketch therefore delivering input structures for the calculation under full periodic boundary conditions and with that for the accurate calculation of NMR data with DFT.

3.2.5 Layered structure - 2D linkage

In all the so far presented examples, from TPP over prednisolone to cyameluric acid and melon more or less detailed structural data from diffraction experiments already existed and could be integrated in the development of model systems. However, the last study presented in this work deals with graphitical C_3N_4, a system for which no experimental structure is available (see publication F). Its composition and conformation are unclear and controversially discussed in the literature. Up to today no bulk synthesis for this system has succeeded. With this the system was ideal to apply a screening approach on a broad scale in which a large number of possible structures was tested. Furthermore, the question was raised how the ^{13}C and ^{15}N chemical shift tensors could be calculated in fully linked aromatic systems where no periodic cells are available and therefore DFT under PBC can not be applied.

All existing structure proposals for g-C_3N_4 are derived from an analogy to graphene. They span from condensed melamine sheets in a trigonal or an orthorhombic linkage to condensed melem based systems in a trigonal linkage (see figure 3.11 for examples of the trigonal linkage with melamine and melem). In addition to these condensed 2D layers hydrogen bonded cyclic melon is of interest for the synthesis of g-C_3N_4. It poses a possible intermediate and therefore was as well investigated.

The screening was carried out with the semiempirical PM3 method in the cluster approach. The comparison of structures resulting from this technique with DFT calculations revealed a qualitatively good structural match. Starting from a single melamine or melem subunit the respective layer was subsequently increased leading to a large ensemble of clusters of different sizes and linkage types. From the geometry optimizations the orthorhombic melamine based layers could immediately be excluded from the possible structure models because systems consisting of more than twelve condensed subunits failed to produce a stable electronic environment.

The general question in the structural investigation was whether the analogy to graphene from which g-C_3N_4 is derived is justified, or in other words, whether these systems really exhibit planar layers. For this purpose all the investigated clusters were optimized in a planar arrangement as well as in a corrugated version. In both the melamine as well as the melem system the corrugated species prove to be energetically more stable (see energy diagram in figure 3.11). Moreover, the source of the corrugation could be determined to repulsive NN contacts within the sheets. A standardization of the energy to the number

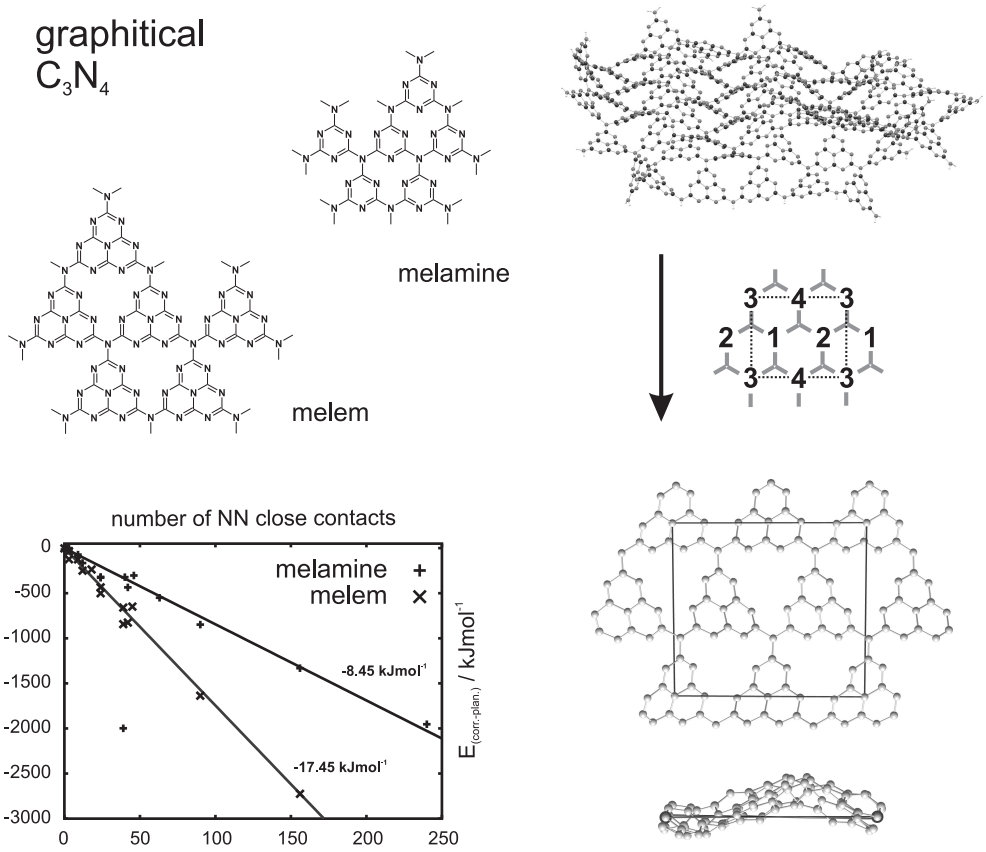

Figure 3.11: In the investigation of graphitical C_3N_4 melamine as well as melem based layers were tested (top); due to repulsive interactions caused by NN close contacts for both types the corrugation of the sheet lead to a significant gain in energy (bottom left); for corrugated melem based C_3N_4 a proposal for a periodic cell could be extracted from the structure of the optimized cluster (right).

of NN sites in the clusters leads to a linear increase in the energy difference between corrugated and planar layers. The melem based layers gain about twice as much energy upon corrugation as the melamine based species and therefore pose the energetically favored systems. In the cyclic melon phase corrugated systems as well are lowest energy.
An advantage of the here chosen cluster approach was that the structures were allowed to freely develop and did not have to follow any symmetry constraints during the optimization runs. Such the distortion of the layers lead to a disorder in the local environments as can well be found in an amorphous material. However, in addition to such disordered arrangements the question of the possible structure of a crystalline material was raised and therefore the largest optimized clusters were closely investigated. It turned out that

for the melem as well as the cyclic melon species the corrugation did not fully occur in a random manner but that regions with a regular arrangement of melem subunits could be found as well (compare to the upper left region of the corrugated melem cluster depicted in figure 3.11). From these ordered regions it was possible to extract the minimal periodic assembly of the melem moieties (right side of figure 3.11). This lead to 2D structure proposals for regular layers which in future works can serve as a base for the construction of unit cells and optimization with DFT methods as was shown in publication E.

Finally the task of the theoretical calculation of the ^{13}C and ^{15}N NMR parameters on the base of the biggest of the optimized structures was tackled. In particular interesting was the outcome for the corrugated layers. As they contained a large number of differently distorted local environments the influence of this distortion on the chemical shift parameters would become apparent. However, in the cluster approach the treatment of such large systems was a non-trivial task.

At first the influence of the limited size and therefore the hydrogen saturation at the border of the clusters had to be investigated. This was carried out for planar and corrugated clusters of the same conformation but with different sizes. PM3 was used for the geometry optimization followed by the calculation of the CS tensors with DFT. Such the convergence of the NMR parameters of the central building block with respect to an increase in the cluster size could be investigated (for more details see publication F). It turned out that the planar and therefore fully aromatic systems are extremely sensitive to border effects. To be able to calculate the NMR parameters of the central unit a minimum of four coordination spheres has to be taken into account. In the corrugated systems the aromaticity is cut down mainly to the local building blocks which shows in a much less sensitive NMR parameters. Here it is sufficient to include two coordination spheres to obtain converged parameters for the central unit.

With this knowledge it was possible to calculate the NMR properties of the respective systems. Still some effort had to made as the above described results clearly stated that a single calculation of a whole cluster would end up in severely different descriptions of the NMR observables at the different local sites of the cluster. In the case of the planar systems this did not pose a problem as due to the intrinsic periodicity it was sufficient to only extract the parameters from the central building unit of a large cluster. For the corrugated systems, however, subclusters, each comprising of a central unit with two coordination spheres, subsequently had to be cut out from a large cluster describing the

overall phase. The central building block in each of these models now represented one local environment of the corrugated cluster and was analyzed with respect to its NMR properties. As this approach involved the treatment of large amounts of data and many different structures the overall procedure it again was automated by self-written computer scripts.

Such the theoretical NMR spectra of the trigonal melamine and melem based and the cyclic melon systems could be presented (see publication F). For the corrugated systems a statistical analysis of the NMR parameters was carried out resulting in mean values and distribution ranges caused by the different distortions in the local environments. For this statistical description it was important to take the span Ω and the skew κ to express the anisotropic part of the chemical shift tensor as in the alternative description via δ_{aniso} and η the parameter δ_{aniso} exhibits a discontinuity for η = 1. The resulting ab initio chemical shift spectra and anisotropy parameters can be used for a future identification of g-C_3N_4 phases by solid-state NMR even if only amorphous samples can be obtained from synthesis.

Summary

The intention of this work was the application of modeling to condensed solid-state systems for the sake of the structure determination and prediction. Besides structural modeling this included the ab initio calculation of the chemical shift tensor which was taken for the simulation of various solid-state NMR experiments and the comparison to NMR measurements.

In this context it was necessary to create a tool which could deal with the analysis of spin systems from arbitrary ab initio calculations. This was accomplished by the development of the Gau2Sim program library. The application of the included functions to a chemical shift tensor yields the isotropic chemical shift δ_{iso} and the anisotropic information in its two established conventions, either expressed via the anisotropy δ_{aniso} and the asymmetry parameter η or via the span Ω and the skew κ. Additionally the tensor orientation as given by the Euler angles α, β and γ can be extracted.

On the base of this tool the combined approach of structural and NMR modeling was applied to the structure determination in a broad range of disordered, semi-ordered and fully crystalline phases. These systems varied from phases comprising of isolated molecules over hydrogen bonded molecular as well as polymeric phases to covalently bonded two-dimensional layered compounds. For the structural modeling in these environments the advantages of force field and semiempirical methods, density functional and perturbation theory calculations were combined with the description of the systems in the cluster or embedded cluster approach as well as with calculations under periodic boundary conditions. Such it was possible to directly validate structure proposals from diffraction measurements or to screen the structure of yet unknown phases on a broad range. In the latter case low level methods like force field or semiempirical calculations prove especially useful and could serve as a source for the extraction of unit cells from molecular

clusters for purpose of calculations under periodic boundary conditions thereby interconnecting both techniques.

The NMR properties of the phases were investigated in minimal structure models in this process testing all parts of the chemical shift tensor for their applicability for structure elucidation. Its easiest measurable parameter is the isotropic chemical shift which successfully was used for an interconnection between NMR experiments and structure models. It served well for the purpose of structure verification and in the case of extended 2D layered systems the impact of random local distortion on the chemical shift spectra could be predicted. However, in addition to that the anisotropic part of the NMR tensor could be used to distinguish between different molecular conformers and similar hydrogen bonding environments. Especially in polarizable moieties such as π systems the anisotropy of the chemical shift is large enough to be evaluated. It proved to be sensitive to the local structural arrangement as well as the electronic environment of the spins. In a test case it could even be shown that the sensitivity of the carbonyl ^{13}C tensor in a hydrogen bridge is large enough to predict the C=O$\cdots$H-N arrangement through the analysis of theoretical calculated NMR hypersurfaces with the anisotropic parameters from NMR measurements. The most difficult information to analyze is the tensor orientation. This was was done by the measurement of 2D rf-driven spin-diffusion spectra for an ^{13}C isotope labeled system. Through the simulation of 2D patterns on the base of theoretical structure models it was then possible to gain insight about the conformational arrangement of molecules in a disordered environment. Even though elaborate this methodological approach yielded highly detailed information about the local as well as intermediate structure of the solid state which was not available with any other method. An advantage of the method is that it can be applied to ordered and disordered phases alike.

This work clearly shows the power of the combination of solid-state NMR measurements with theoretical modeling of the structure and the NMR chemical shift tensor. For future projects the presented Gau2Sim tools provide the basis for a routine analysis of theoretical NMR calculations and a subsequent simulation of spectra which can be compared to arbitrary NMR experiments.

Zusammenfassung

Ziel dieser Arbeit war die Anwendung theoretischer Modellierung in der Strukturaufklärung und -vorhersage von Festkörperphasen. Neben Strukturoptimierungen stand die ab initio Berechnung des chemischen Verschiebungstensors im Vordergrund. So konnten theoretische Modelle direkt mit einer Reihe von NMR Experimenten verglichen und Rückschlüsse auf die reale Struktur gezogen werden.

Für dieses Vorgehen war es notwendig, Spinsysteme aus beliebigen ab initio NMR Rechnungen aufstellen zu können, weshalb im Kontext dieser Arbeit die Gau2Sim Programmbibliothek entwickelt wurde. Sie ermöglicht die komplette Analyse von Verschiebungstensoren, aufgeteilt in die isotrope chemische Verschiebung δ_{iso} und den anisotropen Anteil. Für Letzteren sind beide gängigen Konventionen berücksichtigt, die Beschreibung über die Anisotropie δ_{aniso} und den Asymmetrieparameter η sowie die Beschreibung über die Spanne Ω und den Versatz κ. Zusätzlich wird die Tensororientierung in Bezug auf ein Referenzachsensystem berechnet und über die Eulerwinkel α, β und γ wiedergegeben.

Auf Grundlage dieser Auswertung wurde der Ansatz aus struktureller Modellierung und der theoretischen Berechnung von NMR Daten auf eine Reihe von Festkörpersystemen angewendet. Dabei standen sowohl ungeordnete als auch teilgeordnete und vollständig kristalline Phasen im Fokus der Untersuchungen. Die Bandbreite erstreckte sich von isolierten Molekülstrukturen über wasserstoffverbrückte molekulare und polymere Systeme hin zu kovalent verknüpften Schichtstrukturen. Bei der Modellierung dieser Systeme kamen Kraftfeldmethoden, semiempirische Ansätze, Dichtefunktionaltheorie und Störungsrechnung zum Einsatz. Die Beschreibung der Phase erfolgte je nach Problematik im Clusteransatz, als eingebetteter Cluster oder unter periodischen Randbedingungen. So konnten sowohl Strukturvorschläge aus Diffraktionsmethoden direkt verifiziert, als

auch sinnvolle Modelle für unbekannte Phasen selektiert werden. In letzterem Fall war es möglich, aus Clusterrechnungen Strukturen für die Behandlung unter periodischen Randbedingungen zu extrahieren und somit beide Methodiken zu kombinieren.
Die Berechnung der NMR Eigenschaften erfolgte anhand minimaler Strukturmodelle, wobei alle Bestandteile des Verschiebungstensors auf ihr Potenzial für die Strukturaufklärung hin untersucht wurden. Die isotrope chemische Verschiebung konnte erfolgreich für die Verifizierung von Strukturmodellen aus Diffraktionsmethoden verwendet werden. Außerdem war es möglich, den Einfluss von zufälligen lokalen Verzerrungen auf das NMR Spektrum eines 2D Netzwerk zu simulieren. Darüber hinaus wurde in π Systemen, für die die Anisotropie groß genug ist um ausgewertet werden zu können, eine deutliche Empfindlichkeit des Tensors auf die lokale Struktur und die elektronische Umgebung des Systems nachgewiesen. Diese Tatsache konnte für die Unterscheidung verschiedener Konformere und zwischen ähnlichen wasserstoffverbrückten Netzwerken genutzt werden. Die Empfindlichkeit des ^{13}C Tensors der Carbonylgruppe in einer Wasserstoffbrücke stellte sich als ausreichend spezifisch heraus, um für ein Testsystem die experimentell bestimmte C=O$\cdots$H-N Umgebung durch den Vergleich von theoretischen NMR Hyperflächen mit experimentellen NMR Parametern vorherzusagen. Als besonders schwierig auszuwertende Information konnte letztlich auch die Orientierung des Tensors für die Strukturaufklärung genutzt werden. Hierfür wurden 2D radiofrequenzgetriebene Spindiffusionsspektren an einer isotopenmarkierten Verbindung gemessen. Durch die Kombination mit theoretischen Modellen und die Simulation ihrer charakteristischen 2D Profile wurde die detaillierte Konformerenanalyse in einer ungeordneten Phase möglich. Obwohl dieser Ansatz ein aufwändiges Vorgehen erfordert lassen sich damit dennoch Informationen gewinnen, die mit keiner anderen Methode erhältlich sind. Ein besonderer Vorteil ist zudem der flexible Einsatz sowohl in geordneten als auch in ungeordneten Systemen.
Aus den Ergebnissen dieser Arbeit geht eindeutig hervor, dass die methodische Kombination aus NMR Messungen mit theoretischen Rechnungen auf einer breiten Basis zur Strukturaufklärung in festen Phasen erfolgreich eingesetzt werden kann. Mit der Gau2Sim Programmbibliothek steht für die Zukunft ein Werkzeug zur Verfügung, mit dem in einem Routineverfahren quantenmechanische Rechnungen ausgewertet und NMR Spektren für den Vergleich mit dem Experiment simuliert werden können.

Appendix A

Publications

In the following all publications which resulted from the here presented work are given. For each paper the title, publishing journal, a full list of the authors and the current status of publication as in November 2007 is recorded. A short comment on the impact of the respective paper on the here presented thesis is followed by a detailed listing of my own contributions to the topic as well as the collected contributions of all other authors.

A.1:

A Concerted Approach for the Determination of Molecular Conformation in Ordered and Disordered Materials

J. Sehnert and J. Senker

Chemistry - A European Journal

Chem. Eur. J. 2007, 13, 6339 - 6350
DOI: 10.1002/chem.200601726

The three distinct phases of triphenyl phosphite (TPP) were investigated in a concerted approach which involved selective isotope labeling of the TPP molecule, the performance of solid-state NMR experiments, the development of suitable structure models for each TPP phase and the theoretical calculation of the NMR chemical shift tensor with the subsequent simulation of the NMR experiments.

My personal contributions to this work included the following:

- synthesis of 1-[^{13}C]phenol from 1-[^{13}C]acetate
- synthesis of tri-(1-[^{13}C]phenyl)-phosphite from 1-[^{13}C]phenol
- measurement of 1D ^{13}C and ^{31}P MAS and wide-line spectra
- measurement of 2D wide-line rf-driven spin-diffusion ^{13}C spectra
- calculation of structure models on the base of HF and DFT methods
- calculation of the chemical shif tensor on the base of DFT methods
- simulation of 1D ^{13}C and ^{31}P MAS and wide-line spectra
- simulation of 2D wide-line rf-driven spin-diffusion ^{13}C spectra
- discussion on the presented topic
- main authorship of the article

The contributions of all other authors comprised of:

- discussion on the presented topic
- co-authorship of the article

DOI: 10.1002/chem.200601726

A Concerted Approach for the Determination of Molecular Conformation in Ordered and Disordered Materials

Jan Sehnert and Jürgen Senker*[a]

Abstract: We present the successful application of a concerted approach for the investigation of the local environment in ordered and disordered phases in the solid state. In this approach we combined isotope labeling with computational methods and different solid-state NMR techniques. We chose triphenylphosphite (TPP) as an interesting example of our investigations because TPP exhibits two crystalline modifications and two different amorphous phases one of which is highly correlated. In particular we analyzed the conformational distribution in three of these phases. A sample of triply labeled 1-[^{13}C]TPP was prepared and 1D MAS as well as wide-line ^{13}C NMR spectra were measured. Furthermore we acquired 2D ^{13}C wide-line exchange spectra and used this method to derive highly detailed information about the phenyl orientation in the investigated TPP phases. For linkage with a structure model a DFT analysis of the TPP molecule and its immediate environment was carried out. The ab initio calculations of the ^{13}C chemical shift tensor in three- and six-spin systems served as a base for the calculation of 1D and 2D spectra. By comparing these simulations to the experiment an explicit picture of all phases could be drawn on a molecular level. Our results therefore reveal the high potential of the presented approach for detailed studies of the mesoscopic environment even in the challenging case of amorphous materials.

Keywords: ab initio calculations · chemical shift anisotropy · solid-state NMR spectroscopy · structure elucidation

Introduction

Up to today structure investigations in liquids and glasses prove a challenging task. In particular information from the intermediate range of 10–100 Å is needed to understand glass structures, nucleation and growth mechanisms, self-organization and phenomena such as polymorphism or polyamorphism.[1–5] In this work we will show for triphenylphosphite (TPP) that by choosing a combination of solid-state NMR spectroscopy, computer simulation and isotope labeling detailed structure investigations down to the molecular level become feasible even in amorphous or disordered systems.

Due to substantial progress in both the technical development of NMR spectroscopy and the ab initio calculation of the full chemical shift interaction solid-state NMR serves as an especially powerful tool of analysis in the mesoscopic regime. By combining computational and experimental results today it is even possible to extract structural data from NMR experiments sensitive to the orientation of the chemical shift tensor. This is a non-trivial task because it requires knowledge about the orientation of the NMR tensor towards characteristic building blocks of the system. Beside rotation pattern measurements for single crystals quantum mechanical calculations serve as the only source for this kind of information.[6–8]

With the most commonly used gauge including atomic orbital (GIAO) method[9] NMR tensors can be computed with high accuracy in a reasonable time frame. In the last decade research based on an approach of combined computational and solid-state NMR methodology showed that there is a close relation between NMR tensors and structure.[10–15] This correlation has been used to investigate structural features like for example configuration,[16–20] hydrogen bonding[21,22] or even intermolecular arrangement[23] in the solid state. For a description of the tensor in condensed phases the polarizable continuum model,[24,25] embedded cluster methods[22,24] and computations under full periodic boundary conditions using plane waves[26–29] have been used most recently. All these fundamental studies show that the interplay of solid-state NMR and ab initio calculations has improved to an extent that now it is widely accepted to yield structural in-

[a] J. Sehnert, Prof. Dr. J. Senker
Anorganische Chemie I, Universität Bayreuth
Universitätsstrasse 30, 95447 Bayreuth (Germany)
Fax: (+49) 921-55-2788
E-mail: juergen.senker@uni-bayreuth.de

formation on a nanoscopic scale.[30] However, most of the above-mentioned work dealt with already known crystalline systems. Frequently structure models obtained from X-ray or neutron diffraction data have been used. Up to now there are only a few NMR investigations in disordered condensed phases which apply computational models for structure proposal.[26,31–33]

We now extend the use of ab initio calculations to a concerted approach for structural investigations in arbitrary ordered and disordered materials. This approach is based on a combination of isotope labeling, ab initio calculations and solid-state NMR spectroscopy. In this strategy structure proposals are generated using molecular modeling methods (DFT, semiempirical or force field methods). Such structures then provide a basis for the ab initio calculation of NMR tensors and thereby a fully ab initio simulation of NMR spectra which can be compared with experimentally obtained data.

Whereas in a majority of cases only the isotropic chemical shift is taken into account for structural analysis we focus on the anisotropic properties of the chemical shift interaction, especially the tensor orientation. This is advantageous in terms of the computational effort since it is known that tensor orientations can be calculated with high accuracy at low costs.[25,34–37] Furthermore in previous works it was shown that the orientation correlation of NMR tensors can efficiently be applied to investigate structure in ordered and disordered phases.[38,39] A limitation of this method was that usually the orientation of the tensor towards the structural building block was unknown and could only be estimated. With the inclusion of ab initio calculations a direct interpretation of the spectra in terms of a proposed structure model becomes feasible. On this base radio-frequency-driven spin-diffusion spectroscopy can be transferred to arbitrary spin-$^1/_2$ systems and the full range of organic solid-state systems is accessible to detailed structural NMR investigations. In addition to that synthetic isotope labeling serves as a tool to specifically pick out molecular domains. This influence over the investigated spin system gives the approach a great amount of flexibility.

Results and Discussion

Triphenylphosphite: Triphenylphosphite (TPP) poses an interesting example for our investigations. Even though built up by a small molecule (see Figure 1) the accessible solid-state phases include two different crystalline (c1[40] and c2[41]) and two amorphous states (aI and aII).[39] Of the crystalline phases c1 is the commonly found modification whereas c2 can only be crystallized from an ionic liquid.[41] The amorphous phases can be distinguished between the structural glass (aI with $T_g = 205$ K) and the second phase aII which is produced via annealing the supercooled liquid in a temperature range of $210 \leq T_a \leq 230$ K.[39] This latter phase contains highly correlated domains which have been investigated with ^{31}P rf-driven spin diffusion spectroscopy.[39]

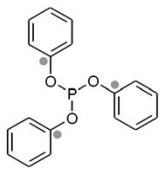

Figure 1. Tri-(1-[^{13}C]phenyl)-phosphite.

Strong evidence was found that the domains consist of clusters a few molecules in size and parallely arranged as seen in the crystalline phase c1. Furthermore, very recently the nature of the phase transformation from aI to aII has been associated with a change in molecular conformation and the demand for the elucidation of the structure on a microscopical regime has been corroborated.[42]

We therefore want to apply the concerted approach to a conformational analysis of the TPP phases aI, aII and c1. For our measurements we synthesized tri-(1-[^{13}C]phenyl)-phosphite. The intramolecular correlation was separated by choosing appropriate mixing times in the rf-driven spin-diffusion experiment. Computationally a conformational description of the TPP system was performed with DFT methods which yield accurate structure models. On that base system sizes up to a maximum of two molecules can be treated.

In the above-mentioned picture the respective phases should be well distinguishable. The glassy phase aI contains a broad distribution of possible conformers. Upon clustering in phase aII it should significantly narrow down to a small distribution about one preferential conformer which resembles the molecular structure found in the crystalline phase c1. Finally in phase c1 only the crystalline conformer is present.

TPP conformers: Figure 2 shows the minima for the conformational study of a single molecule. An overall of eight structures could be found for B3LYP and the use of the 6-31G(d) and 6-31+G(d,p) basis sets. Except for VI and VII both basis sets result in similar structures. Minimum VI is found with 6-31+G(d,p) and transforms into conformer IV upon optimization with 6-31G(d). Structure VII is stable with 6-31G(d) but transforms into conformer VIII with the 6-31+G(d,p) basis set. Minimum I exhibits C_s symmetry whereas VIII is C_3 symmetric. In structure III the C_s symmetry is broken by a slight tilt of the C2 phenyl ring.

It is noteworthy that structures could be found which resemble the crystalline polymorphs c1 (I, Figure 2) and c2 (II, Figure 2). For both the geometry optimization of a single molecule taken from the X-ray structures reproduce the results. In minimum I the overall maximum deviations from the X-ray structure for bond lengths are 0.02 Å, 1° for angles and 2° for dihedral angles. H atoms are excluded from these observations as their positions are not well described through X-ray methods. Bigger differences up to 16° for dihedral angles occur where packing effects account for a distortion of the phenyl rings.[40] As expected gas-phase

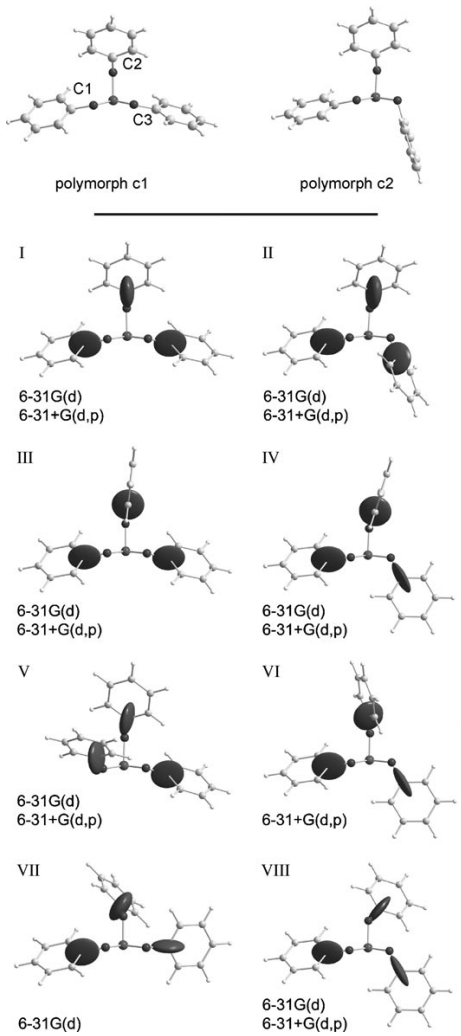

Figure 2. Top: Conformers of the crystalline phases c1[40] and c2;[41] Bottom: DFT calculated minimum structures; ^{13}C ab initio anisotropies are depicted as tensor ellipsoids for the labeled positions (see also Figure 1).

optimizations of polymorph c1 do not reproduce this feature and always result in C_s symmetry (compare the phenyl rings C1 and C3 of structures c1 and I in Figure 2). For c2 the comparison between experiment and calculation in general shows deviations of 0.01–0.05 Å for bond lengths, 1° for angles and 1° for dihedral angles. Again greater differences occur where phenyl rings are distorted due to packing effects (see phenyl rings C2 and C3 in structures c2 and II of Figure 2). In this case deviations in dihedral angles of up to 28° are found. The gas-phase structures of single TPP molecules calculated with B3LYP seem to reproduce experimental structures well with the exception of the torsion of phenyl rings due to crystal packing. Such effects can only be taken into account in the calculation by describing at least the first coordination sphere of the molecular environment. Necessarily for TPP this demands huge system sizes which can only be treated by changing to semiempirical or force-field methods. In our tests both methods fundamentally failed to reproduce the crystalline structures c1 and c2. In the case of force-field methods this general disadvantage might be overcome by using self-made potentials adopted to TPP. However, for the purpose presented herein of creating model structures for a conformational analysis the treatment of a single molecule in good quality is sufficient as will be shown later on.

In Table 1 the energies of minima I to VIII are presented relative to structure I. The energies are spread over a range of 9.2 kJ mol^{-1} for both basis sets. Conformer IV is lowest in energy whereas structure V results the highest energies.

Table 1. B3LYP minimum energies for TPP conformers; all values are given in kJ mol^{-1} and refer to the energy of structure I.

	6-31G(d)	6-31+G(d,p)
I	0.0	0.0
II	−0.9	−1.4
III	−1.4	−1.3
IV	−1.7	−1.8
V	7.2	7.4
VI	(to IV)	−0.9
VII	7.5	(to VIII)
VIII	3.5	2.6

Conformer I corresponds to the thermodynamically stable polymorph c1. It is energetically less favorable than four other structures (II, III, IV and VI) which narrowly distribute in a range of 1 kJ mol^{-1}. At a closer look the conformational arrangement in the gas phase seem to result from an interplay between the requirement to minimize sterical hindrance on the one hand and the formation of six-ring arrangements with intramolecular hydrogen bonds on the other hand (see Figure 2). Structure I exhibits no hydrogen bonds and results exclusively from the minimization of sterical hindrance. All minima lower in energy are stabilized by one or two intramolecular hydrogen-bond formations.

For the overall conformational distribution the range of the minimum energies is only small. This means that in the liquid state all of the energetically favored structures should be found as is later on proven through the comparison of 1D ^{31}P spectra. Also for the solid state no unambiguous preferential conformer can be extracted. As a consequence any observed preference of a conformational arrangement in phase aII should be caused by interactions with the surrounding environment, namely the formation of small clusters of TPP molecules.

Ab initio CSA tensors: In addition to the structures Figure 2 shows ab initio calculated NMR tensors for the labeled TPP sites (see also Figure 1). The ellipsoids represent the traceless symmetric part of the second rank tensor which is characterized via the asymmetry parameter η and the coupling constant δ. The orientation of the ^{13}C tensor with respect to the corresponding phenyl moiety is nearly identical in all

structures. The z axis points along the CO bond with only small aberrations ($\lesssim \pm 5°$) caused by a variation of the local electronic environment due to conformational changes. The x axis appears to be perpendicular to the phenyl plane. With this fixed alignment of the tensors the ^{13}C spin diffusion spectra can be directly interpreted in terms of the structural arrangement of phenyl groups.

The isotropic shift (σ_{iso}) as well as the anisotropy (δ) and asymmetry (η) parameters were extracted for the labeled sites in all single molecule model structures. δ varies in the narrow range of 83.5–89.9 ppm for the CO carbon atoms C1, C2 and C3. Due to this insensitivity towards structural changes this parameter is not suited for a distinction between conformers in the system investigated herein and thus is not taken into account for the following discussion.

Table 2 lists the ab initio values for σ_{iso} and η. C1, C2 and C3 denote the labeled carbon sites in the left, middle and right phenyl ring as shown in Figure 2. Because the calculated data is not referenced, only the relative shifts and the maximum difference $\Delta\sigma_{iso}$ are discussed. It can nicely be seen that the chemical shift gives a direct measure of the molecular symmetry (I and VIII in Table 2). Structure I exhibits C_s symmetry and thereby has two distinguishable signals. The C_3 symmetric structure VIII shows only one isotropic NMR signal. For structure III the above-mentioned broken C_s symmetry is revealed. Even though only slightly different three isotropic shifts can be found for the labeled sites. The relative isotropic shift ranges from 0.00–6.03 ppm with a maximum splitting of 0.00–4.56 ppm for the particular conformer. The asymmetry parameter η ranges from 0.63 to 0.96 with differences of up to 0.33 for the particular conformer.

Table 2. σ_{iso} and η values calculated with B3P86/cc-pVDZ (for definitions and conventions see Figure 2 and Experimental Section); additionally the maximum difference is given as $\Delta\chi = \chi_{max} - \chi_{min}$.

σ_{iso}/ppm	C1	C2	C3	$\Delta\sigma_{iso}$
c1^{DFT}	4.56	0.00	4.39	4.56
I	4.10	0.09	4.10	4.01
II	3.42	0.78	1.59	2.64
III	3.06	3.14	3.00	0.14
IV	3.08	3.41	3.70	0.62
V	6.03	3.34	3.76	2.69
VI	3.32	2.99	3.79	0.80
VII	3.29	3.02	1.05	2.24
VIII	3.40	3.40	3.40	0.00
η	C1	C2	C3	$\Delta\eta$
c1^{DFT}	0.96	0.63	0.94	0.33
I	0.91	0.63	0.91	0.28
II	0.92	0.63	0.75	0.29
III	0.84	0.78	0.84	0.06
IV	0.87	0.73	0.84	0.14
V	0.75	0.76	0.93	0.18
VI	0.90	0.73	0.84	0.17
VII	0.87	0.86	0.74	0.13
VIII	0.85	0.85	0.85	0.00

From that in principle a conformational analysis of TPP is feasible through the comparison of the ab initio values with experimental data obtained at an adequate resolution (0.2–0.3 ppm as found in the MAS spectra of the crystalline phase c1). Unfortunately experimental difficulties restrict the use of MAS to c1. Only wide-line spectra can be recorded for all three TPP phases. Due to the intrinsically lower resolution in these spectra it is questionable whether the calculated differences in $\Delta\sigma_{iso}$, δ and η still allow for a conformational analysis on the base of the ^{13}C nucleus.

Another possibility is to use ^{31}P wide-line spectra. Table 3 lists the ab initio NMR parameters for the phosphorus nucleus in the respective minimum structures. The isotropic shift varies in a range of about −22 up to 25 ppm with respect to structure c1^{DFT}. Furthermore the anisotropy changes up to 22% and η varies from 0.0 to 0.3 (for a comparison, δ changes up to 8% at the carbon nuclei). These major changes allow for at least a qualitative conformational analysis even with low-resolution wide-line spectra. Exemplarily Figure 3 shows ^{31}P spectra which match best with the experimental data for aI, aII and c1 published in the literature.[43] In the simulation phase aI consists of structures I-IV and VI–-VIII. Conformer V had to be excluded from the distribution of the glass. This is a particularly interesting fact since this conformer is found to be amongst the structures highest in energy. The simulation of phase aII bases on structures I and III, thereby significantly narrowing the conformational distribution. Finally c1 is exclusively represented by structure I. This overall situation matches the stepwise narrowing of a conformational distribution as proposed in the Section on Triphenylphosphite and in the literature.[43] However, no detailed picture of the phenyl moieties can be drawn from ^{31}P spectroscopy alone. For example it would not be possible to differentiate between minima III and IV even though these two exhibit pronounced structural differences (see Figure 2 and Table 3 for comparison). Therefore the following discussion exclusively deals with the ^{13}C nucleus.

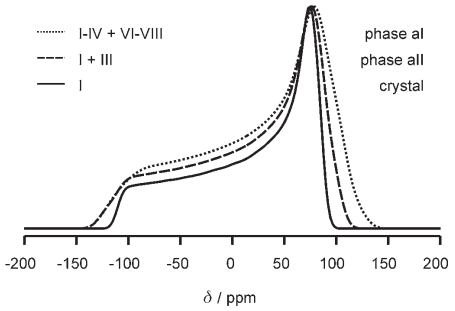

Figure 3. Theoretical simulation of ^{31}P spectra for different conformational distributions in aI, aII and c1 (to account for a glassy state the spectra for aI and aII were treated with an additional Gaussian broadening); the picture matches very well with experimental spectra published by Senker et al.[43]

Table 3. Ab initio parameters for ^{31}P calculated with B3P86/cc-pvdz; σ_{iso} and δ are given in ppm; σ_{iso} is given as a relative shift with respect to structure c1^{DFT}.

	σ_{iso}	δ	η
c1^{DFT}	0.0	−120.1	0.13
I	−4.1	−127.0	0.10
II	−7.1	−132.4	0.07
III	−1.7	−146.7	0.15
IV	−3.3	−145.3	0.09
V	−22.1	−131.9	0.21
VI	0.3	−142.3	0.11
VII	25.4	−138.8	0.17
VIII	15.6	−140.8	0.00

1D ^{13}C NMR spectra: Figure 4a shows the experimental MAS spectra of phase c1 recorded for a spinning frequency of 3 kHz. Three separated signals with maximum splitting of 5.05 ppm can be observed. The emersion of these three signals in the experiment accounts for the broken C_s symmetry due to packing effects in the crystal.[40,44] Furthermore Table 4 shows the ab initio calculated values of conformer

Table 4. Comparison of the ab initio and experimental anisotropy of c1.

	C1	C2	C3	C1	C2	C3
		δ/ppm			η	
c1^{DFT}	83.5	89.9	84.3	0.96	0.63	0.94
FIT	92.3	93.1	86.7	0.79	0.47	0.79

c1^{DFT} together with the results of a fit using three isolated one spin systems. Upon comparison it is evident that no major differences occur, neither for δ nor for η. The ab initio parameters are ratified by the fit in their order of magnitude. Although the absolute ab initio values of η are overestimated by 0.16 compared with the experiment the relative trend for C1, C2 and C3 is well reproduced. This systematic deviation leads to the result that the difference in η can be taken as a measure in addition to the chemical shift in a conformational analysis.

In comparison with the structures I–VIII only I shows a similar wide splitting of the chemical shift (see Table 2). Structure I represents the gas phase minimum structure of polymorph c1. In comparison with the ab initio values of c1^{DFT} an assignment of the signals is possible. According to the definition used above the carbon atoms C1, C2 and C3 exhibit chemical shift values of 153.3, 148.3, and 152.5 ppm, respectively.

Figure 4b shows one-dimensional wide-line ^{13}C spectra for the phases aI, aII and the crystalline phase c1. For the phases aI and aII no difference in the spectral shape is observed. Only in the crystalline phase the different chemical shifts are resolved and lead to a characteristic form of the spectrum. The general difference between the crystalline and glassy phases can nicely be modeled with the use of the ab initio calculated tensors. The crystalline phase has been simulated using structure I as a model. The glassy states of aI and aII are represented by a superposition of simulated

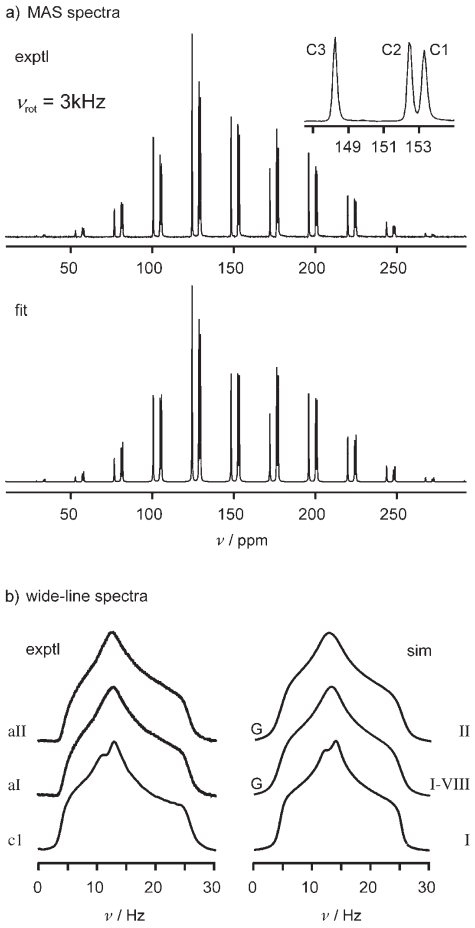

Figure 4. a) MAS spectrum of phase c1 and result of a fit taking the ab initio calculated anisotropy parameters of c1^{DFT} as initial values. b) Measured and ab initio simulated wide-line 1D spectra of the phases aI, aII and c1; for the simulation of a glassy state an additional Gaussian broadening (G) was applied to account for a broad conformational distribution.

spectra for the structures I–VIII. To account for the even broader conformational distribution in a glass a Gaussian line-broadening has been applied. In addition to these models a simulation of the glassy state based exclusively on conformer II has been tried. Even though this would be an unlikely model the qualitative difference between the crystalline and glassy states still is reproduced reasonably well. From these results it is obvious that wide-line 1D spectroscopy is not suited to extract structural details of phase aII. Therefore we additionally performed wide-line 2D rf-driven spin-diffusion measurements.

2D correlation spectroscopy: Spin-diffusion exchange spectroscopy includes the chemical shift parameters σ_{iso}, δ and η as well as the orientation of neighboring tensors towards each other. In a fixed spatial arrangement the orientation correlation causes characteristic ridges in the 2D exchange

experiment.[39] The spin-diffusion range and with that the number of interacting spins can be controlled by the mixing time t_m. During t_m the spin-diffusion spreads into space and leads to off-diagonal ridges for all spins which participate in the exchange. An exception are parallel tensors where the respective signal remains on the diagonal of the spectrum. All spins which did not take part in the exchange appear on the diagonal as well. A more detailed explanation of the method is given in the literature.[39]

For $t_m \rightarrow \infty$ the spectra can be interpreted as a superposition of ridges for all tensor arrangements found in a sample. Due to experimental reasons t_m is limited to a few hundred milliseconds, which is, however, sufficient to reflect a structural picture of the investigated phase on a mesoscopic scale. The observed pattern is much like a fingerprint of the structural environment and highly sensitive to changes in the spatial arrangement. In the case of TPP with the already discussed fixed ^{13}C tensor orientation for the phenyl groups (see section on ab initio CSA tensors) it directly reflects the structural arrangement of the molecules and has a strong potential for an analysis of conformational arrangements even in the disordered phases. TPP spectra were recorded for mixing the times $t_m = 4$, 10 and 40 ms. As it is not likely that isolated spin pairs occur in the TPP phases it can be assumed that the polarization transfer is homogeneous with t_m. As a consequence the off-diagonal part of the 2D spectra can be analyzed in terms of an orientation correlation even for finite t_m and the diagonal part can be neglected.

Figure 5 shows measurements of phases aI, aII and c1 for the three different mixing times. For the crystalline phase c1 the characteristic pattern exhibits two strongly pronounced wings that are connected through a bridge perpendicular to the diagonal of the spectrum. In addition to that two extensions in the off-diagonal corners of the spectrum can be found. These features are observed for all three mixing times. For $t_m = 4$ ms only the most intense features remain clearly visible. Turning to the structural glass aI the characteristic pattern is much different. Here the spectrum shows two straight features which are perpendicular to each other and include an angle of 45° with the diagonal. Again they remain visible for all three mixing times. By comparison of $t_m = 4$, 10 and 40 ms for the respective spectra of c1 and aI it can be stated that our assumption of a homogeneous polarization build-up is justified. No major changes in the spectral patterns are observed.

Starting with the smallest mixing time 4 ms it can be seen that phase aII neither exactly exhibits the pattern found for aI nor the pattern for the crystal. The most emphasized feature is a broad bridge perpendicular to the diagonal. In addition to that wing-like structures similar to the crystalline pattern are found. This similarity to the ordered state c1 becomes more obvious when comparing the spectra for $t_m =$ 10 ms. Again the broad bridge is found for phase aII. Apart from that all features of the crystalline phase are observed as well clearly demonstrating an ordered state similar to c1. For the largest mixing time 40 ms the c1 features are completely obliterated. The spectrum is highly similar to the

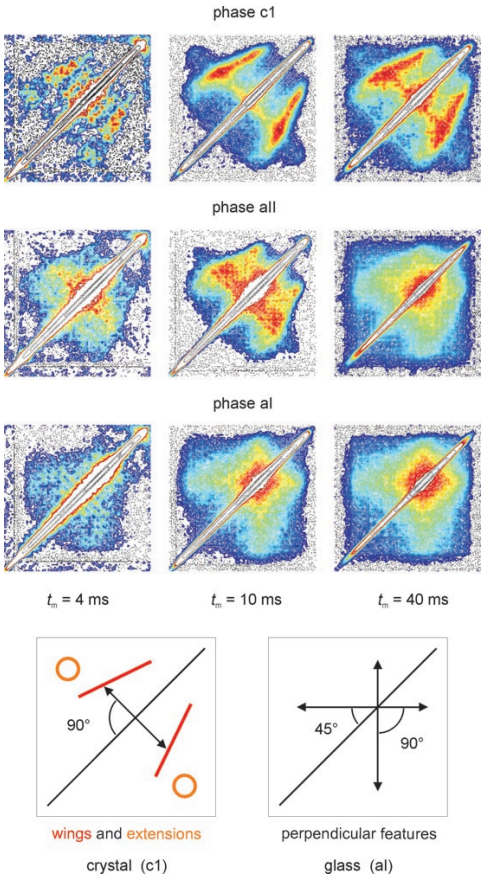

Figure 5. 2D spectra showing the tensorial orientation correlation in the phases aI, aII and c1; for phases aI and c1 the typical features of the ordered and disordered state are sketched.

measurement of phase aI with only minor differences resulting from the underlying crystal-like features. This reflects an amorphous structure of aII as described in the literature.[39]

In general the relationship between the mixing time t_m and the observed spin-diffusion range cannot be expressed analytically, especially not for the disordered phases aI and aII.[39] Nevertheless we can use the mixing time for a qualitative understanding of the structural features of aII by comparing the spectral changes in aI, aII and c1 with t_m. In an intramolecular range (4 and 10 ms) a broad conformational distribution is found for phase aI. After the conversion to phase aII this distribution is significantly narrowed and the spectrum becomes similar to the crystalline phase c1 where only one conformer is present. For an intermolecular range (40 ms) phase aII shows disorder as its dominant structural feature. Even though the measurements clearly reveal different conformational distributions in the TPP phases the description still lacks the explanation on a molecular level. For a more detailed understanding of the observed spin system we carried out simulations of the 2D exchange spectra.

Simulations of 2D exchange spectra: Before turning to a detailed conformational analysis of the 2D spectra we simulated a spectrum for the glassy state. This can be done by a two-dimensional convolution of a wide-line 1D spectrum.[39] Figure 6 (glass) shows such a 2D spectrum created from the 1D ab initio spectrum (I–VIII) presented in Figure 4. In comparison with Figure 5 the simulation nicely matches the measurements of phases aI and aII with $t_m = 40$ ms. Therefore the description of these phases as orientationally disordered states is justified for long exchange ranges. Other than in aII this statement still holds for $t_m = 4$ and 10 ms in phase aI. Thus the molecules in aI are not only randomly oriented towards each other but also show a broad conformational distribution exactly as expected from the common picture of a structural glass. Furthermore, Figure 6 presents

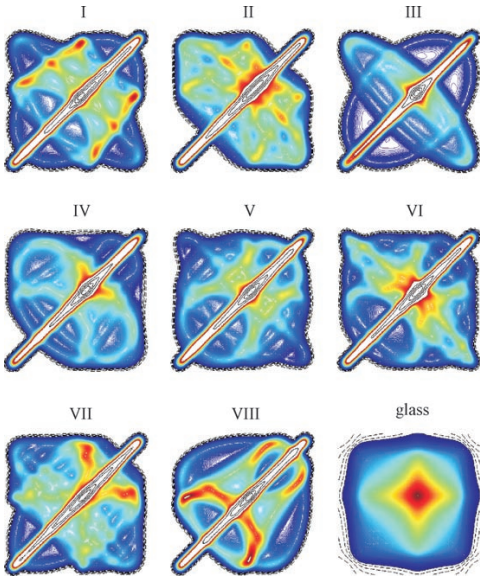

Figure 6. Simulations ($t_m \rightarrow \infty$) of 2D exchange spectra for the model structures I–VIII (see Figure 2) and the glassy state.

the 2D exchange spectra for the structures I–VIII. All eight conformers exhibit a unique spectral pattern characteristic for the particular conformation. This clearly demonstrates the prediction power of orientation correlation spectroscopy for conformational analyses. In comparison with the measurements the simulation for minimum structure I matches the spectra of the crystalline phase c1 best. It is the only case where pronounced and well separated wing structures are found. In addition to the wings the typical extensions observed for c1 occur as well. The interconnecting bridge between the wings is not well represented in the simulation. Another difference is found in the intensity distribution over the wings. These differences can of course originate in the comparison of a simulation for $t_m \rightarrow \infty$ with a spectrum measured for at a finite mixing time. However, if the assumption of a homogeneous polarization transfer is valid it is more likely that the observed features result from a conformational distortion of the ideal gas-phase structure I. In Figure 7 the simulation for conformer $c1^{DFT}$ is shown together with the measurement of c1 for $t_m = 40$ ms. In comparison

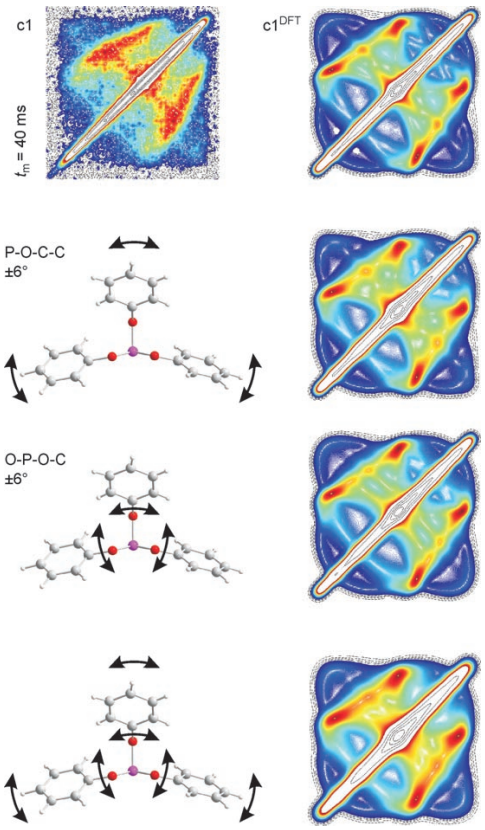

Figure 7. Simulations ($t_m \rightarrow \infty$) and experiment for phase c1; the influence of small variations of the phenyl orientation on the spectral shape is shown.

to the simulation of structure I (see Figure 6) the spectrum of $c1^{DFT}$ resembles the measurements in much more detail. In particular close to the diagonal a bridge-like feature 90° with respect to the diagonal appears. In addition to that the overall shape of the wings is closer to that found in the experiment. To test the relation between the chemical shift principle values and the spectral shape a second simulation has been carried out using the σ_{iso}, δ and η of the experimental fit together with the tensorial orientations of $c1^{DFT}$. It turned out that small changes in these parameters do not have any pronounced influence on the spectrum. With this the orientation of the tensors in the system is the dominant and important variable for the simulations. The clearly different 2D spectra of I (see Figure 6) and $c1^{DFT}$ (see Figure 7) demonstrate the extreme sensitivity of the spectral shape towards minor structural changes. To investigate the importance of such changes for the spectrum of the crystalline phase further model structures have been calculated to-

gether with their 2D spectra. For all three phenyl groups a stochastic distribution of the P-O-C-C and O-P-O-C dihedrals has been assumed and the angles varied in seven steps from −6 to +6° with respect to the orientation in $C1^{DFT}$. Because only small changes were applied the structural relaxation of the molecule was neglected and the models calculated as single points. The resulting 343 NMR spectra have been added up for the respective dihedral angle and the results are shown in Figure 7. The variation of the P-O-C-C angles leads to an overall broadening of the pattern observed for $c1^{DFT}$. In contrary to that the variation of O-P-O-C does not alter the shape of the wings. The spectral pattern remains sharp and two bridges form between the diagonal and the wings. Close to the diagonal the intensity distribution changes its pattern compared to the simulation for $c1^{DFT}$.

Changes about dihedral angles of ±6° are well in agreement with the atomic displacement parameters found for the crystal structure of c1.[40] Thus even for the crystalline phase one can expect that the 2D spectrum results from an ensemble of molecules with small structural deviations from a mean arrangement which is represented by structure $c1^{DFT}$. It should be noted that whereas librational dynamics leads to a partial averaging of the CSA tensor (which is expected to be small at 190 K) the here observed differences in the spectral shape clearly account for a structural distribution representing static disorder in the crystalline phase. To test the overall influence of such a distribution both spectra for variations about P-O-C-C and O-P-O-C were added up and a small additional Gauss broadening was applied. This broadening is meant to account for effects caused by the much higher degree of freedom of the molecule than included in our model system. The result is very close to the experimentally observed spectrum (see Figure 7). Therefore it can be stated that for the simulation of the details of the measurements it is necessary to take into account an ensemble of representative model structures. Because of the high sensitivity to changes in tensorial orientations these structures were generated via a small and stepwise distortion from a proposed mean structure. Through this procedure an analysis of the tensorial orientation within an accuracy of about 10–20° should be possible when large changes in the 2D spectrum are involved.

In a next step a detailed analysis of phase aII was carried out. In particular aII differs from the crystalline phase c1 through the emersion of a pronounced broad bridge in the spectrum for $t_m = 10$ ms (see Figure 5). As seen above such a feature cannot result from small angle deviations. Therefore we generated further model structures for large angle deviations and simulated the respective 2D spectra. For these large variations the structural relaxation of the overall molecule cannot be neglected anymore. Consequently we started our analysis from minimum structure I and gradually created new structures through scans of single dihedral angles as described for the conformational search (see Experimental Section). For symmetry reasons only rotations of the C1 and C2 phenyl rings have to be considered (see Figure 8). First

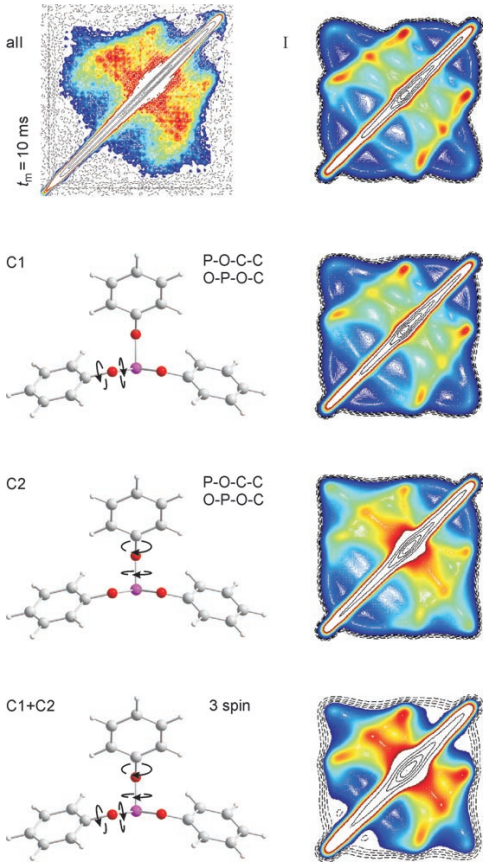

Figure 8. Simulations ($t_m \rightarrow \infty$) and experiment for phase aII demonstrating the influence of large variations in dihedral angles on the spectra for three-spin systems.

the P-O-C-C and O-P-O-C dihedral angles were varied for both rings, then the resulting NMR spectra were added up. Representative results of these investigations are shown in Figure 8. For C1 the scans of P-O-C-C and O-P-O-C were carried out from −14 to 18° and −16 to 43°, respectively. C2 variations ranged from 0 to 39° for P-O-C-C to 0 to 55° for O-P-O-C. The change in C1 appears to have a minor effect on the spectral shape. Compared with the simulation for structure I the overall shape remains the same whereas the intensity distribution along the wings changes. When turning to C2 drastic changes appear in the spectrum. The wing structure is broken up and a broad bridge about 90° with respect to the diagonal arises. This feature fits very well with the experimentally observed bridge. Model systems with structural changes different from the above described procedure have been tried as well but in no case similar features could be found. Furthermore structure I is the only possible choice for a mean structure because all other conformers exhibit strongly diverse spectral patterns (see Figure 6) which do not reproduce the characteristic wings. Thus the distortion of C2 starting from structure I is the most reasonable explanation for the observed 2D spectra of phase aII. This

means that in phase aII a preferential conformer exists which resembles the mean structure I and exhibits a disorder of the phenyl groups in a minor range of the dihedral distortions.

In the overall simulation of phase aII all angular displacements should be represented. Therefore we added up the 2D spectra for C1 and C2. As in the crystalline simulation a small Gaussian broadening has been applied for effects not included in our model. The result is shown in Figure 8 ("C1 + C2"). It nicely reproduces all important spectral features found in the experimental spectrum of phase aII. Even though only this one example is presented in this work other variations of the dihedral angles of C2 have been tried with similar success. It turned out that for the given distortion of the C1 phenyl ring C2 can be varied in a range up to 39–49° for P-O-C-C and 45–65° for O-P-O-C. With that the disorder of the C2 phenyl ring is described very precisely. This is an even more exciting result when considering that this analysis has been carried out for a locally ordered structure in an amorphous phase. Unfortunately changes in the orientation of C1 do not exert a strong influence on the spectrum which is why such a detailed analysis is limited to the middle phenyl ring of structure I.

2D exchange spectra of larger spin systems: A basic assumption in the preceding discussion is that at $t_m = 10$ ms only spectral features resulting from a single TPP molecule are visible. To verify this hypothesis we increased our model to a system containing two TPP molecules, the largest system that could be treated reasonably well with ab initio methods. A TPP pair was cut out from the crystal structure of c1 where the TPP molecules are found to be aligned in parallel.[40,44] This arrangement was taken as a starting structure and optimized further with different methods and basis sets.

With the HF method two different minima could be found which exhibit a strong distortion of the molecules towards each other. This manifests in strongly diverse OH distances and a PP distance which is about 30% longer compared with one in the crystal structure (see Table 5). Changing to the B3LYP functional the molecules tend more towards a parallel orientation, which leads to a smaller PP distance whereas the large value for OH3 still indicates a distortion of the molecules. This changes with the introduction of the PBE1PBE functional. For three different basis sets the mean aberration of the PP distance is only about 3%. The OH distance deviations improve to ≤ 10% with increasing the basis set.

Table 5. Distances and pair-formation energies (minimum and MP2/6-31G(d)) for structures described in Figure 9; all energies have been counterpoise corrected for BSSE[46] and are given in kJ mol^{-1}; distances are given in Å.

	OH1	OH2	OH3	PP	E^{MIN}	E^{MP2}
X-ray	2.99	3.52	2.95	5.72	–	–
1)[a,d]	2.83	3.51	3.50	7.22	−3.3	−21.8
2)[a,d]	2.97	2.88	3.09	7.55	−3.9	−21.5
3)[b,d]	2.60	2.97	4.33	6.39	1.7	−23.3
4)[c,d]	2.72	3.07	3.53	5.90	−5.0	−26.4
5)[c,e]	2.98	3.31	3.30	6.00	−8.2	−25.4
6)[e,f]	3.04	3.33	3.26	5.85	−7.7	−26.3

[a] HF. [b] B3LYP. [c] PBE1PBE. [d] 6-31G(d). [e] 6-31+G(d,p). [f] 6-311++G(d,p).

Table 5 as well lists counterpoise corrected pair-formation energies for the above described structures. Because significant amounts of the dispersion energy are neglected by HF and DFT in addition the results of MP2 calculations are shown. With MP2 all structures pose stable minima with reasonable stabilization energies that match the values that could be expected for a dimer with three weak OH contacts.[45] Even though it cannot be claimed that any of the structures represents a minimum on the MP2 surface, a stability order can be established for the TPP pairs. In comparison with the structural data in Figure 9 it can be seen that

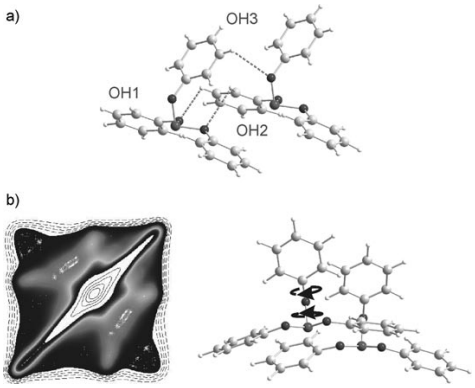

Figure 9. a) Definition of chosen OH contacts for the methodological comparison in Table 5. b) Simulation ($t_m \rightarrow \infty$) of the influence of large variations in dihedral angles for 2D spectra of six-spin systems.

the MP2 energies correlate with the PP distance. The lowest PP distances yield a maximum stabilization of the system (about -26 kJ mol^{-1}). With about -22 kJ mol^{-1} the strongly distorted HF structures give the smallest stabilization energies. Because the PP distance not only correlates with the stabilization energy but also is an indicator for the parallel alignment of the TPP molecules it can be concluded that a parallel arrangement leads to energetically favored structures.

We furthermore repeated the distortional variation of C2 for a TPP pair (see Figure 9b) and calculated the NMR spectrum as a six-spin system. It can be seen that the characteristic bridge completely vanished from the spectrum (compare to Figure 8). The six-spin simulation of C2 differs significantly from the corresponding three-spin system. Consequently, for $t_m = 10$ ms intramolecular arrangements dominate the exchange spectra which can be interpreted in terms of a conformational analysis as it was done above. At a closer look the intensity distribution in the most outstanding region of the six-spin simulation near the diagonal resembles the experiment better than in the three-spin case. Thus it might be that to some percentage the first coordination

sphere is also visible. However, this is only a minor effect and it does not affect the overall interpretation.

These results are of immediate importance for the project of a direct determination of TPP clusters in phase aII. This can be accomplished using the concerted approach described herein. Whereas in the paper at hand we focused on the intramolecular correlation of ^{13}C tensors our current project deals with the separation of intra- and intermolecular exchange. For this the mixing time t_m has to be increased to values above 10 ms. Additionally such measurements can not be performed with triply [^{13}C]-labeled TPP anymore. In such a sample the overlap of intra- and intermolecular interactions completely destructs the necessary sensitivity of the spectral pattern towards structural features (see Figure 9). However, this overlap can be avoided using monolabeled 1-[^{13}C]-TPP. Due to the omnipresent transesterification of mixed aryl phosphites at room temperature and above the preparation of this system affords the development of a low-temperature synthesis. Furthermore, at the computational edge of the approach systems containing a several TPP molecules have to be treated for reasonable structure models. This is only possible by using force field methods which are manually adapted to the TPP system. All this work is currently in progress in our group and will be published in a forthcoming paper.

Conclusions

Our concerted approach including synthesis, computational chemistry and solid-state NMR spectroscopy for structural investigations was successfully applied to unravel the distribution of conformers in one ordered (c1) and two disordered phases (aI and aII) of triphenylphosphite.

In a conformational analysis based on DFT eight different minimum structures were identified for TPP, two of them representing the conformations of the crystalline phases c1 and c2. Apart from distortions caused by crystal packing the gas-phase calculations match the experimental structures surprisingly well. The energies show that none of the structures is unambiguously favored over the others. The structures served as a base for the ab initio calculation of the chemical shift tensors and a subsequent simulation of NMR experiments.

For a sample of tri-(1-[^{13}C]phenyl)-phosphite a variety of 1D MAS and wide-line spectra were measured and their potential for a conformational analysis in the different TPP phases were investigated. In the case of the crystalline phase c1 MAS experiments are well suited for a conformational analysis. The comparison of the chemical shift values σ_{iso} and η with their ab initio counterparts allow for an unequivocal assignment. However, the 1D ^{13}C wide-line spectra do not allow to distinguish between different conformational distributions.

Furthermore all of the TPP phases were investigated by 2D rf-driven spin-diffusion spectroscopy. With this method a detailed picture of aI, aII and c1 could be achieved. On a larger length scale aI and aII appear as disordered phases whereas c1 is clearly crystalline and exhibits a well defined long range order. The intramolecular arrangement differs significantly in all the three phases. Phase c1 exhibits only one conformation as expected for a crystalline phase. In aI a broad distribution of conformations is observed, consistent with the picture of a structural glass. Phase aII, however, consists of a mean preferential conformer similar to that in phase c1. Nevertheless, in contrary to c1 a significant conformational distribution is still present. By comparison with simulations this distribution could be attributed to the middle phenyl ring which is distorted in the narrow range of 10–20° about two dihedral angles.

We could show that the use of the concerted approach in combination with 2D exchange spectroscopy has a strong potential for the investigation of the local order in disordered materials. The approach is highly adjustable to the individual problem. Therefore it is well suited for the investigation of similar structural problems as there exist many. Self-assembly studies in highly disordered environments should become accessible like the investigation of the aggregation of nucleating agents in polypropylene.[47] Another great area of application is for biological systems. Here the disruption of lipid bilayer membranes by antimicrobial peptides is a good example for examination.[48] Finally trendsetting research topics like nucleation and growth or nanoscopic self-assembly have a high demand for innovative analytical methods as on the here important length scale classical methods like X-ray diffraction fail to reveal the important structural details.[1–5,49]

Experimental Section

Synthesis: The wide-line NMR experiments presented in this work demand a sufficient amount of tri-(1-[^{13}C]phenyl)-phosphite which can be synthesized from PCl_3 and 1-[^{13}C]phenol.[50] The products have been confirmed using liquid ^1H, ^{13}C and ^{31}P NMR performed on a JEOL Eclipse 400 spectrometer. Enrichment and purity of the 1-[^{13}C]phenol was determined by GC/MS on a Agilent HP 6890/MSD 5973 apparatus.

We decided to prepare monolabeled phenol from sodium 1-[^{13}C]acetate (EURISOTOP, 99% ^{13}C), following the seven-step synthesis of Rieker et al.[51] An overall yield of 70% 1-[^{13}C]phenol with respect to the educt could be gained (lit.: 67%). No traces of impurities could be found in ^1H NMR and GC/MS measurements. The degree of isotope enrichment could be determined to 97% from mass spectrometry results.

The high purity of educts is the essential factor in the following synthesis of tri-(1-[^{13}C]phenyl)-phosphite from PCl_3 and 1-[^{13}C]phenol. Freshly received PCl_3 (Merck, 99%) was distilled twice (b.p. 72 °C) and stored in dry flasks under argon. To prevent oxidation the synthesis as well was carried out under argon atmosphere. 1 equiv PCl_3 were added dropwise to 3.5 equiv 1-[^{13}C]phenol over 45 minutes. In the beginning of the reaction the development of HCl and cooling of the mixture could be noticed. The mixture was heated to 120 °C for 2 h until no gas production could be observed anymore. The surplus of phenol was then removed through vacuum distillation at 120–125 °C and 1×10^{-3} mbar. This procedure yielded a residue of colorless tri-(1-[^{13}C]phenyl)-phosphite (99% with respect to PCl_3). Solution ^1H and ^{31}P NMR determined the purity of the sample to 100%.

Solid-state NMR measurements: ^{13}C NMR measurements were performed on a conventional DSX Avance spectrometer (Bruker, Germany)

operating at a ^{1}H frequency of 500 MHz. For MAS and wide-line experiments the crystalline phase c1 was prepared at 250 K from the supercooled liquid outside the spectrometer. In contrary phases aI and aII were directly prepared inside the spectrometer using the procedures described by Senker et al.[39] 213 K has been chosen as annealing temperature for phase aII. The temperature was adjusted via a constant flow of cold, dry nitrogen with an accuracy of ± 2 K. Static samples were degassed using the pump and freeze technique and sealed off under vacuum. Liquid NMR measurements showed that the main impurity in these samples was less than 3% triphenylphosphate.

1D MAS spectra were recorded at 200 K with a commercial 4 mm MAS probe (Bruker) and referenced to TMS. For data acquisition a ramped cross-polarization pulse sequence with a contact time of 5 ms and a 90° pulse length of 3.4 μs was used. During acquisition proton decoupling was achieved with a TPPM pulse sequence.[39]

Samples for wide-line experiments were mounted in a commercial CP double resonance probe (Bruker) equipped with a 5 mm solenoid coil. All measurements were carried out at 190 K to eliminate all relaxation processes of supercooled liquids and to reduce an averaging of the CSA interaction by librational dynamics.[52] 1D spectra were recorded with a Hahn-echo pulse sequence where the preceding 90° pulse was replaced by ^{1}H,^{13}C cross polarization (contact time 3 ms). The investigation of the orientation of neighboring molecules was carried out using two-dimensional radio-frequency-driven spin-diffusion[53] exchange spectroscopy[38,39] with a WALTZ17 composite spin-lock sequence. 90° Pulse lengths were set to 2.5–3.0 μs, in the composite lock a nutation frequency of 125 kHz was used. For methodological details the reader is referred to the literature.[38,39,53] Continuous wave broadband proton decoupling was applied during the evolution and acquisition periods.

Computational methods: Quantum chemical calculations were performed with the Gaussian03[54] package on ordinary linux clusters. Resources ranged from 32 bit systems with one or two Pentium4 (3 GHz) processors to 64 bit platforms with four parallel Itanium2 (1.3 GHz) processors and were applied as required by the system size or level of calculation. All investigations were based on polymorph c1 as a starting point (see Figure 2). To find a suitable computational level we tested a broad range of Pople basis sets (from STO-3G to 6-311G) by way of geometry optimization of the c1 crystal molecule with the B3LYP functional. In comparison with the crystal structure 6-31G(d) and 6-31+G(d,p) mirrored the experiment best.

The conformational search was performed via scans of the potential energy surface on a computational level of B3LYP/STO-3G. Three different dihedral angles have been varied in the TPP molecule (two about the PO bonds of the middle and right phenyl ring and one about the OC bond of the middle phenyl ring, see Figure 8 for comparison). For each point of the scan one or a maximum of two dihedral angles were fixed whereas the rest of the molecule was allowed to fully relax. Based on these calculations several single points were chosen and further optimized using the bigger basis sets 6-31G(d) and 6-31+G(d,p). For the NMR tensor calculations an additional model system (referred to as c1^{DFT}) was calculated on the base of the X-ray structure of polymorph c1. The c1 conformer was relaxed with B3LYP/6-31G(d) under the constraint of fixed phenyl orientations. In particular this procedure compensated for the experimentally poorly described H atom positions and thus allowed to calculate ab initio NMR tensors for the experimental structure.

In the TPP system containing two molecules a variety of methods (HF, B3LYP and PBE1PBE) and different basis sets has been tested in geometry optimization. Due to their lack of electron correlation which significantly contributes to the pair formation energy for all minima the MP2 single point energy was calculated. The pair formation energies have been corrected for the basis set superposition error (BSSE) using the counterpoise (CP) correction.[46]

The ab initio ^{13}C NMR tensors were calculated using the GIAO method[9] on the B3P86/cc-pVDZ level of theory. In a benchmark study comparing 102 organic systems it was found that even in combination with small basis sets this functional yields good results for aromatic ^{13}C tensors.[55] The here presented isotropic shifts are not referenced and therefore exclusively discussed in terms of their relative positions. For convenience the values are related to the smallest calculated isotropic shift (C2 carbon atom in structure c1^{DFT}).

Spectra simulations: MAS spectra were simulated with the SIMPSON[56] NMR tool. Simulations of wide-line spectra were carried out using self-written programs based on the GAMMA[57] C++ library considering three- and six-spin systems.

For the use of these programs the full ab initio chemical shift tensor as given by Gaussian 03 had to be converted which was done by a self-developed MATLAB[58] interface. In this script first the symmetric and antisymmetric parts are separated by way of tensor reduction: $\sigma = \sigma^{anti} + \sigma^{sym}$.[59] A following solution of the eigenvalue problem for the symmetric part yield the principle values and vectors in the principle axis system (PAS). The anisotropy and asymmetry parameters δ and η are derived from the symmetric tensor according to the conventions used in SIMPSON ($\sigma_{iso} = {}^1/_3(\sigma_{xx}+\sigma_{yy}+\sigma_{zz})$, $\delta_{CS} = \sigma_{zz}-\sigma_{iso}$, $\eta = (\sigma_{yy}-\sigma_{xx})/\delta_{CS}$ with $|\sigma_{zz}-\sigma_{iso}| \geq |\sigma_{xx}-\sigma_{iso}| \geq |\sigma_{yy}-\sigma_{iso}|$).[57] The Euler angles (α, β, γ) are given for the transformation from the principle axis system to a reference axis system which is the internal coordinate system of the Gaussian 03 calculation: $\sigma^{sym}(RAS) = \boldsymbol{R}(\alpha,\beta,\gamma)\cdot\sigma^{sym}(PAS)\cdot\mathbf{R}^{-1}(\alpha,\beta,\gamma)$.[59] The output of calculated values can directly be used with SIMPSON and GAMMA. Beside that an additional output allows the pictorial presentation of the anisotropic part of the tensor with DIAMOND.[60]

Acknowledgements

We would like to thank Denis Golovanov for sharing the crystallographic data of polymorph c2.

[1] C. A. Angell, *J. Non-Cryst. Solids* **1985**, *73*, 1–17.
[2] O. Mishima, H. Stanley, *Nature* **1998**, *396*, 329–335.
[3] M. Jansen, B. Jäschke, T. Jäschke, *Struct. Bonding (Berlin)* **2002**, *101*, 137–191.
[4] D. Kivelson, G. Tarjus, *J. Non-Cryst. Solids* **2002**, *307–310*, 630–636.
[5] J. L. Yarger, G. H. Wolf, *Science* **2004**, *306*, 820–821.
[6] C. M. Carter, D. W. Alderman, J. C. Facelli, D. M. Grant, *J. Am. Chem. Soc.* **1987**, *109*, 2639–2644.
[7] M. H. Sherwood, J. C. Facelli, D. W. Alderman, D. M. Grant, *J. Am. Chem. Soc.* **1991**, *113*, 750–753.
[8] R. J. Iuliucci, C. G. Phung, J. C. Facelli, D. M. Grant, *J. Am. Chem. Soc.* **1996**, *118*, 4880–4888.
[9] K. Wolinski, J. F. Hinton, P. Pulay, *J. Am. Chem. Soc.* **1990**, *112*, 8251–8260.
[10] J. C. Facelli, D. M. Grant, *Nature* **1993**, *365*, 325–327.
[11] R. Salzmann, C. J. Ziegler, N. Godbout, M. T. McMahon, K. S. Suslick, E. Oldfield, *J. Am. Chem. Soc.* **1998**, *120*, 11323–11334.
[12] K. Eichele, R. E. Wasylishen, J. F. Corrigan, N. J. Taylor, A. J. Carty, K. Feindel, G. M. Bernard, *J. Am. Chem. Soc.* **2002**, *124*, 1541–1552.
[13] D. Stueber, D. M. Grant, *J. Am. Chem. Soc.* **2002**, *124*, 10539–10551.
[14] A. Poon, J. Birn, A. Ramamoorthy, *J. Phys. Chem. B* **2004**, *108*, 16577–16585.
[15] J. Birn, A. Poon, Y. Mao, A. Ramamoorthy, *J. Am. Chem. Soc.* **2004**, *126*, 8529–8534.
[16] W. Wang, C. G. Phung, D. W. Alderman, J. Pugmire, D. M. Grant, *J. Am. Chem. Soc.* **1995**, *117*, 11984–11988.
[17] J. Heller, D. D. Laws, M. Tomaselli, D. S. King, D. E. Wemmer, A. Pines, E. Oldfield, *J. Am. Chem. Soc.* **1997**, *119*, 7827–7831.
[18] K. Aimi, A. Yamane, S. Ando, *J. Mol. Struct.* **2002**, *602–603*, 417–428.
[19] D. Colombo, P. Ferraboschi, F. Ronchetti, L. Toma, *Magn. Reson. Chem.* **2002**, *40*, 581–588.
[20] J. K. Harper, J. C. Facelli, D. H. Barich, G. McGeorge, A. E. Mulgrew, D. M. Grant, *J. Am. Chem. Soc.* **2002**, *124*, 10589–10595.
[21] M. J. Potrebowski, X. Assfeld, K. Ganicz, S. Olejniczak, A. Cartier, C. Gardiennet, P. Tekely, *J. Am. Chem. Soc.* **2003**, *125*, 4223–4232.

[22] A. Zheng, M. Yang, Y. Yue, C. Ye, F. Deng, *Chem. Phys. Lett.* **2004**, *399*, 172–176.
[23] C. Ochsenfeld, S. P. Brown, I. Schnell, J. Gauss, H. W. Spiess, *J. Am. Chem. Soc.* **2001**, *123*, 2597–2606.
[24] C. Benzi, O. Crescenzi, M. Pavone, V. Barone, *Magn. Reson. Chem.* **2004**, *42*, S57–S67.
[25] C. Benzi, M. Cossi, V. Barone, R. Tarroni, C. Zannoni, *J. Phys. Chem. B* **2005**, *109*, 2584–2590.
[26] T. Charpentier, S. Ispas, M. Profeta, F. Mauri, C. J. Pickard, *J. Phys. Chem. B* **2004**, *108*, 4147–4161.
[27] C. Gervais, M. Profeta, V. Lafond, C. Bonhomme, T. Azais, H. Mutin, C. J. Pickard, F. Mauri, F. Babonneau, *Magn. Reson. Chem.* **2004**, *42*, 445–452.
[28] C. Gervais, R. Dupree, K. J. Pike, C. Bonhomme, M. Profeta, C. J. Pickard, F. Mauri, *J. Phys. Chem. A* **2005**, *109*, 6960–6969.
[29] R. K. Harris, S. A. Joyce, C. J. Pickard, S. Cadars, L. Emsley, *Phys. Chem. Chem. Phys.* **2006**, *8*, 137–143.
[30] a) M. Baldus, *Angew. Chem.*, 2006, 118, 1204–1207; b) M. Baldus, *Angew. Chem.* **2006**, *118*, 1204–1207; *Angew. Chem. Int. Ed.* **2006**, *45*, 1186–1188.
[31] J. C. Facelli, A. M. Orendt, Y. J. Jiang, R. J. Pugmire, D. M. Grant, *J. Phys. Chem.* **1996**, *100*, 8268–8272.
[32] O. Walker, P. Mutzenhardt, P. Tekely, D. Canet, *J. Am. Chem. Soc.* **2002**, *124*, 865–873.
[33] H. Kaji, T. Yamada, N. Tsukamoto, F. Horii, *Chem. Phys. Lett.* **2005**, *401*, 246–253.
[34] M. Gee, R. E. Wasylishen, K. Eichele, J. F. Britten, *J. Phys. Chem. A* **2000**, *104*, 4598–4605.
[35] J. R. Brender, D. M. Taylor, A. Ramamoorthy, *J. Am. Chem. Soc.* **2001**, *123*, 914–922.
[36] S. Macholl, F. Börner, G. Buntkowsky, *Z. Phys. Chem. (Muenchen Ger.)* **2003**, *217*, 1473–1505.
[37] S. Wi, H. Sun, E. Oldfield, M. Hong, *J. Am. Chem. Soc.* **2005**, *127*, 6451–6458.
[38] J. Senker, L. Seyfarth, J. Voll, *Solid State Sci.* **2004**, *6*, 1039–1052.
[39] J. Senker, J. Sehnert, S. Correll, *J. Am. Chem. Soc.* **2005**, *127*, 337–349.
[40] J. Senker, J. Lüdecke, *Z. Naturforsch.* **2001**, *56b*, 1089–1099.
[41] D. G. Golovanov, K. A. Lyssenko, M. Y. Antipin, Y. S. Vygodskii, E. I. Lozinskaya, A. S. Shaplov, *CrytEngComm* **2005**, *7*, 465–468.
[42] R. Kurita, H. Tanaka, *Phys. Rev. B* **2006**, *73*, 104202.
[43] J. Senker, E. Rössler, *J. Phys. Chem. B* **2002**, *106*, 7592–7595.
[44] O. Hernandez, A. Hedoux, J. Lefebvre, Y. Guinet, M. Descamps, R. Papoular, O. Masson, *J. Appl. Crystallogr.* **2002**, *35*, 212–219.
[45] T. Steiner, *Angew. Chem.* **2002**, *114*, 50–80; *Angew. Chem. Int. Ed.* **2002**, *41*, 48–76.
[46] F. B. van Duijneveldt, J. G. C. M. van Duijneveldt-van de Rijdt, J. H. van Lenthe, *Chem. Rev.* **1994**, *94*, 1873–1885.
[47] M. Blomenhofer, S. Ganzleben, D. Hanft, H. W. Schmidt, M. Kristiansen, P. Smith, K. Stoll, D. Mäder, K. Hoffmann, *Macromolecules* **2005**, *38*, 3688–3695.
[48] K. A. Henzler Wildman, D.-K. Lee, A. Ramamoorthy, *Biochemistry* **2003**, *42*, 6545–6558.
[49] P. Jonkheijm, P. van der Schoot, P. H. J. Schenning, E. W. Meijer, *Science* **2006**, *313*, 80–83.
[50] B. E. Schwickert, S. R. Kline, H. Zimmermann, K. M. Lantzky, J. L. Yarger, *Phys. Rev. B* **2001**, *64*, 045410/1-6.
[51] A. Rieker, K. Schefler, E. Müller, *J. Liebigs Ann. Chem.* **1963**, *670*, 23–30.
[52] K. J. Hallock, D. K. Lee, A. Ramamoorthy, *J. Chem. Phys.* **2000**, *113*, 11187–11193.
[53] B. H. Meier, *Adv. Magn. Opt. Reson.* **1994**, *18*, 1–116.
[54] Gaussian 03, Revision B.01, M. J. Frisch, G. W. Trucks, H. B. Schlegel, G. E. Scuseria, M. A. Robb, J. R. Cheeseman, J. A. Montgomery Jr., T. Vreven, K. N. Kudin, J. C. Burant, J. M. Millam, S. S. Iyengar, J. Tomasi, V. Barone, B. Mennucci, M. Cossi, G. Scalmani, N. Rega, G. A. Petersson, H. Nakatsuji, M. Hada, M. Ehara, K. Toyota, R. Fukuda, J. Hasegawa, M. Ishida, T. Nakajima, Y. Honda, O. Kitao, H. Nakai, M. Klene, X. Li, J. E. Knox, H. P. Hratchian, J. B. Cross, C. Adamo, J. Jaramillo, R. Gomperts, R. E. Stratmann, O. Yazyev, A. J. Austin, R. Cammi, C. Pomelli, J. W. Ochterski, P. Y. Ayala, K. Morokuma, G. A. Voth, P. Salvador, J. J. Dannenberg, V. G. Zakrzewski, S. Dapprich, A. D. Daniels, M. C. Strain, O. Farkas, D. K. Malick, A. D. Rabuck, K. Raghavachari, J. B. Foresman, J. V. Ortiz, Q. Cui, A. G. Baboul, S. Clifford, J. Cioslowski, B. B. Stefanov, G. Liu, A. Liashenko, P. Piskorz, I. Komaromi, R. L. Martin, D. J. Fox, T. Keith, M. A. Al-Laham, C. Y. Peng, A. Nanayakkara, M. Challacombe, P. M. W. Gill, B. Johnson, W. Chen, M. W. Wong, C. Gonzalez, J. A. Pople, Gaussian, Inc., Wallingford, CT, **2004**..
[55] T. H. Sefzik, D. Turco, J. R. Iuliucci, J. C. Facelli, *J. Phys. Chem. A* **2005**, *109*, 1180–1187.
[56] M. Bak, J. T. Rasmussen, N. C. Nielsen, *J. Magn. Reson.* **2000**, *147*, 296–330.
[57] S. A. Smith, T. O. Levante, B. H. Meier, R. R. Ernst, *J. Magn. Reson.* **1994**, *106a*, 75–105.
[58] MATLAB, The language of technical computing, Math Works Inc., 24 Prime Park Way, Natick, MA 01760-1500, Copyright **1984–2004**.
[59] A. Steigel, H. W. Spiess, Dynamic NMR Spectroscopy, Springer, **1978**.
[60] Scientific Computing World, **2002**, *63*, 19–21.

Received: December 3, 2006
Published online: May 11, 2007

A.2:

Structural, Thermodynamic and Kinetic Aspects of the Polymorphism and Pseudopolymorphism of Prednisolone

V. Suitchmezian, I. Jeß, J. Sehnert, L. Seyfarth, J. Senker and C. Näther

Crystal Growth & Design

Accepted for publication in November 2007

The methodological combination of solid-state NMR and structural calculations as well as the computation of the chemical shift and its contribution for structure determination and verification was tested on the polymorphs **I** and **II** of Prednisolone.

My personal contributions to this work included the following:

- structure calculations under periodic boundary conditions on the base of force field methods and evaluation of the thermodynamic stable polymorph
- development of structure models for the calculation of the NMR chemical shift from the combination of semiempirical methods with structural X-ray data
- computation of the ^{13}C chemical shift tensor with DFT methods and assignment of the experimental NMR data through a comparison with the theoretical results
- discussion on the presented topic
- co-authorship of the article

The contributions of all other authors comprised of:

- synthesis of prednisolone polymorphs through re-crystallization
- measurement of powder X-ray diffraction data for prednisolone polymorphs
- structure solutions from powder X-ray diffraction data
- measurement of DSC and DTA-TG data for prednisolone polymorphs
- thermomicroscopy on prednisolone polymorphs
- ^{13}C solid-state NMR measurements on prednisolone polymorphs
- discussion on the presented topic
- authorship and co-authorship of the article

Structural, Thermodynamic and Kinetic Aspects of the Polymorphism and Pseudopolymorphism of Prednisolone

Viktor Suitchmezian[a], Inke Jeß[a], Jan Sehnert[b], Lena Seyfarth[b], Jürgen Senker[b], and Christian Näther[a]*

[a] Institut für Anorganische Chemie der Christian-Albrechts-Universität zu Kiel, Olshausenstraße 40, D-24098 Kiel, Germany.
[b] Anorganische Chemie I der Universität Bayreuth, Universitätstr. 30, 95447 Bayreuth

*Reprint requests to PD Dr. Christian Näther, Olshausenstr. 40, 24098 Kiel, Germany. Fax +49-(0)431-8801520. E-mail: cnaether@ac.uni-kiel.de

Keywords: Prednisolone, Polymorphism, Pseudopolymorphism, Hydrate, Crystal structures, Thermodynamic Aspects, Solid-state NMR, Ab initio Calculations.

Abstract

For prednisolone two polymorphic modifications (form **I** and **II**) and one sesquihydrate were found. Form **I** crystallizes in the monoclinic space goup $P2_1$, whereas form **II** and the sesquihydrate crystallize orthorhombic in space group $P2_12_12_1$. In all forms the molecules are connected via O-H···O hydrogen bonding. Solvent mediated conversion experiments reveal that form **II** represents the thermodynamically stable form at room temperature, whereas form **I** is metastable. This observation could also be confirmed by force field calculations. DSC measurements indicate no polymorphic transformation of one form into the other. The melting point of form **I** is significantly higher than that of form **II**, indicating that form **I** represents the thermodynamically most stable form at higher temperatures and that both modifications behave enantiotropic. This was proven by solvent mediated crystallization experiments which show that above 140° form **II** transforms into form **I**. Dehydration of the sesquihydrate results in the formation of modification **I**. The ^{13}C NMR spectra allow to distinguish between the three phases and confirm the crystallographic symmetry. By combining the NMR data with quantum chemical shift calculations furthermore packing effects were probed.

1. Introduction

Polymorphism, which is defined as the ability of a compound to exist in more than one crystalline modification is for several reasons an important phenomenon in academic and industrial research [1-9]. As the chemical composition of different modifications is identical, changes in the properties of these modifications can be traced back directly to differences in their crystal structure. In view of this, such investigations provide information on intermolecular interactions in crystals and the study of structure property relationships in solids.

In industrial research drug polymorphism continues to be an active field of interest [10-18]. This includes aspects of the patent law, investigations on the influence of a given phase on the chemical, biological or physical properties of a drug and requirements set by the responsible authorities for the accreditation of a drug [10-18]. In addition, such investigations can also be of importance for the sterilization of a drug, which is performed in the industry by different methods. An elegant method is the sterile filtration, which is often used for the preparation of sterile glucocorticoids as well as other drugs. In this procedure the drug is dissolved in a given solvent, filtered off under pressure and afterwards the solvent is vaporized, the drug is dried and finally micronized. By this procedure different polymorphic modifications can either be obtained directly or by decomposition of solvates and in the end it must be guaranteed that the only form present is that preferred by the manufacturer. This was one of our starting points to investigate glucocorticoids, which belong to the most versatile and effective drugs worldwide [19-25]. Although they are known for several decades, their polymorphism and pseudopolymorphism has not been investigated in detail and sometimes controversial results have been reported. Surprisingly only a few crystal structures are available in the Cambridge Structure Database (CSD).

In our own investigations we have discovered a large number of hitherto unkown modifications and we have studied their stability and transition behaviour in detail [26-32]. In recent investigations our interest focus on prednisolone (scheme 1), which possesses a strong anti-rheumatic activity and little undesired effects [33,34].

The polymorphism of prednisolone was investigated for example using thermoanalytical methods and IR-spectroscopy [34-41]. It has been reported that this drug exists in two different polymorphic forms (form 1 and 3) and one hydrate (form 2) [34, 42, 43]. All forms were characterized by X-ray powder diffraction and the cell parameters for form 1 and 3 were presented [34, 43]. Surprisingly the powder patterns for form 1 and 3 are very similar and all of these patterns are different from those measured for the forms presented in this paper. In

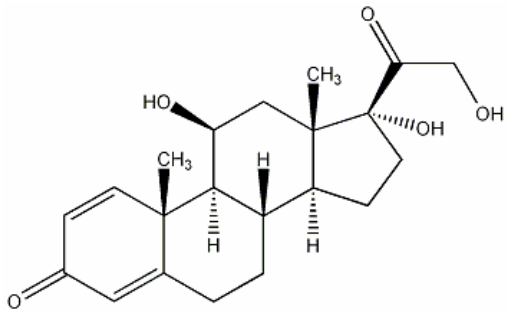

(1)

addition, it was reported that form 3 crystallizes monoclinic [34], which is not the case (see below). None of these forms were characterized by single crystal X-ray diffraction and it was not investigated which of these forms represents the thermodynamically most stable form as function of temperature and how the different forms are related. In view of this, we have investigated prednisolone for polymorphism in more detail by means of X-ray single crystal and powder diffraction, solid-state NMR spectroscopy, thermal analysis, thermomicroscopy and molecular modeling.

2. Experimental Section

2.1 Chemicals

Prednisolone is commercial available and was procured from HPP pharmaceuticals.
All solvents used for the crystallization experiments were of analytical grade.

2.2 X-ray powder diffraction experiments

X-Ray powder diffraction experiments were performed using a STOE STADI P transmission powder diffractometer with an 4° or 45° PSD (position sensitive detector) as well as an image plate detector using CuKα-radiation (λ = 1.540598 Å).

2.3 Crystal structure determination

All data were measured at 170 K using a STOE IPDS-1 Imaging Plate Diffraction system. Structure solutions were performed with direct methods using SHELXS-97 [44]. The structure refinements were performed against F^2 using SHELXL-97 [4]. All non-hydrogen atoms were refined using anisotropic displacement parameters. The C-H hydrogen atoms were positioned with idealized geometry (methyl H atoms were allowed to rotate but not tip) and refined with isotropic displacement parameters with $U_{iso}(H) = 1.2 \times U_{eq}(C_{methin/methylene}) =$

1.5 × $U_{eq}(C_{methyl})$ using a riding model with C-H_{methin} = 0.99 Å, C-$H_{methylene}$ = 0.98 Å, C-H_{methyl} = 0.97 Å for prednisolone. The O-H hydrogen atoms were located in difference map but positioned with idealized geometry allowed to rotate but not tip and were refined using isotropic displacement parameter with $U_{iso}(H) = 1.5 \times U_{eq}(O)$ using a riding model with O-H = 0.83 Å. The water hydrogen atoms were located in difference map, their bond lengths set to ideal values of 0.86 Å and afterwards they were refined isotropic $U_{iso}(H) = 1.5 \times U_{eq}(O)$ using a riding model. In the absence of anomalous scattering atoms the absolute structure and absolute configuration could not be determined. Therefore, Friedel equivalents were merged and the absolute configuration was assigned based on the known absolute configuration of the starting compound. Details of the structure determination are given in table 1.

Crystallographic data have been deposited with the Cambridge Crystallographic Data Centre (CCDC XXXX, form **I**; CCDC XXXX, form **II**; CCDC XXXX, sesquihydrate). Copies may be obtained free of charge on application to the Director, CCDC, 12 Union Road, Cambridge CB2 1E2, UK (fax: Int. Code +(44)01223/3 36-033, e-mail: deposit@chemcrys.cam.ac.uk).

2.4 Differential thermal analysis, thermogravimetry and mass spectroscopy

DTA-TG measurements were performed in Al_2O_3 crucibles using a STA-409CD thermo balance from Netzsch. Several measurements under nitrogen atmosphere (purity 5.0) with 4°C/min were performed. All measurements were performed with a flow rate of 75 ml/min and were corrected for buoyancy and current effects.

2.5 DSC investigations

DSC investigations were performed with the DSC 204/1/F device from Netzsch. The measurements were performed in Al pans with heating rates of 3°C /min. The instrument was calibrated using standard reference materials.

2.6 Thermomicroscopy

The thermomicroscopic investigations were performed using a hot stage from Linkam and a microscope from Olympus. The measurements were performed with 2°C/min in an argon atmosphere.

Table 1: Crystal data and results of the structure refinement for form **I**, **II** and the sesquihydrate.

Data	**Form I**	**Form II**	**Hydrate**
Empirical Formula	$C_{21}H_{28}O_5$	$C_{21}H_{28}O_5$	$C_{21}H_{28}O_5 \cdot 1{,}5\ H_2O$
MW / g·mol^{-1}	360.43	360.43	387.46
Crystal color	colorless	colorless	Colorless
Crystal size/mm^3	0.5 x 0.45 x 0.5	0.3 x 0.25 x 0.2	0.3 x 0.2 x 0.25
Crystal system	Monoclinic	orthorhombic	Orthorhombic
Space group	$P2_1$	$P2_12_12_1$	$P2_12_12_1$
A / Å	6.3052(5)	5.9774(3)	6.3945(3)
B / Å	12.9392(7)	11.7916(7)	24.5789(10)
C / Å	10.9984(9)	25.5228(14)	24.8376(11)
β / °	91.167(9)	-	-
V / Å^3	897.11(11)	1798.93(17)	3903.7(3)
Temperature / K	170(2)	170(2)	170(2)
Z	2	4	8
$D_{calculated}$ / g·cm^{-3}	1.334	1.331	1.319
F(000)	388	776	1672
2θ-range / °	5 - 56	5 - 54	5 – 54
H/k/l ranges	$-8 \le h \le 8$	$-7 \le h \le 7$	$-8 \le h \le 7$
	$-16 \le h \le 17$	$-15 \le h \le 15$	$-19 \le h \le 31$
	$-14 \le h \le 14$	$-22 \le h \le 32$	$-31 \le h \le 31$
μ(MoKα) / mm^{-1}	0.094	0.094	0.100
Measured reflexes	8673	9157	17461
$R_{int.}$	0.0580	0.0501	0.0646
Independent refl.	2246	2253	4707
Refl. with I > 4σ(I)	2086	1886	3483
Refined parameters	241	241	506
R_1 [$F_o > 4\sigma(F_o)$]	0.0337	0.0351	0.0423
wR_2 [all data]	0.0894	0.0881	0.0933
GooF	1.053	1.019	0.974
Min./max. res. /e·Å^{-3}	0.206 and -0.172	0.216 and -0.154	0.193 and -0.175

2.7 NMR spectroscopy

Solid-state ^{13}C MAS-NMR spectra were measured with a conventional impulse spectrometer AvanceII (Bruker) operating with a resonance frequency of 300 MHz for ^{1}H (B_0 = 7 T). The samples were filled in zirconia rotors (diameter 4 mm) and mounted in a standard triple-resonance MAS probe (Bruker). The acquisition of the 1D spectra was performed with a ramped ^{1}H-^{13}C cross-polarization double resonance sequence where the ^{1}H radiation power decreases linearly from 100% to 50 % during the contact time t_H [45]. A t_H of 5 ms ensured the excitation of all heteroatoms even those not covalently bonded to hydrogen. For these measurements the rotation frequency ν_{rot} was adjusted to 7.5 kHz. To enable a complete assignment additionally for form **II** cross-polarisation polarisation-inversion (CPPI) spectra were recorded as a function of the inversion time t_i [46]. For these experiments zirconia rotors with a diameter of 7 mm were used and mounted in standard double-resonance MAS probes (Bruker). ν_{rot} equalled 5 kHz and the inversion time was varied between 10µs and 600µs. In all cases the FIDs were recorded using broadband proton decoupling with a SPINAL64 sequence [47] and the ^{13}C resonances are reported with respect to TMS.

2.8 Calculations

The geometry optimization of the structures of forms **I** and **II** under periodic boundary conditions was carried out with MS Modelling 4.0. For both polymorphs the experimental unit cell and the fractional coordinates of all atoms were freely relaxed in *P*1 symmetry using the COMPASS with force field assigned charges [48]. The computation of the NMR chemical shift for **I** and **II** was performed with Gaussian03 [49]. A single molecule was cut out from each X-ray structure and the hydrogen positions were relaxed under the constraint of fixed dihedral distortions using the semiempirical PM3 method [50]. Based on the such derived models the NMR chemical shielding was calculated with the PBE1PBE hybrid density functional and the 6-31G(d) basis set. All calculated isotropic shifts are referenced to TMS computed on the same level of theory.

3. Results and discussion

3.1 Crystallization experiments

Crystalline suspensions of commercial prednisolone (form **I**) were stirred in different solvents for two weeks and afterwards the residues obtained were investigated by X-ray powder diffraction. In most solvents the powder patterns of the residues are identical to that of form **I** (Table 2). Different patterns were observed in methanol (form **II**) and in aqueous solutions. TG measurements clearly prove that form **II** does not contain solvent, whereas the residue obtained in aqueous solution represents a sesquihydrate.

In order to determine, which of the two solvent free forms represents the thermodynamically most stable modification at room temperature, crystalline suspensions of a mixture of form **I** and form **II** were stirred in methanol, ethanol and acetonitrile. Surprisingly, the powder patterns of all residues are in perfect agreement with that of form **II**. Therefore, form **II** must represent the thermodynamically most stable form at room temperature whereas form **I** is metastable.

Table 2: Results of the solvent mediated conversion experiments starting from form **I**.

Solvent	**Form**	**Solvent**	**Form**
Methyl isobutyl ketone	**I**	2-Butanone	**I**
Toluene	**I**	1-Butanol	**I**
Heptane	**I**	Tetrahydrofurane	**I**
1-Methyl-2-pyrrolidon	**I**	Acetone	**I**
n-Propanol	**I**	Methylene chloride	**I**
Ethanol	**I**	Ethanol/H_2O = 90/10	**I**
Methylacetate	**I**	Carbon tetrachloride	**I**
Chloroform	**I**	Ether	**I**
2-Butanol	**I**	Methanol	**II**
2-Propanol	**I**	NaCl solution (150 mM)	**hydrate**
Acetonitrile (ACN)	**I**	ACN/H_2O = 90/10	**hydrate**
Cyclohexane	**I**	Acetone/H_2O = 90/10	**hydrate**
Ethylacetate	**I**	Water	**hydrate**
Tert. butyl methyl ether	**I**	Hydrochloric acid pH=1	**hydrate**

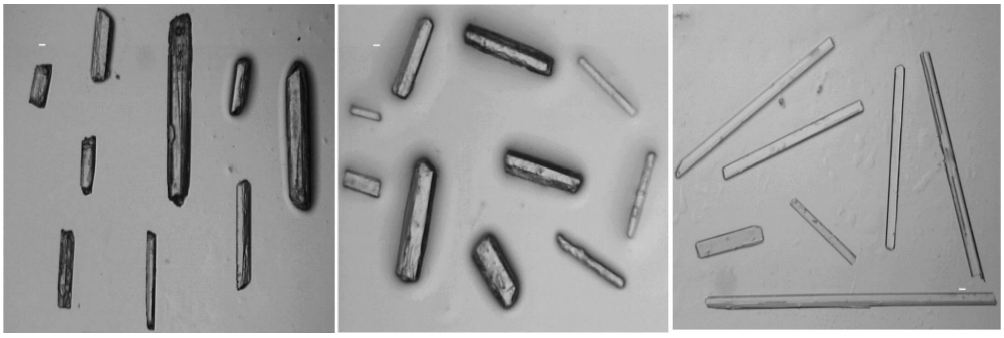

Figure 1: Microscopic images of crystals of form **I** (left) **II** (mid) and the sesquihydrate (right).

Crystallization experiments were performed in order to prepare crystals, suitable for single crystal structure analysis. Single crystals of all forms were prepared by slow evaporation of the solvent from a saturated solution of prednisolone in ethanol (form **I**), methanol (form **II**) and acetonitrile/water 90:10 (sesquihydrate). The morphology of the crystals of form **I** and **II** are similar, but the crystals of form **II** are in most cases thicker (Figure 1). The sesquihydrate crystallizes as very thin plate like needles (Figure 1).

3.2 Crystal structures

Form **I** of prednisolone crystallizes in the monoclinic and non-centrosymmetric space group $P2_1$ with Z = 2 and all atoms in general positions (Figure 2: top and Table 1). In the crystal structure the molecules are connected via O-H···O hydrogen bonding between the hydroxyl hydrogen atom at O2 and the hydroxy oxygen atom O3 as well as between the hydroxyl hydrogen atom at O3 and the carbonyl oxygen atom O1. The geometry of these interactions indicates that these are strong hydrogen bonds (Table 3). From this arrangement layers are formed, which are parallel to the b/c plane (Figure 2: bottom). Within the molecules a very weak intramolecular hydrogen bond is found between the hydroxyl hydrogen atom at O5 and the carbonyl group at O4.

Form **II** crystallizes in the primitive, orthorhombic space group $P2_12_12_1$ with Z = 4 and all atoms in general positions (Figure 3: top and Table 1). As in form **I** the molecules are connected via intermolecular O-H···O hydrogen bonding but the topology of the hydrogen bonded network is different (Figure 3: top and Table 3).

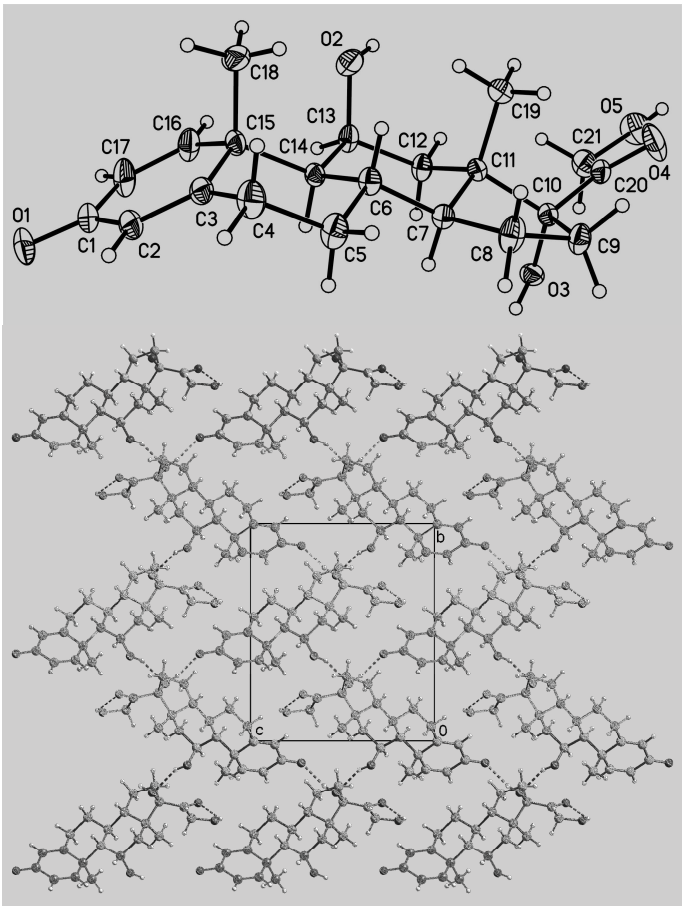

Figure 2: Crystal structure of form **I** with labelling and displacement ellipsoids drawn at the 50% probability level (top) and with view in the direction of the a-axis (bottom) (Intramolecular hydrogen bonding is not shown for clarity).

Table 3: Hydrogen bonding interaction in form **I** and form **II**.

O-H···O	**d(O-H)**	**d(H···O)**	**<OHO**	**d(O···O)**	**Form**
O2-H2···O3A	0.830	2.099	155.89	2.877	**I**
O3-H3···O1B	0.830	1.952	159.73	2.746	**I**
O5-H5···O4	0.830	2.158	115.18	2.621	**I**
O2-H2···O4C	0.830	2.436	115.47	2.892	**II**
O3-H3···O1D	0.830	1.970	165.02	2.780	**II**
O5-H5···O4	0.830	2.257	112.17	2.682	**II**
O5-H5···O2E	0.830	2.403	153.36	3.167	**II**

Symmetry codes: A = -x+2, y-1/2, -z+1 ; B = -x+2, y+1/2, -z+2 ;
C = -x+1, y-1/2, -z+1/2 ; D = x, y+1, z ; E = -x+1, y+1/2, -z+1/2.

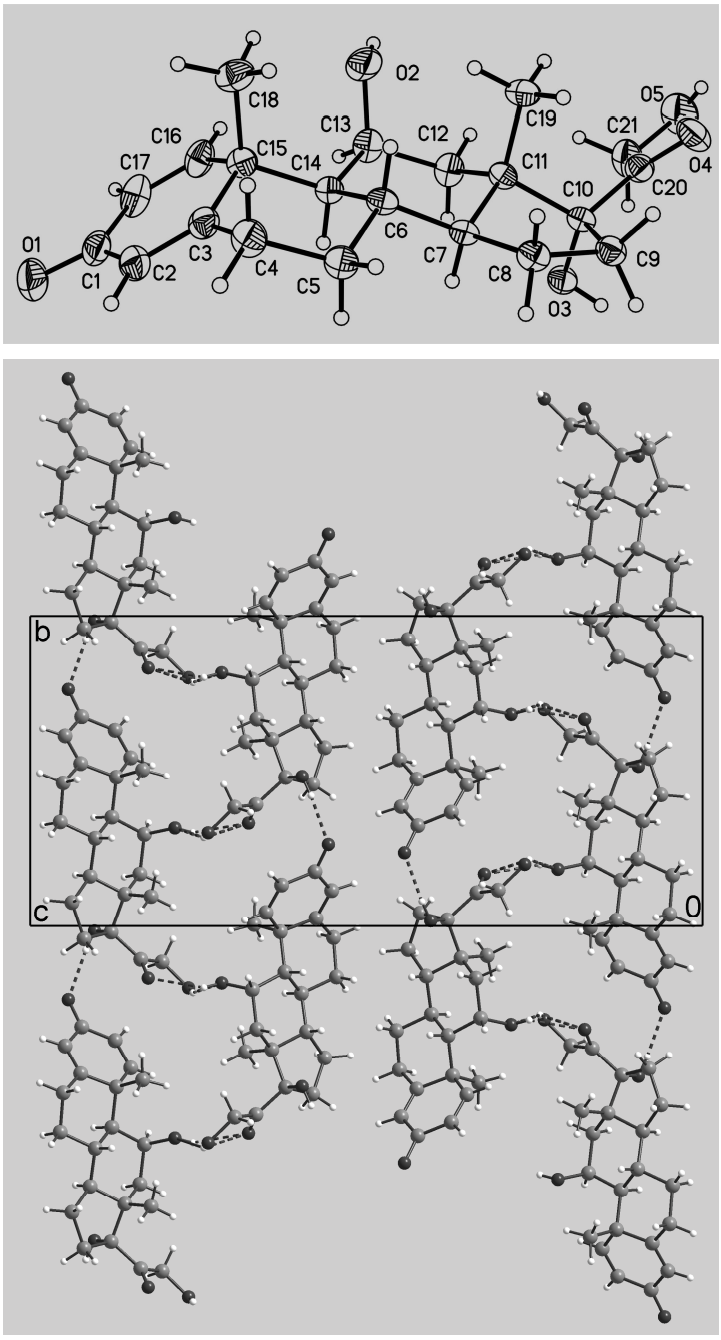

Figure 3: Crystal structure of form **II** with labelling and displacement ellipsoids drawn at the 50% probability level (top) and with view in the direction of the a-axis (bottom).

In form **II** the molecules are connected by the carbonyl oxygen atom O1 and the hydroxyl hydrogen atom at O3 into chains that elongate in the direction of the a axis (Figure 3: top).

These chains are further connected by O-H···O hydrogen bonding between the hydroxyl hydrogen atom H5 and the hydroxyl oxygen atom O2 (Table 3). As in form **I** H5 is also involved in a weak intramolecular hydrogen bond to O4. In addition O4 is involved in a weak hydrogen bond with the hydroxyl hydrogen atom H2 (Table 3). The hydrogen bonds connect the single chains into double chains that elongate in the direction of the a-axis.

The sesquihydrate crystallizes in the orthorhombic, non-centrosymmetric space group $P2_12_12_1$ with Z = 8 and two crystallographically independent prednisolone molecules as well as three crystallographically independent water molecules in general positions (Figure 4: top and Table 1). As in form **I** and **II,** the molecules are connected by intermolecular O-H···O hydrogen bonding (Figure 4: bottom and Table 4).

Altogether 12 hydrogen bonds between the prednisolone molecules, the water and the prednisolone molecules as well as different water molecules are found. (Figure 4: bottom and Table 4). All hydrogen atoms of the water molecules are involved in hydrogen bonding. The water oxygen atom O33 acts in addition as an acceptor for one hydrogen atom whereas the water oxygen atoms O32 and O33 are involved in altogether 4 hydrogen bonds within distorted tetrahedra. From this arrangement a complicated 3D hydrogen bonded network is found (Figure 4: top).

Table 4: Hydrogen bonding interaction in prednisolone sesquihydrate.

Form B O-H···O	**d(O-H)**	**d(H···O)**	**<OHO**	**D(O···O)**
O2-H2···O21A	0.830	2.013	170.57	2.835
O3-H3···O31	0.830	2.047	177.77	2.876
O5-H5···O25B	0.830	1.901	164.60	2.710
O22-H22···O5C	0.830	2.119	167.72	2.936
O23-H23···O32D	0.830	2.116	158.89	2.906
O25-H25···O32	0.830	1.982	165.17	2.973
O31-H1O···O24E	0.830	1.922	179.79	2.782
O31-H2O···O1F	0.860	2.033	174.53	2.890
O32-H3O···O4G	0.860	1.996	163.30	2.830
O32-H4O···O33H	0.860	2.163	128.30	2.779
O33-H5O···O1	0.860	2.074	150.90	2.856
O33-H6O···O31I	0.860	1.998	163.33	2.833

Symmetry codes: A = x+1/2, -y+1/2, -z+1 ; B = x, y, z-1 ; C = x+1/2, -y+1/2, -z+1 ;
D = x-1, y, z ; E = x, y, z-1 ; F = -x+3/2, -y+1, z-1/2 ; G = x+1, y, z+1;
H = -x+5/2, -y+1, z+1/2 ; I = -x+5/2, -y+1, z+1/2.

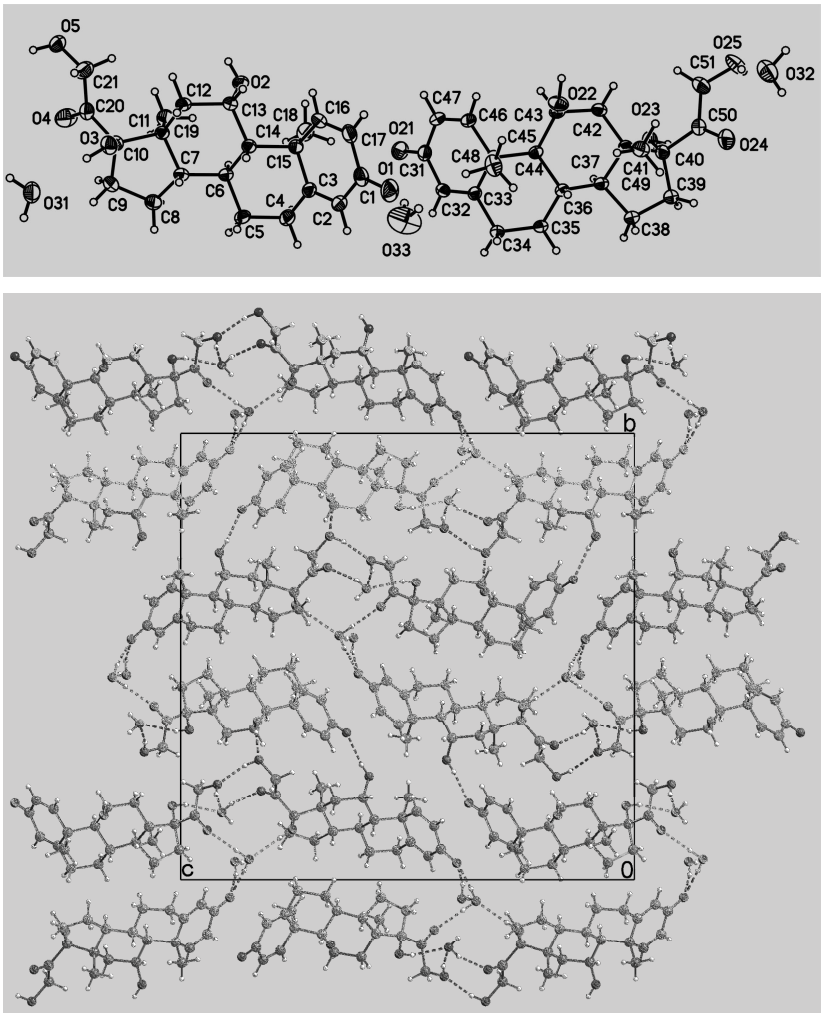

Figure 4: Crystal structure of predinisolone sesquihydrate with labelling and displacement ellipsoids drawn at the 50% probability level (top) and with view in the direction of the a-axis (bottom).

Most changes are found in the packing of the prednisolone molecules in the different forms, whereas only minor changes are found in the conformation of the glucocorticoid molecules. This is obvious if the molecules in form **I** – **III** are fitted onto each other (Figure 5). As expected, most of the changes are found in the side chain but even if the sorrounding of the carboxyl group is different in all forms, their conformation is similar in all modifications.

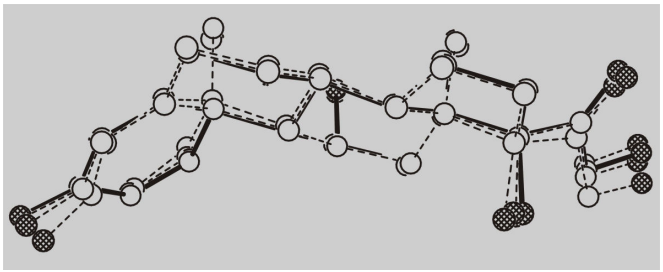

Figure 5: Structures of the molecules in form **I**, **II** and in the sesquihydrate of prednisolone fitted onto each other.

3.3 Investigations on the desolvation of the sesquihydrate

Measurements on the sesquihydrate using thermogravimetry and differential thermoanalysis (DTA-TG) show two mass steps in the TG curve, which are accompanied with two endothermic events at T_p = 106°C and T_p =234°C in the DTA curve (Figure 6). The second DTA signal at 234°C indicates the melting point and the corresponding mass step to the vaporization of the solvent free modification formed by desolvation of the sesquihydrate (Figure 6). The experimental mass loss in the first step of 6.2 % is in good agreement with that calculated for a sesquihydrate of 6.9 %.

The X-ray powder pattern of the residue formed after the first TG step, corresponds to that of form I clearly showing that this modification is formed on dehydrations (Figure 7).

3.4 Temperature dependent X-ray powder diffraction

Form **I**, **II** and the sesquihydrate were investigated using temperature dependent X-ray powder diffraction to determine if a polymorphic phase transition occurs on heating (Figure 8). For form **I** and form **II** no changes in the powder patterns are observed on heating, which shows that no polymorphic transition occurs under these conditions until melting (Figure 8). These measurements show, that the melting point of form **I** is significantly higher than that of form **II**. In contrast, the sesquihydrate on heating transforms into form **I** at about 90°C. On further heating only melting of form **I** is observed (Figure 8).

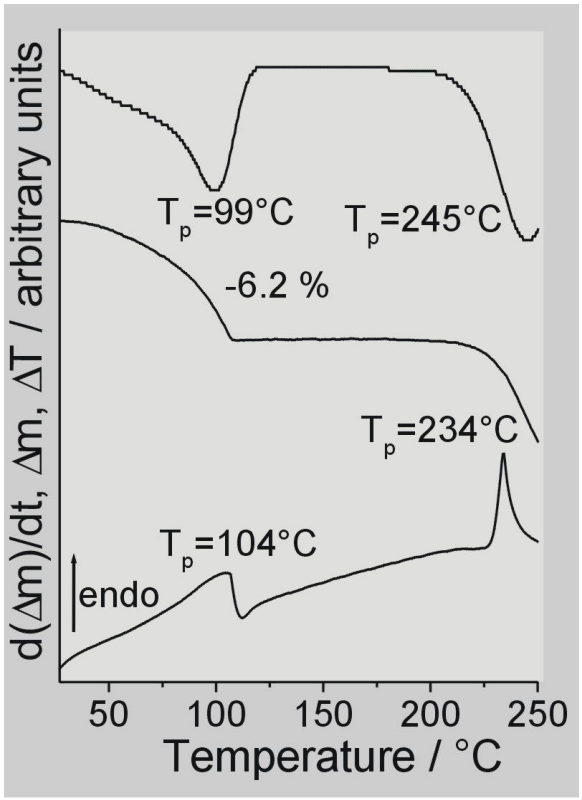

Figure 6: DTA, TG and DTG curve of prednisolone sesquihydrate (T_p = peak temperature).

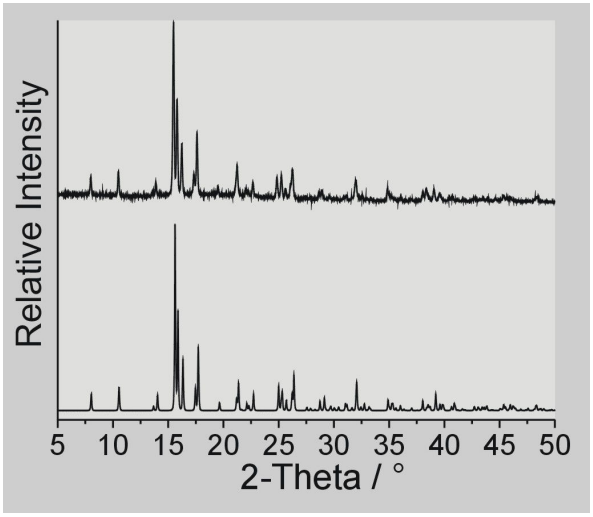

Figure 7: X-ray powder pattern of the residue obtained after the first TG step of prednisolone sesquihydrate (top) and X-ray powder pattern of form **I** calculated from single crystal data (bottom).

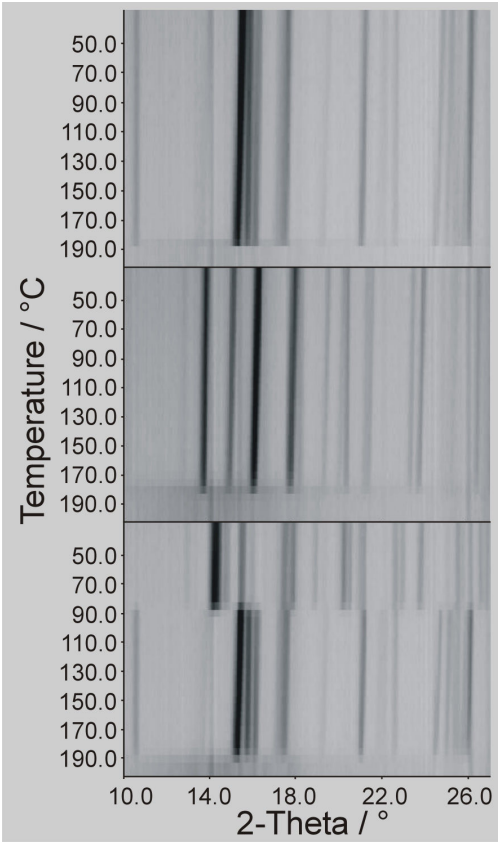

Figure 8: Temperature dependet X-ray powder patterns for form **I** (top), form **II** (mid) and prednisolone sesquihydrate (bottom).

3.5 Differential scanning calorimetry investigations

On heating, form **I** displays a single endothermic signal in its DSC thermogram at T_o = 239°C, which corresponds to the melting point of this form (Figure 9: top and Table 4). A similar behaviour is observed for form **II** but the melting point of T_o = 227°C is significantly lower than that of form **I** (Figure 9: mid and Table 4). As expected two endothermic signals are observed for the sesquihydrate on heating, the first of which corresponds to the removal of the crystal water, whereas the second signal corresponds to the melting of modification **I**, which is formed by desolvation (Figure 9: bottom and Table 4).

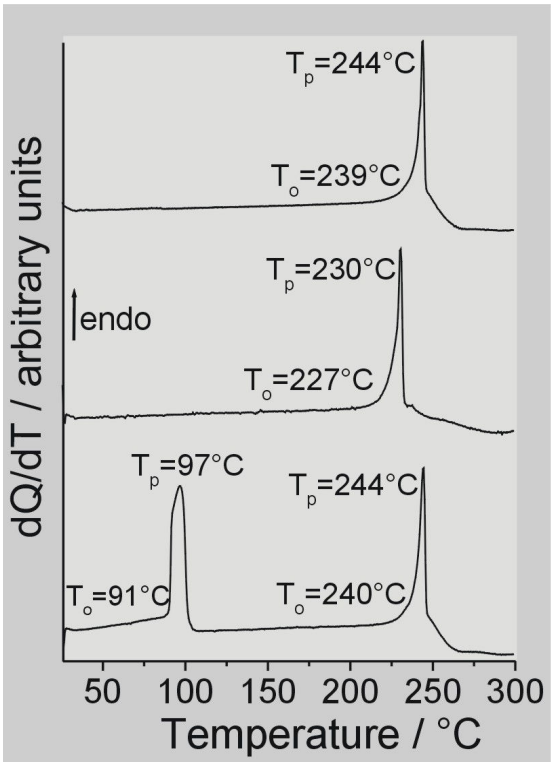

Figure 9: DSC curves for forms **I** (top), form **II** (mid) and the sesquihydrate the prednisolone (bottom) (T_o = (extrapolated) onset temperature, T_p = peak temperature).

The DSC measurements reveal, that the melting point of form **I** is significantly higher than that of form **II**, whereas the heat of fusion and the melting entropy is significantly lower (Table 4). The results of our DSC measurements are in agreement with that of previously reported thermoanalytical measurements performed by Veiga et al. [42]. Although some differences are found in the absolute numbers, all trends remain the same.

Table 4: Results of the DSC measurements on form **I**, **II** and the sesquihydrate of prednisolone (T_o = extrapolated onset temperature; T_p = peak temperature). For the sesquihydrate only the DSC data for the melting of form **I** are given.

	Form **I**	Form **II**	sesquihydrate
T_o/°C	236.5-239.0	223.8-227.7	238.3-238.8
T_p/°C	241.8-243.7	228.4-230.3	243.6-244.3
$\Delta_{fus}H$/kJmol^{-1}	26.5-29.7	34.37-35.80	26.2-29.4
$\Delta_{fus}S$/Jmol^{-1}K^{-1}	108.74-122.83	149.24-157.43	107.24-120.69

3.6 Thermomicroscopy

All forms were investigated by thermomicroscopy. Decomposition of the sesquihydrate is observed at about 130°C and is complete at about 140°C (Figure 10). During this transformation the crystal develops cracks, which shows that this event is reconstructive. On further heating, melting of form **I** is observed at about 242°C, whereas melting of form **II** starts at about 245°C. Because on desolvation of the sesquihydrate modification **I** is formed, the sesquihydrate and form **I** melts at the same temperature.

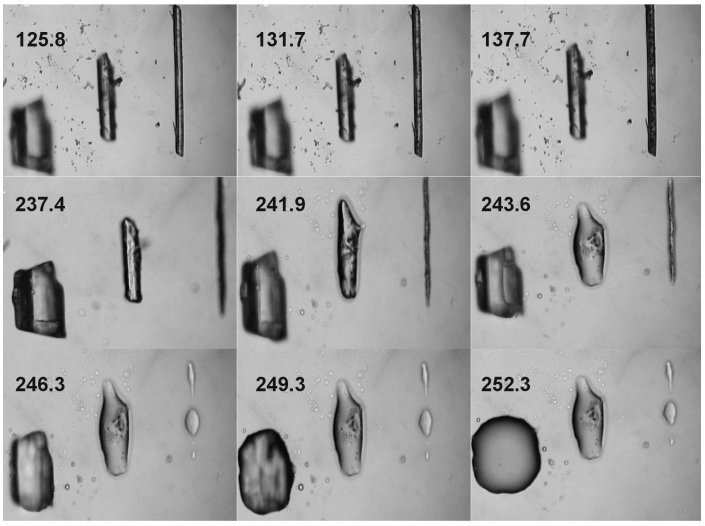

Figure 10: Results of the thermomicroscopic experiments on form **II** (left), form **I** (mid) and the sesquihydrate of prednisolone (right) (heating rate 2°C/min).

*3.7 Solubility measurements on form **I** and **II***

The solubility of both polymorphic modifications was determined in methanol and ethanol at room temperature. In this experiment a crystalline suspension of each form in 1.000 µL of each solvent were stirred for 1 h. Afterwards 250 µL of the clear solution were removed, the solvent vaporized and the residue weighed. The solid residue was immediately investigated by X-ray powder diffraction in order to prove that no phase transformation occurred. Always four of such measurements were performed for each form in each solvent. It was found that in ethanol the solubility of form **I** is 28.9(4) g/L whereas that of form **II** is 20.8(4) g/L. The same trend is observed in methanol, in which the solubility of both forms are higher (form **I** = 46.8(8) g/L and form **II** = 37.6(9) g/L).

3.8 Force field calculations

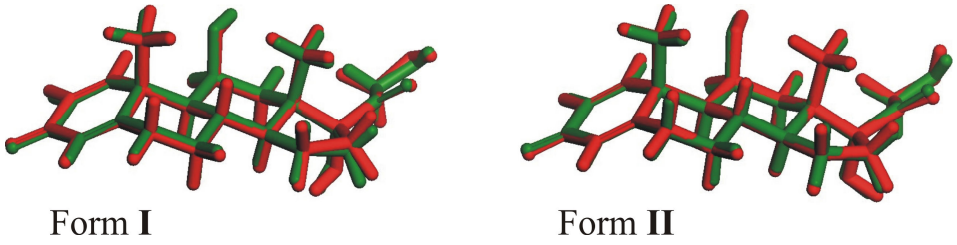

Figure 11. Comparison of the asymmetric units of form **I** and **II** as found in the X-ray structure (green) and from the COMPASS force field optimizations (red).

To check the thermodynamic stability of form **I** and **II** the two X-ray structures were freely optimized in *P*1 symmetry using the COMPASS force field. The experimental and the calculated structures show an excellent match. Although the calculations were carried out in *P*1 and therefore did not bear any symmetry constraints the crystal symmetry as found in the X-ray structure was conserved and the maximum deviation of the lattice parameters is below 3% (Table 5).

Figure 11 shows a comparison between the asymmetric unit as obtained from the single crystal data and from the force field calculations. The largest deviations are found for the side

Table 5: Results of the free geometry optimization of forms **I** and **II** with the COMPASS force field in *P*1.

Data	**Form I**		**Form II**	
	Exp.	Calc.	Exp.	Calc.
space group	$P2_1$	*P*1	$P2_12_12_1$	*P*1
A / Å	6.3052(5)	6.351	5.9774(3)	5.839
B / Å	12.939(1)	12.692	11.792(1)	11.844
C / Å	10.998(1)	10.932	25.523(2)	24.854
α / °	-	90.00	-	90.00
β / °	91.17(1)	91.35	-	90.00
γ / °	-	90.00	-	90.00
Z	2	2	4	4
E_{tot} / kJ·mol^{-1}		-786.8		-1659.9
E_{mol} / kJ·mol^{-1}		-393.4		-415.0

chain –CO-CH_2OH, its neighboring OH and the methylene group of the five membered ring. In form **II** these deviations are less pronounced than in form **I**. The molecular conformation of both polymorphs is nearly identical with the experimental structures. Table 5 as well lists the energies (total energy of the cell and energy per molecule) of form **I** and **II**. With respect to one molecule the calculated energy of form **II** is by 21.6 kJ/mol lower than the one of form **I**. Thus based on the force field calculations form **II** is predicted to be the thermodynamic stable polymorph which agrees well with the results of the DSC (Figure 9 and Table 4) and crystallization experiments (Table 2).

3.9 Solid state NMR spectroscopy

^{13}C CP MAS spectra were measured for form **I**, **II** and the sesquihydrate (Figure 12). Although similar shifts are observed for all three phases the differences are large enough to clearly distinguish the individual polymorphs based on ^{13}C NMR spectroscopy. The spectra of form **I** and **II** depict 21 well resolved resonances whereas in the case of the sesquihydrate nearly all of these are split into doublets. This is in perfect agreement with the results of the single crystal structure analysis (Table 1). For the forms **I** and **II** one complete molecule is located in the asymmetric unit with all atoms on the general positions leading to 21 crystallographically unequal carbon atoms all well resolved in the ^{13}C NMR spectra. In the case of sesquihydrate the asymmetric unit contains two inequivalent molecules giving rise to a maximum of 42 resonances in the ^{13}C NMR spectrum. The doublet character (Figure 12) demonstrates that both molecules have similar but not identical surroundings.

As mentioned above the resonances for the individual carbon atoms in the different phases are similar (the maximum deviation is about 5 ppm) indicating that the molecular conformation is closely related in all three phases. The largest variations occur in the regions 200 - 220 ppm, 150 - 180 ppm and 120 - 130 ppm. For an analysis of packing effects these regions seems therefore most promising. Such an analysis however requires an unequivocally assignment of all resonances in the ^{13}C MAS spectra not possible based on the values of the isotropic shifts alone. Thus we carried out CPPI experiments for form **II** as a function of the inversion time t_i. The analysis of the dependence of the signal intensity of each individual resonance allows for a classification as CH_3, CH_2 and CH groups or as quaternary carbon atoms [46]. In figure 13 two CPPI spectra are depicted exemplarily with inversion times of 0 µs and 300 µs. For the latter t_i the intensity of CH carbons is distinctly reduced whereas CH_2 groups exhibit already negative intensities. Due to their reorientational disorder the methyl groups are only slightly affected and the quaternary carbon atoms remain nearly unaltered.

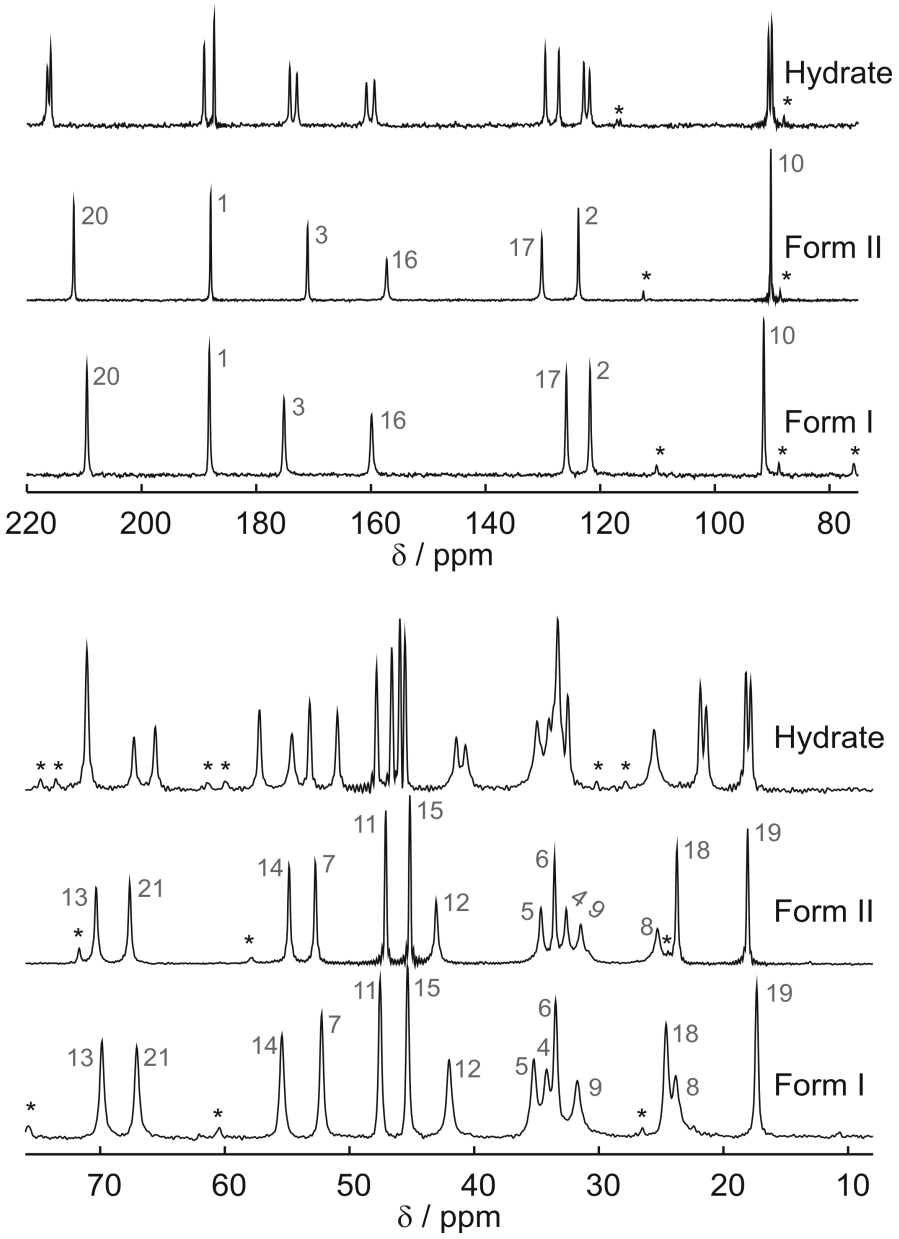

Figure 12: ^{13}C MAS NMR spectra of form **I**, **II** and the sesquihydrate for the low field (top) and the high field (bottom) regions. The assignment for the resonances polymorphs **I** and **II** is based on CPPI data (see figure 13) and results of quantum chemical calculations (see figure 14). The asterisks denote spinning sidebands.

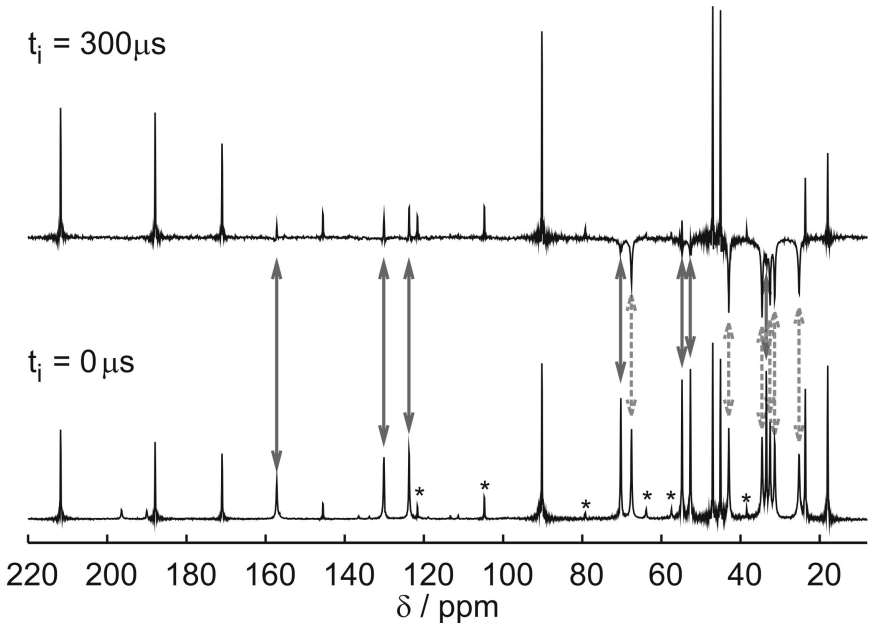

Figure 13: ^{13}C CPPI MAS NMR spectra of form **II** for an inversion time t_i = 0 µs (bottom) and t_i = 300µs (top). The drawn through and dashed arrows mark the signals for CH and CH_2 groups, respectively.

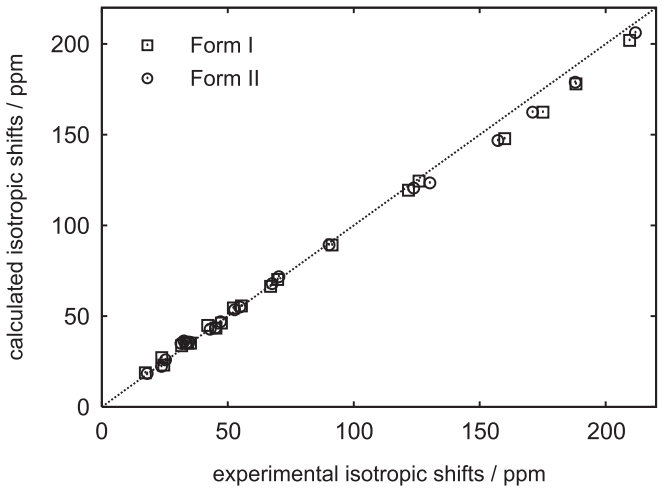

Figure 14: Comparison of experimentally determined and calculated ^{13}C isotropic chemical shifts for the forms **I** and **II** of prednisolone. The theoretical model comprised of a single molecule cut out of the X-ray structures. The H positions were optimized with PM3 under the constraint of fixed dihedral distortions and the DFT calculated shifts referenced for TMS. The dashed line represents a guide for the eye with an intercept of 0.0 and a slope of 1.0.

Additionally an ab initio calculation of the chemical shifts was carried out for isolated molecules taken from the X-ray structures of forms **I** and **II**. These models did not include the electronic influence of hydrogen bonding on the ^{13}C chemical shifts but only the steric in the molecules due to crystal packing. Nevertheless combined with the results of the CPPI experiments all resonances in the ^{13}C spectra of form **I** and **II** could unequivocally be assigned (Table 6). Figure 14 shows a correlation plot for the assigned theoretical and experimental values. Below 120 ppm the average deviation of the chemical shift is 1.6 ppm and the maximum deviation is about 3 - 4 ppm for both forms. However, above 130 ppm with up to 13 ppm the deviations are much larger. This difference is caused by the effect of the electronic environment on the chemical shifts. The theoretical values are systematically

Table 6: Measured (δ_{exp}) and calculated (δ_{calc}) isotropic chemical shifts in ppm for the ^{13}C resonances of the forms **I** and **II**.

Label	Form **I**		Form **II**	
	δ_{exp}	δ_{calc}	δ_{exp}	δ_{calc}
1	188.2	178.0	187.9	178.9
2	121.7	119.4	123.8	120.6
3	175.1	162.4	171.0	162.4
4	33.4	35.5	32.6	34.9
5	35.2	35.1	34.6	35.7
6	34.1	35.1	33.5	35.0
7	52.2	54.5	52.7	53.5
8	23.8	27.1	25.3	25.9
9	31.7	33.7	31.4	36.3
10	91.4	89.2	90.2	89.3
11	47.5	46.2	47.1	46.9
12	42.0	44.9	43.0	42.8
13	69.8	70.2	70.3	71.7
14	55.4	55.6	54.8	55.0
15	45.3	43.4	45.1	43.5
16	159.9	147.8	157.2	146.8
17	125.9	124.4	130.2	123.4
18	24.6	23.0	23.7	22.3
19	17.3	18.8	18.0	18.4
20	209.5	202.0	211.8	206.2
21	67.0	66.4	67.6	67.9

smaller when compared to the experiment indicating a deshielding of the nuclei through hydrogen bonding. This effect is most pronounced for C1, C3 and C16 which are interconnected in a system of conjugated double bonds (see Figures 2 and 3). For the carboxylic nucleus C20 the deshielding effect is slightly less pronounced. It is interesting to note that the electronic environment of the π systems in prednisolone is more sensitive to the hydrogen bonding than the one of the aliphatic region. The chemical shifts of the aliphatic C-OH groups which are involved in hydrogen are described by the consideration of the distortion of the OH group due to crystal packing. This effect is included in the here used model systems through the constrained distortional angles of the H atoms which explains the good match with the experimental data.

3.8 Thermodynamic aspects

The crystallization experiments clearly prove that form **II** represents the thermodynamically stable form at room temperature, whereas form **I** is metastable. This is in agreement with the solubility measurements which show, that form **I** is more soluble than form **II**. As form **II** exhibits a higher melting energy than form **I**, this modification should also represent the thermodynamically most stable form at lower temperatures. This is in agreement with our packing calculations, which shows that form **II** should be more stable than form **I** by about 50 kJ/mol. In force field calculations form **II** is by about 22 kJ/mol lower in energy than form **I**. Although the energy difference is much too high in the packing calculations, qualitatively the overall trend matches. The findings are in contrast to the density rule but the difference in density is insignificant as exceptions from this rule are well known.

The melting point of form **I** is significantly higher than that of form **II**. Therefore form **I** should be more stable at higher temperatures and both forms should behave enantiotropic. This is in agreement with the melting entropy rule, which states that in the case of enantiotropy the higher melting form must have the lower melting entropy, whereas in the case of monotropy the higher melting form must have higher melting entropy [4]. (Compare table 4). Unfortunately no polymorphic transformation of form **II** into form **I** was observed on heating in all of our investigations. Therefore, we have performed solvent mediated conversion experiments at higher temperatures, in which crystalline suspensions of mixtures of both forms were stirred for a day. Interestingly, if a mixture of form **I** and form **II** is stirred in ethanol for a day at 130°C, a conversion of the complete material to form **I** is observed, whereas at 120°C all of the material transforms into form **II** (Figure 15). The outcome of this

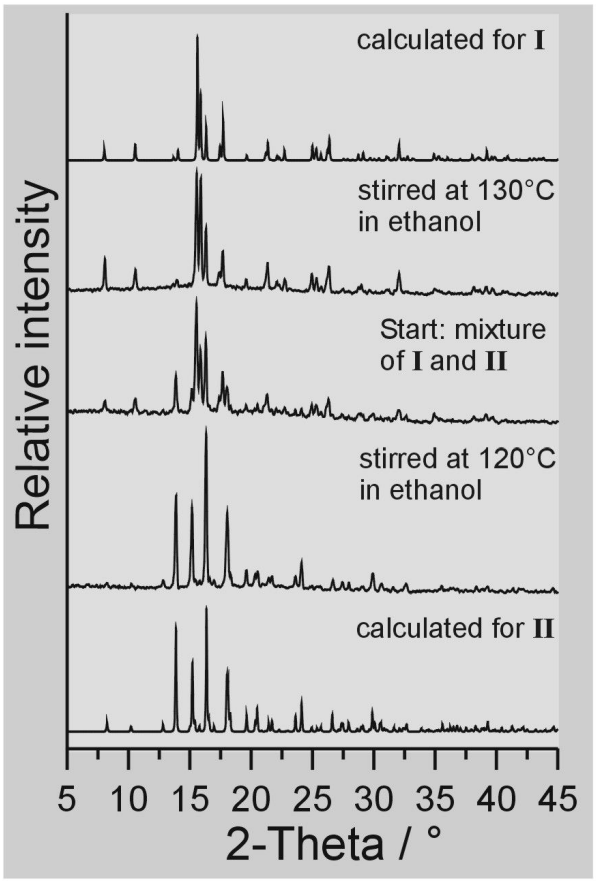

Figure 15: Experimental X-ray powder pattern of a mixture of form **I** and form **II** (top) and of the residue obtained if this mixture is stirred in ethanol at 120°C and 130°C for one day.

experiment is same if the mixture is stirred in acetonitrile. In methanol this experiment cannot be performed, because in this case the solid transforms into form **II** because the thermodynamic transition point is reached. Therefore, above the transition point no crystals of form **I** are present and the transformation into form **I** is obviously kinetically hindered.

The above experiments clearly demonstrate, that form **I** becomes more stable at temperatures above 120°C and that both forms behave enantiotropic. According to our experiments the thermodynamic transition point should be between 120 and 130°C. From these results a qualitative energy temperature diagram can be drawn which shows the relation between the different forms (Figure 16).

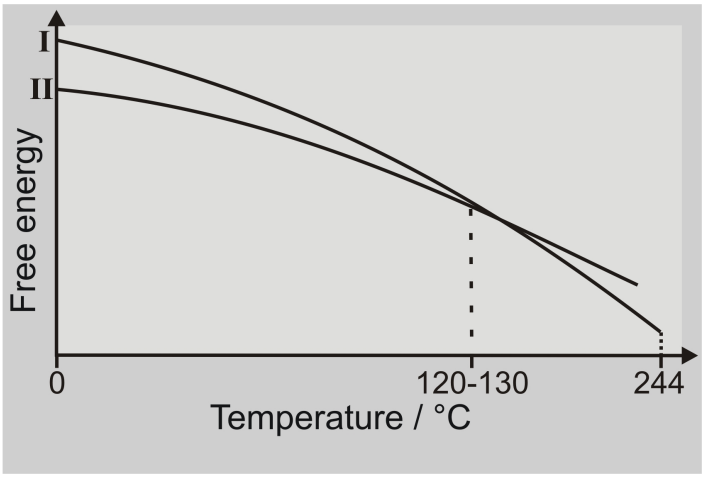

Figure 16: Qualitative energy temperature diagram for the two polymorphic modifications of prednisolone.

4. Conclusion

In this work we have characterized the two polymorphic modifications as well as the sesquihydrate of the glucocorticoid prednisolone for the first time by single crystal X-ray diffraction. We have conclusively shown that form **II** represents the thermodynamically most stable form at room temperature, whereas form **I** is metastable. We also have shown that decomposition of the sesquihydrate leads to the formation of form **I**. Interestingly in almost all solvents in which the sesquihydrate does not form, no transformation of the metastable form **I** into the stable form **II** is observed unless some crystals of the stable form **II** are added. In contrast, in methanol form **I** transforms immediately into form **II** even in the absence of crystals of the room temperature stable form **II**. The reason for this behaviour is absolutely unclear and will be the subject of further investigations. However, this is a surprising and interesting observation which shows that experiments for the identification of a thermodynamically most stable form should be performed in many different solvents in order to be somewhat sure, that the most stable modification has formed at a given temperature.

Acknowledgements

This work was supported by the State of Schleswig-Holstein. We thank Professor Dr. Wolfgang Bensch for access to his equipment.

References

[1] J. Bernstein, *Polymorphism in Molecular Crystals*, Clarendon Press, Oxford, **2002**.

[2] G. R. Desiraju, *Crystal Engineering*, Mat. Sci. Monogr., Elsevier, Amsterdam, **1989** and references therein.

[3] J. Bernstein in *Organic Solid State Chemistry: Conformational Polymorphism* (Ed.: G. R. Desiraju), Elsevier, Amsterdam, **1987**, p. 471, and references therein.

[4] J. Bernstein, R Davey, O. Henck, *Angew. Chem.* **1999**, *111*, 3646-3669 and *Angew. Chem. Int. Ed.* **1999**, *38*, 3440-3461; e) J. D. Dunitz, *Acta Crystallogr.* **1995**, *B51*, 619-631.

[5] J. D. Dunitz, J. Bernstein, *Acc. Chem. Res.* **1995**, *28*, 193-200.

[6] J.-O. Henck, J. Bernstein, A. Ellern, R. Boese, *J. Am. Chem. Soc.* **2001**, *123*, 697-706;

[7] P. Vishweshwar, J. A. McMahon, M. J. Zaworotko in *Frontiers in Crystal Engineering*, Vol. 1 (Eds.: E. R. T. Tiekink, J. J. Vittal), John Wiley & Sons Ltd., Hobocken, New Jersey, **2006**, Chapter 2, pp. 25-49

[8] P. K. Thallapally, R. K. R. Jetti, A. K. Katz, H. L. Carell, K. Singh, K. Lahiri, S. Kotha, R. Boese, G. R. Desiraju, *Angew. Chem.* **2004**, *116*, 1169-1175 and *Angew. Chem. Int. Ed.* **2004**, *49*, 1149-1155.

[9] J. L. Atwood, L. J. Barbour, G. O. Lloyd, P. K. Thallapally, *Chem. Commun.* **2004**, *8*, 922-923; l)

[10] U. J. Griesser, A. Burger, K. Mereiter, *J. Pharm. Sci*. **1997**, *86*, 352-358;

[11] J. Bernstein in *X-Ray Crystallography and Drug Action* (Eds.: A. S. Horn, C. J. De Ranter), Clarendon Press, Oxford, **1984**, p. 23, and references therein.

[12] H. G. Brittain, *Polymorphism in pharmaceutical Solids*, Vol. 23, Marcel Dekker Inc., New York, **1999**.

[13] S. R. Vippagunta, H. G. Brittain, D. J. W. Grant, *Adv. Drug. Deliver. Rev.* **2001**, *48*, 3-26.

[14] H. G. Brittain, *Am. Pharm. Rev.* **2000**, *3*, 67-68.

[15] K. R. Morris, U. J. Griesser, C. J. Eckhardt, J. G. Stowell, *Adv. Drug. Deliver. Rev.* **2001**, *48*, 91-114.

[16] S. R. Chemburkar, *Org. Process. Rev. Dev.* **2000**, *4*, 413-417.

[17] B. Bechtlov, S. Nordhoff, J. Ulrich, *Cryst. Res. Technol.* **2001**, *36*, 1315-1328.

[18] J. -O. Henck, U. J. Griesser, A. Burger, *Pharm. Ind.* **1997**, *59*, 165-169.

[19] G. Neeck, Neuroendocrine Immune Basis of the Rheumatic Diseases, Vol. II, Acad Sciences, New york **2002**, pp28.

[20] P. R. Alimkhodzhaeva, *Bull. Exp. Biol. Med*. **2002**, *133*, 47.

[21] H. J. Hatz, Glucocorticoide, Wissenschaftliche Verlagsgesellschaft mbH Stuttgart, **2005**.

[22] B. S. McEwen, E. R. De Kloet, W. Rostene, *Physiol. Rev.* **1986**, *66*, 1121-1188.

[23] J. E. Parrillo, A.S. Fauci, *Annu. Rev. Pharmacol. Toxicol.* **1979**, *19*, 179-201.

[24] B. S. McEwen, E. R. De Kloet, W. Rostene, *Physiol. Rev.* **1986**, *66*, 1121-1188.

[25] J. E. Parrillo, A.S. Fauci, *Annu. Rev. Pharmacol. Toxicol.* **1979**, *19*, 179-201.

[26] I. Jeß, C. Näther, *Angew. Chem.* **2006**, *118*, 6592-6531 and *Angew. Chem. Int. Ed.* **2006**, *45*, 6381-6383.

[27] V. Suitchmezian, I. Jeß, C. Näther, *Int. J. Pharm.* **2006**, *323*, 101-109.

[28] V. Suitchmezian, I. Jeß, C. Näther, *Solid State Sciences* **2006**, *8*, 1373-1379.

[29] V. Suitchmezian, I. Jeß, C. Näther, *Acta Crystallogr.* **2006**, *E62*, o788-o790.

[30] V. Suitchmezian, I. Jeß, C. Näther, *Acta Crystallogr.* **2006**, *E62*, o960-o962.

[31] V. Suitchmezian, I. Jeß, C. Näther, *Cryst. Growth & Des.* **2007**, in press.

[32] V. Suitchmezian, I. Jeß, C. Näther, *Chem. Eur. J.* **2007**, submitted.

[33] H. L. Herzog, A. Nobile, S. Tolksdorf, W. Charney, E. B. Hershberg, Pl. L. Perlman, *Science*, **1955**, *121*, 176.

[34] K. Florey, H. G. Brittain (Ed.), Syed Laik Ali, Analytical Profiles of Drug Substances, Vol. 22, Academic Press, (1993) and literature cited therein.

[35] M. Kuhnert-Brandstätter, *Microchim. Acta*. **1968**, 115.

[36] D. E. Wurster, P. W. Taylor, J. Pharm. Sci. **1968**, *54*, 670.

[37] M. Kuhnert-Brandstätter, *Pharm. Ind*. **1977**, *39*, 377.

[38] M. Kuhnert Brandstätter, E. Junger, A. Koffler, *Microchem. J*. **1965**, *9*, 105.

[39] M. Kuhnert-Brandstätter, Thermomicroscopy in the Analysis of Pharmaceuticals, *International Series of Monographes in Analytical Chemistry*, Pergamon press, Oxford, **1971**, vol. 45.

[40] R. Y. Mesley, *Spectrochim. Acta*, **1966**, *22*, 889.

[41] M. Kuhnert-Brandstätter, P. Gasser, *Microchem. J*. **1971**, *16*, 577.

[42] M. D. Veiga, R. Cadorniga and R. Lozano, *Thermochim. Acta*, **1985**, *96*, 111.

[43] M. D. Veiga, *Il Farmaco Edizione Pratica*, **1987**, *42*, 93.

[44] G. M. Sheldrick, SHELXS-97 and SHELXL-97, programs for the solution and refinement of crystal structures, University of Göttingen, Germany, **1997**.

[45] a) S.C. Shekar, A. Ramamoorthy, *Chem. Phys Lett.* **2001**, *342*, 127. b) G. Metz, X.L. Wu, S.O. Smith, *J. Magn. Reson.* **1994**, *A110*, 219.

[46] a) X. Wu, K. W. Zilm, *J. Magn. Reson*. **1993**, A102, 205; b) B. Jürgens, E. Irran, J. Senker, P. Kroll, H. Müller, W. Schnick, *J. Am. Chem. Soc.* **2003***, 125,* 10288; c) A. Sattler, W. Schnick, *Z. Anorg. Allg. Chem.* **2006**, 632, 238.

[47] B. M. Fung, A. K. Khitrin, K. Ermolaev, *J. Magn. Reson.* **2000,** *142,* 97.

[48] H. Sun, *J. Phys. Chem. B* **1998,** *102,* 7338.

[49] Gaussian 03, Revision D.01, M. J. Frisch, G. W. Trucks, H. B. Schlegel, G. E. Scuseria, M. A. Robb, J. R. Cheeseman, J. A. Montgomery, Jr., T. Vreven, K. N. Kudin, J. C. Burant, J. M. Millam, S. S. Iyengar, J. Tomasi, V. Barone, B. Mennucci, M. Cossi, G. Scalmani, N. Rega, G. A. Petersson, H. Nakatsuji, M. Hada, M. Ehara, K. Toyota, R. Fukuda, J. Hasegawa, M. Ishida, T. Nakajima, Y. Honda, O. Kitao, H. Nakai, M. Klene, X. Li, J. E. Knox, H. P. Hratchian, J. B. Cross, V. Bakken, C. Adamo, J. Jaramillo, R. Gomperts, R. E. Stratmann, O. Yazyev, A. J. Austin, R. Cammi, C. Pomelli, J. W. Ochterski, P. Y. Ayala, K. Morokuma, G. A. Voth, P. Salvador, J. J. Dannenberg, V. G. Zakrzewski, S. Dapprich, A. D. Daniels, M. C. Strain, O. Farkas, D. K. Malick, A. D. Rabuck, K. Raghavachari, J. B. Foresman, J. V. Ortiz, Q. Cui, A. G. Baboul, S. Clifford, J. Cioslowski, B. B. Stefanov, G. Liu, A. Liashenko, P. Piskorz, I. Komaromi, R. L. Martin, D. J. Fox, T. Keith, M. A. Al-Laham, C. Y. Peng, A. Nanayakkara, M. Challacombe, P. M. W. Gill, B. Johnson, W. Chen, M. W. Wong, C. Gonzalez, and J. A. Pople, Gaussian, Inc., Wallingford CT, 2004.

[50] J. J. P. Stewart, *J. Comput. Chem.* **1989,** *10,* 221.

[51] R. K. Harris, S. Cadars, L. Emsley, J. R. Yates, C. J. Pickard, R. K. R. Jetti, U. J. Grieser, *Phys. Chem. Chem. Phys.* **2007**, *9*, 360.

[52] L. Seyfarth, J. Sehnert, N. El-Gamel, W. Milius, E. Kroke, J. Breu, J. Senker, *J. Am. Chem. Soc.* **2007** submitted.

A.3:

Structure Elucidation of Cyameluric Acid by Combining Solid-State NMR Spectroscopy, Molecular Modeling and Direct-Space Methods

L. Seyfarth, J. Sehnert, N. El-Gamel, W. Milius, E. Kroke, J. Breu and J. Senker

European Journal of Inorganic Chemistry

Submitted in October 2007

The structure determination of solvent free cyameluric acid from powder X-ray data could only be accomplished by the application of a set of complementary methods, among them solid-state NMR spectroscopy and theoretical calculations.

My personal contributions to this work included the following:

- re-crystallization of cyameluric acid from dry methanol
- calculation of structure models and NMR chemical shift data for different isolated conformers of cyameluric acid on the base of DFT
- development of structure models for the crystalline phase of cyameluric acid with a combination of semiempirical and DFT methods as well as periodic approaches in different symmetries using DFT with plane waves
- calculation of the NMR chemical shift for all of the abovementioned structure models using DFT in the cluster approach and with PBC and plane waves
- investigation of the distance dependence of the asymmetry parameter η in a small model system of cyanuric acid and pyroll
- discussion on the presented topic
- co-authorship of the article

The contributions of all other authors comprised of:

- synthesis of solvent free cyameluric acid
- measurement of ^{13}C and ^{15}N solid-state NMR spectra for cyameluric acid
- measurement of X-ray powder diffraction data for cyameluric acid
- crystal structure solution from powder diffraction data
- discussion on the presented topic
- authorship and co-authorship of the article

Structure Elucidation of Cyameluric Acid by Combining Solid-State NMR Spectroscopy, Molecular Modeling and Direct-Space Methods

Lena Seyfarth[1], Jan Sehnert[1], Nadia El-Gamel[2], Wolfgang Milius[1], Edwin Kroke[2], Josef Breu[1], Jürgen Senker[1]*

[1] L. Seyfarth, J. Sehnert, Dr. W. Milius, Prof. Dr. J. Breu, Prof. Dr. J. Senker
Anorganische Chemie I
Universität Bayreuth
Universitätsstrasse 30, 95440 Bayreuth (Germany)
Fax: +49 921 55 2788
e-mail: juergen.senker@uni-bayreuth.de

[2] Dr. N. El-Gamel, Prof. Dr. E. Kroke
Institut für Anorganische Chemie
TU Bergakademie Freiberg
Leipziger Strasse 29, 09596 Freiberg (Germany)

1 Keywords

Cyameluric Acid · Molecular Modeling · Solid-State NMR Spectroscopy · X-ray diffraction

2 Abstract

We present the structure solution for solvent-free cyameluric acid which has first been synthesized more than 150 years ago. By densely intertwining the complementary methods solid-state NMR spectroscopy, molecular modeling as well as direct-space methods for the analysis of the X-ray powder diffraction data we succeeded although only microcrystalline material can be obtained.

In a first step the correct tautomer was identified by combining solid-state NMR and ab-initio calculations. The quantum-chemically optimized molecule was further employed in direct-space methods for the crystal structure solution. After a subsequent Rietveld refinement the positions of the hydrogen atoms in the crystal were determined by comparing experimental and calculated NMR chemical shift parameters. In this context especially the sensitivity of the anisotropy δ_{aniso} and the asymmetry parameter η of the carbonyl ^{13}C towards the hydrogen bonding environment proved to be valuable for this structural analysis.

Cyameluric acid crystallizes in space group $P2_12_12_1$ (a = 6.4701(5)Å, b = 9.9340(6)Å, c = 12.0985(7)Å, Z = 4) with one complete molecule in the asymmetric unit. It consists of the symmetric trioxo tautomer which is arranged in a 3-dimensional hydrogen bond network where all three amide groups interact with carbonyl groups.

3 Introduction

Nowadays the design of new materials with tailored properties is a central topic in material research. A key position in this target-oriented approach is the understanding of relationships between the chemical structure and its specific physical properties. For the investigation of such structure-property relationships it is essential to determine the structures of a broad variety of material classes.

For single crystals the structure solution can be performed routinely with X-ray diffraction techniques. A challenge then pose only the localization of light atoms because of their low scattering forces and the differentiation of atoms with adjacent atomic numbers due to their similar scattering forces. Compounds with good crystallization properties have therefore thoroughly been characterized over the last 50 years.

Materials for which only microcrystalline powder can be obtained pose a greater challenge. The structure solution from powder diffraction data is distinctly more demanding as in this case the 3-dimensional information about the crystal structure is reduced to 1-dimensional data. In addition, severe overlap of the diffraction reflexes often further complicates the analysis. In most cases a routine analysis is hence not possible and individual strategies have to be developed for each structure solution depending on the structural details of the material.[1–4]

For molecular crystals the application of direct-space methods to powder diffraction data has proven particularly effective.[5,6] The advantage of this approach is that constraints can directly be included in the structure solution either as a starting point or as a cost function. This distinctly scales down the dimensionality of the hypersurface of possible trial structures which is usually searched through with Monte Carlo algorithms. The establishment of such constraints may result from complementary methods like liquid and solid-state NMR, IR spectroscopy or molecular modeling.[7–11] The structure solution thus succeeds due to a clever combination of these methods which either are sensitive to the long-range order or to the local environment in the system.

In particular the exploitation of solid-state NMR experiments for the structure solution of crystals has recently become a fast growing field.[7,12–27] NMR can help to confirm an already solved crystal structure if the solution from powder data is not perfectly reliable.[21,23] The structure verification can be achieved e.g. from the assignment of the NMR resonances to the crystallographic sites or from the identification of existent building units. Another possibility is the extraction of versatile information about the system from NMR experiments in advance of the structure solution.[14,22] Here the number and the relative intensities of resonances lead to the Wyckoff spectra which help to determine the space group.[12,16,19,27] The

identification of structural elements or the generation of structure proposals can be derived from dipolar coupling measurements. Thereby the scalar dipolar (J) coupling is utilized for the measurements of homo- and heteronuclear connectivities (e.g. with INADEQUATE [28], R-TOBSY[29] and HMQC[30]).[7,15,19,25,26,31] The determination of distances becomes possible through the direct dipolar coupling (e.g. with RFDR[32], POST-C7[33], HETCOR[34] or REDOR[35]).[13,17,18,20,24]

A further important contribution of NMR to crystal structure determination is the localization of H atoms which often cannot be achieved based on X-ray diffraction data. Spectral-editing experiments like solid-state APT[36] and CPPI[37] identify XH_n groups (X = ^{13}C, ^{15}N, etc.) whereas X-H distance measurements reveal information about hydrogen bond strengths.[38–40]

However, for nuclei with low natural abundance like ^{13}C and ^{15}N a lot of difficulties arise in all these dipole-coupling based experiments. The main problem is that measurements of (pseudo-)2D spectra as they are mostly necessary for the determination of dipolar couplings become extremely time-consuming. In contrast, the chemical shift which bears a lot of useful information can often be extracted from a single 1D MAS spectrum. Nevertheless, it is scarcely employed in NMR crystallography as its interpretation is not straightforward due to the interplay of many different influences.[42] This difficulty can be overcome by utilizing molecular modeling. Recent examples have shown that ab initio chemical shifts have by now reached an impressive level of accuracy.[3,26,43] For known crystal structures the chemical shift can be calculated under periodic boundary conditions. Without a prior knowledge of the crystal structure calculations on molecular clusters may serve to understand the investigated system.

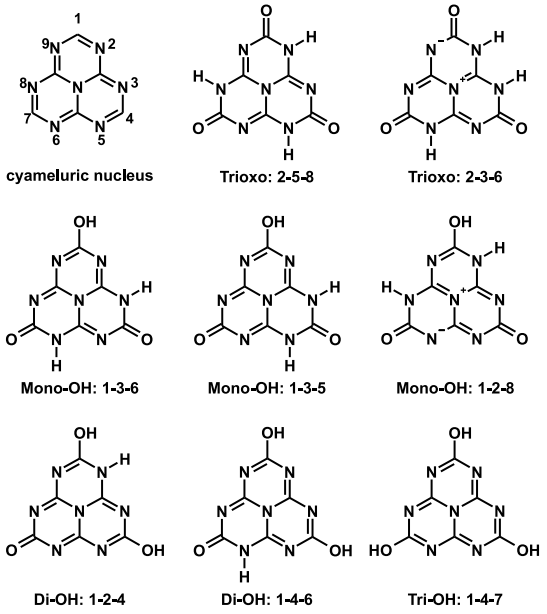

Figure 1: *Cyameluric nucleus (top left; with numbering scheme as used for H positions in tautomers) and selected tautomers of cyameluric acid (for complete set of the 17 tautomers see ref.[41])*

The combination of direct-space methods with solid-state NMR spectroscopy and molecular modeling therefore seems to be very promising for the structure determination of microcrystalline materials, especially in the field of molecular crystals.

Here we present the application of this approach to the structure solution of solvent-

free cyameluric acid ($C_6N_7O_3H_3$). Recent interest in cyameluric acid and related compounds arose due to their potential as precursor in the synthesis of graphitical carbon(IV) nitrides.[44] Further possible applications as burn-rate suppressant are based on its high thermo stability which was already reported two centuries ago by Henneberg and Liebig when they synthesized this compound for the first time.[45,46]

In the early 20th century first concepts about the structure of cyameluric acid were developed. 1937 Pauling proposed the existence of a cyameluric nucleus (Figure 1 top, left) consisting of three fused *s*-triazine rings from comparison with the cyanuric nucleus and energetic considerations.[47] After the confirmation of this proposal by Finkel'shtein via IR spectroscopy the first complete characterization of a cyameluric derivative (sym-heptazine $C_6N_7H_3$) was achieved in 1982 by single crystal X-ray diffraction analysis.[48,49] Subsequently further examples like the trichloride $C_6N_7Cl_3$ and melem ($C_6N_7(NH_2)_3$) were reported.[44,50]

For the solvent-free acid single crystals could never be obtained impeding a structure solution up to now. Besides the internuclear arrangement the much discussed question about the correct position of the H atoms thus remained unsolved (for possible tautomers see Figure 1). Various theoretical calculations proposed the trioxo tautomers to be energetically favored.[51–53] The single crystal structure solutions of the solvates $C_6N_7O_3H_3$·3DMSO and $C_6N_7O_3H_3$·$3H_2O$ point into the same direction.[54,55] However, for the smaller analog cyanuric acid ($C_3N_3O_3H_3$) both the amido and the hydroxyl form exist.[56] Additionally, for both forms derivatives of cyameluric acid could be synthesized recently.[41]

Thus, the structure solution of cyameluric acid not only has to be performed from powder data but is in addition complicated through the unknown position of the hydrogen atoms and the exclusive presence of atoms with similar scattering forces (C,N,O). Therefore it poses an excellent example for demonstrating the efficiency of the above presented approach for molecular crystals.

4 Results and Discussion

4.1 Determination of tautomer

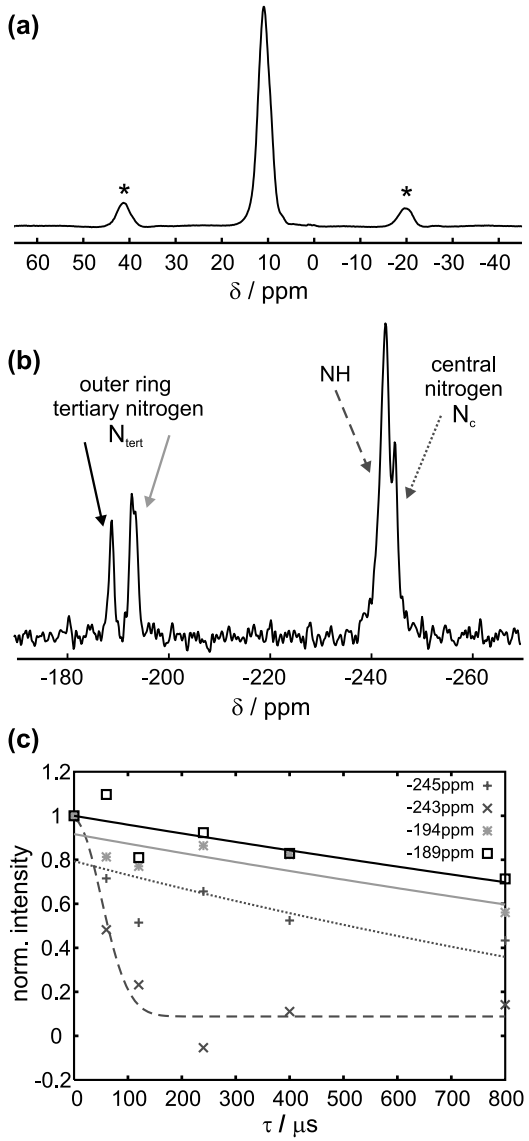

Figure 2: *(a) ^1H MAS (ν_{rot} = 12 kHz) and (b) ^{15}N CP-MAS NMR spectrum of cyameluric acid (ν_{rot} = 7 kHz); (c) Evolution of the normalized ^{15}N CPPI signal intensities as a function of the inversion time τ (ν_{rot} = 5 kHz).*

The structure solution of cyameluric acid requires the determination of the position of the hydrogen atoms in addition to the solution of the 3-dimensional structure. An overall number of 17 tautomers are theoretically possible which can be classified as trioxo, trihydroxyl and mixed oxo-hydroxyl tautomers (see Figure 1). A localization of the H atoms from our X-ray powder diffraction data is not possible due to the low scattering forces of three hydrogen atoms compared to 16 heteroatoms. To make further progress we therefore employed solid-state NMR and molecular calculations.

Figure 2 (a) shows a ^{1}H MAS NMR spectrum of cyameluric acid which reveals one signal at 10.9 ppm. For mixed tautomers which contain both OH and NH groups two signals however are to be expected as the proton signal of OH groups is significantly high-field shifted relative to those of NH groups. For the following discussion we therefore excluded mixed tautomers and focused on the trioxo and trihydroxyl molecules.

For the differentiation between the trioxo and trihydroxyl tautomers we additionally measured a ^{15}N CP-MAS NMR spectrum (see Figure 2 (b)) which consists of four resolved signals at -189, -194, -243 and -245 ppm. From comparison with similar compounds the signals at -189 and -194 ppm can be assigned to the outer ring tertiary nitro-

gen atoms (N_{tert}).[41,50] The resonances arising at -243 and -245 ppm may either originate from the NH groups or from the central nitrogen atom (N_c). It has to be noted that we may not draw any conclusions from the relative intensities of the CP-MAS spectrum as the nitrogen atoms in cyameluric acid are located in very different hydrogen environments. Therefore, it was necessary to perform a CPPI (cross polarization combined with polarization inversion) experiment which is suitable to discriminate NH groups and tertiary nitrogen atoms. The complete polarization inversion curves are depicted in Figure 2 (c). The signal intensity for the signals at -189 and -194 ppm decreases monoexponentially as typical for tertiary nitrogen atoms. The signal -245 ppm also exhibits a monoexponential behavior while the signal at -243 ppm shows a biexponential decay with an inflection point at roughly zero intensity. With these information we unambiguously assign the ^{15}N signals at -189 and -194 ppm to the outer ring tertiary nitrogen atoms, the signal at -245 ppm to the center nitrogen atom and the signal at -243 ppm to NH groups. Consequently, the ^{15}N spectrum clearly identifies a NH signal while the ^{1}H spectrum indicates that in cyameluric acid there are either NH or OH groups. From these two experiments we thus conclude that solvent-free cyameluric acid crystallizes as a trioxo tautomer.

This leaves the four trioxo tautomers to be considered (see Figure 3 top). To distinguish between them we made use of quantum chemical calculations. Figure 3 shows the comparison between the experimental ^{15}N CP-MAS spectrum and the ^{15}N isotropic chemical shifts calculated for the optimized monomers. It becomes obvious that the calculated spectra differ distinctly in both the number and the relative isotropic chemical shifts of the resolved signals. For a reasonable assignment one has to be aware that the theoretical spectra reflect isolated molecules without environmental influences. In the crystal intramolecular symmetry may be broken generating

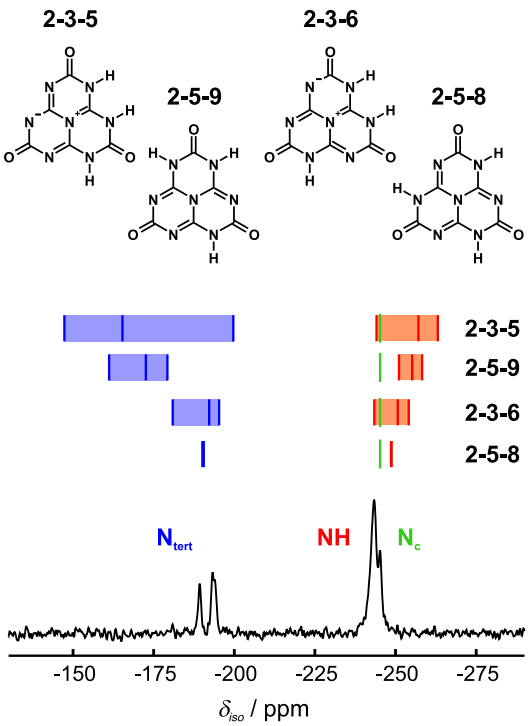

Figure 3: *Comparison of the experimental ^{15}N spectrum of cyameluric acid with the ab-initio calculated isotropic chemical shifts of the four possible monomeric trioxo tautomers. As only relative shifts are discussed in the text the calculated spectra were shifted in a way that all N_c signals coincide.*

splittings of theoretically identical signals. Additionally, resonances may be shifted due to packing effects or intermolecular interactions like hydrogen bonding. It will however be shown later (see Figure 8) that the influence of the crystal environment is below 8 ppm. Consequently, the Trioxo:2-3-5 tautomer can be excluded as the signals of the outer ring nitrogens (N_{tert}) spread over a region of more than 50 ppm whereas the corresponding experimental signals only show a splitting about 5 ppm. For the tautomer Trioxo:2-5-9 the signals of the N_{tert} atoms are distributed over a range of only 20 ppm which suits to the experiment within the above stated accuracy. However, the relative shift between the NH and the N_{tert} signals is with over 80 ppm too large to reproduce the experimental value of about 56 ppm. The two remaining tautomers, Trioxo:2-3-6 and Trioxo:2-5-8, agree well with the experimental spectrum and both have to be taken into account for the further discussion.

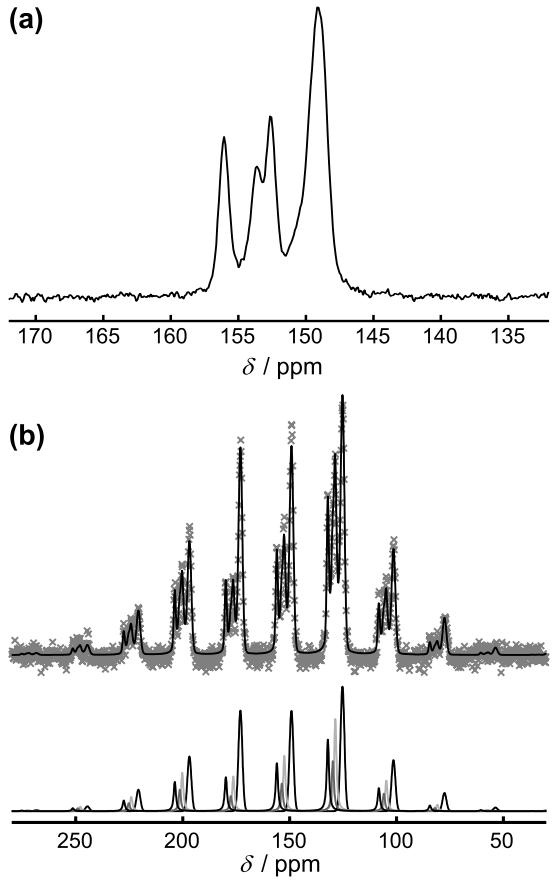

Figure 4: *^{13}C CP-MAS solid-state NMR spectra of cyameluric acid at spinning frequencies of (a) 12 kHz and (b) 3 kHz : top: experimental spectrum (crosses) with profile fit (black line); bottom: deconvoluted signals.*

In order to allow for a final decision for the correct tautomer we analyzed the ^{13}C CP-MAS spectrum which is depicted in Figure 4 (a). It reveals four signals at 149.2, 152.5, 153.7 and 156.0 ppm with an approximate intensity ratio of 1:1:1:3. These four signals originate from carbon atoms of the same molecule as it will be shown later from diffraction data that there is one complete molecule in the asymmetric unit of the unit cell. The experimental signals are grouped within a small chemical shift range rendering an assignment exclusively from the isotropic shift impossible. In order to determine additionally the anisotropic chemical shift properties we repeated the measurement at low spinning frequency (see Figure 4 (b) top). The isotropic shift δ_{iso}, the anisotropy δ_{aniso} and the asymmetry parameter η were extracted by line shape simulation (see experimental details and Figure 4

(b) bottom) and are summarized in Table 1. As for the isotropic shifts the values for the anisotropy vary only slightly (75 to 87 ppm) and are therefore too similar to be used for a differentiation of the signals. In contrast, the asymmetry parameters takes values between 0.3 and 0.9 and thus spread nearly over the full possible range from 0 to 1.

Table 1 also presents the calculated ^{13}C chemical shift parameters for the two possible trioxo monomers. In the calculations the tautomer Trioxo:2-5-8 shows only two resonances due to its intramolecular 3-fold symmetry while for the tautomer Trioxo:2-3-6 all six carbon atoms differ in their parameters. The isotropic shifts of the molecule Trioxo:2-5-8 coincide while they spread over a region of 9 ppm for the molecule Trioxo:2-3-6. As one has to account additionally about ±2 ppm for the accuracy of the calculations the calculated values of δ_{iso} differ too little for an unique assignment to the experiment. The size of the anisotropy δ_{aniso} is for both tautomers about 70 ppm for the CN_3 groups and about 90 to 100 ppm for the CNO(NH) groups. It can therefore not serve for a discrimination between the two molecules. In contrast, the values of the asymmetry differ distinctly for the tautomers. For the tautomer Trioxo:2-5-8 the CN_3 group reveals a η of 0.68 while for the tautomer Trioxo:2-3-6 it spreads over the full range from 0.02 to 0.97. The CNO(NH) group exhibits an asymmetry of 0.10 for the tautomer Trioxo:2-5-8 and values between 0.19 to 0.47 for the tautomer Trioxo:2-3-6. Thus, the tautomers show a large variety in their asymmetry parameter but so far both do not seem to suit to the experimental data.

Table 1: *Results of the profile fit of the ^{13}C spectrum at ν_{rot} = 3 kHz (Figure 4 (b)) and ab initio chemical shift values of tautomers Trioxo:2-5-8 and Trioxo:2-3-6. For a better comparison the calculated δ_{iso} were shifted as described in the experimental details.*

		int	δ_{iso}	δ_{aniso}	η
experi-	CN_2(NH)	3	149.16(1)	75(1)	0.86(1)
mental	CNO(NH)	1	152.50(1)	83(1)	0.41(2)
		1	153.65(2)	87(2)	0.31(6)
		1	155.98(1)	79(1)	0.53(2)
Trioxo:	CN_2(NH)	3	149.2	72.3	0.68
2-5-8	CNO(NH)	3	149.2	96.3	0.10
Trioxo:	CN_3	1	144.5	70.3	0.02
2-3-6	CN_2(NH)	1	151.2	-64.5	0.97
	$CN(NH)_2$	1	151.9	-74.6	0.28
	$C^1NO(NH)$	1	143.0	99.8	0.47
	$C^4NO(NH)$	1	145,2	100.4	0.25
	$C^7NO(NH)$	1	148.2	95.8	0.19

δ_{iso} and δ_{aniso} are given in ppm. The numbering x of the carbon atom of the $C^xNO(NH)$ group is as for the cyameluric nucleus in Fig. 1.

This arose the question to what extent the chemical shift values are affected from intermolecular interactions, especially as from calculations of amino acids the great impact of the hydrogen bonding on the chemical shift parameters of the participating carbonyl group is well known.[57] The influence of the O···H distance of a hydrogen bond was studied with a model system composed of cyanuric acid providing the C=O group and pyrrole for the NH group. These molecules were selected in order to maintain the general chemistry of the

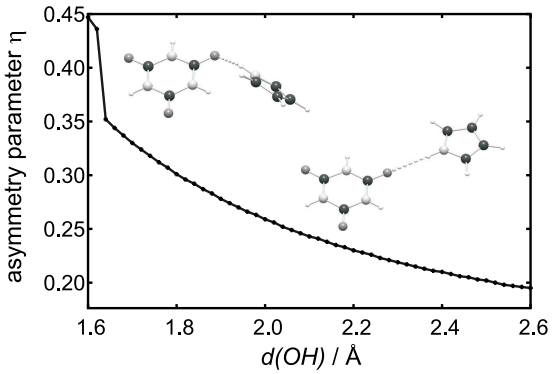

Figure 5: *Evolution of the ab-initio calculated η of the ^{13}C=O group as a function of the H$\cdots$O distance. For distances of 1.63 to 2.60 Å the geometry of the N-H$\cdots$O=C system reveals linearity. The jump at 1.62 Å originates from an orientation change of the two molecules as can be seen from the two inserted structures.*

hydrogen bond system in cyameluric acid but nevertheless to decrease calculation times via a reduced number of atoms. We focused thereby on the asymmetry parameter η as from the above made considerations it seems to be the most promising parameter for a decision between the two tautomers. The O$\cdots$H distance was systematically varied from 1.6 to 2.6 Å, a range typical for hydrogen bonds. The calculations reveal a strong correlation between η and d(OH) as depicted in Figure 5. The asymmetry parameter of the carbonyl ^{13}C increases through hydrogen bonding whereby the absolute change is roughly 0.3 from weak to strong bonds. However, the jump of η at 1.62 Å shows the complexity of the system. The sudden increase is not only caused by the decrease of d(OH) but also from a change of the relative orientation of the two molecules. Obviously other geometric parameters like angles and dihedral angles also affect the asymmetry. A strict correlation of η and the hydrogen bond distance is therefore not possible. For the here presented analysis it is however sufficient to focus on the maximal expected changes of η. We can assume that starting from the monomeric tautomers the asymmetry can experience an increase of more than 0.3 for the carbonyl group when it is embedded in a hydrogen bond network. As the carbon atom of the CN_3 group is not directly involved in hydrogen bonding the change of the corresponding asymmetry is not expected to exceed this amount.

The experiment reveals a signal with an intensity reflecting three nuclei with an asymmetry of 0.86. With a maximum increase of η of 0.3 through hydrogen bonding the calculations for the monomer have to reveal three nuclei with an asymmetry parameter of more than 0.5 in order to match the experiment. Tautomer Trioxo:2-3-6 however exhibits only two suiting carbon atoms and four carbon atoms with η smaller than 0.4. Therefore the experimental data can not be reproduced by the signals of tautomer Trioxo:2-3-6 wherefore it has to be excluded.

The theoretical values of η of Trioxo:2-5-8 can be assigned to the experimental values taking into account the hydrogen bonding. The CN_2(NH) groups are rarely affected from the hydrogen bonds wherefore they agree in their chemical shift parameters. They correspond to

the experimental signal at 149 ppm with an asymmetry of 0.86. This suits to the theoretical value of 0.68 which is slightly increased due to the remote hydrogen bonds. The CNO(NH) groups respond more sensitively to hydrogen bonds and thus reveal different values for δ_{iso}, δ_{aniso} and η. The increase of η from the theoretical value of 0.1 to 0.3 - 0.5 in the experiment is well in the range as found for the model system for hydrogen bonding. This finally leaves only tautomer Trioxo:2-5-8 as molecular unit for the structure model of cyameluric acid.
Based on the dependency of the asymmetry parameter on the O$\cdots$H distance we can even go a step further and employ η as an indicator of the hydrogen bonding situation in cyameluric acid. The model calculations demonstrate that the magnitude of η is correlated with the hydrogen bond strength. The experimental values of 0.31, 0.41 and 0.53 are all distinctly larger than the theoretical value of 0.1 for an isolated molecule. Thus, we can assume that all carbonyl groups are involved in hydrogen bonding and furthermore that these three hydrogen bonds vary considerably in their strength.

4.2 Solution of the crystal structure

For the determination of the 3-dimensional structure of cyameluric acid X-ray powder diffraction data were employed. Hydrogen atoms were excluded from the analysis as in comparison with the heteroatoms their scattering force is too low to give reasonable results.
The powder pattern was successfully indexed with an orthorhombic unit cell (a = 6.47Å, b = 9.93Å, c = 12.10Å, V = 777.9 Å^3) and a figure-of-merit M(20) = 45.6. In the range from 31.7 to 34° 2θ the pattern reveals a region of broad and unresolved reflections. This part of the powder pattern could not be indexed unambiguously and was therefore excluded from the indexing and the structure solution. A careful analysis of systematic absences was carried out manually. Since none of the integral reflection conditions for centered cells is fulfilled only primitive space groups had to be considered. Glide planes could as well be excluded due to the existence of at least one reflection violating the corresponding conditions. This left only six possible orthorhombic space groups, namely $P222$, $P222_1$, $P2_12_12$, $P2_12_12_1$, $Pmm2$ and $Pmmm$.
With this information we attempted to solve the structure based on direct methods. Numerous trials were performed with the program EXPO2000.[58] However, we could only identify 6-membered rings, a further expansion to the full cyameluric nucleus was never achieved. Therefore, we decided to employ direct-space methods where we can incorporate information about the molecule already achieved from solid-state NMR and molecular modeling.
A Pawley refinement[59] of the diffraction pattern was performed in order to determine the profile parameters. These serve in the direct-space cycles for the calculation of theoretical

patterns of trial structures which are then compared with the experimental pattern. The achieved wR_p of 4.15% additionally was employed for the evaluation of the structure proposals from direct-space methods. Reasonable structures should exhibit a wR_p value within 2 to 3 times of the Pawley profile R value.

As starting model for the direct-space methods a reasonable number of molecules has to be placed in the unit cell. Based on the cell volume of 778 Å^3 we can deduce from comparison with similar compounds (e.g. melem[50]) that the unit cell embodies most likely four molecules of cyameluric acid. Space group *Pmmm* reveals a multiplicity of eight for its general position. Thus, a structure solution in this space group implies that the complete molecule is located on a mirror plane which corresponds to a multiplicity of four. Then however symmetry elements would generate four molecules on one face of the unit cell which is impossible without overlap of the molecules. Space group *Pmmm* could therefore be excluded.

For the remaining five space groups the multiplicity of the general position is four which suits to the proposed number of molecules in the unit cell. The molecule could however also be situated on a special position with a multiplicity of two which would demand a second independent molecule in the unit cell. The five space groups exhibit as symmetry elements 2-fold screw axes, 2-fold rotation axes as well as mirror planes (the latter only for *Pmm*2). The location of cyameluric acid on mirror planes (of space group *Pmm*2) creates a second molecule in the same plane due to the 2-fold rotation axes situated in the mirror plane. As these two molecules then are arranged like mirror images they cannot build H bonds which is

Table 2: *Crystallographic data for cyameluric acid after Rietveld refinement.*

Formula	$C_6N_7O_3H_3$
M_r	221.13
Crystal system	Orthorhombic
Space group	$P2_12_12_1$
a (Å)	6.4701(5)
b (Å)	9.9340(6)
c (Å)	12.0985(7)
V (Å^3)	777.62(11)
Z	4
D_{calc} (g/cm^{-3})	1.89
2θ range (°)	10 - 90 (31.7 to 34.0 excluded)
Wavelength (Å)	1.788965 (Co)
Chebychev background polynomial order	8
Total number of parameters	68
R_p	0.0390
wR_p	0.0535
R(F^2)	0.0809 ($F^2 > 1\sigma(F^2)$), 0.09865 (all)

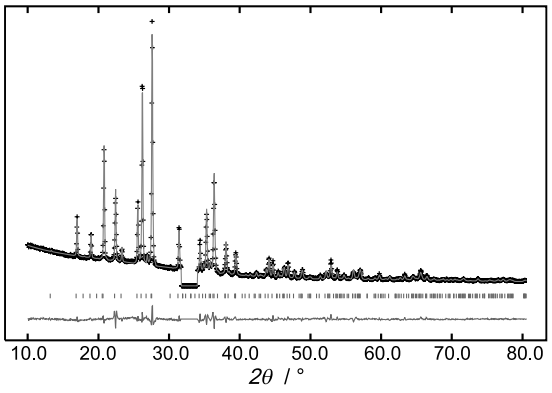

Figure 6: *Observed powder pattern (crosses), calculated (overlying gray line) and difference pattern (lower trace). The vertical bars indicate the position of the Bragg peaks.*

contradictory to the analysis of the ^{13}C NMR experiments from the previous section. All other remaining special positions are confined in two or even three dimensions. This renders impossible that the complete molecule is situated on a special position. We can therefore deduce that only one crystallographically independent molecule is located in the unit cell.
Accordingly, for the structure solution direct-space methods were applied for the five remaining space groups with one complete molecule which was arbitrarily placed in the unit cell with all atoms on general positions. Only for space group $P2_12_12_1$ a successful solution with an wR_p value of 9.6 % was found which was reconfirmed in all simulated annealing cycles. For the four other remaining space groups none of the ten simulated annealing cycles achieved a wR_p value below 18 % which definitely exceeds the limit set by the Pawley refinement.
The atomic parameters as found for space group $P2_12_12_1$ were refined with the Rietveld method. Using initially a rigid body for the complete molecule the refinement resulted in a R(F^2) value of 0.1171. The subsequent refinement with free atomic coordinates gave a R(F^2) value of 0.0809. Thereby the molecules became non-planar and distorted which is probably due to the weak intensity of the reflections at larger values of 2θ inhibiting a precise determination of the positions of the atoms. Details of the refinement are summarized in Table 2 and the corresponding calculated and observed powder patterns are shown in Figure 6.

4.3 Localization of the H atoms

From the X-ray powder pattern the location of the H atoms could not be determined and within the structure solution their positions can be set in two contrary ways. Employing the numbering scheme as used in Figure 1 for the cyameluric nucleus the H atoms are situated either at positions 2-5-8 or 3-6-9 which makes no difference for a single molecule but changes the H bonding situation in the crystal. In the following the two systems will be referred to as model H1 (with hydrogen atoms located at N2, N4, N6 in Figure 10) and H2 (N1, N5 N7), respectively.
In model H1 the H bonds are built between the NH group and the carbonyl oxygen while in model H2 they are also formed between the NH group and the outer ring tertiary nitrogen atoms. Although the distances are shorter for the former alternative one can not exclude the second model as the confirmation of the existence of the trioxo tautomer has proven the high basicity of the ring nitrogen atoms.
Therefore, the stability of model H1 and H2 was examined using molecular modeling. We performed both cluster calculations and calculations with periodic boundary conditions (PBC).

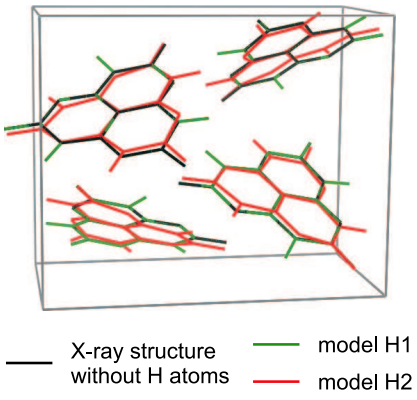

Figure 7: *Comparison of the X-ray structure solution with models H1 and H2 after optimization with periodic boundary conditions (PBC) in space group P1.*

In the cluster calculations the stability of the central molecule is probed in the potential of the fixed environment of its neighboring molecules as given from the crystal structure while for the PBC calculations the complete crystal structure is optimized. Both methods give in principle the same results. However, the PBC results are more pronounced wherefore they will be presented here. A discussion about the cluster calculations and a comparison of the two methods can be found in the supporting information.

The calculations with periodic boundary conditions (PBC) were performed in space group $P1$ to ensure maximal degrees of freedom. As the unit cell parameters are well determined from the powder pattern only fractional coordinates were optimized in order to minimize calculation times. Remarkably for both models H1 and H2 the two optimizations conserved the symmetry of space group $P2_12_12_1$ although the four molecules in the unit cell could evolve independently without symmetry restrictions.

A comparison of the unit cells for both models H1 and H2 with the X-ray structure solution is depicted in Figure 7. It becomes clear that both models are stable as the three-dimensional arrangement is maintained in both optimizations. The optimized structure of model H1 reproduces excellently the diffraction structure solution. The structure of model H2 deviates stronger from the X-ray structure. This deviation is however within the expected accuracy of the calculations and of the structure refinement. The lattice energies of the two models differ more distinctly. Model H1 is relative to model H2 about 100 kJ/molecule more stable and thus energetically clearly the favored model.

The great sensitivity of the NMR chemical shift tensor to the environment of the nucleus was already demonstrated for the determination of the correct tautomer. Therefore we employed once again the chemical shift for an independent determination of the H atoms' positions. The ^{13}C and ^{15}N chemical shift data were calculated for both models in the PBC approach. The results are depicted in Figure 8. In the following we will discuss only relative shifts as the results were not referenced and were shifted according to the experimental details. Since we included here the complete environment of the molecule the precision of the data is now only limited by the accuracy of the calculations ($\approx \pm 2$ ppm).

For ^{13}C the simulated spectra show that as expected the environmental influence on the CN_2O signals is larger as on the CN_3 signals. Both models represent the experimental data within the given accuracy very well. Model H1 shows a rather too large overall splitting while for the resonances of model H2 the splitting is underestimated. The resonances of the simulated ^{15}N spectra of models H1 and H2 are shifted by at most 8 ppm compared to the isolated molecule through intermolecular interactions. The experimental overall splitting is thereby very well reflected from the calculation of model H1. For model H2 the splitting is overestimated by about 10 ppm. Thus, the ^{15}N data prefer model H1 over model H2.

We additionally analyzed the anisotropy δ_{aniso} and the asymmetry parameter η of ^{13}C (see Table 3). Both models H1 and H2 equally well reproduce the experimental anisotropy for the CN_3 group. In contrast, for the carbonyl group only the simulated values of model H1 match to the experimental data of 79 to 87 ppm. Model H2 gives too large values of 95 to 99 ppm. This better agreement of model H1 to the experiment is also reflected by the asymmetry parameter. The data of model H1 exhibit a maximum deviation of only 0.06. The values for model H2 do not fit at all, especially the η of 0.08 to 0.15 of the carbonyl groups are distinctly too small compared with 0.31 to 0.53 of the experiment.

Concluding, both the energetical aspects as well as the analysis of the chemical shift

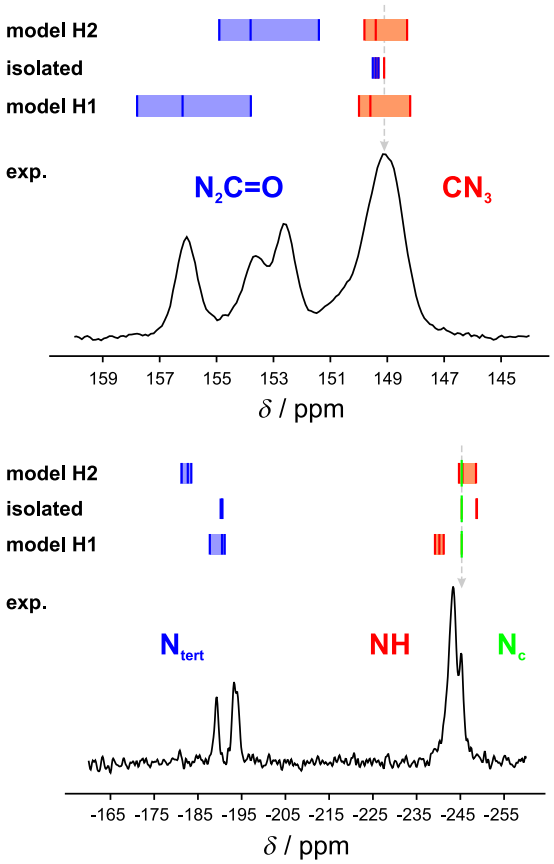

Figure 8: *Comparison of experimental spectrum (black line) with the calculated (vertical bars) ^{13}C (top) and ^{15}N (bottom) chemical shifts of model H1 and H2 calculated with PBC as well as of the monomeric Trioxo:2-5-8 molecule. The gray dashed line indicates the position of the experimental signal which was used as reference.*

Table 3: *^{13}C anisotropy (ppm) and asymmetry parameters of the experiment and of PBC calculations for model H1 and H2.*

	experiment	model H1	model H2
CN_3	75 / 0.86	73 / 0.89	75 / 0.77
CNO(NH) (1)	87 / 0.31	86 / 0.37	98 / 0.08
CNO(NH) (2)	83 / 0.41	88 / 0.43	95 / 0.15
CNO(NH) (3)	79 / 0.53	80 / 0.57	99 / 0.13

anisotropy favor model H1 over H2. Thus, model H2 has to be excluded while model H1 is unambiguously the structure solution of cyameluric acid.

4.4 Discussion of the structure

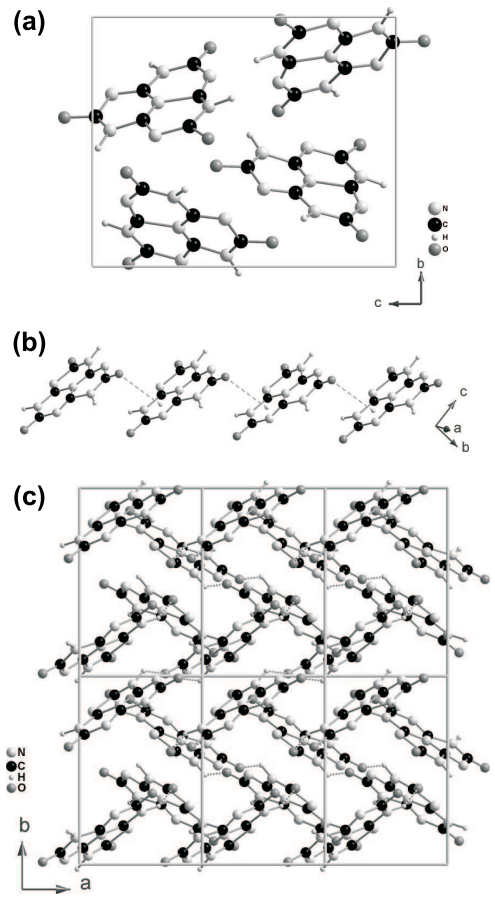

Figure 9: *(a) View along the a axis of the unit cell; (b) Strand of molecules connected via π-π stacking; (c) View along the c axis revealing the interfering herringbone pattern.*

In the crystal structure of cyameluric acid the molecules are interconnected in a 3-dimensional network. The unit cell is depicted in Figure 9 (a) with view along the a axis showing the four molecules which are related via 2-fold screw axes. The molecules build zigzag strands along the a axis which are displayed in Figure 9 (b). Within the strands the molecules are slightly overlapping so that the carbonyl oxygen is placed over the center of one of the rings of a neighboring molecule. The corresponding distance of 3.2 Å as shown by the dashed lines in Figure 9 (b) is indicative for a π-π interaction between the molecules. Figure 9 (c) shows the view along the c axis which is reminiscent of interpenetrating herringbone patterns.

The structure of cyameluric acid shows no similarity with its smaller analog cyanuric acid.[60] The triazine based acid is built of planar layers containing two hydrogen bonds along one axis and one further hydrogen bond perpendicular to it. Two neighboring layers are arranged staggered and the interaction is based on van-der-Waals forces only. The two acids have in common that their structure is dominated by a strong hydrogen bond network. The hydrogen bond system of cyameluric acid is shown in Figure 10 and the structural parameters from the diffraction data solution as well as the PBC calculations are given in Table 4. Due to the above mentioned distortion of the molecules in the X-ray solution the experimental and calculated values are to some extent dissimilar. Nevertheless, they agree in the ordering of the strength of the

hydrogen bonds and in their overall features.

All three carbonyl groups are involved in hydrogen bonds with NH groups of neighboring molecules. The strongest bond is located between N6 and O2 with an O···H distance of about 1.7 Å and corresponds to a moderate hydrogen bond.[61] The hydrogen bond between N2 and O1 is distinctly weaker with an O···H distance of about 2.0 Å. The geometry for these two bonds differs from linearity but exhibits reasonable hydrogen bond angles. The weakest hydrogen bond is between N4 and O3 with an O-H distance of 2.1 Å. This bond shows a rather extreme arrangement for hydrogen bonds with an C=O···H angle of about 90°.

In addition to the structure the NMR ^{13}C asymmetry parameter η for each hydrogen bond is known from the calculation. As expected the strongest hydrogen bond exhibits the highest η value of 0.57. The weaker bonds show lower values of 0.37 and 0.43.

Based on η the experimental NMR signals can be assigned to the different hydrogen bonding sites. The signal at 156.0 ppm unambiguously corresponds to the carbon atom C1 in the N6···O2 site. All three NMR parameters δ_{iso}, δ_{aniso} and η show an excellent agreement between experiment and calculation. For the remaining hydrogen bonds an unequivocal assignment is more difficult. However, the best match for the η parameters results for an assignment of the carbon C5 to 153.6 ppm and of the carbon C6 to 152.5 ppm.

Regarding the geometry of the molecules one has to be aware that the position of the heteroatoms in the PBC data differ dis-

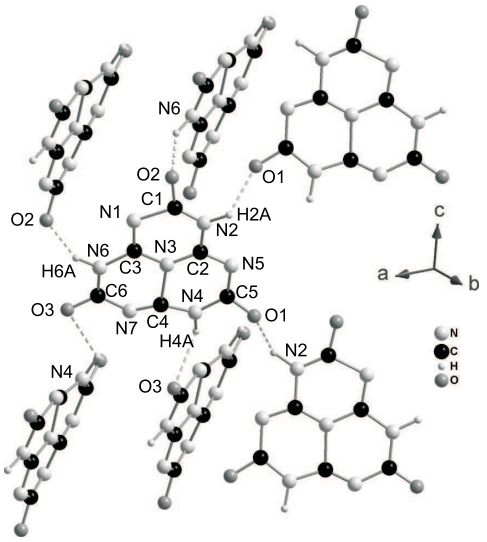

Figure 10: *Hydrogen bonds in the crystal structure of cyameluric acid.*

Table 4: *Atomic distances and angles of the hydrogen bonding environment in cyameluric acid as well as the calculated ^{13}C anisotropy parameters of the corresponding C=O groups.*

	N6-H6A···O2	N2-H2A···O1	N4-H4A···O3
Diffraction data (after Rietveld refinement with free atoms):			
d(OH)/Å	1.75	2.03	2.26
d(NO)/Å	2.67	2.81	2.90
∠(O···H-N)/°	146	130	118
∠(C=O···H)/°	126	149	88
PBC calculation:			
d(OH)/Å	1.63	1.93	1.98
d(NO)/Å	2.67	2.90	2.91
∠(O···H-N)/°	171	155	149
∠(C=O···H)/°	120	152	95
δ_{iso} (^{13}C) / ppm	158.4	154.5	156.8
δ_{aniso} (^{13}C) / ppm	80	86	88
eta (^{13}C)	0.57	0.37	0.43

tinctly from the X-ray structure solution due to the distortions therein. However, from the PBC calculations we know that the molecule inhibits approximately a 3-fold symmetry. This symmetry of the cyameluric nucleus was also found in related compounds like the salts of cyameluric acid ($C_6N_7O_3H_x^{(3-x)}$, x=0-2) of which the structures were solved via single crystal analysis more precisely.[41] In our X-ray structure solution the distances which should be equivalent through the 3-fold symmetry differ by 0.3 Å due to the signal damping at higher 2θ values in the X-ray powder pattern. However, the distances and angles as found in the PBC optimized cell agree very well with the topology of the X-ray crystal structure but do not exhibit the distortions and the deviation from planarity. They are also consistent with the geometric parameters found for other *s*-heptazine compounds.[41]

5 Conclusion

We present the structure solution for cyameluric acid 150 years after it was first synthesized. Due to the unavailability of single crystals it was necessary to combine the complementary techniques molecular modeling, solid-state NMR and direct-space methods to X-ray powder data. This enabled an unambiguous solution which was accomplished in three successive steps.

In the first step hydrogen atoms were localized on the outer ring nitrogen atoms based on ^{15}N and ^{1}H spectra as well as a CPPI experiment. Out of the four possible trioxo tautomers the correct one, namely Trioxo:2-5-8 (see Figure 1), was then identified comparing experimental and theoretical ^{13}C and ^{15}N NMR spectra. Thereby we found the anisotropy δ_{aniso} and the asymmetry parameter η of ^{13}C to be sensitive to the local environment. We could show that η can serve for an estimation of the hydrogen bond strength.

The 3-dimensional structure solution was achieved from X-ray powder data with direct-space methods using the simulated annealing algorithm. The subsequent Rietveld refinement resulted in a R(F^2) value of 0.0809. Although the correct tautomer had been determined in advance hydrogen atoms were omitted in this step as compared to the heteroatoms their X-ray scattering force is too low for an unequivocal localization.

The positions of the hydrogen atoms were subsequently determined with complementary methods. Therefore, theoretical calculations were performed for the two possibilities models H1 and H2 of placing tautomer Trioxo:2-5-8 in the crystal structure. Geometry optimizations, calculated lattice energies as well as the comparison of the calculated with the experimental chemical shifts favor model H1. In this context the anisotropy δ_{aniso} and the asymmetry parameter η of the carbonyl ^{13}C resonances were most expressive.

The structure of cyameluric acid could thus completely be elucidated with an orthorhombic

metric in space group $P2_12_12_1$. The molecules in this structure are arranged in a three-dimensional hydrogen bonding network. All amide groups are involved in hydrogen bonds with carbonyl groups. Furthermore, the molecules form zigzag strands along axis a revealing a shortest intermolecular distance of 3.2 Å.

For the structure solution of cyameluric acid the here presented combination of methods turned out to be very effective. The success of this methodical approach encourages for further applications in the field of molecular crystals. Especially, the correlation of the anisotropy and the asymmetry parameter with the strength of a hydrogen bond proved to be very promising. In order to examine this potential in more detail we expanded our theoretical study of the model system of cyanuric acid and pyrrole in a separate publication.[62] The influence of the complete geometry of the H bond system on the carbonyl ^{13}C chemical shift parameters was extensively investigated. It turned out that the chemical shift parameters in combination with molecular modeling can serve for an estimation of the strength and geometry of hydrogen bonds. This may be a crucial factor for a successful structure solution for molecules which show a broader conformational variety than cyameluric acid, e.g. due to the mobility of single bonds. The associated increase of degrees of freedom for the crystal structure can make the application of direct-space methods extremely time-consuming. Structural constraints are then decisive for a solution in a reasonable timescale. Therefore, work is under progress to implement results from molecular modeling and solid-state NMR directly into the algorithms of direct-space methods.

6 Experimental Details

Synthesis:

Cyameluric acid $C_6N_7O_3H_3$ was synthesized as described in the literature.[63] In brief, a suspension of melon powder (25 g) in a 2.5 molar aqueous KOH solution (250 ml) was heated under reflux for 45 min. The hot reaction mixture was filtered and slowly cooled to room temperature. Tripotassium cyamelurate was separated, washed with ethanol and dried at 100°C under vacuum. The acid was obtained by precipitation with an excess of HCl (37%). The white precipitate was immediately filtered off, washed with distilled water and dried at 100°C under vacuum. For an improvement of the crystallinity the powder then was recrystallized in dry methanol (MERCK, SeccoSolv, $\leq$0.005% H_2O).

Solid-state NMR spectroscopy:

Solid-state NMR experiments were performed on commercial BRUKER DSX Avance spec-

trometers with a field of 9.4 T for ^{1}H and ^{15}N and 11.7 T for ^{13}C. Samples were contained in 4 mm ZrO_2 rotors and mounted in standard 4 mm double resonance MAS probes (Bruker). ^{1}H and ^{13}C shifts are reported with respect to TMS and ^{15}N shifts were referenced to nitromethane.

A ramped cross-polarization sequence was employed to excite both ^{13}C and ^{15}N nuclei via the proton bath where the power of the ^{1}H radiation was linearly varied about 50 %. Contact times of 20 and 40 ms were used for ^{13}C and ^{15}N, respectively. Spinning frequencies were set to 3 to 12 kHz. A ^{15}N CPPI (cross-polarization combined with polarization inversion) experiment[37] was performed to investigate the position of the hydrogen atoms. Here, a spinning frequency of 5 kHz and a initial contact time of 20 ms was used. For all these experiments a broadband proton decoupling via a TPPM sequence[64] was applied during the data collection.

For the acquisition of the ^{1}H spectrum three back-to-back 90° pulses were used in order to eliminate unwanted contributions from the probe.[65] The 90° pulse length was adjusted to 3 μs and the recycle delay was set to 160 s to guarantee total rebuild of magnetization due to spin-lattice relaxation.

Deconvolution and integration of the MAS spectra were carried out with the commercial program package MATLAB.[66] The chemical shift anisotropy parameters of ^{13}C were extracted from the spectrum with 3 kHz spinning frequency. Theoretical spectra were therefore simulated as a sum of four isolated nuclei with the NMR simulation program SIMPSON[67]. A least-squares fit to the experimental data was then performed using the fit routines of MATLAB[66] in a self-written script which internally calls the program SIMPSON.

Computational methods:

All quantum mechanical calculations on molecular clusters were performed with the gaussian03 package.[68] A structural optimization of four cyameluric acid trioxo isomers (2-3-6, 2-3-5, 2-5-9 and 2-5-8, compare to Figure 1) was carried out with the PBE1PBE hybrid functional and the 6-31++G(d,p) basis set followed by a calculation of the NMR chemical shift tensor on the same level of theory.

To investigate the influence of the hydrogen bonding environment on the asymmetry parameter η of the ^{13}C carbonyl nucleus a complex of pyrrole and cyanuric acid was employed for a scan of the O$\cdots$H distance between the two molecules. Within the semiempirical AM1 method the scan parameter was varied and for each point a full geometry optimization carried out followed by a NMR calculation on the PBE1PBE/6-31++G(d,p) level of theory.

The structure solution of cyameluric acid after Rietveld refinement with rigid bodies was taken for geometry optimizations and NMR calculations under periodic boundary condi-

tions. This solution however does not include hydrogen atoms. As the positions of the H atoms in the crystal can be set in two contrary ways two models (H1 and H2) had to be taken into account. For both models DFT calculations under periodic boundary conditions were carried out with the CASTEP code as implemented in the MS modeling 4.0 package. [69,70] The axes of the unit cell were fixed with length and angles as found in the X-ray structure solution. The fractional coordinates were relaxed within the symmetry of the space group $P2_12_12_1$ and in $P1$ using the PBE functional, ultrasoft pseudopotentials, plane waves with an energy cutoff of 340 eV and k-point sampling over 4 and 12 points, respectively. For the optimized structures with $P2_12_12_1$ symmetry the NMR tensors were calculated with an energy cutoff of 550 eV and k sampling over 4 points for the wave function followed by sampling over 2 points for the NMR tensors.

For all NMR calculations the analysis of the calculated ^{13}C and ^{15}N NMR chemical shift tensors was carried out with the use of self-written MATLAB scripts.[66,71] These scripts allow for the extraction of the symmetric part of the tensor via the isotropic chemical shift δ_{iso}, the anisotropy δ_{aniso} and the asymmetry parameter η. While δ_{aniso} and η can directly be compared with results from MAS experiments the calculated isotropic chemical shifts are not referenced. However, relative isotropic shifts proved to bear the required information for our analysis. For a convenient depiction of the data we shifted each calculated spectrum in a way that the inner tertiary nitrogen and the mean values of the CN_3 carbons match with the experimental values (see dotted arrows in Figure 8). The CN_3 carbon and the inner tertiary nitrogen shifts were selected for ^{13}C and ^{15}N, respectively, as they are the least influenced from environmental effects.

Powder X-ray diffraction and structure solution with simulated annealing:

X-ray diffraction pattern were recorded on a STOE Stadi P diffractometer using CoK_α radiation (λ = 1.78896 Å) and a Ge monochromator. Data was collected in transmission geometry with a position sensitive detector and the sample held in a rotating flat specimen holder. The measurements were performed at room temperature over a 2θ range of 10 - 90° with a step width of 0.05° and a counting time of 50 s per step.

Peak search and indexing was performed with the WinXPOW software supplied by STOE.[72] Using the first 20 reflections an orthorhombic unit cell was obtained with both DICVOL91 and TREOR90.

For the determination of the profile parameters a Pawley refinement of the diffraction pattern was performed. Peak shapes were thereby modeled with Pseudo-Voigt functions. As refinement parameters the background, U/V/W, the peak shapes and the cell parameters were used.[59]

The structure solution was then performed with PowderSolve[73] as implemented in the simulation software MS Modeling.[74] Here numerous trial structures are generated and evaluated in direct space with simulated annealing based on the metropolis algorithm. For the evaluation of each trial structure a combined figure-of-merit R_{comb} is calculated according to:

$$R_{comb} = (1 - \alpha) \cdot wR_p \ + \ \alpha \cdot R_{Energy}, \tag{1}$$

where wR_p is determined according to the Rietveld method[75] as the agreement of the experimental diffraction pattern with a simulated pattern calculated via the Pawley profile parameters. R_{Energy} evaluates the energy potential and secures that the molecules exhibit reasonable intermolecular distances. For this structure solution the weighting factor α was set to 0.5. As starting geometry one molecule of the DFT optimized correct tautomer was placed arbitrarily in the unit cell and defined as rigid body in the following simulated annealing runs. The hydrogen atoms were excluded from the structure determination. For every space group ten optimization cycles with each 70 000 steps were performed.
The final structure model was then refined with the Rietveld method as implemented in GSAS.[76] After refining the background, U/V/W, zero shift, the cell constants and the profile parameters all heteroatoms were defined as a rigid body. The position of the rigid body was subsequently refined with respect to translation, rotation and the overall transition length which allows the molecule to contract or expand but not to change the angular frame.[77] Eventually positions of all atoms were individually refined. The thermal displacement parameters were set equal for each atom type for their refinement.
In the final structure solution the hydrogen atoms were added using SHELXTL.[78] A N-H distance of 1.03 Å was used based on the values found for cyanuric acid and in the theoretical calculations.[60]
Crystallographic details about the structure may be obtained from Fachinformationszentrum Karlsruhe, 76344 Eggenstein-Leopoldshafen, Germany (fax: (+49)7247-808-666; e-mail: crysdata@fiz-karlsruhe.de, http://www.fiz-karlsruhe.de) on quoting the depository number CSD-418277.

7 Acknowledgments

We thank Dr. Frank Haarmann, MPI Dresden, for the measurement of the ^{13}C solid-state NMR spectra at a field of 11.7 T and Prof. Ernst Rössler, Universität Bayreuth, for making available his NMR equipment. We gratefully acknowledge financial support that was granted from the Deutsche Forschungsgemeinschaft (DFG) (projects SE-1417/1-1 and SE-1417/2-1).

References

[1] W. I. F. David, K. Shankland, L. McCusker, C. Baerlocher *Structure Determination from Powder Diffraction Data*. IUCr Monographs on Crystallography. Oxford University Press, 2002.

[2] K. D. M. Harris, E. Y. Cheung *Chem. Soc. Rev.*, **2004**, *33*, 526–538.

[3] R. K. Harris, S. Cadars, L. Emsley, J. R. Yates, C. J. Pickard, R. K. R. Jetti, U. J. Griesser *Phys. Chem. Chem. Phys.*, **2007**, *9*, 360–368.

[4] R. Černý *Croat. Chem. Acta*, **2006**, *79*, 319–326.

[5] L. M. González-Méndez, F. L. Cumbrera, M. C. García-Cuesta, F. Sánchez-Bajo, A. L. Ortiz, F. J. Higes-Rolando, F. Luna-Giles *Materials Letters*, **2004**, *58*, 672–678.

[6] M. Tremayne *Phil. Trans. R. Soc. Lond. A*, **2004**, *362*, 2691–2707.

[7] J. Dutour, N. Guillou, C. Huguenard, F. Taulelle, C. Mellot-Draznieks, G. Férey *Solid State Sci.*, **2004**, *6*, 1059–1067.

[8] R. K. Harris *J. Pharm. Pharmacol.*, **2007**, *59*, 225–239.

[9] D. A. Middleton, X. Peng, D. Saunders, K. Shankland, W. I. F. David, A. J. Markvardsen *Chem. Commun.*, **2002**, pp 1976–1977.

[10] H. Putz, J. C. Schön, M. Jansen *J. Appl. Cryst.*, **1999**, *32*, 864–870.

[11] M. Rukiah, J. Lefebvre, M. Descamps, S. Hemon, A. Dzyabchenko *J. Appl. Cryst.*, **2004**, *37*, 464–471.

[12] N. Bestaoui, X. Ouyang, F. Fredoueil, B. Bujoli, A. Clearfield *Acta Cryst. B*, **2005**, *61*, 669–674.

[13] D. H. Brouwer, P. E. Kristiansen, C. A. Fyfe, M. H. Levitt *J. Am. Chem. Soc.*, **2005**, *127*, 542–543.

[14] S. P. Brown, H. W. Spiess *Chem. Rev.*, **2001**, *101*, 4125–4155.

[15] J. Brus, A. Jegorov *J. Phys. Chem. A*, **2004**, *108*, 3955–3964.

[16] J. F. Colin, T. Bataille, S. E. Ashbrook, N. Audebrand, L. L. Pollès, J. Y. Pivan, E. L. Fur *Inorg. Chem.*, **2006**, *45*, 6034–6040.

[17] S. Dusold, J. Kümmerlen, T. Schaller, A. Sebald, W. A. Dollase *J. Phys. Chem. B*, **1997**, *101*, 6359–6366.

[18] B. Elena, L. Emsley *J. Am. Chem. Soc.*, **2005**, *127*, 9140–9146.

[19] E. Gaudin, F. Boucher, M. Evain, F. Taulelle *Chem. Mater.*, **2000**, *12*, 1715–1720.

[20] X. Helluy, C. Marichal, A. Sebald *J. Chem. Phys.*, **1997**, *107*, 346–354.

[21] F. W. Karau, L. Seyfarth, O. Oeckler, J. Senker, W. Schnick *Chem. Eur. J.*, **2007**, *13*, 6841–6852.

[22] D. D. Laws, H.-M. L. Bitter, A. Jerschow *Angew. Chemie*, **2002**, *114*, 3224–3259.

[23] T. Loiseau, L. Lecroq, C. Volkringer, J. Marrot, G. Férey, M. Haouas, F. Taulelle, S. Bourrelly, P. L. Llewellyn, M. Latroche *J. Am. Chem. Soc.*, **2006**, *128*, 10223–10230.

[24] J. Schmedt auf der Günne *J. Magn. Reson.*, **2003**, *165*, 18–32.

[25] J. Schmedt auf der Günne, J. Beck, W. Hoffbauer, P. Krieger-Beck *Chem. Eur. J*, **2005**, *11*, 4429–4440.

[26] N. Mifsud, B. Elena, C. J. Pickard, A. Lesage, L. Emsley *Phys. Chem. Chem. Phys.*, **2006**, *8*, 3418–3422.

[27] F. Taulelle *Solid State Sci.*, **2004**, *6*, 1053–1057.

[28] A. Lesage, M. Bardet, L. Emsley *J. Am. Chem. Soc.*, **1999**, *121*, 10987–10993.

[29] J. C. C. Chan, G. Brunklaus *Chem. Phys. Lett.*, **2001**, *349*, 104–112.

[30] A. Lesage, D. Sakellariou, S. Steuernagel, L. Emsley *J. Am. Chem. Soc.*, **1998**, *120*, 13194–13201.

[31] L. Beitone, C. Huguenard, A. Gansmüller, M. Henry, F. Taulelle, T. Loiseau, G. Férey *J. Am. Chem. Soc.*, **2003**, *125*, 9102–9110.

[32] A. E. Bennett, J. H. Ok, R. G. Griffin, S. Vega *J. Chem. Phys.*, **1992**, *96*, 8624–8627.

[33] M. Hohwy, H. J. Jakobsen, M. Eden, M. H. Levitt, N. C. Nielsen *J. Chem. Phys.*, **1998**, *108*, 2686–2694.

[34] B.-J. van Rossum, H. Förster, H. J. M. de Groot *J. Magn. Reson.*, **1997**, *124*, 516–519.

[35] T. Gullion *Concepts in Magn. Reson.*, **1998**, *10*, 277–289.

[36] A. Lesage, S. Steuernagel, L. Emsley *J. Am. Chem. Soc.*, **1998**, *120*, 7095–7100.

[37] X. Wu, K. W. Zilm *J. Magn. Reson. Ser. A*, **1993**, *102*, 205–213.

[38] G. R. Goward, I. Schnell, S. P. Brown, H. W. Spiess, H.-D. Kim, H. Ishida *Magn. Reson. Chem.*, **2001**, *39*, 5–17.

[39] M. Schulz-Dobrick, T. Metzroth, H. W. Spiess, J. Gauss, I. Schnell *Chem. Phys. Chem.*, **2005**, *6*, 315–327.

[40] X. Zhao, J. L. Sudmeier, W. W. Bachovchin, M. H. Levitt *J. Am. Chem. Soc.*, **2001**, *123*, 11097–11098.

[41] N. E. A. El-Gamel, L. Seyfarth, J. Wagler, H. Ehrenberg, M. Schwarz, J. Senker, E. Kroke *Chem. Eur. J.*, **2007**, *13*, 1158–1173.

[42] R. K. Harris *Solid State Sci.*, **2004**, *6*, 1025–1037.

[43] R. K. Harris, S. A. Joyce, C. J. Pickard, S. Cadars, L. Emsley *Phys. Chem. Chem. Phys.*, **2006**, *8*, 137–143.

[44] E. Kroke, M. Schwarz, E. Horvath-Bordon, P. Kroll, B. Noll, A. D. Norman *Chem. Rev.*, **2002**, *102*, 613–628.

[45] W. Henneberg *Ann. Chem.*, **1850**, *73*, 228–255.

[46] J. Liebig *Ann. Chem.*, **1855**, *95*, 257–282.

[47] L. Pauling, J. H. Sturdivant *Proc. Nat. Acad. Sci. USA*, **1937**, *23*, 615–620.

[48] A. I. Finkel'shtein, N. V. Spiridonova *Russ. Chem. Rev.*, **1964**, *33*, 400–405.

[49] R. S. Hosmane, M. A. Rossman, N. J. Leonard *J. Am. Chem. Soc.*, **1982**, *104*, 5497–5499.

[50] B. Jürgens, E. Irran, J. Senker, P. Kroll, H. Müller, W. Schnick *J. Am. Chem. Soc.*, **2003**, *125*, 10288–10300.

[51] I. Alkorta, N. Jagerovic, J. Elguero *ARKIVOC*, **2004**, *4*, 130–136.

[52] X. Liang, W. Zheng, N.-B. Wong, J. Li, A. Tian *J. Mol. Structure*, **2004**, *672*, 151–159.

[53] X. Liang, W. Zheng, N.-B. Wong, Y. Shu, A. Tian *J. Mol. Structure*, **2005**, *732*, 127–137.

[54] A. Sattler, W. Schnick *Z. Anorg. Allg. Chem.*, **2006**, *632*, 1518–1523.

[55] J. Wagler, N. E. A. El-Gamel, E. Kroke *Z. Naturforsch. B*, **2006**, *61*, 975–978.

[56] G. B. Seifer *Russ. J. Coord. Chem.*, **2002**, *28*, 301–324.

[57] R. A. Burton, N. Tjandra *J. Am. Chem. Soc.*, **2007**, *129*, 1321–1326.

[58] A. Altomare, M. C. Burla, B. Carrozzini, G. Cascarano, C. Giacovazzo, A. Guagliardi, A. G. G. Moliterni, G. Polidori, R. Rizzi *J. Appl. Cryst.*, **1999**, *32*, 339–340.

[59] G. S. Pawley *J. Appl. Cryst.*, **1981**, *14*, 357–361.

[60] P. Coppens, A. Vos *Acta Cryst. B*, **1971**, *27*, 146–158.

[61] T. Steiner *Angew. Chem. Int. Ed.*, **2002**, *41*, 48–76.

[62] J. Sehnert, K. Bärwinkel, J. Senker *J. Mol. Struct. (THEOCHEM)*, **2007**, *submitted*.

[63] E. Horvath-Bordon, E. Kroke, I. Svoboda, H. Fueß, R. Riedel, S. Neeraj, A. K. Cheetam *Dalton Trans.*, **2004**, pp 3900–3908.

[64] A. E. Bennett, C. M. Rienstra, M. Auger, K. V. Lakshmi, R. G. Griffin *J. Chem. Phys.*, **1995**, *103*, 6951–6958.

[65] S. Zhang, X. Wu, M. Mehring *Chem. Phys. Lett.*, **1990**, *173*, 481–484.

[66] MATLAB. *The Language of Technical Computing.* Math Works Inc., 24 Prime Park Way, Natick, MA 01760-1500. Copyright 1984-2004.

[67] M. Bak, J. T. Rasmussen, N. C. Nielsen *J. Magn. Reson.*, **2000**, *147*, 296–330.

[68] Pople et al. *Gaussian 03, Revision D.01.* Gaussian, Inc., Wallingford, CT, 2004.

[69] C. J. Pickard, F. Mauri *Phys. Rev. B*, **2001**, *63*, 245101.

[70] M. D. Segall, P. J. D. Lindan, M. J. Probert, C. J. Pickard, P. J. Hasnip, S. J. Clark, M. C. Payne *J. Phys.: Condens. Matter*, **2002**, *14*, 2717.

[71] J. Sehnert, J. Senker *Chem. Eur. J.*, **2007**, *13*, 6339–6350.

[72] *STOE WinXPOW Version 1.07.* STOE Cie GmbH, Darmstadt, Germany, 2000.

[73] G. E. Engel, S. Wilke, O. König, K. D. M. Harris, F. J. J. Leusen *J. Appl. Cryst.*, **1999**, *32*, 1169–1179.

[74] MS Modeling v4.0.0.0. Accelerys Software Inc. Copyright 2005.

[75] H. M. Rietveld *J. Appl. Cryst.*, **1969**, *2*, 65–71.

[76] A. C. Larson, R. B. von Dreele *GSAS, a General Structure Analysis System.* Los Alamos National Laboratory Report, LAUR 86-748, 2000.

[77] R. E. Dinnebier *Powder Diffraction*, **1999**, *14*, 84–92.

[78] G. M. Sheldrick *SHELXTL. Version 5.1.* Bruker AXS Inc., Madison, Wisconsin, USA, 1998.

8 Graphical Abstract

By densely intertwining complementary methods we were able to solve the 150 year old mystery about the structure of solvent-free cyameluric acid. The correct tautomer was revealed with experimental and simulated solid-state NMR spectra while direct-space methods served for the analysis of X-ray powder data. Our approach is very promising for further applications of ab initio structure determination of micro-crystalline molecular materials.

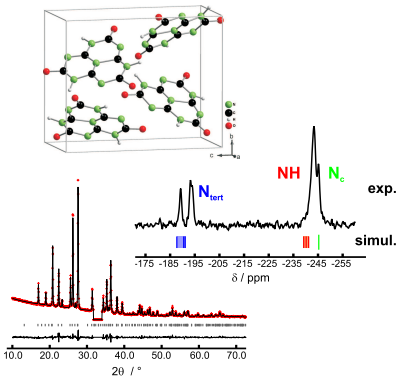

Carbon Nitride Materials

L. Seyfarth, J. Sehnert, N. El-Gamel, W. Milius, E. Kroke, J. Breu, J.Senker*

.....**XXX-XXX**

Structure Elucidation of Cyameluric Acid by Combining Solid-State NMR Spectroscopy, Molecular Modeling and Direct-Space Methods

Keywords: Cyameluric Acid / Molecular Modeling / Solid-state NMR / X-ray diffraction

Supporting Information

Structure Elucidation of Cyameluric Acid by Combining Solid-state NMR Spectroscopy, Molecular Modeling and Direct-Space Methods

Lena Seyfarth, Jan Sehnert, Nadia El-Gamel, Wolfgang Milius, Edwin Kroke, Josef Breu, Jürgen Senker

For the localization of the hydrogen atoms in the crystal structure molecular modeling was employed in order to differentiate between the two possible models H1 and H2. Additionally to the calculations under periodic boundary conditions (PBC) we performed embedded cluster calculations. The results of the PBC calculations proved to be more pronounced than the cluster calculations. For purposes of clarity we thus did not present the cluster results within the article. The comparison of the two different methodical approaches will therefore be presented in the following.

Computational methods for the cluster calculations:

The structure solution after Rietveld refinement with rigid bodies was taken as a base for the calculation of hydrogen bonded clusters. A central molecule was cut out together with the first coordination sphere of surrounding molecules. This cluster contains 15 molecules and does not include hydrogen atoms. With Trioxo:2-5-8 as the correct tautomer the positions of the H atoms in the crystal can be set in two contrary ways. The addition of hydrogen thus resulted in the two initial models H1 and H2 which were further treated identically.

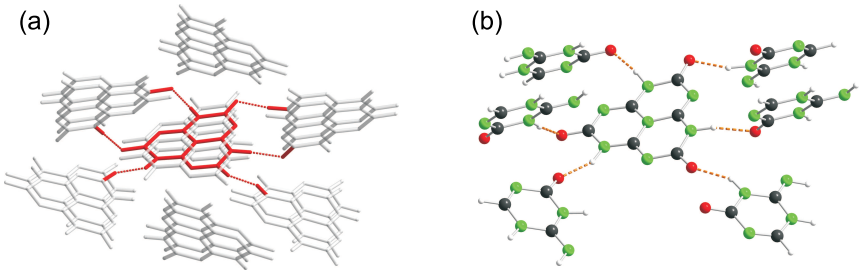

Figure 1: *(a) Embedded cluster for the geometry optimization of a central cyameluric acid molecule in the rigid potential of its environment; (b) Model system for the calculation of the ^{13}C NMR chemical shift tensors including the influence of hydrogen bonding.*

The hydrogen positions were preoptimized with the semiempirical PM3 method whereas the position of all non-hydrogen atoms was frozen. Then an embedded cluster model was defined within a two region PBE1PBE/6-31++G(d,p):PM3 ONIOM approach.[1] The high level region included the central cyameluric acid molecule and the C=O as well as N-H groups of all hydrogen bonds towards the sourrounding coordination sphere (see Figure 1(a)). The remaining atoms of the coordination sphere formed the low level region and were frozen in the subsequent geometry optimization. This way the central molecule was allowed to relax in a potential of its first coordination sphere including a full description of the hydrogen bonding environment.

For the calculation of high quality chemical shifts of the central molecule the system size had to be further reduced. First all molecules from the coordination sphere which did not take part in hydrogen bonding were removed leaving a cluster of seven molecules. Then each hydrogen bonded cyameluric acid molecule was cut down to the first aromatic ring involved in the hydrogen bonding (see Figure 1(b)). The resulting ligands were saturated with hydrogen atoms and the H positions optimized with PM3 whereas all other atoms were frozen. Then the NMR properties of the central molecule were calculated with PBE1PBE and the 6-31++G(d,p) basis set.

Results and Discussion:

Figure 2 compares the structures of model H1 and H2 in the simulations with the crystal structure after the Rietveld refinement with rigid bodies. For the cluster calculations (Figure 2 (a)) the center molecule of the cluster is depicted whose stability was probed in the potential of the fixed environment of its neighboring molecules as given from the crystal structure. For the PBC calculations the asymmetric unit is shown (Figure 2 (b)) which contains one complete molecule. The position and the geometry of the molecule in model H1 has scarcely changed for both the cluster as well as the PBC calculations. In contrast, for model H2 we observed a tilting of the molecule for both methods. In the cluster calculations the molecule additionally becomes distorted from planarity in order to improve the geometry

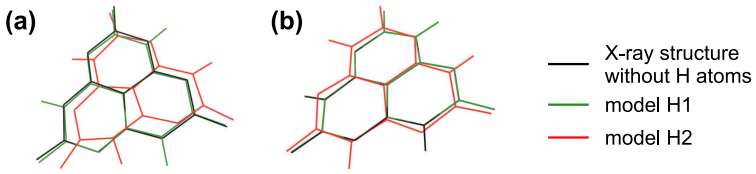

Figure 2: *Comparison of the X-ray structure solution with optimized models H1 and H2. (a) Center molecule after optimization in the embedded cluster model. (b) Asymmetric unit of unit cell after optimization with periodic boundary conditions (PBC) in space group P1.*

and the strength of the hydrogen bonds. Thus model H1 is preferred in both approaches. The deviation of model H2 is however not pronounced enough to unambiguously exclude one of the models.

The simulated ^{13}C and ^{15}N spectra for both models and approaches are depicted in Figure 3. For ^{13}C all simulations except the one of the monomeric molecule reproduce the experimental spectrum within the expected accuracy. The experimental ^{15}N overall splitting of about 56 ppm is very well reflected by model H1 for both the cluster as well as the PBC calculation. For model H2 this splitting is overestimated by about 10 - 19 ppm in both simulations. In the cluster calculation of H2 the chemical shifts of the three CN_2NH groups (N_{tert}) additionally cover a broad range of more than 20 ppm which cannot be found in the experiment. It stems from the deviation from planarity of these atoms which obviously has a great impact. Thus, this splitting nicely shows the influence of a large structural change in the molecule on the isotropic shifts.

In summary, both methodical approaches come to the same conclusions. However in the crystal rather a cooperative rearrangement of the molecule through symmetry will arise than a distortion from the planarity. This rearrangement cannot not be reproduced from the cluster calculations which has a great impact on both the geometry optimization and the NMR simulations. Thus, although the embedded cluster calculcations lead to the same

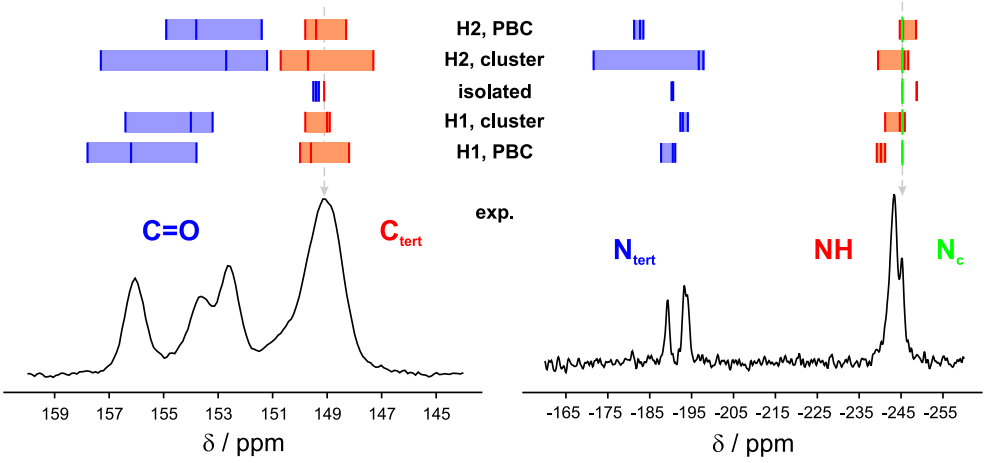

Figure 3: *Comparison of experimental spectrum (black line) with the calculated (vertical bars) ^{13}C (left) and ^{15}N (right) chemical shifts of model H1 and H2 calculated with PBC and the cluster approach as well as of the monomeric Trioxo:2-5-8 molecule. The gray dashed line indicates the signal used for referencing.*

conclusions as the PBC calculations the resulting distortions distinctly complicate the analysis of the cluster data.

References:

[1] Maseras, F.; Morokuma, K. *J. Comp. Chem.*, **1995**, *16*, 1170-1179.

A.4:

The Theoretical calculation of hypersurfaces of the ^{13}C chemical shift anisotropy in the C=O$\cdots$H-N hydrogen bond and the benefit for the ab initio structure determination

J. Sehnert, K. Bärwinkel and J. Senker

Journal of Molecular Structure (THEOCHEM)

J. Mol. Struct. (THEOCHEM) 2007, 824, 58-70
DOI: 10.1016/j.theochem.2007.08.029

This paper deals with the systematic investigation of the dependency of the asymmetry of the chemical shift tensor from the structural changes in a hydrogen bond environment of a model system consisting of pyroll and cyanuric acid. The potential for the prediction of the hydrogen bond structure in cyameluric acid on the base of the η parameters of the model system was revealed.

My personal contributions to this work included the following:

- development of models systems suited for a systematic investigation of the C=O$\cdots$H-N environment
- calculation of hypersurfaces for the abovementioned model systems
- analysis of the data with the use of self-written MATLAB scripts
- prediction of the C=O$\cdots$H-N environment from experimental data and comparison with the X-ray structure of cyameluric acid
- discussion on the presented topic
- main authorship of the article

The contributions of all other authors comprised of:

- support in the development of the self-written computer scripts
- discussion on the presented topic
- co-authorship of the article

ELSEVIER

Journal of Molecular Structure: THEOCHEM 824 (2007) 58–70

THEO CHEM

www.elsevier.com/locate/theochem

Theoretical calculations of hypersurfaces of the ^{13}C chemical shift anisotropy in the C═O···H—N hydrogen bond and the benefit for the ab initio structure determination

Jan Sehnert, Kilian Bärwinkel, Jürgen Senker *

Anorganische Chemie I, Universität Bayreuth, Universitätsstr. 30, D-95440 Bayreuth, Germany

Received 1 August 2007; accepted 22 August 2007
Available online 4 September 2007

Abstract

We investigated the influence of structural changes on the anisotropic part of the carbonyl ^{13}C chemical shift tensor in a model complex containing hydrogen bonded cyanuric acid and pyrrole. The model was chosen for its chemical resemblance to cyameluric acid. In the solid state this compound comprises three different hydrogen bonds which are well distinguishable based on the anisotropy parameters δ_{aniso} and η of the carbonyl ^{13}C atoms. The variation of six relevant structural variables in the model system produced hypersurfaces for the isotropic shift, δ_{aniso} and η. Our goal was to investigate whether such surfaces can be used for the ab initio structure determination of hydrogen bonds. With a medium size basis set it could be shown that although the absolute values differ DFT describes the relative change in δ_{aniso} and η close to the quality of MP2 calculations. Due to the high dimensionality of the hypersurface we had to reduce the number of variables in our study. We systematically created subsurfaces each described by three of the six variables and investigated their isolated influence on the NMR observables. We identified the most important structure parameters and on this base built a minimal model. For a fixed NO distance the hydrogen bond arrangement was altered by two angular variations and one dihedral distortion. In this model evidence was found that the η surfaces for different NO distances exhibit a uniform shape and can be transformed into one another by a simple shift and multiplication by a mean factor. Furthermore, the experimental parameters δ_{aniso} and η of cyameluric acid were taken as a base for the extraction of structures from the hypersurfaces. δ_{aniso} and η unequivocally selected ensembles of similar structure and the COHN arrangement in two of the three cyameluric hydrogen bonds could be predicted with good quality from the theoretical model. Our results show that it is possible to predict the distance and at least qualitatively the orientation in a hydrogen bond environment from an analysis of the anisotropic part of the ^{13}C chemical shift tensor.

Keywords: DFT calculation; Chemical shift calculation; ^{13}C MAS NMR; Hydrogen bond

1. Introduction

Hydrogen bonds affect the structure, the functionality and the dynamics in a large variety of systems [1–4]. They are found in inorganic chemistry as well as in mineralogy or material science, furthermore in organic chemistry and biological systems with pharmaceutical applications. The hydrogen bond arrangement in these vastly differing systems occur in a versatile manner and often it is this interaction which controls the structure of the overall system. Therefore it is of high interest to be able to investigate the arrangement of the hydrogen bond itself which can only be done given an appropriate observable that is sensitive to its structure.

In the past solid-state NMR has proven to be a powerful tool for the investigation of the hydrogen bond in condensed phases [2–6]. Due to its relevance for organic and biological systems the C═O···H—N bond is one of the most frequently investigated systems with the use of ^{1}H, ^{13}C and ^{15}N NMR spectroscopy. In principle the structural arrangement can directly be characterized by measuring the

* Corresponding author.
E-mail address: juergen.senker@uni-bayreuth.de (J. Senker).

0166-1280/$ - see front matter © 2007 Elsevier B.V. All rights reserved.
doi:10.1016/j.theochem.2007.08.029

^{1}H–^{13}C, ^{13}C–^{15}N and ^{1}H–^{15}N distances [3]. However, such techniques are often obscured by strong homonuclear ^{1}H dipolar coupling and can only be applied easily to isotope enriched samples. A commonly used alternative is the investigation of the hydrogen bond by the analysis of the ^{1}H, ^{13}C or ^{15}N chemical shift [2–37].

Usually it is the distance within hydrogen bonds which is correlated to the isotropic shift. However, the knowledge about a single distance does not give the full information about the overall arrangement. Therefore additional sources have to be included which yield information about the three-dimensional structure. In this context the analysis of the structural dependencies of *J*-couplings can give further insight and is achieved through the comparison between experimental results and theoretically calculated NMR data [10,38,39]. An alternative to the time consuming computation of *J*-couplings is the calculation of the chemical shift tensor which can be done in a much shorter time frame. In combination with solid-state NMR experiments the use of the principle components of this tensor can give deeper insight than the analysis of the isotropic shift alone [7,8,12–14,16,22–25,31,32,35,37,40,41].

In ^{13}C MAS experiments at low spinning frequencies the principle tensor components δ_{11}, δ_{22} and δ_{33} can be obtained from an evaluation of the side-band pattern. Because of the dominant ^{1}H–^{1}H dipole interactions in condensed phases this approach is restricted to the ^{13}C nucleus [3]. In cases where an overlap of signals complicates the analysis of the spectra, experiments like RAI or 2D PASS can be used to separate the signals of an individual nuclei [14,25,32]. By this means a specific sensitivity of the in-plane components δ_{11} and δ_{22} of the carbonyl ^{13}C tensor towards the hydrogen bonding environment could be revealed [3,7,32,42–45]. This fact is especially well proven for peptide systems where it is generally accepted that the analysis of δ_{11} and δ_{22} is suited for a characterization of the hydrogen bond strength.

These results indicate that it should be possible to extend such analyses to a more general basis which is why we chose cyameluric acid for this study. Cyameluric acid is an important precursor for CN polymers which make up a whole area of research in material science [46]. A recent study from our group revealed three different kinds of C═O···H─N hydrogen bonds in the crystal structure which could be differentiated by the measurement of the anisotropy δ_{aniso} and the asymmetry parameter η in ^{13}C MAS experiments [47]. We want to answer the general question whether it is possible to analyze the hydrogen bonding environment in a given system by investigating a minimal structure model which is chemically similar to this system. In such a small model the carbonyl ^{13}C tensor can be calculated for a broad range of structural arrangements. The idea is to use a systematical interconnection between tensor and structure for the prediction of the hydrogen bond arrangement in the real system. The success of such an approach would be very valuable for the structure determination in systems dominated by hydrogen bonding. Possible applications range from the unraveling of peptide structures in biological systems to the use of the knowledge about local hydrogen bond arrangements as a constraint in the direct structure solution from X-ray powder patterns.

We chose pyrrole and cyanuric acid as a model system because its environment is chemically similar to the hydrogen bonding of cyameluric acid. For this system hypersurfaces for the NMR parameters δ_{aniso} and η were calculated dependent from six structural variables, one distance, two angles and three distorsions. δ_{aniso} and η describe the symmetric anisotropic part of the chemical shift tensor and are mathematically expressed via the tensor components δ_{11}, δ_{22} and δ_{33}. Therefore a similar sensitivity of these parameters towards hydrogen bonding as found for the principle values themselves is to be expected. However, δ_{aniso} and η bear the advantage that they are directly available from MAS experiments. By comparison with the experimental values from cyameluric acid we tackle the question whether an analysis of the full chemical shift tensor is suited for the structure prediction of hydrogen bond environments.

2. Experimental details

2.1. Structure models

For our study we investigated the C═O···H─N bond in a small complex build from cyanuric acid and pyrrole. Altogether seven systems were analyzed which result from two principle models with differently defined structural variables (compare to Figs. 1 and 2). In systems (a) to (e) the aim was to systematically vary the hydrogen bond thereby considering its most significant structural changes including the immediate neighboring atoms. Fig. 1 shows a sketch of the model complex with an assignment of the independently examined structure variables. The strongest influence is expected from a change in the OH distance taken into account by the variable *d* [3,15,20,42]. Another source for the change of the observable is the angular bending in the C═O···H─N arrangement [15]. In our model this is described by the COH angle α_1 and the OHN angle α_2. Finally dihedral distortions might exert some influence, too. Therefore we included β_1, β_2 and β_3 which describe rotations about the NCOH, COHN and OHNC dihedral angles. β_1 and β_3 rotate the cyanuric acid and the pyrrole molecules with respect to the hydrogen bond whereas β_2 distorts the system about the hydrogen bond itself. In the systematic variation of these parameters we moved from the cyanuric acid part of the bond to the pyrrole side which led to the structure models (a) to (c) (compare to Fig. 1). Due to its potentially strong influence on the observable all models contain the distance variable *d*.

Table 1 gives an overview over the values of the respective variables in each investigated structure model together with the values of the fixed parameters. Model (a) combines the parameters α_1 and β_1 with α_2 set to 180° (due to the necessities of the here used *z*-matrix formalism in the calculation the angle was set to 179.999° but for the

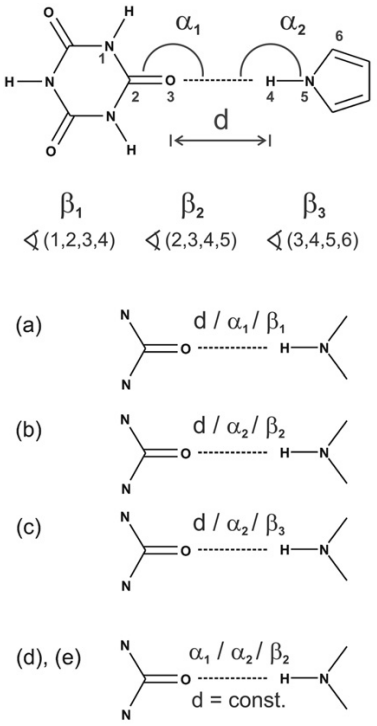

Fig. 1. Hydrogen bonded model system of pyrrole and cyanuric acid; (top) the hydrogen bond environment is described by six variables, one distance, two angles and three dihedral distortions; (a–e) systematic investigation of the hydrogen bond structure in subsystems, each described by three variables.

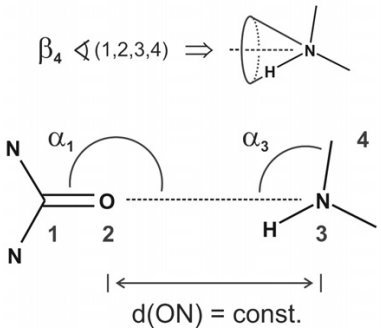

Fig. 2. Systems (f) and (g): the variation of the hydrogen bond structure is described for fixed ON distances (see also Table 1); α_1 is defined according to systems (a)–(e); α_3 and β_4 include the pyrrole nitrogen and its neighboring carbon atom; the variation of β_4 for a given α_3 leads to a conical movement of the pyrrole molecule about the interconnection between O2 and N3.

presentation in this work we will refer to such angles as 180°). Therefore structural changes in this system probe the C═O environment for the case of a linear and thus strongest O···H—N interaction. In model (b) angle α_2 is varied thereby directly investigating the change of the observable due to a weakening of the hydrogen bond

Table 1
Variation of the variables in the investigated systems (a)–(g) (see Figs. 1 and 2 for comparison); systems (d) and (e) vary in d(OH), (f) and (g) differ in d(ON)

System	Min	Max	Stepsize
(a) $\{d,\alpha_1,\beta_1\}^{\alpha_2=180^\circ,\beta_2=180^\circ,\beta_3=180^\circ}$			
d	1.6 Å	2.4 Å	0.1 Å
α_1	120°	180°	10°
β_1	−180°	−90°	10°
(b) $\{d,\alpha_2,\beta_2\}^{\alpha_1=180^\circ,\beta_1=180^\circ,\beta_3=0^\circ}$			
d	1.6 Å	2.3 Å	0.1 Å
α_2	100°	180°	10°
β_2	−180°	−90°	10°
(c) $\{d,\alpha_2,\beta_3\}^{\alpha_1=180^\circ,\beta_1=180^\circ,\beta_2=0^\circ}$			
d	1.6 Å	2.3 Å	0.1 Å
α_2	100°	180°	10°
β_3	0°	90°	10°
(d)/(e) $\{\alpha_1,\alpha_2,\beta_2\}^{d=1.8/2.1\text{Å},\beta_1=0^\circ,\beta_3=0^\circ}$			
α_1	120°	180°	10°
α_2	120°	180°	10°
β_2	40°	180°	10°
(f)/(g) $\{\alpha_1,\alpha_3,\beta_4\}^{d=2.7/2.9\text{Å},\beta_1=0^\circ}$			
α_1	120°	180°	10°
α_3	100°	150°	10°
β_4	180°	270°	10°

interaction. α_1 is fixed to 180° and the distortion of the hydrogen bond itself is described by variations of β_2. Model (c) resembles model (b) with the difference that β_3 is changed instead of β_2 which is fixed. Through this the pyrrole molecule is rotated about the H—N bond similar to model (a) where the cyanuric acid molecule is rotated about the C═O bond.

Necessarily models (a) to (c) represent chosen subsystems of the overall hypersurface. For the sake of manageability in each system the maximum number of variations had to be set to three parameters. However, for the chosen fixed angles of 180° the variables reduce in a natural way. For example, in model (b) where α_1 is set to 180° a change in β_1 now produces exactly the same variation of the structure as a variation of β_2, namely the distortion of the hydrogen bond about O···H and the models $\{d,\alpha_2,\beta_1\}^{\alpha_1=180^\circ}$ and $\{d,\alpha_2,\beta_2\}^{\alpha_1=180^\circ}$ become alike. For the same reason $\{d,\alpha_1,\beta_2\}^{\alpha_2=180^\circ}$ matches $\{d,\alpha_1,\beta_3\}^{\alpha_2=180^\circ}$. Both latter systems rotate the pyrrole molecule about a linear O···H—N arrangement. However, this alternation does not describe a change in the direct vicinity of the investigated variable α_1. Furthermore, for O···H—N the local electron density of the molecule orbitals can be expected to exhibit cylindrical symmetry about H—N and therefore a rotation about this bond will not pronouncedly mediate the electron density of C═O. For this reason system $\{d,\alpha_1,\beta_2\}^{\alpha_2=180^\circ}$ was excluded from our investigations. Models (d) and (e) result from a variation of α_1, α_2 and β_2 with fixed OH distances of 1.8 and 2.1 Å, respectively (compare to Fig. 1 and Table 1). With this constraint on the strongest influence on the observable the systems reflect the change in the NMR parameters upon angular and

distortional variations around the center of the hydrogen bond.

Fig. 2 finally shows the setup of systems (f) and (g) (compare also to Table 1). These two models are also set up with a fixed distance (d(ON) = 2.7 and 2.9 Å, respectively). This is especially useful for the comparison with the experiment because these distances were confirmed in the X-ray structure solution of cyameluric acid [47]. Just like in systems (a) to (e) α_1 was defined for an angular variation of the hydrogen bond about the carbonyl group. The combination of α_3 and β_4 results in a conical rotation of the pyrrole molecule about the interconnection between the atoms O2 and N3 (compare to Fig. 2). In this new arrangement a coupled description of α_2 and the dihedral distortions about β_2 and β_3 was obtained thereby reducing the number of variables which define the arrangement of the hydrogen bond structure.

2.2. Calculations

All calculations were carried out with the Gaussian03 package [48]. The structures of isolated pyrrole and cyanuric acid molecules were fully relaxed with the PBE1PBE hybrid functional and the 6-31++G(d,p) basis set. From these optimized structures the abovementioned models were built (compare to chapter 2.1 as well as Figs. 1, 2 and Table 1). The calculation of the NMR chemical shift tensors as well was carried on the PBE1PBE/6-31++G(d,p) level of theory. In the methodological test of the reliability of the NMR parameters the chemical shift tensors were calculated on the PBE1PBE/6-31++G(d,p), PBE1PBE/6-311++G(3df,3pd), B3P86/6-31++G(d,p), B3P86/6-311++G(3df,3pd), and MP2/6-31++G(d,p) levels of theory. The isotropic chemical shift δ_{iso} was referenced to TMS calculated with PBE1PBE/6-31++G(d,p) in both the geometry optimization and the NMR evaluation.

2.3. NMR parameters

The ab initio NMR chemical shift tensor was analyzed with the use of self-written MATLAB scripts yielding the isotropic chemical shift δ_{iso}, the chemical shift anisotropy δ_{aniso} and the asymmetry parameter η [40,41]. Whereas the tensor σ_{CS} from the ab initio calculations is expressed in the shielding convention the comparison with the experiment demands the change to the here used deshielding picture which gives $\delta_{CS} = -\sigma_{CS}$ [49]. δ_{CS} is reduced to its isotropic, antisymmetric and asymmetric parts. The isotropic and the traceless symmetric part are collected in the symmetric part of the tensor δ_{CS}^{sym} which can be expressed in its principle axis system (PAS):

$$\delta_{CS}^{sym} = \begin{pmatrix} \delta_{11} & 0 & 0 \\ 0 & \delta_{22} & 0 \\ 0 & 0 & \delta_{33} \end{pmatrix} \quad (1)$$

The principle axes are sorted for their size according $\delta_{11} \geqslant \delta_{22} \geqslant \delta_{33}$. In the here treated hydrogen bonded environments δ_{33} aligns perpendicular to the sp^2 plane of the carbonyl C atom. δ_{22} points along the C=O bond and δ_{11} is perpendicular to both δ_{33} and δ_{22} [32]. The representation of the tensor as used in the solid-state NMR community differs from this picture and δ_{CS}^{sym} is usually written as [40,50]:

$$\delta_{CS}^{sym} = \begin{pmatrix} \delta_{xx} & 0 & 0 \\ 0 & \delta_{yy} & 0 \\ 0 & 0 & \delta_{zz} \end{pmatrix} = \delta_{iso} \begin{pmatrix} 1 & 0 & 0 \\ 0 & 1 & 0 \\ 0 & 0 & 1 \end{pmatrix} + \delta_{aniso} \begin{pmatrix} -\frac{1}{2}(1+\eta) & 0 & 0 \\ 0 & -\frac{1}{2}(1-\eta) & 0 \\ 0 & 0 & 1 \end{pmatrix} \quad (2)$$

Here the tensor axes are ordered in size according to $|\delta_{zz} - \delta_{iso}| \geqslant |\delta_{xx} - \delta_{iso}| \geqslant |\delta_{yy} - \delta_{iso}|$. In this definition δ_{xx} points along δ_{33}, δ_{yy} along δ_{22} and δ_{zz} along the δ_{11} axis in the ^{13}C of the C=O···H—N arrangement. The isotropic shift δ_{iso}, the anisotropy δ_{aniso} and the asymmetry η are defined via δ_{xx}, δ_{yy} and δ_{zz} and therefore also related to δ_{11}, δ_{22} and δ_{33} [51]:

$$\begin{aligned} \delta_{iso} &= \frac{1}{3} \cdot (\delta_{xx} + \delta_{yy} + \delta_{zz}) = \frac{1}{3} \cdot (\delta_{11} + \delta_{22} + \delta_{33}) \\ \delta_{aniso} &= \frac{2}{3} \cdot \left(\delta_{zz} - \frac{\delta_{xx} + \delta_{yy}}{2} \right) = \frac{2}{3} \cdot \left(\delta_{11} - \frac{\delta_{33} + \delta_{22}}{2} \right) \\ \eta &= \frac{\delta_{yy} - \delta_{xx}}{\delta_{zz} - \delta_{iso}} = \frac{\delta_{22} - \delta_{33}}{\delta_{11} - \delta_{iso}} \end{aligned} \quad (3)$$

3. Results and discussion

3.1. Reliability of the method

For the use in structure prediction the reliability of the here used DFT approach is an important feature. The key question is how well the respective NMR parameter can be determined and how stable the results are with respect to the basis set. For this reason the here used PBE1PBE functional was compared to the B3P86 functional and the perturbational MP2 method with the 6-31++G(d,p) basis set. Furthermore, NMR tensors were calculated with PBE1PBE and B3P86 using the large triple-zeta 6-311++G(3df,3pd) basis set. Fig. 3 shows the results of this comparison for ten representative structures taken from models (a) and (b) equally. The arrangements were randomly picked only satisfying the condition that the whole range of calculated η values (0.22–0.45) is covered. The parameters of these ten structures are included as Supplementary information (compare Appendix A). On the left part of Fig. 3 the absolute calculated NMR parameters are given whereas the right part shows the same values relative to the respective parameter of structure 1.

For the 6-31++G(d,p) basis set the isotropic chemical shift δ_{iso} is slightly sensitive to changes in the DFT

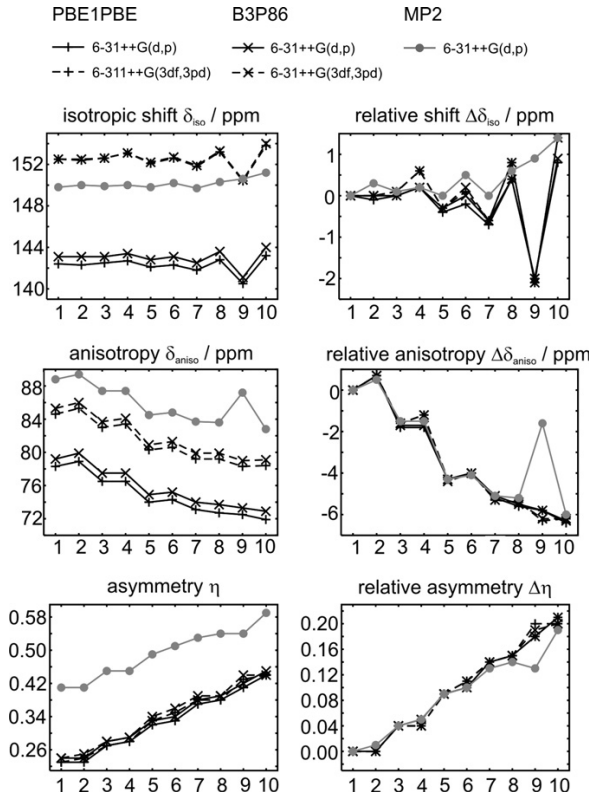

Fig. 3. Calculation of the isotropic chemical shift δ_{iso}, the anisotropy δ_{aniso} and the asymmetry parameter η for ten structures taken from systems (a) and (b) (see also Section 2); on the left the absolute values are given, the right part shows the plot of the difference with respect to the result of structure 1.

functional. For both functionals a large shift to lower field by about 5 ppm occurs with a change to the large 6-311++G(3df,3pd) basis set. The MP2 values are found between the DFT results for 6-31++G(d,p) and 6-311++G(3df,3pd) but closer to the large basis set. The size of the anisotropy δ_{aniso} is underestimated in all DFT calculations. With the large basis set the difference to MP2 is reduced to about 4 ppm whereas the small basis set differs by about 11 ppm. For both basis sets the choice of the functional produces changes of about 1 ppm in δ_{aniso}.

The most stable value is the asymmetry parameter η. With a largest absolute difference of about 0.04 it is described nearly the same with all DFT methods. The MP2 parameters are by about 0.16–0.17 shifted to higher η values. Even though all parameters are sensitive to the level of theory, especially when compared to the MP2 results, the similarity of the relative differences of the values between the ten structures is striking.

We therefore created difference plots for δ_{iso}, δ_{aniso} and η in which the respective value of structure 1 was taken as a reference in each curve (right side of Fig. 3). These curves represent the relative change of a NMR parameter as a function of the structural variation. As can be seen for the anisotropy δ_{aniso} and the asymmetry parameter η this change is very well described by DFT methods in comparison to MP2. Furthermore, it is not sensitive to the choice of the basis set which means it can be calculated in a quick computation using the smaller basis set. For the isotropic chemical shift δ_{iso} deviations of up to 0.8 ppm have to be taken into account. The anisotropy as well exhibits a maximum deviation of 0.8 ppm for the relative values and η varies by about 0.02. In the real system of cyameluric acid the NMR parameters differ about 3.5 ppm for δ_{iso}, 7.2 ppm for δ_{aniso} and 0.2 for η [47]. This means that the accuracy of the calculated isotropic chemical shift is not suited to differentiate between various hydrogen bond environments even if only relative changes are discussed. However, the precision in the relative values of the anisotropy δ_{aniso} and the asymmetry η is high enough to be able to distinguish between different hydrogen bond environments.

Finally the significant difference between the DFT and MP2 results of the parameters δ_{iso}, δ_{aniso} and η in structure 9 has to be addressed. These deviations can be explained by a closer look at the representing structure (Fig. 4). In system 9 the OH distance is set to 1.6 Å with an OHN angle of only 100° in a staggered arrangement between pyrrole and cyanuric acid. This leads to a very close contact between the two molecules with a H atom positioned over

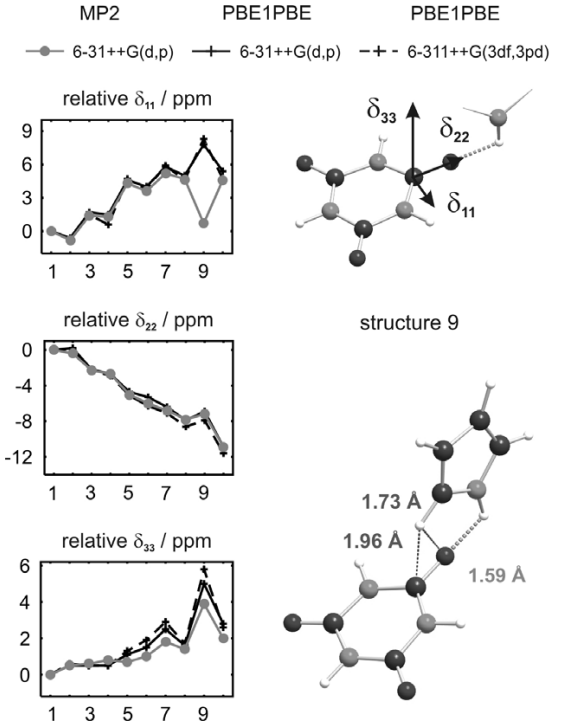

Fig. 4. (left) Relative changes of δ_{11}, δ_{22} and δ_{33} upon a structural change in the hydrogen bond environment with respect to structure 1; (right) hydrogen bond arrangement in structure 9 and orientation of the tensor components in the C=O group; as B3LYP and PBE1PBE yield highly similar results here only the structure for the latter functional is shown.

the C═O group. The interstitial distances are 1.73 Å for HO and 1.96 Å for HC leading to a through space interaction which obviously influences the ^{13}C tensor (compare to Fig. 4). For its theoretical description electron correlation has to be taken into account. This is given only to a minor extend with DFT but recovered for a good part in the MP2 method thereby explaining the occurring differences between the methods.

To show the influence of electron correlation on the tensor components the relative changes of δ_{11}, δ_{22} and δ_{33} are shown in Fig. 4 as a function of the 10 sample structures. Upon the comparison of the curves for PBE1PBE/6-311++G(d,p) and MP2/6-31++G(d,p) it becomes obvious that the interaction between the hydrogen and the C═O group leads to a pronounced deshielding of component δ_{11} when described by MP2 which is the reason for the different values in δ_{aniso} and η for structure 9. In general the relative curves of δ_{11} and δ_{22} calculated with PBE1PBE match remarkably well with the MP2 calculated changes. Showing a maximum deviation from the MP2 results of about 1 ppm the relative change in δ_{33} is the worst described value with DFT. The influence of these fluctuations of δ_{33} on δ_{aniso} and η is much less pronounced than on δ_{iso} (compare to Figs. 3 and 4). Thus the mathematical expressions for δ_{aniso} and η seem to be well suited to compensate for deviations in the principle values as they occur when using different levels of theory for the calculation of the NMR tensor (compare to Eq. (3)). This is especially true for the relative values of these two parameters. Another advantage in using δ_{aniso} and η is that they are directly available from a lineshape analysis of MAS experiments at low rotational frequencies.

For the following calculation of NMR hypersurfaces two consequences can be derived from the above performed analysis. First it is obvious that the relative changes in the NMR chemical shift tensors are very well described with PBE1PBE/6-31++G(d,p). Second, care has to be taken for models comprising of small angles as in such cases additional through-space interactions can come into play which are not well described by DFT.

3.2. Hypersurfaces

3.2.1. The distance dependency of the NMR parameters δ_{aniso} and η

Apart from an exponential behavior of the isotropic chemical shift δ_{iso} with respect to the O···H distance of the hydrogen bond little systematic dependencies are known in the literature [3,15,20,42]. It therefore is important to extend the analysis to the anisotropic chemical shift properties δ_{aniso} and η. To separate the strongest influence caused by the O···H distance dependence from the effect bending and distorting the hydrogen bond environment (compare to Fig. 1) exerts we followed a procedure described below.

The whole range of the NMR parameters of one hypersurface was divided into regular arrays with the number of variations of the distance d. Then for each variation of this variable the number of structures found in the parameter arrays was counted. The result gave a three-dimensional histogram for the NMR observable and regions of the structural variation in d (Fig. 5, top). For fixed values of the distance d the distribution in the histogram results from changes in the NMR parameter upon the variation of the two remaining structural variables α and β. This way the correlation between d and the respective NMR parameter can easily be visualized and the less the NMR parameter is distributed the stronger the parameter is correlated to d. By the extraction of the mean values and standard deviations of the individual distributions for fixed d values the analysis can be simplified through a projection into 2D (Fig. 5, bottom). The data points in this depiction represent the mean values whereas the error bars show the standard deviation.

Fig. 6 shows the distance dependence of the anisotropy δ_{aniso} and the asymmetry η as resulting from this analysis in systems (a), (b) and (c). For the models (d) and (e) the OH distance was fixed and thus could not be investigated in this context (compare to Section 2.1 for details on the structure models). In systems (a) to (c) the mean values of δ_{aniso} lower with a decrease of the OH distance whereas η rises. For both NMR parameters this behavior is nonlinear which for example can well be reproduced by a fit of the mean values with an exponential function.

The anisotropy δ_{aniso} is distributed in a range of about 72–80 ppm and the asymmetry η stretches from 0.24 to 0.44 for all three systems. The standard deviations of δ_{aniso}

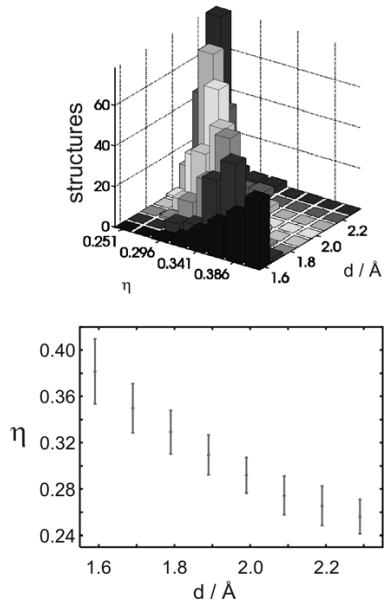

Fig. 5. Top: Example for a three-dimensional histogram for system (b) and the correlation between η and the distanced. Bottom: By evaluation of the mean values and standard deviations for each distance the histogram can be reduced to a 2D plot.

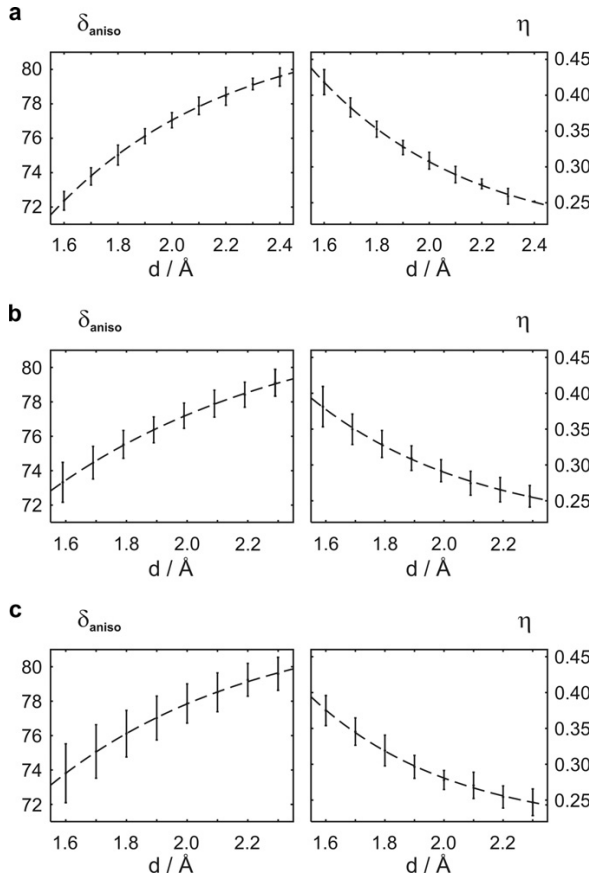

Fig. 6. Dependency of the parameters η and δ_{aniso} from the OH distance; the standard deviation from the mean values is caused by an alteration of the remaining variables describing the respective angular and dihedral distortions in the systems; the development of the mean values is nonlinear (shown by exponential functions which are given as a guide for the eye).

rise from systems (a) to (c) indicating an increasing influence of the angle and dihedral distortion. For η in system (a) the distribution due to the angular variables is smallest and rises when changing to systems (b) and (c) where the standard deviations are comparable in size. For both parameters and all systems the deviations are largest for the smallest distance of 1.6 Å indicating that the stronger the hydrogen bond in a system becomes the more important it is to include the correct description of the angular and distortional arrangement for a realistic description of δ_{aniso} and η.

3.2.2. The angular dependencies of the NMR parameters δ_{aniso} and η

To further investigate the influence of angles and dihedral distortions on the NMR parameters we fixed the distance to the lowest value of 1.6 Å and plotted the δ_{aniso} and η hypersurfaces of systems (a) to (c) (Fig. 7). These surfaces therefore represent the strongest possible influence of the structural variations for the here discussed hydrogen bond. In all systems (a) to (c) δ_{aniso} changes as a function of the respective angle and dihedral distortion. From the curvature of the surfaces it can be stated that bending exerts a stronger influence on the NMR parameter than dihedral distortions. In systems (b) and (c) the strongest influence of the distortion is found for the smallest angles (100–120°). In the subsurfaces of system (a) the distortion about β_1 only plays a minor role in the whole range of the variation of α_1 and for η the effect is negligible. In the systems (b) and (c) for α_2 in a range of 140–180° the effect of distortion upon η is negligible but exerts a stronger influence for smaller angles of 100–140°.

These results are important in the context of the structure prediction via δ_{aniso} and η. The OH distance as well as the angles α_1 and α_2 have to be included in a hydrogen bond model suited for that purpose. From the dihedral angles β_1 can be left out especially if only η is used for structure prediction. However, to account for their influence at small angles β_2 and β_3 should be included into the model. This poses a problem as the resulting hypersurface which is needed to fully describe the influence of structural changes on the NMR parameters is still dependent from five variables. The number of variables has to be reduced further to still be able to calculate hypersurfaces of applicable size within an acceptable time frame. It is therefore reasonable to confine angle α_2 to values between 120° and 180°. This is an especially convenient choice as through this problematic structures as discussed in Section 3.1 can be excluded at the same time. Whereas the influence of β_3 on the NMR parameters then becomes negligible β_2 still has to be taken into account.

On the base of these findings we put up the structure models (d) and (e) which each comprises of a fixed O···H distance (compare to Fig. 1 and Table 1). To allow for a comparison with the real system of cyameluric acid the O···H distances were set to 1.8 and 2.1 Å which pose the values as found from the X-ray structure solution. As a consequence systems (d) and (e) exclusively reflect the influence of bending and distorting about the variables α_1, α_2 and β_2 upon the NMR parameters. The aim was to see whether the resulting angular surfaces exhibit any similarity, in other words whether the change of the hydrogen bond orientation for a given distance would change the NMR parameters in a uniform way. Such a resemblance would mean it is possible to interpolate the values for different distances resulting in a whole set of subsurfaces at low computational cost.

Unfortunately, such a similarity could not be found in the systems (d) and (e). For set values of β_2 the α_1/α_2 surfaces showed a highly individual curvature with few obvious interconnection. Furthermore, no systematics could be observed from the analysis of the subsurfaces $\{\alpha_1, \beta_2\}^{\alpha_2=\text{fix}}$ and $\{\alpha_2, \beta_2\}^{\alpha_1=\text{fix}}$. Since it is obvious that no general trend can be derived from the hypersurfaces of the models (d) and (e) we omitted a graphical presentation.

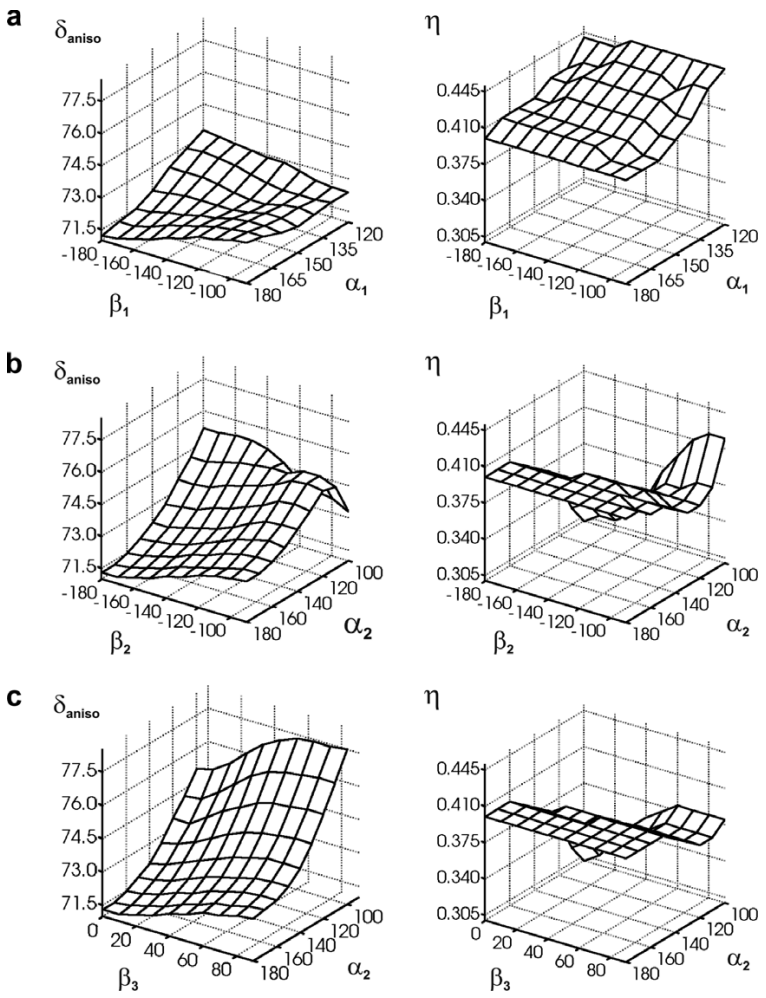

Fig. 7. Subsurfaces of the parameters η and δ_{aniso} as a function of the angular arrangement at the lowest OH distance (1.6 Å); compare to models (a) to (c) in Fig. 1 and also to Table 1.

3.3. Unification of hypersurfaces

In the next step we therefore changed our system to the structure models (f) and (g) (see Fig. 2 and Table 1). Again both systems comprise of the same angular and dihedral variations for two differently set distances. The intention was to further reduce the complexity of the dependencies by a coupling of structural variables. The central geometric feature now was the connection between the carbonyl oxygen of the cyanuric acid and the nitrogen of the pyrrole molecule. The distance d(NO) was fixed to values of 2.7 and 2.9 Å as found in the X-ray structure of cyameluric acid. All structural variations were related to this central NO line (compare to (f)/(g) in Fig. 2). The angle α_1 bends the cyanuric acid molecule and the distorsion β_4 rotates the pyrrole on a cone with an aperture angle depending from α_3.

Fig. 8 exemplarily shows η subsurfaces for system (f) (left side, 2.7 Å) and system (g) (right side, 2.9 Å) and four different dihedral distortions about β_4. The surfaces of (f) are generally shifted towards higher η values due to the lower NO distance which increases the hydrogen bond strength (compare to tendencies Fig. 6). Not surprisingly the greatest influence in both systems is exerted from α_3. Upon changing this variable the OH distance is slightly varied which has the strongest influence on the NMR parameters. The next important variable is α_1. β_4 causes the smallest changes of the NMR parameter (Fig. 8). The depicted surfaces do not only have the advantage of a reduced number of variables but furthermore exhibit a similar curvature. This implies that for a fixed dihedral distortion β_4 it should be possible to transform surface $\eta\{\alpha_1,\alpha_3\}^{2.7\text{ Å},\beta_4}$ of system (g) into surface $\eta\{\alpha_1,\alpha_3\}^{2.9\text{ Å},\beta_4}$ of system (f) or visa verse. In the following we will show that such a parametrization is in principle possible. As a first step in this procedure we subtracted the respective mean value $\eta_{mean}^{d(NO),\beta_4}$ from each surface

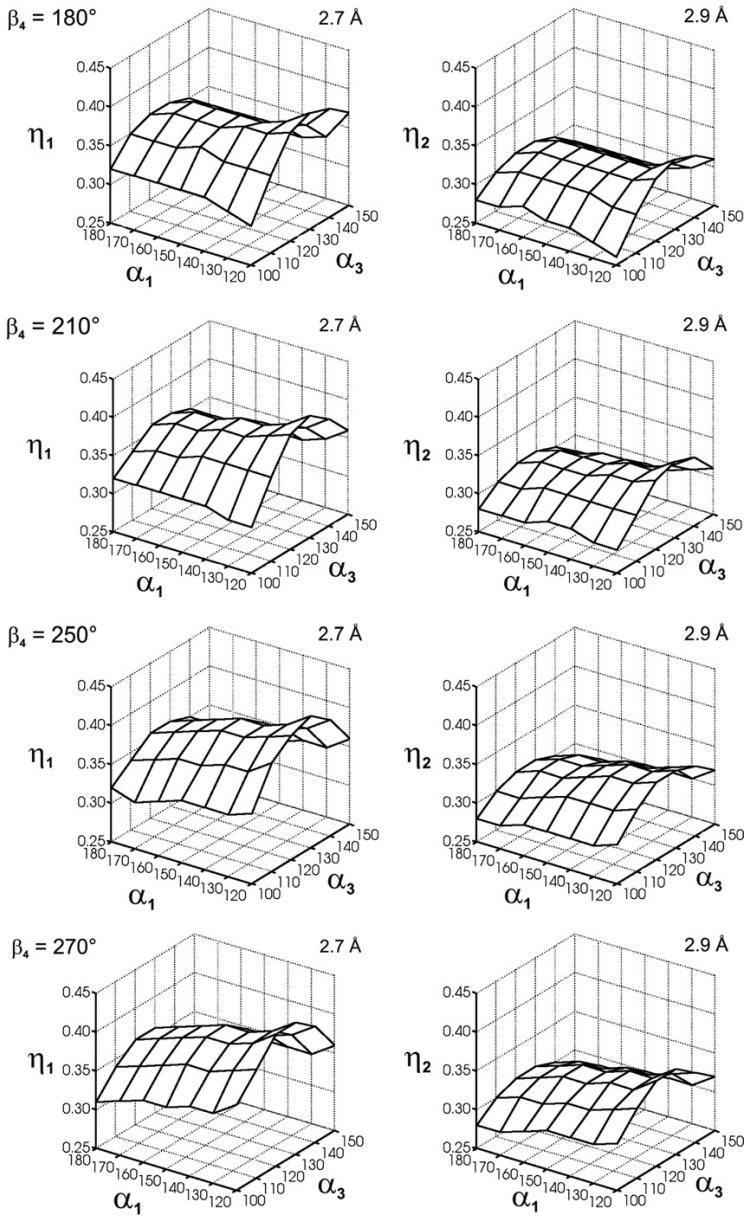

Fig. 8. η subsurfaces of the systems (f) and (g) depending from α_1 and α_2 for fixed dihedral distortions β_4 (compare also to Fig. 2 and Table 1); the surfaces for $d(\mathrm{NO}) = 2.7$ and 2.9 Å show a high similarity and can be transformed into one another by the application of a shift and multiplication by a mean factor (see Table 2).

$\eta\{\alpha_1, \alpha_3\}^{d(\mathrm{NO}),\beta_4}$ (compare to Eq. (4)). The difference between the mean values of the two surfaces $\Delta^{\beta_4}_{\mathrm{mean}}$ is given in Table 2.

After this the two surfaces were left on top of each other and varying about zero. Then for each point on the surface the factor $\langle f \rangle$ between the η values of the two systems was determined and the mean value of $\langle f \rangle$ calculated from the resulting ensemble. The shifted surface of $\eta\{\alpha_1, \alpha_3\}^{2.9\ \mathrm{\AA},\beta_4}$ was then multiplied by $\langle f \rangle$ to match the shifted surface of $\eta\{\alpha_1, \alpha_3\}^{2.7\ \mathrm{\AA},\beta_4}$:

$$\left[\eta\{\alpha_1, \alpha_3\}^{2.7\ \mathrm{\AA},\beta_4} - \eta^{2.7\ \mathrm{\AA},\beta_4}_{\mathrm{mean}}\right] = \langle f \rangle \cdot \left[\eta\{\alpha_1, \alpha_3\}^{2.9\ \mathrm{\AA},\beta_4} - \eta^{2.9\ \mathrm{\AA},\beta_4}_{\mathrm{mean}}\right] \tag{4}$$

Table 2 lists the factor $\langle f \rangle$ for the chosen systems with the respective fixed values for β_4. The described procedure resulted in two highly similar surfaces. These surfaces were subtracted to yield a difference function with values randomly scattering about zero. From this function the mean difference and its standard deviation were

Table 2
Systematic relationship between the hypersurfaces of systems (f) and (g) for different dihedral distortions about β_4; $\Delta^{\beta_4}_{\text{mean}}$ denotes the difference between the two mean values of the surfaces; $\langle f \rangle$ is the mean factor by which the shifted surfaces can be transferred onto each other; the mean deviation (dev.) is derived from the difference surface calculated for the such manipulated systems (f) and (g); compare also to Fig. 8 and Eq. 4; for δ_{aniso} the shifts and deviations are given in ppm

	β_4	$\Delta^{\beta_4}_{\text{mean}}$	$\langle f \rangle$	Dev.
δ_{aniso}	180°	1.9	1.32	0.1(1)
	210°	1.9	2.07	0.5(3)
	240°	1.8	1.51	0.1(1)
	270°	1.7	1.49	0.1(1)
η	180°	0.05	1.06	0.006(4)
	210°	0.05	1.41	0.004(3)
	240°	0.05	1.36	0.005(4)
	270°	0.05	1.34	0.004(3)

derived (Table 2). For all dihedral angles β_4 the deviations are very small.

This procedure simply transfers the surfaces of (f) and (g) onto each other by using a mean shift and a mean factor which both can be determined straightforwardly. Furthermore, the shift value for η seems to be unique for all possible dihedral angles (compare to Table 2). Merely the factor varies between the subsurfaces stating that their curvature but not their mean value is β_4 dependent.

For the anisotropy δ_{aniso} the interrelation between the surfaces is not as simple. The shift parameter $\Delta^{\beta_4}_{\text{mean}}$ takes individual values for different β_4 and the shifted surfaces cannot be transferred onto each other by a simple mean factor $\langle f \rangle$. This is the reason for the large deviation as found for a β_4 value of 210° (see Table 2). However, at a closer look the difference surface reveals that the values causing this aberration do not randomly scatter around zero but deviate in a systematic way. This implies that instead of using a constant factor the transformation of the anisotropy surfaces may still be carried out by some mathematical function $f(\alpha_1, \alpha_3)^{\beta_4=\text{fix}}$. These results demonstrate that the hypersurface calculated with models (f) and (g) reveal a high potential for the hydrogen bond structure determination by comparison with the experiment. Especially the asymmetry parameter η appears to give robust information about the C═O···H─N environment. A possible strategy for a characterization of the full hypersurface as a function of d(NO), α_1, α_3 and β_4 could start with the determination of the NO distance dependency of the mean η (similar to Fig. 6). This would give the shift values $\eta^{d(\text{NO}),\beta_4}_{\text{mean}}$ for the angular subsurfaces $\eta\{\alpha_1, \alpha_3\}^{d(\text{NO}),\beta_4}$. In the next step for three or more distances these subsurfaces could be calculated and the necessary set of factors f determined. With these factors it should be possible to interpolate between the calculated subsurfaces and get a full description of the hypersurface at low computational cost. The calculated surfaces are expected to be dependent on the investigated system and this approach has to be carefully tested. However, as the use of such parametrized hypersurfaces was not the key feature of the here presented work in the next step we turned to the comparison with the experiment.

3.4. Prediction of the hydrogen bond structure in cyameluric acid

For a prediction of the hydrogen bond arrangement in cyameluric acid from a comparison of the measured NMR parameters δ_{aniso} and η with the calculated hypersurfaces (f) and (g) some differences between the real and the model system have to be taken into account. In the experiment three C═O resonances were observed at 152.5, 153.7 and 156.0 ppm [47]. These sites comprise anisotropies δ_{aniso} and asymmetry parameters η of 83.1, 86.5 and 79.3 ppm and 0.41, 0.31 and 0.53, respectively. In the model systems (f) and (g) the smallest η was 0.26 and its maximum value 0.42. The model system therefore underestimates the absolute magnitude of the experimental parameters and with 0.16 compared to 0.22 the difference between the minimum and maximum value of η is smaller than in the experiment. Such a discrepancy can well result from the different chemical natures of the compared systems. Whereas the model system comprises one isolated hydrogen bond in cyameluric acid three hydrogen bonds interact in an overall aromatic system. In such aromatic systems local changes in the electron density as for example caused by a hydrogen bond can spread over the molecule leading to concerted effects [41]. In our approach we evaded difficulties in the comparison between the model and the experiment by using the relative values of δ_{aniso} and η in the comparison and by fixing the NO distances to the experimentally found values. The idea behind this is that the relative change in the NMR parameter upon a change in structure is similar in both the theoretical and the real system, even if the absolute range for the parameters is different.

It is important to mention that the results from the curvature of the hypersurfaces as presented above clearly state that there is an order in which these variables have to be interpreted. The distance and the angles have a strong influence on the NMR parameters and therefore they should match well with the experimental structure. As it is coupled to the OH distance via the angle α_3 this should especially be true for the OHN arrangement (compare to Fig. 2). The influence of the dihedral distortion β_4 of the pyrrole molecule can only be interpreted for OHN angles which appropriately deviate from linearity. β_1 is defined the same as in system (a) where it was shown that it did not play any role for the parameter η (compare to Section 3.2.2). For this reason the distortion of the cyanuric acid molecule about the C═O bond cannot be expected to match the arrangement found in the experiment. Furthermore, due to the necessarily limited size of the hypersurfaces not all possible structures could be included and thus only the most probable arrangements are chosen in the comparison of the NMR parameters.

The relation between the experimental values for δ_{aniso} and η of the three signals at 152.5, 153.7 and 156.0 ppm

was calculated in percent. This yielded 52.8%, 100% and 0% with a maximum difference of 7.2 ppm for δ_{aniso} and 45.5%, 0.0% and 100.0% with a maximum difference of 0.22 for η. The lowest value for η was exclusively found in the hypersurface for d(NO) equal to 2.9 Å. Ensemble (I) in Fig. 9 shows the superposition of the structures which represent this η value of 0.26–0.27 (0% in the theoretical model). Altogether six arrangements were found, all very similar to each other. α_1 is determined to 100°, α_3 stretches from 120° to 130° and the distortion β_4 varies from 180° to 200°. For the highest η value of 0.42 (100% in the theoretical model) eight structures were found (see Fig. 9, ensemble (II)). They all are members of the hypersurface calculated for d(NO) equal to 2.7 Å and again the ensemble consists of hydrogen bond environments highly similar to each other. α_1 varies from 120° to 130°, α_3 is fixed to 120° and the dihedral distortion β_4 stretches from 230° to 270°. For both ensembles, I and II, the structural selection was exclusively based on the asymmetry parameter η. The

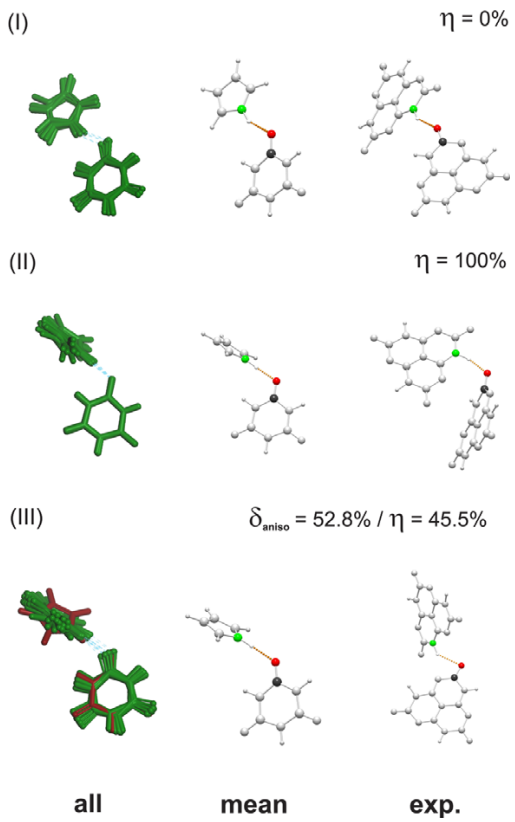

Fig. 9. Left side: defined ensembles of hydrogen bond arrangement derived from fixed relative values of η (I and II) and the combination of relative values of δ_{aniso} and η (III); middle: mean structures of the such chosen ensembles for a comparison with the experiment; right side: hydrogen bond environments from the X-ray structure solution [47]; only the COHN environment (colored atoms) can be taken for a comparison between the model system and the experimental structures. (For interpretation of the references in color in this figure legend, the reader is referred to the web version of this article.)

mean anisotropy of arrangements I is 78.7(1) and 74.7(2) ppm for structures II. Even though in both cases δ_{aniso} slightly scatters, the standard deviations are small enough to claim that each ensemble exhibits a collective value for the anisotropy. This means that within a reasonably small range the combination of η and δ_{aniso} selectively specifies a hydrogen bonding environment.

Based on this knowledge we looked for structures representing the third value of $\eta = 0.34$ (45.5% in the theoretical model). This value was found in both hypersurfaces, (f) and (g) thereby drastically increasing the number of possible arrangements. We used the anisotropy δ_{aniso} to further narrow down the selection. Based on the theoretical anisotropies of the arrangements I and II and the relative magnitude of 52.8% known from the experiment the expected anisotropy for the third hydrogen bond was calculated to 76.8 ppm. Within a variation of this value of up to 0.2 ppm three structures with d(NO) = 2.7 Å and 15 structures with d(NO) = 2.9 Å were found. Therefore the latter distance clearly is preferred over 2.7 Å. Ensemble III in Fig. 9 depicts the superposition of these arrangements. Again a group of similar hydrogen bond environments was determined. α_1 varies from 120° to 150°, α_3 from 120° to 140° and the dihedral distortion β_4 stretches from 240° to 270°. With $\beta_4 = 210°$ only one structure markedly deviates from these values (see brown structure in Fig. 9, (III)).

The collected structures of (I), (II) and (III) furthermore served as a base for the comparison with the X-ray structure of cyameluric acid. For each ensemble a mean arrangement was calculated and compared to the respective hydrogen bond environment (see middle and right structures in Fig. 9). The analogy between the model and the experiment was further analyzed with respect to the COHN environment (compare to the colored atoms in Fig. 9). The extracted values included the NO distance, the COH and OHN angles and the COHN distortion of the hydrogen bond.

Starting with arrangement I the theoretical and experimental structures match very closely (compare to Fig. 9 and Table 3). The NO distance was found correctly and

Table 3
Comparison of HB arrangements (I)–(III) in Fig. 9; distances and angles are given for the model structure, the experimental structure and the difference between these two arrangements [47]

	α_{COH}	α_{OHN}	β_{COHN}
$(I)^{mean}$	122°	157°	−171°
$(II)^{mean}$	118°	172°	−112°
$(III)^{mean}$	131°	173°	72°
$(I)^{exp}$	151°	155°	−158°
$(II)^{exp}$	120°	171°	0°
$(III)^{exp}$	95°	149°	171°
$(I)^{diff}$	29°	2°	13°
$(II)^{diff}$	2°	1°	112°
$(III)^{diff}$	36°	24°	99°

the deviations of the COH and OHN angles as well as the distortion about COHN are reasonably small (compare to $(I)^{diff}$ in Table 3). With 29° the largest deviation is found for the COH angle. The match even improves when turning to arrangement II. Again the correct distance was found and the COH and OHN angles match very well. The deviation of the COHN distortion is given but has no influence on a structural interpretation because the OHN angle is close to 180°. Therefore the cone that can be formed by the variation of β_4 has a very small aperture angle and all structures created by such a variation are highly similar (compare to Fig. 2). The same line of reasoning has to be used when comparing structure III. The angles of the theoretical structures II and III are very similar and the main difference between the systems is the NO distance which is 2.7 Å for arrangement II and 2.9 Å for system III. Compared to the experiment only the approximate orientation of the hydrogen bond environment III matches. This might be due to the reason that the conditions for a comparison of this arrangement are not well set. With 95° the COH angle in the X-ray structure is very small. Such small angles were not included in the calculation of the hypersurfaces (f) and (g) where α_1 only varied from 120° to 180°. Furthermore the experimental C═O···H─N arrangement does not pose a good example as it markedly deviates from a typical hydrogen bonding situation. Through the small COH angle the N─H hydrogen is positioned in the middle of the C═O oxygen and its vicinal nitrogen (compare to Fig. 9). Such a situation resembles the problematic structure 9 discussed in Section 3.1 which is why DFT cannot be expected to yield good NMR parameters for this case (see also Fig. 4).

The results are encouraging in the context of hydrogen bond structure prediction. In all cases the correct distance was chosen from the two possibilities and it can be expected that the precision in the analysis of the distance is about 0.1 Å or even higher. Furthermore, the angular orientation of the hydrogen bond environments (I) and (II) could be reproduced at least qualitatively well. As the influence of the angles on the NMR parameters is much weaker than the influence of the distance, deviations of up to 30° have to be taken into account. For OHN angles smaller than about 160° the distortion of the hydrogen bond could successfully be analyzed in addition to the distance and angles. Together these structural parameters give a quite precise picture of the hydrogen bond arrangement.

4. Summary

Our results clearly show that the hydrogen bond strength correlates with the anisotropic part of the chemical shift tensor. This correlation can be used for structure prediction through a comparison of experimental values with NMR hypersurfaces calculated for a small chemically similar model system. In our approach we investigated the relative change of the anisotropy δ_{aniso} and the asymmetry parameter η upon variations of the hydrogen bonding environment in the model system of pyrrole and cyanuric acid.

We found that the relative change of the NMR parameters can be described with DFT and a moderate double zeta basis set in a quality comparable to MP2 calculations. This allows for the fast computation of the anisotropy δ_{aniso} and asymmetry η hypersurfaces revealing detailed information about the influence of structural parameters. The greatest changes occur upon a variation of the NO or OH distances in the C═O···H─N hydrogen bond. The next important influence comes from bending of the hydrogen bond about the COH or OHN angle. In the cases were the OHN angles become small (lower than 160° thereby deviating from a linear arrangement) the dihedral distortion of the hydrogen bond gains an increasing influence upon δ_{aniso} and η. Distortions of the cyanuric acid molecule about the carbonyl group were shown to have no influence on the anisotropic part of the chemical shift tensor.

In addition to this general behavior we found a minimal structural description of the hydrogen bond system based on the NO distance, two angles (COH and OHN) and one dihedral distortion (CONC) which seems to be well suited for the prediction of hydrogen bond environments from the NMR parameters δ_{aniso} and η. For fixed NO distances the dependency reduced to only three variables which made the calculation of hypersurfaces accessible. The η surfaces for different distances showed a remarkable similarity and could be transferred into one another by the application of a simple shift accompanied by the application of a mean factor.

Using δ_{aniso} and η of the carbonyl atoms as indicators for two of the three hydrogen bonds observed for cyameluric acid similar structural arrangements were found for our model system based on pyrrole and cyanuric acid. A given set of the parameters δ_{aniso} and η clearly chooses a well defined ensemble of hydrogen bond arrangements. In general it can be said that distances from the analysis of anisotropic NMR values are given with an accuracy of at least 0.1 Å. Furthermore, the bending within the hydrogen bond might be determined with a maximum deviation of about 30°. If the OHN angle differs significantly from 180° additionally the distortion of the hydrogen bond arrangement becomes accessible as well.

We suggest that the here presented approach might be used to improve the analysis of hydrogen bond environments. It should not be necessary to calculate hypersurfaces for each individual system, but the idea is to calculate a reasonable model system for a whole group of chemically similar systems. For example the hydrogen bond environment in peptides could become accessible by calculations on model systems with simple amino acids. Such calculations then could provide a database for the structural investigation of the hydrogen bond environments by comparison to solid-state NMR measurements.

Appendix A. Supplementary data

Supplementary data associated with this article can be found, in the online version, at doi:10.1016/j.theochem.2007.08.029.

References

[1] T. Steiner, Angew. Chem. Int. Ed. 41 (2002) 48–76.
[2] E. Oldfield, Ann. Rev. Phys. Chem. 53 (2002) 349–378.
[3] A.E. Aliev, K.D.M. Harris, Struct. Bonding 108 (2004) 1–53.
[4] R.K.J. Harris, Pharm. Pharmacol. 59 (2006) 225–239.
[5] W.W. Bacovchin, Magn. Res. Chem. 39 (2001) S199–S213.
[6] S. Grzesiek, M. Allan, F. Cordier, D. Häussinger, P. Jensen, J. Kahmann, S. Meier, H.J. Sass, Pure Appl. Chem. 77 (2005) 1409–1424.
[7] R.A. Burton, N. Tjandra, J. Am. Chem. Soc. 129 (2007) 1321–1326.
[8] M.D. Esrafili, F. Elmi, N.L.J. Hadipour, Phys. Chem. A 111 (2007) 963–970.
[9] J. Palomar, V.R. Ferro, M.A. Gilarranz, J.J. Rodriguez, J. Phys. Chem. B 111 (2007) 168–180.
[10] A.V. Afonin, I.A. Ushakov, L.N. Sobenina, Z.V. Stepanova, O.V. Petrova, B.A. Trofimer, Magn. Res. Chem. 44 (2006) 59–65.
[11] C.E. Lobat-Garcia, P. Guadarrama, C. Lozada, R.G. Enriquez, D. Gnecco, W.F. Reynolds, J. Mol. Struct. 786 (2006) 53–64.
[12] M. Wolniak, M. Tomczyk, J. Gudej, I. Wawer, J. Mol. Struct. 825 (2006) 26–31.
[13] M. Tafazolli, S.K. Amini, Chem. Phys. Lett. 431 (2006) 421–427.
[14] R. Witter, U. Sternberg, S. Hesse, T. Kondo, F.-T. Koch, A.S. Ulrich, Macromolecules 39 (2006) 6125–6132.
[15] J.R. Yates, T.N. Pham, C.J. Pickard, F. Mauri, A.M. Amado, A.M. Gil, S.P. Brown, J. Am. Chem. Soc. 127 (2005) 10216–10220.
[16] F. Cheng, H. Sun, Y. Zhang, D. Mukkamala, E. Oldfield, J. Am. Chem. Soc. 127 (2005) 12544–12554.
[17] M. Sigalov, A. Vashchenko, V. Khodorkovsky, J. Org. Chem. 70 (2005) 92–100.
[18] A. Kaczor, L.M. Proniewicz, J. Mol. Struct. 704 (2004) 189–196.
[19] C. Aleman, J. Casanovas, J. Mol. Struct. (Theochem) 675 (2004) 9–17.
[20] J. Stare, A. Jezierska, G. Ambrozic, I.J. Kosir, J. Kidric, A. Koll, J. Mavri, D. Hadzi, J. Am. Chem. Soc. 126 (2004) 4437–4443.
[21] C. Benzi, O. Crescenzi, M. Pavone, V. Barone, Magn. Res. Chem. 42 (2004) S57–S67.
[22] X. Chen, C.-G. Zhan, J. Mol. Struct. (Theochem) 682 (2004) 73–82.
[23] A. Zheng, M. Yang, Y. Yue, C. Ye, F. Deng, Chem. Phys. Lett. 399 (2004) 172–176.
[24] S. Macholl, F. Börner, G. Buntkowsky, Z. Phys. Chem. 217 (2003) 1473–1505.
[25] M.J. Potrebowski, X. Assfeld, K. Ganicz, S. Olejniczak, A. Cartier, C. Gardiennet, P. Tekely, J. Am. Chem. Soc. 125 (2003) 4223–4232.
[26] K. Oku, H. Watanabe, M. Kubota, S. Fukuda, M. Kurimoto, Y. Tsujisaka, M. Komori, Y. Inoue, M. Sakurai, J. Am. Chem. Soc. 125 (2003) 12739–12748.
[27] D. Godzisz, M.M. Ilczyszyn, M. Ilczyszyn, J. Mol. Struct. 606 (2002) 123–137.
[28] G. Litwinienko, E. Megiel, M. Wijnicz, Org. Lett. 4 (2002) 2425–2428.
[29] A.V. Afonin, I.A. Ushakov, S.Y. Kuznetsova, O.V. Petrova, E.Y. Schmidt, A.I. Mikhaleva, Magn. Res. Chem. 40 (2002) 114–122.
[30] M. Lopez de la Paz, G. Ellis, M. Perez, J. Perkins, J. Jimenez-Barbero, C. Vicent, Eur. J. Org. Chem. 5 (2002) 840–855.
[31] J.R. Brender, D.M. Taylor, A. Ramamoorthy, J. Am. Chem. Soc. 123 (2001) 914–922.
[32] Y. Wei, D.-K. Lee, A. Ramamoorthy, J. Am. Chem. Soc. 123 (2001) 6118–6126.
[33] R.M. Claramunt, D. Sanz, S.H. Alarcon, M.P. Torralba, J. Elguero, C. Focus-Focus, M. Pietrzak, U. Langer, H.-H. Limbach, Angew. Chem. Int. Ed. 40 (2001) 420–423.
[34] E. Kleinpeter, L. Hilfert, A. Koch, J. Phys. Org. Chem. 13 (2000) 473–479.
[35] J. Czernek, R. Fiala, V. Sklenar, J. Magn. Res. 145 (2000) 142–146.
[36] C. Viragh, T.K. Harris, P.M. Reddy, M.A. Massiah, A.S. Mildvan, I.M. Kovach, Biochemistry 39 (2000) 16200–16205.
[37] Y. Wei, A. de Dios, A.E. McDermott, J. Am. Chem. Soc. 121 (1999) 10389–10394.
[38] H. Zhao, Q. Pan, I. Carmichael, A.S. Serianni, J. Org. Chem. (2007), published on the web.
[39] N.C. Maiti, Y. Zhu, I. Carmichael, A.S. Serianni, V.E. Anderson, J. Org. Chem. 71 (2006) 2878–2880.
[40] J. Sehnert, J. Senker, Chem. Eur. J. 13 (2007) 6841–6852.
[41] J. Sehnert, K. Bärwinkel, J. Senker, J. Phys. Chem. B 111 (2007) 10671–10680.
[42] M. Ilczyszyn, D. Godzisz, M.M. Ilczyszyn, K. Mierzwicki, Chem. Phys. 323 (2006) 231–242.
[43] Z. Gu, R. Zambrano, A. McDermott, J. Am. Chem. Soc. 116 (1994) 6368–6372.
[44] Z. Gu, A. McDermott, J. Am. Chem. Soc. 115 (1993) 4282–4285.
[45] Z. Gu, Hydrogen Bonding in Biological Systems: What Solid-state NMR Can Tell, Ph.D. thesis, Columbia University, 1996.
[46] E. Kroke, M. Schwarz, Coord. Chem. Rev. 248 (2004) 493–532.
[47] L. Seyfarth, J. Sehnert, N. El-Gamel, W. Milius, E. Kroke, J. Breu, J. Senker, Eur. J. Inorg. Chem., submitted for publication.
[48] J. Pople et al., Gaussian 03, Revision D.01, Gaussian, Inc., Wallingford, CT, 2004.
[49] M.H. Levitt, J. Magn. Res. 126 (1997) 164–182.
[50] M. Bak, J.T. Rasmussen, N.C. Nielsen, J. Magn. Reson. 147 (2000) 296–330.
[51] J. Mason, Solid State Nucl. Magn. Reson. 2 (1993) 285–288.

A.5:

Unmasking Melon by a Complementary Approach Employing Electron Diffraction, Solid-State NMR Spectroscopy, and Theoretical Calculations - Structural Characterization of a Carbon Nitride Polymer

B. V. Lotsch, M. Döblinger, J. Sehnert, L. Seyfarth, J. Senker, O. Oeckler and W. Schnick

Chemistry - A European Journal

Chem. Eur. J. 2007, 13, 4969 - 4980
DOI: 10.1002/chem.200601759

The here presented solution of the Melon structure from TEM data required a confirmation from independent sources. In this context theoretical modeling of the structure as well as solid-state NMR measurements and the combination of both methods came into play.

My personal contributions to this work included the following:

- geometry optimizations with semiempirical methods on single melon strings as well as hydrogen bonded melon clusters
- the development of a three-dimensional structure model from a combination of TEM and X-ray data and the results of the semiempirical structure optimization
- calculations on the 3D structure model under periodic boundary conditions using DFT with plane waves as well as force field methods
- the calculation of the theoretical ^{13}C and ^{15}N chemical shifts and comparison with the experiment
- discussion on the presented topic
- co-authorship of the article

The contributions of all other authors comprised of:

- synthesis of melon from melamine
- measurement of X-ray powder diffraction data for melon
- IR measurements on melon
- scanning electron microscopy on melon
- electron diffraction (ED) and transmission electron microscopy (TEM) on melon
- structure solution from ED and TEM data
- measurement of ^{15}N and ^{13}C solid-state NMR spectra for melon
- discussion on the presented topic
- authorship and co-authorship of the article

DOI: 10.1002/chem.200601759

Unmasking Melon by a Complementary Approach Employing Electron Diffraction, Solid-State NMR Spectroscopy, and Theoretical Calculations—Structural Characterization of a Carbon Nitride Polymer

Bettina V. Lotsch,[a] Markus Döblinger,[a] Jan Sehnert,[b] Lena Seyfarth,[b] Jürgen Senker,*[b] Oliver Oeckler,[a] and Wolfgang Schnick*[a]

Dedicated to Professor Wolfgang Beck on the occasion of his 75th birthday

Abstract: Poly(aminoimino)heptazine, otherwise known as Liebig's melon, whose composition and structure has been subject to multitudinous speculations, was synthesized from melamine at 630 °C under the pressure of ammonia. Electron diffraction, solid-state NMR spectroscopy, and theoretical calculations revealed that the nanocrystalline material exhibits domains well-ordered in two dimensions, thereby allowing the structure solution in projection by electron diffraction. Melon ($[C_6N_7(NH_2)(NH)]_n$, plane group $p2gg$, $a=16.7$, $b=12.4$ Å, $\gamma=90°$, $Z=4$), is composed of layers made up from infinite 1D chains of NH-bridged melem ($C_6N_7(NH_2)_3$) monomers. The strands adopt a zigzag-type geometry and are tightly linked by hydrogen bonds to give a 2D planar array. The inter-layer distance was determined to be 3.2 Å from X-ray powder diffraction. The presence of heptazine building blocks, as well as NH and NH_2 groups was confirmed by ^{13}C and ^{15}N solid-state NMR spectroscopy using ^{15}N-labeled melon. The degree of condensation of the heptazine core was further substantiated by a ^{15}N direct excitation measurement. Magnetization exchange observed between all ^{15}N nuclei using a fp-RFDR experiment, together with the CP-MAS data and elemental analysis, suggests that the sample is mainly homogeneous in terms of its basic composition and molecular building blocks. Semiempirical, force field, and DFT/plane wave calculations under periodic boundary conditions corroborate the structure model obtained by electron diffraction. The overall planarity of the layers is confirmed and a good agreement is obtained between the experimental and calculated NMR chemical shift parameters. The polymeric character and thermal stability of melon might render this polymer a pre-stage of g-C_3N_4 and portend its use as a promising inert material for a variety of applications in materials and surface science.

Keywords: ab initio calculations · carbon nitrides · electron diffraction · solid-state NMR spectroscopy · solid-state structures

Introduction

The quest for binary carbon nitride C_3N_4, whose postulated material properties are believed to push the borders of ultra-hard materials, has provided a tight link between Liebig's historic work and modern materials chemistry.[1] While being re-invented in a new context in the 1980s, carbon nitride had been discussed as the ultimate de-ammonation product of a series of "ammonocarbonic acids" such as cyanamide or melamine as early as 1834.[2] All attempts to synthesize pure carbon nitride were invariably spoiled by the presence of hydrogen, yielding an amorphous, infusible material which was first obtained by Berzelius and given the name "melon" by Liebig.[2,3] As reviewed by Franklin,[3] the latter was obtained by heating to redness the yellow precipi-

[a] Dr. B. V. Lotsch, Dr. M. Döblinger, Dr. O. Oeckler, Prof. Dr. W. Schnick
Department Chemie und Biochemie
Ludwig-Maximilians-Universität
Butenandtstrasse 5–13 (D), 81377 München (Germany)
Fax: (+49) 89-2180-77440
E-mail: wolfgang.schnick@uni-muenchen.de

[b] J. Sehnert, L. Seyfarth, Prof. Dr. J. Senker
Anorganische Chemie I
Universität Bayreuth
Universitätsstrasse 30, 95447 Bayreuth (Germany)
Fax: (+49) 921-55-2788
E-mail: juergen.senker@uni-bayreuth.de

Supporting information for this article is available on the WWW under http://www.chemeurj.org/ or from the author.

tate formed by the action of chlorine on a solution of potassium or sodium thiocyanate, by heating ammonium or mercury thiocyanate, and as the final de-ammonation product on heating mixed "aquo-ammonocarbonic acids" such as ammeline or urea.[4,5] Owing to its unusual thermal stability, some doubt arose whether melon should be classified as an organic or an inorganic compound. Despite the lack of sharply defined composition, melon was assigned the empirical formula $H_3C_6N_9$, which led Redemann and Lucas to draw two alternative planar structure models based on the heptazine (cyameluric) core C_6N_7 (Scheme 1, **1a + 1b**). Alternatively, a symmetric triangular form was proposed, whose empirical formula approaches asymptotically the limit C_3N_4 if condensations extend indefinitely (Scheme 1, **1c**).[4]

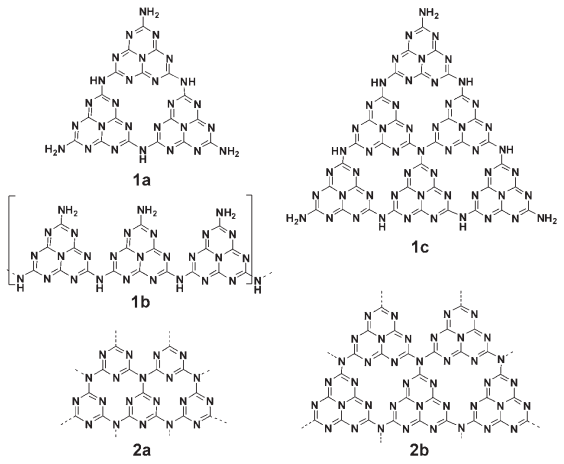

Scheme 1. Structure models proposed for melon (**1a**, **1b**) and cutouts of hypothetical structure models of graphitic carbon nitride based on triazine (**2a**) and heptazine building blocks (**2b**). The melon-derived structure "$C_{36}N_{52}H_{12}$" (**1c**) has an empirical formula intermediate between melon and g-C_3N_4.

Other structure models, including triazine-based variants, have been put forward for melon owing to the lack of detailed knowledge on the structure of its presumed monomer, melem.[6] Franklin found that the empirical composition of melon varied with the method of preparation, as he obtained samples with a hydrogen content between 1.1 and 2.0 wt%. Products with a hydrogen content of only 0.6 wt% were rationalized by assuming a mixture of several "compact" condensation products of triangular shape as for example model **1c** (Scheme 1).[3,4a] On this background, it was conjectured that "it is probably incorrect to assign any one structure to melon, for it is more than likely a mixture of molecules of different sizes and shapes. This gives rise to its amorphous character".[4a]

The gap between historic and modern carbon nitride chemistry is bridged by the hypothetical graphitic modification of C_3N_4 (g-C_3N_4), which has been calculated to be the most stable form of carbon nitride, and owing to its analogy with graphite was attributed the triazine core C_3N_3 as elementary building block (Scheme 1, **2a**).[1,7] Since then, a plethora of experimental and theoretical efforts have been made to elucidate the structure of g-C_3N_4, which failed due to the ill-defined nature of the obtained polymers.[7,8]

The search for graphitic carbon nitride typically emanates from derivatives or precursors of triazine, whose structural integrity is believed to be preserved upon thermal treatment of the starting materials. Thus, a considerable number of possible triazine-based structures—akin to graphite—has been devised and their topologies as well as their relative stabilities computed.[1d,8,10,11] For example, Kawaguchi et al. synthesized a material with the presumed formula $[(C_3N_3)_2(NH)_3]_n$ ($\equiv C_6N_9H_3$) by polycondensation of cyanuric chloride and melamine, whose electron diffraction pattern was indexed on a hexagonal cell with $a = 8.2$ Å and $d_{100} = 7.1$ Å.[7b] Demazeau et al. reported on the solvothermal synthesis of g-C_3N_4 by reacting melamine with hydrazine as a nitriding agent under supercritical conditions.[7a,g,l,o,11]

Only recently, an alternative structure model based on the heptazine nucleus emerged (**2b**, Scheme 1), reminiscent of the extensive work on melon, which still represents a highly controversial chapter in the history of C/N chemistry.[8a,12–15] Although the heptazine-based nitrogen compounds such as melem or cyameluric acid had been known for decades, the significantly less stable unsubstituted nucleus, tri-*s*-triazine, was synthesized and structurally characterized only in the 1980s.[16] Komatsu proposed polymers of melem to form upon polycondensation/pyrolysis of NH_4SCN and various heptazine derivatives.[9b,c] The as-obtained graphite-like "pseudo carbon nitrides" were classified according to their composition as "symmetric triangular forms" (cf. model **1c**, Scheme 1) or as partially condensed, irregular forms of heptazine-based polymers. In addition, the synthesis of a "cyameluric high polymer" by thermal de-ammonation of melon via a melem-dimer was postulated, affording a linear polymer composed of 42 monomers.[9d] In most cases, the X-ray powder patterns were indexed on orthorhombic unit cells ($a = 7.104$, $b = 16.190$, $c = 12.893$ Å;[9b] $a = 7.229$, $b = 21.512$, $c = 13.589$ Å).[9d] In contrast, the attempt to prepare carbon nitrides by polycondensation of melamine with the Lewis acid $ZnCl_2$ afforded a polymer with similar orthorhombic metrics, which was assigned a vacancy-network structure consisting of triazine cores.[9a]

As outlined above, the synthetic strategy that appears to be most promising to obtain reasonably well-defined carbon nitride materials includes the controlled pyrolysis of CN_xH_y precursors.[15] However, the advantage of comparatively high crystallinity usually accompanies the presence of hydrogen in the products, which at the same time seems to stabilize the structure and to function as defect site. On the other end of the experimental spectrum, high-energy techniques (ion beam sputtering, CVD, laser- or shock-wave techniques) almost exclusively afford amorphous materials with substoichiometric nitrogen content with respect to the idealized formula C_3N_4.

In this work we present the 2D structure of a material, subject to numerous speculation, that has commonly been identified with graphitic carbon nitride. We thus provide the first structural characterization of a polymeric carbon(IV) nitride based on electron diffraction and solid-state NMR spectroscopy, which at the same time resolves the controversial identity of melon.

Results and Discussion

Synthesis and characterization: A brownish polymer of the approximate composition $C_3N_{4.4}H_{1.8}$, (N: 61.2; C: 36.0; H: 1.8) determined from elemental analysis and with an average C/N ratio of 0.68 (theor. for C_3N_4: 0.75) was obtained by heating melamine (triamino-*s*-triazine) in sealed silica glass ampoules at 630 °C. Whereas at temperatures below 620 °C, melem ($C_6N_7(NH_2)_3$) was found in the products, thermolysis above 640 °C leads to rapidly increasing carbonization. It should be pointed out that heating melamine at 500 °C in an open system for several hours affords polymeric materials with different colors ranging from light yellow to dark beige. Whereas under these conditions, largely amorphous compounds are obtained, the crystallinity is significantly enhanced by pyrolyzing melamine in a closed system under an autogenous pressure of ammonia that arises from the condensation reactions. The brownish color of the as-obtained products suggests that crystallization accompanies the onset of carbonization of the sample. Small amounts of oxygen (up to 2 wt %; typically 0.5–0.7 wt %) detected in the bulk suggest that the material is prone to water absorption, as was pointed out in the literature.[17] In addition, melamine crystals were detected as impurities, which likely result from depolymerization of the product induced by ammonolysis at elevated temperatures and pressure of ammonia.[18] Possible depolymerization products other than melamine, such as dicyandiamide, were not observed as crystalline side phases; however, the presence of very small amounts of amorphous by-products such as (poly)imides below the detection level of solid-state NMR spectroscopy ($\leq$5 % for CP measurements) may not entirely be excluded. Also, the comparatively harsh synthetic conditions applied in the present context likely induce heterogeneous crystallization and probably yield a broad spectrum of differently ordered domains, ranging from amorphous to nanocrystalline. Presumably, a mixture of polymers with different chain lengths is obtained, which can be considered a feature intrinsic to thermally induced polymerization processes. In this sense, the as-synthesized material, which will be referred to as "C/N/H-graphite" owing to its commonly inferred graphite-like character,[7] cannot be considered an overall homogeneous phase.

In situ temperature-programmed X-ray powder diffraction shows that the material is stable up to about 770 °C without passing through phase transitions prior to its decomposition. The observed thermal stability of this lightweight material is therefore comparable to or somewhat higher than that of aromatic polyamides and -imides.[9d]

The FTIR spectrum of C/N/H-graphite is displayed in Figure 1. Owing to obvious analogies with the vibrational spectra of melon already present in the literature,[9d,19] we will only focus on the most important results here. The well-

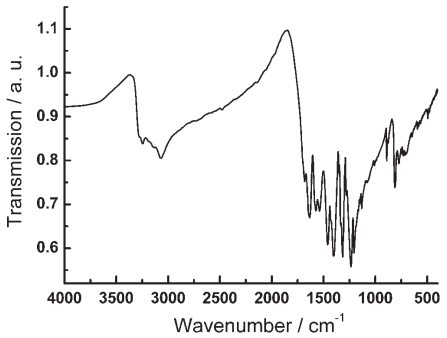

Figure 1. FTIR spectrum of melon recorded as a KBr pellet between 400 and 4000 cm^{-1}.

resolved bands indicate a fairly high degree of ordering. Whereas the sharp band at about 810 cm^{-1} can be attributed to the ring-sextant out-of-plane bending vibration characteristic of both triazine or heptazine ring systems,[13,15,20] the prominent absorption bands at 1206 and 1235 cm^{-1} and possibly 1316 cm^{-1} have been shown to be characteristic of the C–NH–C unit in melam.[19,21,22] Therefore, a similar structural motif, corresponding to either trigonal C–N(-C)–C (full condensation) or bridging C–NH–C units (partial condensation), can be inferred for the polymer. Absorption found in the N–H stretching region between 3250 and 3070 cm^{-1} proves the presence of NH and/or NH_2 groups, which are most likely integral parts of the structure.

Scanning electron microscopy images demonstrate the micro- and nanocrystalline character of the CN_xH_y material as shown in Figure 2. The morphology of the material resembles that of microcapsules, the hollow tubes and spheres with a diameter of several micrometers containing nanocrystallites. While the crystalline particles appear to be platelike, the spheres presumably result from the isotropic bulging of the particles during gas evolution in the course of condensation. Owing to the small crystallite size, structure elucidation by X-ray methods does not seem to be particularly promising.

In accordance with literature data, the X-ray diffraction pattern is indicative of a layered substance with an interlayer spacing of 3.19 Å.[7,8,14,15,24] The powder pattern resembles that of graphite, which has an interlayer spacing slightly larger than that of the carbon nitride material (3.33 Å) as shown in Figure 3. Remarkably, the strong reflection, which is commonly indexed as 002 by analogy with graphite, is sharp, whereas all *hk*0 and *h*0*l* reflections—if present at all—are weak and broadened. In addition, asymmetric shapes of the reflections ("tailing" towards higher 2θ values, as seen for the low-angle reflection at $2\theta \approx 12.6°$), are visible. These features could result from "streaking" along c^* due to

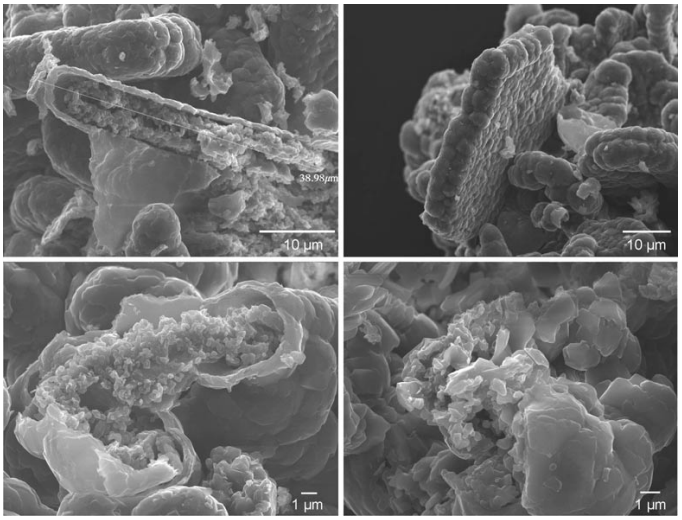

Figure 2. Scanning electron microscopy images of C/N/H-graphite, taken from various sample regions. The images reveal crystallite sizes on the nanometer- and micrometer-length scales, as well as the "porous" morphology of the sample.

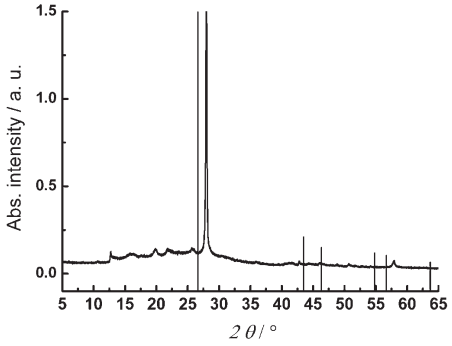

Figure 3. X-ray powder pattern ($Cu_{K\alpha1}$ radiation) of C/N/H-graphite (continuous line) and simulation for graphite (bars). The interlayer distance (strong reflection) amounts to 3.19 Å.

2D planar disorder. However, the sharp main reflection and absence of splitting of the latter points to the layers being planar with a sharply defined interlayer spacing.

Solid-state NMR spectroscopy: Solid-state NMR spectroscopy is a valuable tool for probing the structure of semicrystalline or amorphous materials on local and intermediate length scales, as it is not dependent on the long-range order in contrast to diffraction techniques. Owing to the low sensitivity of the ^{15}N nucleus, a ^{15}N-enriched C/N/H-graphite (degree of enrichment of $\approx$25%) was synthesized starting from ^{15}N-labeled melamine.

The ^{15}N CP-MAS spectrum of the C/N/H-graphite is displayed in Figure 4 (top). The comparatively high resolution is diagnostic of a semicrystalline rather than an amorphous material. For a reliable signal assignment (as indicated in Figure 4), a CPPI (cross-polarization with polarization inversion) experiment was carried out. By evaluating the characteristic time dependence of the polarization inversion dynamics of the different ^{15}N nuclei, the number of protons covalently bonded to the latter can be ascertained. As outlined in Figure 5, three types of signals can be distinguished: The signals between $\delta = -177$ and -195 ppm, as well as the resonance at $\delta = -225$ ppm exhibit a moderate intensity loss, the continuous, slow decrease of the polarization being characteristic of tertiary nitrogen atoms. In contrast, the polarization of the signals at $\delta = -245$ and -265 ppm follows a two-step process induced by the covalently bonded protons. The intensity at the cross-over

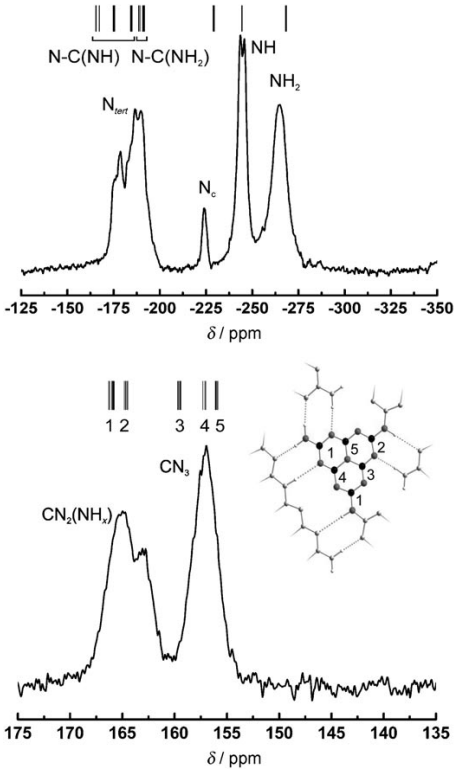

Figure 4. ^{15}N (top) and ^{13}C (bottom) CP-MAS solid-state NMR spectra of the C/N/H-graphite. The signal assignments according to ab initio calculations of the chemical shift values for the DFT-optimized cell (see inset) are indicated on top of the experimental spectra. The respective carbon sites in the structure are indicated by numbers (black: C, gray: N).

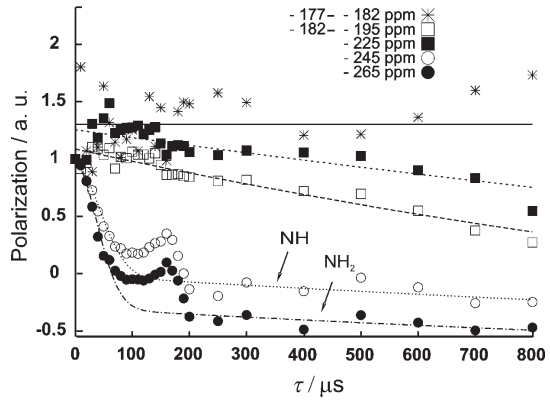

Figure 5. Evolution of the signal intensities (cf. Figure 4) during the course of a ^{15}N CPPI experiment. The polarization of the ^{15}N nuclei is given as a function of the inversion time τ_i.

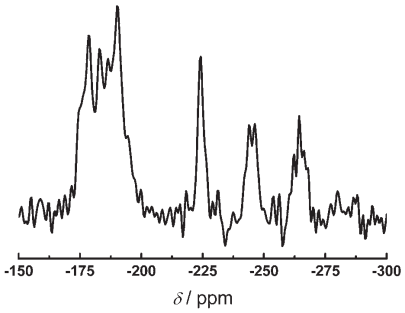

Figure 6. ^{15}N direct excitation spectrum using a recycle delay of 8 h as estimated from a ^{15}N T_1 measurement to ensure a total recovery of the magnetization. Number of scans: 16; spinning frequency: 9 kHz.

between the dipolar and spin-diffusion regime is given by $[2/(n+1)] - 1$ ($n = 0,1,2$), thereby allowing the differentiation between NH (crossover at 0) and NH_2 (crossover at $-1/3$) nitrogen nuclei.[13,25]

Therefore, the assignment of all signals according to the proton environment of the ^{15}N nuclei is feasible. Notably, apart from tertiary nitrogen atoms expected for a fully condensed network, NH and NH_2 groups are present, which suggest the formation of an only partially condensed C/N/H network.

Information on the nature of the building blocks can be obtained from the isolated signal at $\delta = -225$ ppm in the ^{15}N spectrum. This tertiary nitrogen resonance is strongly reminiscent of the central nitrogen atom ("N_c") of the heptazine core, since it exhibits an up-field shift compared to the outer nitrogen nuclei of the ring in essentially all heptazine-based compounds studied so far.[13,26] For example, this nitrogen resonance is observed at $\delta = -234.2$ ppm for melem.[13,24] Thus, these findings furnish the first significant indication of the heptazine-based nature of the graphitic C/N/H material.

The ^{13}C CP-MAS spectrum of the product shows remarkable similarity with that of melem. In detail, two signal groups are found with peak maxima at $\delta \approx 164$ and 157 ppm. In melem, two groups of carbon resonances are observed at $\delta = 164.3/166.4$ and 155.1/156.0 ppm, respectively, where the low-field signals ($\delta = 164$–166 ppm) were assigned to the carbon positions adjacent to the amino groups.[13,24] Based on DFT calculations, an analogous assignment of the low-field signals ($\delta = 163$–165 ppm) to $CN_2(NH_x)$ and the high-field signal ($\delta = 157$ ppm) to CN_3 moieties was accomplished for the C/N/H-graphite as will be discussed below. The use of different CP contact times τ_c corroborates this assignment.

To quantify the relative ^{15}N signal intensities and to draw conclusions on the degree of condensation of the presumed heptazine core, an experiment using direct excitation of the ^{15}N nuclei was carried out (Figure 6). In this experiment, the magnetization transfer from the abundant protons to the ^{15}N nuclei is circumvented, thereby rendering the signal intensities independent of the number of protons in spatial proximity. Owing to the very long relaxation time of the ^{15}N nuclei, a recycle delay between successive scans of 8 h had to be applied to ensure total magnetization recovery before each scan. Comparatively long relaxation times are diagnostic of well-ordered materials. Owing to the isotopic enrichment of melon, 16 scans were sufficient to acquire a spectrum with a reasonable signal-to-noise ratio. As depicted in Figure 6, the signal intensities show significant variations as compared to the CP-MAS spectrum in Figure 4. As expected, the tertiary nitrogen resonances gained intensity at the expense of the protonated nitrogen signals. A quantitative fit of the relative intensities indicates a ratio of the four signal groups N_{tert}:N_c:NH:NH_2 roughly corresponding to 7:1:1:1. In particular, the equal intensities of N_c, NH, and NH_2 suggests a degree of condensation approximately corresponding to that expected for melon (6:1:1:1, cf. **1a + 1b**, Scheme 1). To sum up, evidence of only one single type of building block—heptazine—is provided by the CP-MAS and direct excitation spectra. Since atom connectivities and, hence, local structural motifs dominate the chemical shift of the nuclei, this missing spread in chemical shift values renders the presence of triazine ring systems highly unlikely. In addition, DFT calculations of the chemical shift parameters of fully condensed triazine- and heptazine-based C_3N_4 systems suggest that the chemical shift range expected for triazine-based structures would spread out way downfield as compared to the observed data, for both planar and corrugated structures.[27] This adds to the above evidence that the C/N/H-graphite is composed of heptazine rather than triazine building blocks. Accordingly, the somewhat higher intensity observed for N_{tert} may result from the admixture of minor, heptazine-based side phases exhibiting a slightly higher degree of condensation (cf. for instance structure **1c**, Scheme 1). The line width observed in the NMR spectra is slightly increased (by a factor of about 2) as compared to typical line widths of crystalline molecular compounds. This is indicative of varying chemical environments of the heptazine nuclei, which depend on the orientation of the adjacent layers as determined by the local stacking sequence. Similar

effects may be induced by different polymer lengths, which give rise to slightly altered local magnetic fields at the sites of nuclei in the vicinity of chain or layer terminations. In contrast, for a completely amorphous material the line widths should be increased by a factor of 10 to 20.

A fp-RFDR experiment was carried out to probe the homonuclear, through-space magnetization transfer between the ^{15}N nuclei. It can therefore be considered as a sensor for spatial proximities of the nuclei in the sample. By selectively exciting the NH_2 signal, the time dependence of the magnetization transfer to the surrounding ^{15}N nuclei (other than NH_2) was monitored by successively varying the mixing time in small intervals. Figure 7 (top spectra) outlines the

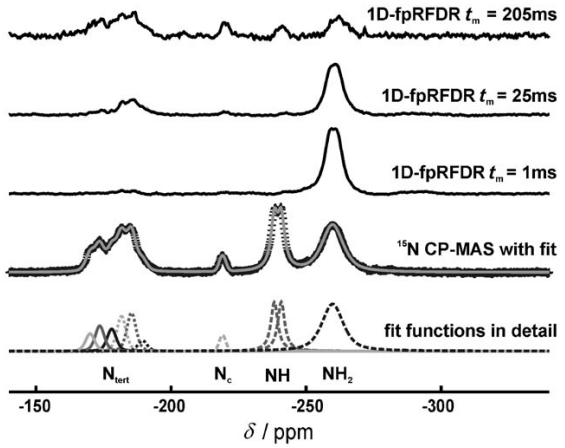

Figure 7. ^{15}N CP-MAS spectrum of the C/N/H-graphite and the corresponding overall fit (gray line; 2nd spectrum from bottom). Individual resonances of the fits (cf. Figure 8) (bottom), and 1D-fpRFDR spectra for mixing times $t_m = 1$, 25, 205 ms.

1D-RFDR spectra obtained for three mixing times ($t_m = 1$, 25, and 205 ms) corresponding to short, intermediate and long periods of magnetization transfer. Whereas for $t_m =$ 1 ms no magnetization transfer to the other nitrogen nuclei is visible, exchange commences at $t_m = 25$ ms for the high-field part of the tertiary nitrogen signals, which is visible by the growing intensity of the latter. Very weak signals can also be distinguished for the N_c and NH resonances. For long mixing times, all initial resonances are observable, which indicates a dipolar exchange of magnetization among the NH_2 nitrogen and *all* other ^{15}N nuclei in the sample. This observation is confirmed by the build-up curves (see Figure S4 in the Supporting Information), which trace the increase of magnetization at the tertiary and NH nitrogen nuclei and the concomitant loss of signal intensity at the selectively excited NH_2 nitrogen atoms. Build-up is fastest for the tertiary ^{15}N nuclei from $\delta = -195$ to -187 ppm, which therefore represent the closest neighbors of the NH_2 group. This finding is in agreement with the ab initio ^{15}N chemical shift parameters calculated for the DFT-optimized cell based on the structure solution from electron diffraction, as will be detailed below (see also Figure 4). This exchange behavior suggests homogeneity of the sample in a regime up to 30 Å. Note that the coexistence of different domains is thus limited to different stacking variants and possibly heptazine-based structural isomers, which do not give rise to additional signals in the 1D CP-MAS spectrum as outlined above. Summing up, this experiment suggests that all ^{15}N nuclei are in spatial neighborhoods and no structurally distinct phases are detectable by ^{15}N NMR spectroscopy.

Electron diffraction: Electron diffraction (ED) can provide structural insights into nanometer-sized materials. The dimensions of the C/N/H-graphite particles can be estimated to amount to 50–200 nm by transmission electron microscopy (TEM, Figure 8). In the diffraction mode, the presence of domains (Figure 9) of varying crystallinity is evident, as can

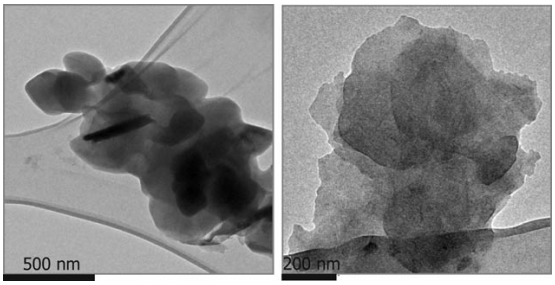

Figure 8. TEM images of the C/N/H-graphite on a carbon coated copper grid, showing the platelike nano- and microcrystals.

be seen by the asymmetric peak shapes and diffuse scattering, the latter being either intrinsic or due to amorphous cover layers. In agreement with the platelike character of the crystallites, the preferred orientation is such that most diffraction patterns are taken along the [001] zone axis, other zone axes are hardly accessible. As indicated by the X-ray powder patterns, varying degrees of "streaking" along c^* are observable (Figure 10, right), resulting from planar defects or possibly turbostratic stacking disorder. Nevertheless, SAED patterns of crystalline domains with perfect pe-

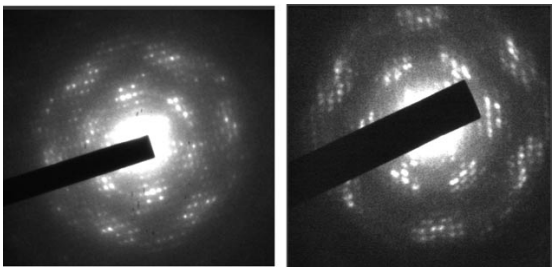

Figure 9. Selected area electron diffraction (SAED) patterns of the *hk*0 plane (zone axis [001]) of the C/N/H-graphite. All patterns exhibit different degrees of diffuse scattering and are indicative of partial disorder and/or thick sample sizes.

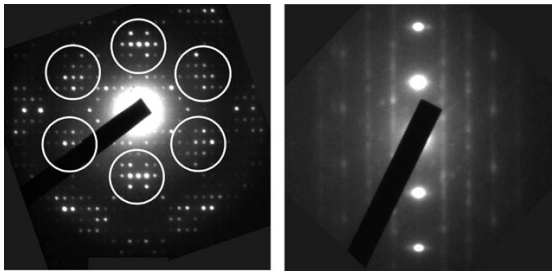

Figure 10. Left: Electron diffraction pattern of the *hk*0 plane (zone axis [001]). The pseudo-hexagonal intensity distribution is indicated by white circles. Merging the reflection groups contained in the circles (shown exemplarily; the same applies for all reflection groups) into one single spot would generate a diffraction image similar to that of graphite. Right: SAED pattern viewed perpendicular *c**. Whereas the 00*l* reflections are clearly visible, "diffuse bars" are observed parallel to *c** with a non-discrete intensity distribution ("streaking").

riodicity at least in two dimensions can be obtained, which are unaffected by the stacking disorder (Figure 10, left).

The commonly claimed graphite-like character of this material, which has led to the assumption that it is related to graphitic carbon nitride, is associated with the pseudo-hexagonal intensity distribution in the *hk*0 plane. Groups of strong reflections can be correlated with reflections of graphite with respect to their symmetry as well as the encoded distance information (Figure 10, left). Indexing the *hk*0 patterns yields a rectangular mesh with cell parameters $a=16.7$, $b=12.4$ Å. These values are similar to those determined by Komatsu from X-ray powder patterns ($a=7.104$ ($\equiv$ 2c), $b=16.190$ ($\equiv$ a), $c=12.893$ Å ($\equiv$ b)) given the layer spacing of 3.2 Å.[9b] Taking advantage of a number of beneficial factors, such as the planarity of the layers, the light atom structure, and large unit cell (small structure factors, minimum multiple scattering), the structure was solved in projection based on the electron diffraction data. Owing to the small sample thickness, the kinematical approximation $I_{hkl} \propto |F_{hkl}|^2$ could be used. Evaluation of the observed absences in the base plane (*h*0: $h=2n+1$; 0*k*: $k=2n+1$) allows for the plane group *p*2*gg*. Strong reflections remain sufficiently strong to find phase relationships using direct methods,[28a] and, thus, a figure of merit of 20.06% was obtained by employing SIR-97[29] for structure solution. Reducing the symmetry to *p*2 and introducing the mirror planes as a twin law yields better residuals. However, the data/parameter ratio obtained is very low. Therefore, the improvement of the residuals is not significant and is accompanied by an unreasonable distortion of the heptazine rings. Upon regularizing the heptazine units, the residuals again increase, so that the twin approach does not lead to a real improvement.

All carbon and nitrogen atoms could be located with reasonable bond angles and distances. Upon refinement (208 reflections, 46 parameters), *R*1 was 26.44%. As reflection intensities are affected by dynamical diffraction, better residuals have not been obtained; however, they lie in the range usually reported for refinements based on electron diffraction data.[28] After refinement, the difference Fourier synthesis has no significant maxima, which can be demonstrated by arbitrarily removing one atom from the structure model. The removed atom then yields by far the highest difference Fourier peak. The bond length precision after refinement is 0.045 Å, within this experimental error (neglecting systematic errors), the distances and angles calculated are reasonable within a 2σ interval. Crystallographic data are summarized in Table 1.[31]

Table 1. Crystallographic data of the structure solution and refinement of melon based on ED data.

formula	$C_6N_9H_3$
M_w [g mol^{-1}]	201
plane group	*p*2*gg*
instrument type	JEOL 2011 TEM
instrument details	single tilt holder, TVIPS CCD camera (F114)
incident radiation energy [kV]	200
d_{min} [Å]	0.65
a [Å]	16.7[a]
b [Å]	12.4[a]
layer distance along *c* [Å]	3.2[b]
symmetry-independent reflections	208
number of parameters	46
*R*1	26.44%
R_{rim}[29]	40.2%

[a] The error for determination of the lattice parameters from ED is estimated to be $\approx$5%. [b] Determined from X-ray powder diffraction.

To countercheck the consistency of the structure model, kinematical SAED diffraction patterns based on the structural parameters were calculated. The simulation of the *hk*0 plane is shown in Figure 11 (right), together with experimental patterns used for structure solution. The patterns agree well, although the experimental intensity distribution deviates slightly from the *mm*2 symmetry of the plane group. Note however, that the symmetry of the precession patterns is significantly less violated.

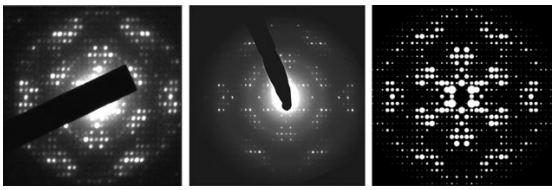

Figure 11. Experimental (left, middle) *hk*0 diffraction patterns, from which the structure solution in projection was accomplished. The left diffraction pattern was recorded under "static" conditions and its intensities merged with a second pattern (not shown); the middle pattern was recorded by using the precession technique.[27g,30] Right: Simulation of an SAED pattern of the 0th layer based on the proposed structural model, assuming ideal kinematical scattering of electrons.

The 2D projection of the crystal structure is displayed in Figure 12. The layers comprise infinite chains of "melem-monomers" condensed via N(H) bridges, thereby forming a

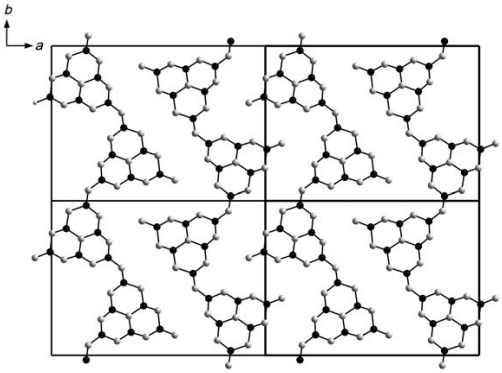

Figure 12. Projection of the structure of melon. Hydrogen atoms and molecular fragments from adjacent strands are omitted for clarity; black: C, gray: N.

closely packed two-dimensional array. The heptazine strands are arranged in a zigzag-type fashion, allowing close N···N contacts of 3.1–3.4 Å between adjacent strands, which are bridged by medium strong hydrogen bonds between the ring-nitrogen atoms and the NH and NH_2 groups, respectively. Covalent interactions within the heptazine backbone and formation of a delocalized π system seem to play a pivotal role in fixing the planar geometry of the strands. Van der Waals-type interactions between the layers are likely to contribute significantly to the overall stabilization of the system; however, they appear to be largely unselective toward a particular kind of stacking sequence.

As the structure is built up from infinite 1D chains instead of 2D atomic arrays it does not represent any structure model postulated for hypothetical g-C_3N_4. In contrast, it corresponds to the "polymer" structure model proposed for melon (**1b**, Scheme 1),[3,4,9b] whose existence has therefore been substantiated. Detailed statements on the structure of the melon strands are now possible, as for instance the zigzag-type arrangement of the heptazine motifs as well as the close packing of the chains leading to a tightly hydrogen-bonded 2D array. Furthermore, the alternative structure model postulated for melon, which is based on a triangular-shaped trimer of melem (**1a**, Scheme 1), can be discarded at least in the present case. However, this does not in principle disavow the existence of this structural isomer of melon.

The structure solution presented above allows the unique determination of the 2D structure of melon, and is in full agreement with the spectroscopic data presented above. However, the stacking disorder of the bulk sample seems to impede a comprehensive 3D approach, as due to the disorder it may not seem straightforward that the projection yields the structure of a single layer. Nevertheless, possible interpretations of the structure projection will be delineated in the following.

As a starting basis, we assume that the 2D projection delineated above is only compatible with some sort of AAA… type stacking. Given the fact that X-ray powder patterns, theoretical calculations (see below), and the expected planarity of heptazine cores and amide/imide moieties[7a–c,8,14] indicate overall planarity of the layers, the maximum symmetry of a 3D structure in the case of eclipsed layers is given by space group *Pbam*. However, theoretical calculations (see below) suggest a lateral displacement of adjacent layers to be far more likely. These displacements become favorable, since π-stacking interactions usually require a slight displacement of adjacent layers to prevent repulsion of the negatively polarized π orbitals.[32] The above requirements can be met by considering layer-offsets in which *p2gg* symmetry is retained in the projections. In other words, it is reasonable to assume monoclinic 3D symmetry, which implies that the layers are laterally shifted along either *a* or *b* with a monoclinic angle $\neq$ 90° and an AAA… type of stacking. When viewed along [001], the associated diffraction patterns are very similar to those obtained for an orthorhombic setting. Therefore, the structure can alternatively be solved in the $P2_1/a$ space group (cell setting $a = 12.4$, $b = 16.7$ Å, β between 92 and 115°, layers shifted along the *a* axis). Note that a layer offset along the *b* axis has the same negligible effect on the structure solution. Apart from slight distortions of the heptazine building blocks for $\beta \neq 90°$, the structure projection of eclipsed layers using orthorhombic and monoclinic variants, respectively, are hardly distinguishable. Other ordered models, such as those with an ABA… layer sequence, are incompatible with the experimental data; however, alternative explanations might be considered.

It seems unlikely that the thickness of the sample corresponds to only a few layers, which would yield 2D scattering and lead to an interpretation of the diffraction pattern in terms of a section through diffuse streaks along c^*. However, in the case of statistically shifted (but not rotated) layers, without any periodicity of the stacking sequence (cf. powder diagram, Figure 3), the *z* component of Patterson vectors is lost, and the *hk*0 section would be likewise representative of interatomic distances only perpendicular to *c*. In other words, a structure determination would yield the structure of a single layer. Diffraction patterns like that shown in Figure 10 (right) might corroborate this situation;[33] however, it is impossible to ascertain the exact zone axis orientation. Therefore, we can conclude that the true situation is to be found between the borderline cases outlined here.

Theoretical calculations: Theoretical calculations were used as an independent verification of the structure model obtained from electron diffraction. To this end, complementary calculations were carried out based on three different computational methods. Both a single chain comprising nine heptazine molecules, as well as an array of six chains containing six heptazine monomers each were optimized by using the PM3 method.[34,35]

Energy minimization reveals that the single zigzag chain as found by ED already possesses a stable molecular arrangement in the gas phase. Its geometry after optimization is outlined in Figure 13 (right). As an alternative, the classically proposed straight melon chain bends upon energy minimization as demonstrated in Figure 13 (left). The tendency

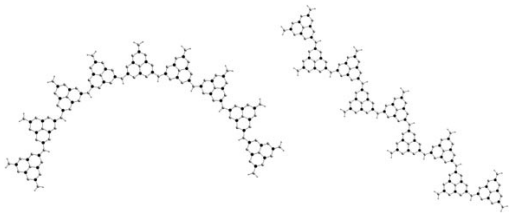

Figure 13. PM3-optimized polymeric models of melon. Left: "Classical" model of an initially linear (starting geometry) melon chain with identical alignment of the heptazine monomers. The linear chain bends upon energy minimization. Right: Zigzag chain of melon as obtained from ED. Gray: N; black: C; gray: H; the positions of the latter are empirically fitted.

of a pair of NH-bridged heptazine rings to bend apart is also visible in the linear zigzag arrangement, whereby the alternating curvatures about every NH bridge compensate, yielding an overall linear array. When assembling six zigzag chains into a 2D arrangement according to the structure proposed by ED, a planar oligomer is obtained upon optimization, which is highly stabilized by a tight hydrogen-bonding network (compare Figure 14).

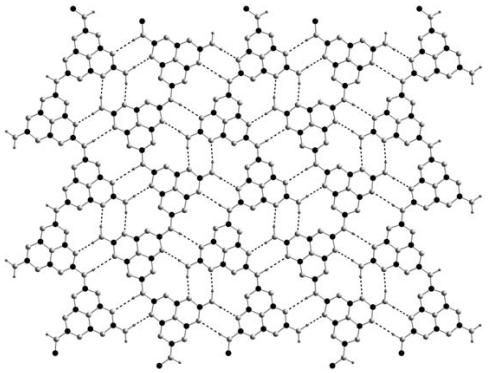

Figure 14. Planar cluster of melon after geometry optimization under periodic boundary conditions using CASTEP. The hydrogen positions are empirically fitted and the hydrogen-bonding network is indicated by black dots. Gray: N; black: C; gray: H.

To calculate the NMR chemical shift parameters for a single layer of melon, the latter was further optimized by using DFT (Figure 14).[36] The periodicity of the PM3-optimized core region of the above planar oligomer allowed the extraction of the *a*/*b* cell parameters and the establishment of a rectangular unit mesh. Although symmetry restrictions were not applied during structure optimization, a planar structure with a rectangular mesh was retained. Whereas the resulting *b* axis matches the value found by calculations at the PM3 level, the *a* axis is slightly elongated as outlined in Table 2. The overestimation of the *a* axis can be rationalized by the poor description of dispersion forces in hydrogen-bonding networks obtained by using DFT. Furthermore, attempts to optimize an orthorhombic unit cell with an interlayer spacing of 3.2 Å does not lead to a minimum on the energy surface. This renders orthorhombic metrics associated with an AAA… stacking extremely unlikely.

Table 2. Experimental and calculated lattice parameters for the structure of melon obtained from ED and different theoretical approaches.

Method	*a* [Å]	*b* [Å]	Interlayer distance [Å]
CASTEP[a]	17.1	12.8	(4.43)[a]
PM3[b]	16.6	12.7	
DREIDING	16.7–16.8	12.8	3.2–3.4
TEM/XRD	16.7[c]	12.4[c]	3.2[d]

[a] Constrained during geometry optimization. [b] Cluster of 36 hepatazine units arranged in six planar zigzag chains. [c] Estimated error ≈5%. [d] X-ray powder diffraction.

An overall description including dispersion interactions between individual layers is possible based on force field methods.[37,38] The *a* and *b* axes are in excellent agreement with the values calculated by using PM3 and CASTEP (Table 2). For an eclipsed layer arrangement, which is considered to be energetically unfavorable in terms of interlayer van der Waals interactions, the repulsive inter-planar forces are maximized, and a layer distance of 3.4 Å is obtained. In contrast, for layer arrangements exhibiting an offset stacking—not complying with orthorhombic metrics—cells with interlayer distances of 3.2 Å were found, as observed in the experiment.

For the DFT-optimized unit mesh, ab initio ^{13}C and ^{15}N NMR chemical shift parameters were calculated. As demonstrated in Figure 4, the calculated ^{13}C and ^{15}N chemical shifts are in good agreement with those in experimental spectra and confirm the overall signal assignments extracted from the CPPI experiment. The ^{13}C chemical shift range is reproduced by the calculations; in the theoretical ^{15}N spectrum, the resonance of the central nitrogen atom is slightly shifted towards higher field; the same tendency is observed for the NH and NH_2 groups. The calculated chemical shifts also allow one to distinguish between tertiary nitrogen atoms bonded to different NH_x groups, since they are directly affected by the surrounding NH (low-field shift) and NH_2 moieties (high-field shift), respectively. These observations match well with the results from the 1D fp-RFDR NMR experiment and confirm the structure model derived from the ED experiments.

Conclusion

The above results shed light on the long-standing debate concerning the identity of Liebig's inert compound "melon", whose structure has now been proven for the first time. The 2D structure of melon reveals the heptazine molecular building blocks and polymeric nature of this important CN_x precursor. Owing to the weak attractive interlayer forces, the "bulk" 3D structure is intrinsically affected by inherent planar defects associated with translations of the layers. Different energetically similar stacking modes with various translational layer offsets are likely to contribute to the

overall 3D structure.[39] This feature adds to the special importance of understanding the 2D arrangement of the molecular building blocks.

Considering the fact that melon is composed of planar layers built up by a carbon(IV) nitride core (heptazine units), this compound may be considered as a "defective g-C_3N_4" material, whose graphite-like topology may in fact result from the presence of network terminations in the form of NH and NH_2 groups. These function as triggers for strain release in such a way that buckling of the sheets is prevented. As has recently been noted,[14b] melon (in that work called g-C_3N_4) may therefore be considered a promising functional material in catalysis or surface science, and at the same time represent a pre-stage of graphitic carbon nitride. Along the same lines, the recently synthesized sp^3-hybridized carbon nitride imide $C_2N_2(NH)$, which represents a formal pre-stage of 3D C_3N_4, can be considered the high-pressure analogue of melon.[40]

However, the existence of melon highlights characteristic differences between graphite and "graphitic" carbon nitride materials, and in doing so, demonstrates that the analogy between the two systems is clearly limited both with respect to chemical and structural aspects. Given the fact that essentially all attempts to prepare g-C_3N_4 from hydrogen-containing precursors yield materials with similar structural features and hydrogen contents, we hypothesize that the products of the frequently claimed syntheses of graphitic carbon nitride have in fact rather been polymers such as melon or related compounds.[7,14,11,9a–c] We can thus add the first direct evidence to the ongoing debate on the structure of the hypothetical g-C_3N_4, that triazine-based models, which are still predominantly being discussed in the literature, should henceforward be assessed very critically. Therefore, the present work may stimulate a careful re-evaluation of commonly accepted paradigms about the existence and structure of graphitic carbon nitride.

Experimental Section

Synthesis of melon: Pyrolyses of melamine were carried out in sealed silica glass ampoules under vacuum at temperatures between 560 and 600 °C, or predominantly under dry argon at temperatures between 620 and 640 °C. Typically, melamine (230 mg, 1.83×10^{-3} mol; $\geq$ 99 %, Fluka) was transferred into a thick-walled silica glass tube ($\varnothing_{ext.}$ 15 mm, $\varnothing_{int.}$ 11 mm), from which water had been removed by thorough heating and evacuation. The tube was sealed by using a hydrogen burner at a length of about 120 mm. The ampoule was then placed in a vertical tube furnace and heated (1 K min^{-1}) to 630 °C, at which temperature the sample was held for 12 to 36 h. The cooling rates did not notably affect the crystallinity of the products, so that the furnace was typically switched off and the sample was allowed to cool down to room temperature over several hours. The sample was then isolated by carefully breaking the ampoule, upon which a significant amount of HCN and ammonia was released. The yield of brownish residue typically amounted to 38–57 %; approximately 8–10 % were recovered from the top of the ampoule in the form of a brown sublimate mixed together with long, needle-shaped melamine crystals. To purify the residue and eliminate melamine and—present to only a small extent—melem crystals, the product ($\approx$80–100 mg) was transferred into a Duran ampoule (pre-dried in vacuo under heating), which was sealed off under an atmosphere of argon and heated to temperatures around 600 °C (1 K min^{-1}) for at least 12 h. Alternatively, admixtures of the starting material melamine were removed by sublimation using a cold finger integrated into a glass tube. Upon purification, the brownish material lightened up, thereby changing its color into reddish-brown.

^{15}N-enriched melamine was prepared according to the procedure introduced by Jürgens et al.[13,24] Sodium tricyanomelaminate $Na_3[C_6N_9]$ was prepared by heating sodium dicyanamide $Na[N(CN)_2]$ (2 g; $\geq$96 %, Fluka) to 500 °C (5 K min^{-1}) in a quartz tube under pressure equalization and subsequently reacting the as-obtained material (742.5 mg, 2.78 10^{-3} mol) with $^{15}NH_4Cl$ (183 mg, 3.36×10^{-3} mol, $\geq$98 %, Cambridge Isotopes) in a Duran tube (length: 160 mm, $\varnothing_{ext.}$: 26 mm, $\varnothing_{int.}$: 24 mm) at 470 °C (1 K min^{-1}) for 12 h.[13,24] The raw material was further purified by sublimation (1 Pa, 220 °C).

General techniques: Elemental analyses were performed by using a commercial C, H, N elemental analyzer system Vario EL (Elementar Analysensysteme GmbH).

XRD measurements were performed on a Stoe-Stadi P diffractometer. High-temperature in situ X-ray diffraction was carried out on a STOE Stadi P powder diffractometer (Ge(111)-monochromated $Mo_{K\alpha1}$ radiation, λ = 70.093 pm) with an integrated furnace using unsealed quartz capillaries ($\varnothing$ 0.5 mm) as sample containers.

FTIR measurements were carried out on a Bruker IFS 66v/S spectrometer. Spectra of the samples were recorded by utilizing KBr pellets (1 mg sample, 500 mg KBr, hand press with press capacity 10 kN) in an evacuated cell equipped with a DLATGS detector at ambient conditions between 400 and 4000 cm^{-1}.

Scanning electron microscopy was performed on a JEOL JSM-6500F equipped with a field emission gun at an acceleration voltage of 10 kV. Samples were prepared by putting the powder specimen on adhesive conductive pads and subsequently coating them with a thin conductive carbon film.

Solid-state NMR spectroscopy: ^{13}C and ^{15}N CP-MAS solid-state NMR spectra were recorded at ambient temperature on the conventional impulse spectrometers DSX Avance 500 (Bruker) and DSX Avance 400 (Bruker) operating at a proton resonance frequency of 500 MHz and 400 MHz, respectively. The samples were contained in 4-mm ZrO_2 rotors, which were mounted in standard double-resonance MAS probes (Bruker). The ^{13}C and ^{15}N signals were referenced with respect to TMS and nitromethane, respectively. Data collection of all experiments was performed applying broadband proton decoupling using a TPPM sequence.[41] For the CP MAS spectra of both nuclei a ramped cross-polarization sequence was employed where the ^{1}H pulse amplitude was decreased linearly by 50 %. Contact times between 10 ms and 20 ms were used and the recycle delay was chosen to allow a nearly complete magnetization recovery optimized via ^{1}H spin-lattice relaxation experiments. The spinning frequencies ν_{rot} varied between 7 and 12 kHz. To determine the number of covalently bonded protons to the nitrogen atoms, a ^{15}N CPPI[25] (cross-polarization combined with polarization inversion) experiment was performed (ν_{rot} = 6 kHz). The polarization inversion behavior was probed by varying the inversion time from 0.2 to 800 μs (28 spectra), with an initial contact time of 2 ms. ^{15}N direct excitation spectra were acquired with three back-to-back 90° pulses to eliminate unwanted contributions from the probe and ringing effects.[42] The nutation frequency and the recycle delay were adjusted to 75 kHz and 28800 s (= 8 h) (estimated from a ^{15}N T_1 measurement) to ensure a total recovery of the magnetization. A total amount of 16 scans was collected and the spinning frequency was set to 9 kHz. To probe homonuclear ^{15}N connectivities and distances, selective excitation fp-RFDR experiments were performed by using a XY-16 phase cycle.[42] For the fp-RFDR mixing block active rotor synchronization was applied with ν_{rot} = 15 kHz. The length of the soft 180° pulse in the middle of each rotor period was adjusted according to $p(180°) = 0.3\cdot1/\nu_{rot}$ corresponding to a nutation frequency of 25 kHz. To ensure a selective excitation of the ^{15}N resonance of the NH_2 groups a CP sequence with a short CP contact time (90 μs) was followed by a comb of two 90° pulses (3.4 μs) on-resonant on the NH_2-signal with an interpulse spacing τ between 280 μs and 340 μs corresponding to τ =

$^1/_4(\nu(NH)-\nu(NH_2))^{-1}$. The short contact time excites only NH and NH_2 resonances significantly. Afterwards the comb of 90° pulses allows one to dephase the magnetization of the off-resonant resonance while preserving the magnetization of the on-resonant one.

Electron diffraction/transmission electron microscopy: ED and TEM measurements were carried out on a JEOL 2011 instrument equipped with a tungsten cathode operating at 200 kV. The images were recorded using a TVIPS CCD camera (F114). The sample was finely dispersed by sonication in ethyl alcohol suspension for 30 minutes, and a small amount of the suspension was subsequently dispersed on a copper grid coated with holey carbon film. The grids were mounted on a single tilt holder with a maximum tilt angle of 30° and subsequently transferred to the microscope. Suitable crystallites were singled out among those yielding diffraction patterns of main poles, typically with the zone axis [001] aligned along the electron beam. The selected-area aperture was adapted in each case to the size of the selected thin crystalline domains. Precession experiments were conducted by using a FEI Tecnai 12 transmission electron microscope with a LaB_6 cathode, operating at 120 kV and equipped with a Spinning Star precession interface (NanoMEGAS). A precession angle of approximately 1.5° was applied. The images were recorded on a TVIPS 2k CCD camera (F224HD) with a dynamic range exceeding 25000:1. Reflection intensities were extracted by using the ELD program package;[44] for simulation of the kinematical diffraction patterns the program JSV1.08 Lite[45] was employed. Calculation of the electron diffraction patterns was done using the programs VEC[46] and JEMS.[47] In principle, it is possible to solve a structure provided the strong reflections remain sufficiently strong to find phase relationships using direct methods.[28a] To quantify all strong *hk*0 reflections, intensities of two *hk*0 diffraction patterns were merged, yielding a dataset of 208 independent reflections. Evaluation of the observed absences in the base plane (*h*0: $h=2n+1$; 0*k*: $k=2n+1$) indicates the presence of the plane group *p*2*gg*. Owing to the lack of detailed three-dimensional information, the structure was solved by using the space groups $P2_12_12$ or *Pbam*, which correspond to the plane group *p*2*gg* in (001) projection. The most probable solution as found by SIR-97[29a] had a figure of merit of 20.06%.[29b] The heptazine molecular unit was obtained without prior fixation of parameters. Refinement of the ED data for calculation of Fourier maps was done with the program SHELX-97,[48] using the electron form factors as given by Doyle and Turner.[49]

Calculations: In the cluster approach the semiempirical PM3 method[34] was used for structure optimization with the Gaussian03 program package.[35] The input structures were created from the ED structure solution with hydrogen added to the NH and NH_2 groups. DFT calculations under periodic boundary conditions were performed with the MS Modelling 4.0 package by Accelrys. The input cell was created in orthorhombic symmetry from a cutout in the core region of the PM3-optimized structure. For the CASTEP[36] calculations the PBE functional and ultrasoft pseudopotentials were taken with sampling over 6 k-points. In the structure optimization of the input cell an energy cutoff of 280 eV was used. To ensure that the dispersion interaction between neighboring layers become negligible, a constrained slab of 4.43 Å along the *c* axis was introduced. NMR parameters were calculated with a cutoff of 350 eV for the optimized cell. For a core cutout of the PM3-optimized cluster the Hirschfeld charges were determined with the $DMol^3$ program, the PBE functional and the DNP basis set.[38] These partial charges were used in flexible body structure optimizations of the input cell with the Dreiding force field.[37] By default, 1,4-intramolecular electrostatic interactions were excluded from the energy evaluation.

Acknowledgements

We gratefully acknowledge financial support that was granted from the Deutsche Forschungsgemeinschaft (DFG) (projects SCHN 377/12–1 and SE 1417/2–1), Fonds der Chemischen Industrie (FCI), the BMBF, and the Studienstiftung des Deutschen Volkes (scholarships for B. V. Lotsch). We gratefully acknowledge NanoMEGAS and TVIPS for providing us with their equipment and for experimental support to obtain the precession pattern, especially I. Daberkow and J. Portillo. We also thank Prof. E. Rössler (University of Bayreuth) for making available his NMR equipment, and Mrs. C. Buhtz for her support with the data analysis.

[1] a) M. L. Cohen, *Phys. Rev. B* **1985**, *32*, 7988; b) A. Y. Liu, M. L. Cohen, *Science* **1989**, *245*, 841; c) C.-M. Sung, M. Sung, *Mater. Chem. Phys.* **1996**, *43*, 1; d) D. M. Teter, R. J. Hemley, *Science* **1996**, *271*, 53.
[2] J. Liebig, *Ann. Pharm.* **1834**, *10*, 10.
[3] E. C. Franklin, *J. Am. Chem. Soc.* **1922**, *44*, 486.
[4] a) C. E. Redemann, H. J. Lucas, *J. Am. Chem. Soc.* **1940**, *62*, 842; b) L. Pauling, J. H. Sturdivant, *Proc. Natl. Acad. Sci. USA* **1937**, *23*, 615.
[5] B. Bann, S. A. Miller, *Chem. Rev.* **1958**, *58*, 131.
[6] a) L. Costa, G. Camino, G. Martinasso, *Polym. Prepr. Am. Chem. Soc. Div. Polym. Chem.* **1989**, *30*, 531; b) H. May, *J. Appl. Chem.* **1959**, *9*, 340.
[7] a) I. Alves, G. Demazeau, B. Tanguy, F. Weill, *Solid State Commun.* **1999**, *109*, 697; b) Kawaguchi, K. Nozaki, *Chem. Mater.* **1995**, *7*, 257; c) E. G. Gillan, *Chem. Mater.* **2000**, *12*, 3906; d) Q. Guo, Y. Xie, X. Wang, S. Lv, T. Hou, X. Liu, *Chem. Phys. Lett.* **2003**, *380*, 84; e) J. L. Zimmermann, R. Williams, N. Khabashesku, J. L. Margrave, *Nano Lett.* **2001**, *1*, 731; f) M. Todd, J. Kouvetakis, T. L. Groy, D. Chandrasekhar, D. J. Smith, P. W. Deal, *Chem. Mater.* **1995**, *7*, 1422; g) H. Montigaud, B. Tanguy, G. Demazeau, I. Alves, S. Courjault, *J. Mater. Sci.* **2000**, *35*, 2547; h) V. N. Khabashesku, J. L. Zimmerman, J. L. Margrave, *Chem. Mater.* **2000**, *12*, 3264; i) J. Kouvetakis, A. Bandari, M. Todd, B. Wilkens, *Chem. Mater.* **1994**, *6*, 811; j) D. R. Miller, D. C. Swenson, E. G. Gillan, *J. Am. Chem. Soc.* **2004**, *126*, 5372; k) D. R. Miller, J. Wang, E. G. Gillan, *J. Mater. Chem.* **2002**, *12*, 2463; l) S. Courjault, B. Tanguy, G. Demazeau, *C. R. Acad. Sci. Ser. IIc: Chim.* **1999**, *2*, 487; m) Z. H. Zhang, K. Leinenweber, M. Bauer, L. A. J. Garvie, P. F. McMillan, G. H. Wolf, *J. Am. Chem. Soc.* **2001**, *123*, 7788; n) Q. Guo, Y. Xie, X. J. Wang, S. Zhang, T. Hou, S. Lv, *Chem. Commun.* **2004**, *1*, 26; o) H. Montigaud, B. Tanguy, G. Demazeau, I. Alves, M. Birot, J. Dunogues, *Diamond Relat. Mater.* **1999**, *8*, 1707.
[8] a) E. Kroke, M. Schwarz, *Coord. Chem. Rev.* **2004**, *248*, 493; b) S. Muhl, J. M. Mendez, *Diamond Relat. Mater.* **1999**, *8*, 1809; c) T. Malkow, *Mater. Sci. Eng. A* **2001**, *302*, 311; d) M. C. dos Santos, F. Alvarez, *Phys. Rev. B* **1998**, *58*, 13918.
[9] a) T. Komatsu, *J. Mater. Chem.* **2001**, *11*, 799; b) T. Komatsu, *J. Mater. Chem.* **2001**, *11*, 802; c) T. Komatsu, T. Nakamura, *J. Mater. Chem.* **2001**, *11*, 474; d) T. Komatsu, *Macromol. Chem. Phys.* **2001**, *202*, 19.
[10] D. T. Vodak, K. Kim, L. Iordanidis, P. G. Rasmussen, A. J. Matzger, O. M. Yaghi, *Chem. Eur. J.* **2003**, *9*, 4197.
[11] G. Demazeau, *J. Mater. Chem.* **1999**, *9*, 15.
[12] E. Kroke, M. Schwarz, E. Horath-Bordon, P. Kroll, B. Noll, A. D. Norman, *New J. Chem.* **2002**, *26*, 508.
[13] B. Jürgens, E. Irran, J. Senker, P. Kroll, H. Müller, W. Schnick, *J. Am. Chem. Soc.* **2003**, *125*, 10288.
[14] a) M. Groenewolt, M. Antonietti, *Adv. Mater.* **2005**, *17*, 1789; b) F. Goettmann, A. Fischer, M. Antonietti, A. Thomas, *Angew. Chem.* **2006**, *118*, 4579; *Angew. Chem. Int. Ed.* **2006**, *45*, 4467.
[15] a) B. V. Lotsch, W. Schnick, *Chem. Mater.* **2005**, *17*, 3976; b) B. V. Lotsch, W. Schnick, *Chem. Mater.* **2006**, *18*, 1891.
[16] a) R. S. Hosmane, M. A. Rossman, N. J. Leonard, *J. Am. Chem. Soc.* **1982**, *104*, 5497; b) A. M. Halpern, M. A. Rossman, R. S. Hosmane, N. J. Leonard, *J. Phys. Chem.* **1984**, *88*, 4324; c) M. Shahbaz, S. Urano, P. R. LeBreton, M. A. Rossman, R. S. Hosmane, N. J. Leonard, *J. Am. Chem. Soc.* **1984**, *106*, 2805.
[17] D. D. Cubicciotti, W. M. Latimer, *J. Am. Chem. Soc.* **1948**, *70*, 3509.
[18] C. Grundmann, A. Kreutzberger, *J. Am. Chem. Soc.* **1955**, *77*, 6559.
[19] a) A. I. Finkel'shtein, N. V. Spiridova, *Russ. Chem. Rev.* **1964**, *33*, 400; b) A. I. Finkel'shtein, *Opt. i Spektr.* **1959**, *6*, 17.
[20] a) M. K. Marchewka, *Bull. Korean Chem. Soc.* **2004**, *25*, 466; b) M. K. Marchewka, *J. Chem. Res. Synop.* **2003**, 518; c) P. J. Larkin,

M. P. Makowski, N. B. Colthoup, *Spectrochim. Acta* **1999**, *55*, 1011; d) W. Jeremy-Jones, W. J. Orville-Thomas, *Trans. Faraday Soc.* **1959**, *55*, 193; e) E. N. Boitsov, A. I. Finkel'shtein, *Russ. Chem. Rev.* **1962**, *31*, 712.
[21] a) M. Takimoto, *Kogyo Kagaku Zasshi* **1961**, *64*, 1452; b) M. Takimoto, *Kogyo Kagaku Zasshi* **1964**, *85*, 168.
[22] B. V. Lotsch, W. Schnick, *Chem. Eur. J.* DOI: 10.1002/chem.200601291.
[23] V. V. Khorosheva, A. I. Finkel'shtein, *Zh. Fiz. Khim.* **1962**, *36*, 1055.
[24] B. Jürgens, Ph. D. thesis, University of Munich (Germany), Shaker, Aachen, **2004**.
[25] C. Gervais, F. Babonneau, J. Maquet, C. Bonhomme, D. Massiot, E. Framery, M. Vaultier, *Magn. Reson. Chem.* **1998**, *36*, 407.
[26] a) A. Sattler, Diploma thesis, University of Munich (Germany), **2005**; b) A. Sattler, L. Seyfarth, J. Senker, W. Schnick, *Z. Anorg. Allg. Chem.* **2005**, *631*, 2545.
[27] J. Sehnert, K. Bärwinkel, J. Senker, *J. Phys. Chem. B*, **2007**, submitted.
[28] a) T. E. Weirich, X. Zou, R. Ramlau, A. Simon, G. L. Cascarano, C. Giacovazzo, S. Hovmöller, *Acta Crystallogr. Sect. A* **2000**, *56*, 29; b) T. E. Weirich, R. Ramlau, A. Simon, S. Hovmöller, X. Zou, *Nature* **1996**, *382*, 144; c) U. Kolb, G. N. Matveeva, *Z. Kristallogr.* **2003**, *218*, 259; d) T. E. Weirich, J. Portillo, G. Cox, H. Hibst, S. Nicolopoulos, *Ultramicroscopy* **2006**, *106*, 164; e) D. L. Dorset, C. J. Gilmore, *Acta Crystallogr. Sect. A* **2000**, *56*, 62; f) D. L. Dorset, *Z. Kristallogr.* **2003**, *218*, 458; g) R. Vincent, P. A. Midgeley, *Ultramicroscopy* **1994**, *53*, 271.
[29] a) A. Altomare, M. C. Burla, M. Camalli, G. L. Cascarano, C. Giacovazzo, A. Guagliardi, A. G. G. Moliterni, G. Polidori, R. Spagna, *J. Appl. Crystallogr.* **1999**, *32*, 115; b) A. Altomare, G. L. Cascarano, C. Giacovazzo, A. Guagliardi, *J. Appl. Crystallogr.* **1993**, *26*, 343.
[30] M. S. Weiss, *J. Appl. Crystallogr.* **2001**, *34*, 130.
[31] The structure solution was verified by using precession intensity data. Owing to their robustness with respect to sample misalignment and less pronounced dynamical effects, the data quality obtained under otherwise identical experimental conditions can be improved. Accordingly, R_{rim} is 20% and the straightforward structure solution has a figure of merit of 19.5%. The structure refinement (184 independent reflections, no. of reflections/parameter ≈ 6, $d_{min.}$ 0.78 Å) was less successful due to the large sample thickness, which gives rise to stronger dynamical effects (cf. Figure 11, middle).
[32] a) C. Janiak, *J. Chem. Soc. Dalton Trans.* **2000**, 3885; b) C. A. Hunter, J. M. Sanders, *J. Am. Chem. Soc.* **1990**, *112*, 5525.
[33] a) J. M. Cowley, *Acta Crystallogr.* **1961**, *14*, 920; b) J. M. Cowley, A. Goswami, *Acta Crystallogr.* **1961**, *14*, 1071.
[34] J. J. P. Stewart, *J. Comput. Chem.* **1989**, *10*, 221.
[35] Gaussian 03, Revision C.02, M. J. Frisch, G. W. Trucks, H. B. Schlegel, G. E. Scuseria, M. A. Robb, J. R. Cheeseman, J. A. Montgomery, Jr., T. Vreven, K. N. Kudin, J. C. Burant, J. M. Millam, S. S. Iyengar, J. Tomasi, V. Barone, B. Mennucci, M. Cossi, G. Scalmani, N. Rega, G. A. Petersson, H. Nakatsuji, M. Hada, M. Ehara, K. Toyota, R. Fukuda, J. Hasegawa, M. Ishida, T. Nakajima, Y. Honda, O. Kitao, H. Nakai, M. Klene, X. Li, J. E. Knox, H. P. Hratchian, J. B. Cross, V. Bakken, C. Adamo, J. Jaramillo, R. Gomperts, R. E. Stratmann, O. Yazyev, A. J. Austin, R. Cammi, C. Pomelli, J. W. Ochterski, P. Y. Ayala, K. Morokuma, G. A. Voth, P. Salvador, J. J. Dannenberg, V. G. Zakrzewski, S. Dapprich, A. D. Daniels, M. C. Strain, O. Farkas, D. K. Malick, A. D. Rabuck, K. Raghavachari, J. B. Foresman, J. V. Ortiz, Q. Cui, A. G. Baboul, S. Clifford, J. Cioslowski, B. B. Stefanov, G. Liu, A. Liashenko, P. Piskorz, I. Komaromi, R. L. Martin, D. J. Fox, T. Keith, M. A. Al-Laham, C. Y. Peng, A. Nanayakkara, M. Challacombe, P. M. W. Gill, B. Johnson, W. Chen, M. W. Wong, C. Gonzalez, and J. A. Pople, Gaussian, Inc., Wallingford CT, **2004**.
[36] M. D. Segall, P. J. D. Lindan, M. J. Probert, C. J. Pickard, P. J. Hasnip, S. J. Clark, M. C. Payne, *J. Phys. Condens. Matter* **2002**, *14*, 2717.
[37] S. L. Mayo, B. D. Olafson, W. A. Goddard III, *J. Phys. Chem.***1990**, *94*, 8897.
[38] a) B. Delley, *J. Chem. Phys.* **1990**, *92*, 508; b) B. Delley, *J. Chem. Phys.* **2000**, *113*, 7756.
[39] J. E. Lowther, *Phys. Rev. B*, **1999**, *59*, 11683.
[40] E. Horvath-Bordon, R. Riedel, P. F. McMillan, P. Kroll, G. Miehe, P. A. van Aken, A. Zerr, P. Hoppe, O. Shebanova , I. McLaren, S. Lauterbach, E. Kroke, R. Boehler, *Angew. Chem.* **2007**, *119*, 1498; *Angew. Chem. Int. Ed.* **2007**, *46*, 1476 .
[41] A. E. Bennett, C. Rienstra, M. Auger, K. V. Lakshmi, R. G. Griffin, *J. Chem. Phys.* **1995**, *103*, 6951.
[42] S. Zhang , X. Wu , M. Mehring, *Chem. Phys. Lett.* **1990**, *173*, 481.
[43] Y. Ishii, *J. Chem. Phys.* **2001**, *114*, 8473.
[44] a) X. D. Zou, Y. Sukharev, S. Hovmöller, *Ultramicroscopy* **1993**, *49*, 147; b) X. D. Zou, Y. Sukharev, S. Hovmöller, *Ultramicroscopy* **1993**, *52*, 436.
[45] S. Weber, *Java Structure Viewer*, v1.08, 1999.
[46] Z. H. Wan, Y. D. Liu, Z. Q. Fu, Y. Li, T. Z. Cheng, F. H. Li, H. F. Fan, *Z. Kristallogr.* **2003**, *218*, 308.
[47] P. A. Stadelmann, *Ultramicroscopy* **1987**, *21*, 129.
[48] G. M. Sheldrick, SHELX-97, Programs for the solution and the refinement of crystal structures, University of Göttingen, Göttingen (Germany), **1997**.
[49] P. A. Doyle, P. S. Turner, *Acta Crystallogr. A* **1968**, *24*, 390.

Received: December 7, 2006
Published online: April 5, 2007

A.6:

The Ab-Initio Calculation of Solid-State NMR Spectra for Different Triazine and Heptazine Based Structure Proposals of g-C_3N_4

J. Sehnert, K. Bärwinkel and J. Senker

Journal of Physical Chemistry B

J. Phys. Chem. B 2007, 111, 10671-10680
DOI: 10.1021/jp072001k

Different structure proposals for triazine and heptazine based fully condensed as well as melon based C_3N_4 layers were developed within this work. For all presented proposals the theoretical NMR spectrum was calculated.

My personal contributions to this work included the following:

- systematic increase and development of triazine and heptazine based structure models with the semiempirical PM3 method
- the analysis of the energy difference between planar and corrugated systems of these structure models
- the extraction of proposals of periodic cells from the cluster calculations
- the development of a strategy for the calculation of NMR data of these extended model systems
- the calculation of the ^{13}C and ^{15}N chemical shift tensors with DFT methods
- the MATLAB script based extraction and analysis of the calculated NMR data
- discussion on the presented topic
- main authorship of the article

The contributions of all other authors comprised of:

- support in the development of the self-written MATLAB scripts
- discussion on the presented topic
- co-authorship of the article

Ab Initio Calculation of Solid-State NMR Spectra for Different Triazine and Heptazine Based Structure Proposals of g-C_3N_4

Jan Sehnert, Kilian Baerwinkel, and Juergen Senker*

Universitaet Bayreuth, D-95440 Bayreuth, Germany

Received: March 12, 2007

We present a comprehensive theoretical study of the structure and NMR parameters of a large number of triazine and heptazine based structure proposals for g-C_3N_4 in different condensation states. This approach includes a detailed investigation of cyclic melon which tends toward the formation of densely packed hydrogen bonded meshes. In all of the investigated systems, we found planar layers to represent saddlepoints on the energy surface, whereas corrugated species were identified as minima. The corrugation source was linked to the repulsion of nitrogen lone pairs in close NN contacts. A linear dependency of the corrugation energy from the number of NN interactions in the investigated clusters was found. Heptazine based systems gain about twice as much energy per NN close contact in comparison to triazine structures which could be understood in terms of the distortion mechanism in the investigated structures. Furthermore, a full study of the ^{15}N and ^{13}C chemical shift tensors was performed for the different C/N layers. The description of the NMR parameters required dividing the investigated systems into subclusters for which the NMR tensors were calculated with density functional theory (DFT) methods. A statistical analysis of these entities allowed for the investigation of the change in the chemical shift upon corrugation and, in the case of the cyclic melon system, hydrogen bonding. With the here presented study, the most prominent structure models for g-C_3N_4 are characterized in terms of the ^{15}N and ^{13}C NMR parameters which now can directly be compared to experimental spectra.

1. Introduction

An important and prevailing topic in solid-state chemistry is the search for ultrahard materials.[1−4] In this context, the sp^3-hybridized species of carbon nitride (C_3N_4) attracted much attention, since theoretical work indicated that such a material could be even harder than diamond.[1,4−7] Within this analogy, graphitical sp^2-hybridized g-C_3N_4 is discussed as a precursor for the bulk synthesis of ultrahard carbon nitride with high pressure methods.[1,8] However, the synthesis and characterization of g-C_3N_4 is a challenging task by itself and up to today a large number of different experimental attempts have been made. A detailed description of these approaches can be found in the literature.[1,9,10] Due to the lack of experimental data, there is a prevailing discussion about possible structure models for g-C_3N_4.

The first structure proposals for g-C_3N_4 were directly derived from a nitrogen substituted graphene sheet and are therefore built up from triazine moieties.[1,8,9,11−31] Structural differences occur in different stacking orders of the respective planar meshes. To match experimental results which indicated an orthorhombic unit cell, additionally an orthorhombic variant of a triazine mesh was introduced.[1,9,18,19,22,26,29] Finally, the idea of heptazine based g-C_3N_4 was brought into the discussion.[9,10,26,32−35] Such structures are promising, since in theoretical calculations they turned out to be energetically favored over their triazine counterparts.[26]

Melamine, melem, and melon as well as their derivatives are therefore important precursors and intermediates in the synthesis of g-C_3N_4.[9,29,32−34] Most recent work shows that indeed the pyrolysis of melamine yields a melon polymer built up from melem units.[10] Due to the poor crystallinity of the samples, the identification of promising candidates for g-C_3N_4 often proves difficult. NMR techniques have successfully been applied in the characterization of C/N compounds and therefore exhibit a strong potential to comply with the requirement for a structural probe.[9,10,12,24,34−38] Furthermore, the comparison of NMR spectra with results of theoretical calculations allows for a straightforward validation of different structure models.[10] Unfortunately, up to now, calculated NMR data are reported only once in the literature—for a triazine based variant of g-C_3N_4.[16]

Although many theoretical articles concerning C_3N_4 exist, most of them focus on triazine based structures.[11,13−17,19−21,25,27−31] Only a few theoretical studies on heptazine based structures are reported.[10,26] An interesting point in the overall discussion is the corrugation of condensed C_xN_y structures due to the repulsion of nitrogen atoms in close contact.[1,15,25,29,39−41] In contrast to the corrugation of graphene sheets which is known to occur on a microscopic range, the here investigated interactions are expected to cause the buckling of layers on much shorter distances.[42] In the early studies of g-C_3N_4, corrugation has been missed due to the use of density functional theory (DFT) with periodic boundary conditions and the therewith accompanied restriction of cell sizes and the high symmetry of the model systems. More recent results of DFT calculations in *P*1 as well as cluster calculations with force field methods show that substantial deviation from the idealized planar geometry is to be expected in triazine based g-C_3N_4.[25,29] These results imply that a substantial influence on the structure of g-C_3N_4 originates in strong interactions within the layers. The three-dimensional stacking of the single sheets in the solid state is directed by weak van der Waals interactions and therefore can be expected to have less influence on the overall structure.

* To whom correspondence should be addressed. E-mail: juergen.senker@uni-bayreuth.de.

10.1021/jp072001k CCC: $37.00
Published on Web 08/22/2007

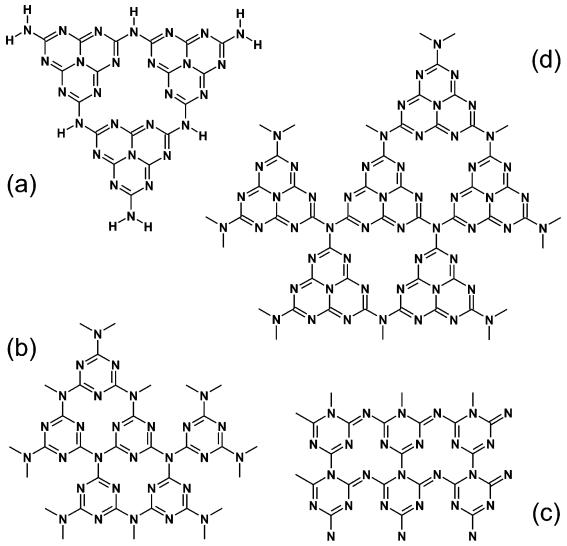

Figure 1. Prominent structure models:[1,10] (a) cyclic melon; (b) classical melamine based sheet; (c) orthorhombic melamine based sheet; (d) classical melem based sheet.

Up to today, no comprehensive theoretical study of the interactions in g-C_3N_4 layers exists. With the here presented work, we intend to close this gap for the most prominent proposals for C/N layers. These include a cyclic melon intermediate differing from the experimentally found polymer[10] as well as melamine and melem based model structures for g-C_3N_4 (see Figure 1). For all of these structures, planar and corrugated variants are calculated and their energies are compared. Furthermore, for comparison with experimental data, we report an analysis of the ^{13}C and ^{15}N NMR parameters in these systems, including the chemical shift as well as the full anisotropic information.

2. Experimental Details

All calculations were carried out using the Gaussian 03 program package.[43] The structures were optimized with the semiempirical PM3 method which was found to qualitatively yield the same results as DFT for C/N systems.[41] This proposition could be affirmed by a comparison of small corrugated PM3 optimized clusters with the respective B3LYP/6-31G(d) structures. With PM3, the bonds are found to be up to 5% longer compared to DFT, and angles differ by a maximum of 4%. Together with only small deviations in the dihedral angles, this leads to an acceptable match for both melamine and melem structures. Due to the bigger size of the melem moiety, the deviations in the absolute atomic coordinates were found to be larger in the melem system compared to the one for the melamine model.

As already mentioned above, the main influence on the structure as well as on the NMR parameters is expected to originate from the electronic influence within the layers. For this reason, we restricted our analysis to clusters describing cutouts of such layers which systematically vary in both the system size and the linkage type between the single building blocks (see Figure 2, I and II). The influence of stacking on the structure and its effect on the NMR observable is therefore not described within this approach. However, as was shown before, the calculation of a single C/N layer yields a good description of the structure and the NMR parameters in these systems.[10] A great advantage of the method is that a large variety of clusters could be investigated in a reasonable time frame. Furthermore, during the optimization, the corrugation of our model systems was not constricted by symmetry.

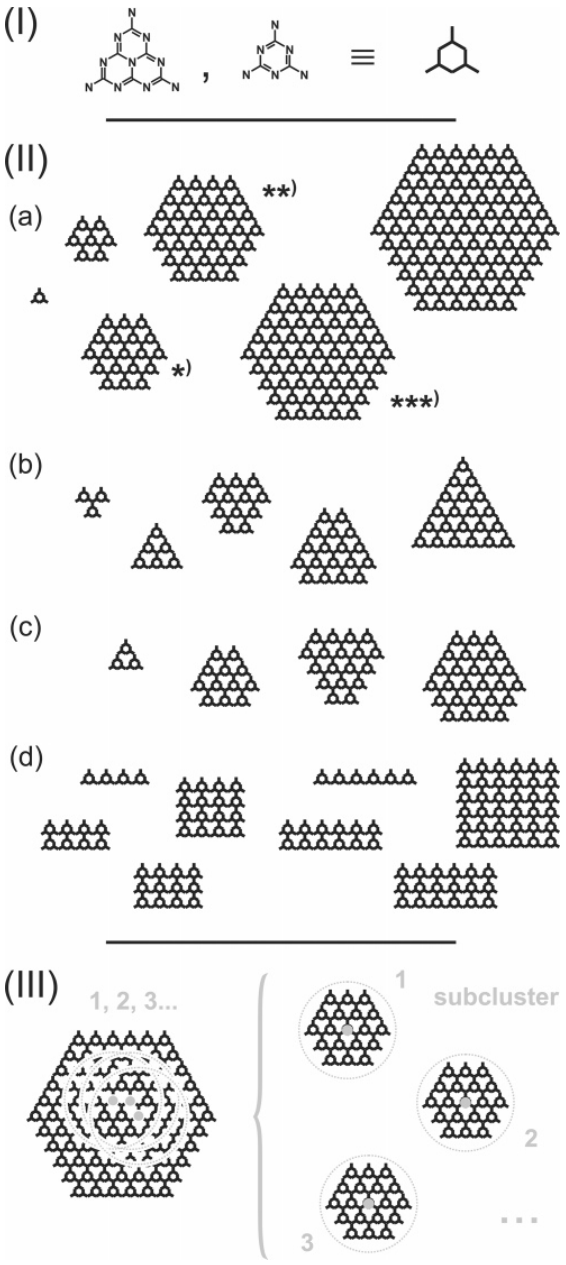

Figure 2. (I) Representation of melem and melamine building blocks in g-C_3N_4 clusters. (II) Different assembly and sizes of g-C_3N_4 clusters using melem (a−c) and melamine (a−d) moieties. (III) Systematic evaluation of NMR parameters using local cutouts as a basis for subclusters.

System sizes up to 910 atoms were evaluated starting from different cluster cores (see smallest units in Figure 2, II(a−c)). For each core, the coordination sphere was systematically increased. The maximum system size corresponds to five coordination spheres for melamine based structures and four coordination spheres for melem based structures with respect

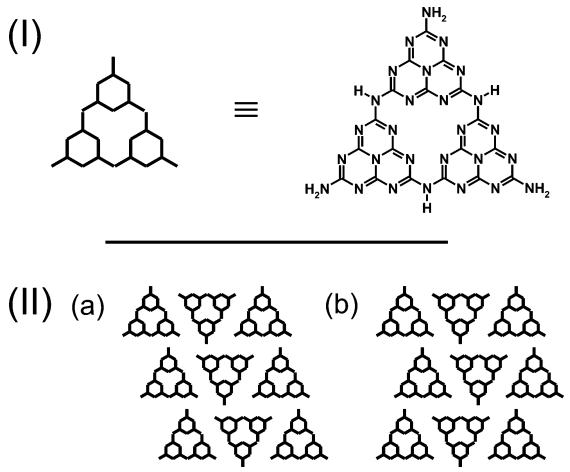

Figure 3. (I) Representation of a cyclic melon building block. (II) Different sequences in a mesh of cyclic melon: (a) ABC...; (b) ABA...

to the central building unit (compare to the two biggest systems in Figure 2, II(a)). The main difference of the depicted clusters is their different ratios between moieties on the cluster edge and building blocks in the cluster core. Furthermore, the structure of the cluster edges varies. Through this, the influence of the edge on the overall structure of the clusters could systematically be investigated. In the case of an orthorhombic linkage of melamine units, the clusters were built starting from single chains of different sizes (see part II(d) in Figure 2). The biggest cluster investigated contained 13 by 13 melamine units (not shown in Figure 2).

Finally, the melon based g-C_3N_4 structure proposals were calculated starting from an isolated cyclic melon unit in the gas phase (see part I in Figure 3). This structure proposal differs from the recently found melon network which is built up from melon polymer chains.[10] The highly functionalized molecule of cyclic melon anticipates a tight hydrogen bond network, as found in the structures of melem and layers of the melon polymer chains.[10,34] Two structural approaches to a modeling of the melon environment were tried which vary in the sequence between hydrogen bonded melon bands (see parts II(a) and (b) in Figure 3).

For all types of clusters, planar as well as corrugated structures were calculated and a subsequent analysis of the vibrational frequencies was performed. The number of NN close contacts was extracted using a self-written MATLAB script.[44] The energy difference between the distorted and planar structures was then analyzed with respect to the number of NN close contacts in the respective cluster.

The planar and corrugated PM3 models shown in Figure 2, II(a), and Figure 3 were further used for the computation of the NMR chemical shift tensor on the PBE1PBE/6-31G(d) and PBE1PBE/6-31G(d,p) level of theory, respectively. The full NMR chemical shift tensor was reduced and transformed into its principal axis system, as described in the literature.[45] The principle values were sorted according to $\sigma_{11} \leq \sigma_{22} \leq \sigma_{33}$ and the anisotropy analyzed in terms of the span, Ω, and skew, κ, of the tensor, as can be found in the literature as well.[46] Using the reported definitions, these values can easily be transformed into the classical descriptions of the NMR tensor, either via the anisotropy, Δ, or the reduced anisotropy, δ, and the asymmetry, η. The isotropic shift, δ_{iso}, is given in ppm relative to tetramethylsilane for C atoms and nitromethane for N atoms, both calculated at the PM3//PBE1PBE/6-31G(d) and PM3//PBE1PBE/6-31G(d,p) levels of theory.

For a description of NMR values in the condensed phases, it was important to investigate the influence of the hydrogen saturation of the cluster edge on the respective local sites in the layers. For that reason, we systematically increased the coordination sphere around a central building block and checked for convergence of the isotropic chemical shift, δ_{iso}, the span, Ω, and the skew, κ (see Figure 2, II(a)). The convergence for carbon sites was 0.3 ppm for δ_{iso}, 1.0% of the span, and 0.05 for the skew. The nitrogen sites were described within an accuracy of 0.8 ppm for δ_{iso}, 1.4% of the span, and 0.03 for the skew. These average values were obtained for a planar melamine structure with four coordination spheres, a planar melem structure with three coordination spheres, and the respective corrugated structures containing two coordination spheres around the central building block (see (***), (**), and (*) in Figure 2, II(a), for comparison).

Due to the intrinsic periodicity of the planar layers, the NMR parameters could directly be extracted from the central building unit of the biggest of the above-mentioned clusters (see Figure 2). In contrast to that, all corrugated minima displayed C_1 symmetry and it was imperative to evaluate the NMR parameters for the local sites separately. The base of this approach was the PM3 optimized structures which were further treated as follows (see Figure 2, III). Small subclusters with the size of two coordination spheres were cut out and saturated with hydrogen atoms. The hydrogen atoms were optimized using PM3 in a fixed cluster geometry of carbon and nitrogen atoms. For these model systems, the NMR tensors were calculated using DFT. Finally, the NMR values for the central building block of all models resulted in a statistical description of the initial cluster, excluding its two outmost coordination spheres. The two investigated melamine based clusters had a size of four and five coordination spheres, whereas the two melem based structures contained three and four coordination spheres (see Figure 2, II(a)). As a consequence, the here presented results pose a statistical description over 56 units in the melamine system and 26 building blocks in the melem system. The median and the standard deviation were calculated for the parameters δ_{iso}, Ω, and κ. The distributions presented in this paper are not Gaussian type. Nevertheless, for the sake of clarity in the discussion, we use the standard deviation as a comparative value which simply represents the width of the respective distributions. The isotropic shifts, δ_{iso}, were further analyzed with respect to the minimum and maximum value of the distribution. In the case of cyclic melon, an isolated molecule as well as hydrogen bonded meshes were calculated for their NMR properties using PBE1PBE/6-31G(d,p) (see Figure 3). For the meshes, a central region was cut out which included all important hydrogen bonds in the systems. These clusters again were saturated with hydrogen, the hydrogen relaxed in a rigid cluster framework, and the NMR tensors calculated using PBE1PBE/6-31G(d,p).

3. Results and Discussion

3.1. Structures. All clusters were prepared from melamine and melem building blocks following the procedure described in section 2. The geometry optimization resulted in one planar and one corrugated structure for every cluster. However, the analysis of the Hessian matrix showed a large number of imaginary frequencies for all planar structures. These frequencies were associated to out-of-plane vibrations, clearly showing that planar structures are saddlepoints on the energy surface which tend to distort into corrugated species. In contrast, frequency

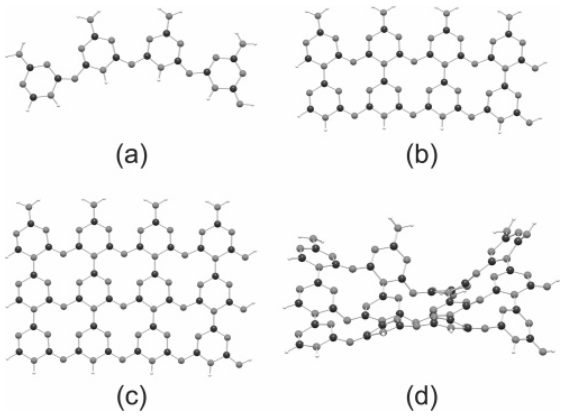

Figure 4. Orthorhombic linkage in melamine based g-C_3N_4: optimized planar (a−c) and corrugated (d) structures starting from a single melamine chain (a); structure d shows the corrugated species of the planar system (c).

calculations on corrugated layers did not reveal any negative values, therefore stating their minimum character.

The broad variety of clusters described in section 2 was mainly used to investigate the NN repulsion within the layers and the effect of the cluster edge on the NMR parameters. Therefore, we exclusively show the biggest calculated systems as examples for the following structural discussion. These clusters best represent the structure of an infinite layer as it would be found in a real material. Furthermore, these clusters were used for the evaluation of the NMR parameters.

Orthorhombic Melamine Based g-C_3N_4. For the orthorhombic melamine based systems, several clusters were tested in structure optimizations (see II(d) in Figure 2). Starting with the condensation of rows of four melamine units, the maximum applicable structure was three rows in size. All structures bigger than that failed to proceed into a wave function in the self consistent field (SCF) cycle. With rows of six melamine units, the biggest cluster applicable was two rows in size. Both planar and corrugated structures were tested. The instability of the wave function for bigger orthorhombic g-C_3N_4 clusters probably reflects the general instability of this connection scheme. Due to the failure to produce reasonably big clusters, these systems were excluded from the NMR evaluation.

Figure 4 exemplarily shows the results of successful structure optimizations for orthorhombically linked g-C_3N_4 based on chains of four melamine units. A single melamine chain (a) significantly bends upon energy minimization, developing into a structure with CNC angles of 128° at the bridging nitrogen atoms and NCN angles of 112° at the proximate C atoms. This result matches with the behavior of a single chain of melem molecules which also significantly bends upon structure optimization.[10] With the condensation of a second chain (b), the curvature of both chains is constrained. Still, CNC angles of about 128° are found at the bridging N atoms, whereas the NCN angles of the neighbors are forced to values of 120−121°. The bending of a single chain can be understood as the result of the repulsive interaction between the N atoms in the melamine rings in close contact.[39] In a condensed structure, this repulsive force cannot be evaded by a bending but leads to the corrugation of the layer (see Figure 4d). As expected, a substantial distortion of the single melamine building blocks occurs upon corrugation, indicating the lack of aromaticity in the orthorhombically linked systems.[1]

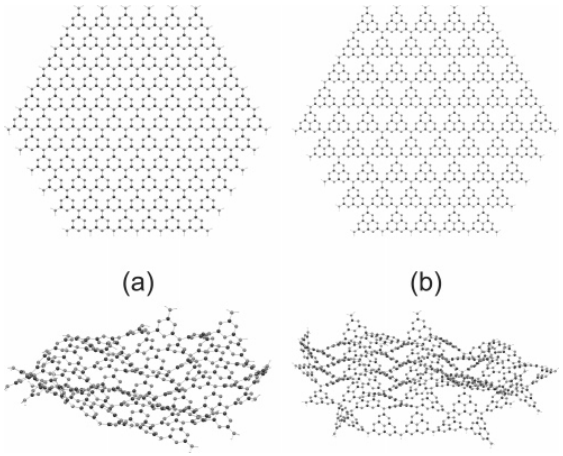

Figure 5. Planar and corrugated examples for the classical g-C_3N_4 structure proposals: (a) melamine based; (b) melem based.

Classical Melamine and Melem Based g-C_3N_4. Figure 5 shows the biggest optimized structures for classical linked melamine- and melem based g-C_3N_4 layers. In all structures, CNC and NCN angles of about 120° are found and all nitrogen atoms display a nearly planar local environment. Again, the close NN contacts produce repulsive forces in the layers and corrugation occurs. In contrast to the orthorhombic linkage of the structures described above, the classical linkage retains the aromaticity of the building blocks. The main effect of corrugation is caused by a rotation about the NC bonds of the interconnecting tertiary N atoms, turning the whole of the planar melamine and melem moieties. It should be pointed out that strictly speaking neither the triazine nor the heptazine based corrugated meshes exhibit any symmetry.

Corrugation leads to layers buckled in an amorphous manner with a large amount of different local environments which individually vary in the melamine and melem structures. In the largest calculated melamine cluster, the local environments are in complete disorder, whereas in the respective melem structure a regular zigzag sequence of building blocks appears in the upper left part of the cluster (compare parts a and b at the bottom of Figure 5). This indicates a tendency to form g-C_3N_4 layers with an orientational periodicity when turning to the larger melem building block. Figure 6a and b shows a pseudoperiodic subcluster cut out from the melem structure depicted in Figure 5.

This structure exclusively comprises a periodic variation in the orientation of the melem units and was further taken to build a proposal for a periodic layer in a potential orthorhombic unit cell (see Figure 6c−e). Four distinguishable melem building blocks with individual orientations could be identified included in a grid with *a* and *b* lattice constants of 13.4 and 12.1 Å, respectively. With angles between the axes of 89−91°, a rectangular arrangement can be proposed. The cell axes nicely form a planar arrangement with only minor distortion, and the cell itself includes one full oscillation of a periodically corrugated structure (see Figure 6e). Even though at the cell boundaries the atom positions do not exactly fit, the deviations reasonably well remain in the range of variation of bonding distances and angles. Therefore, this proposal poses an ideal base for a further structure optimization under periodic boundary conditions.[10] However, as such calculations went beyond the scope of the here presented work and will be done in a future project.

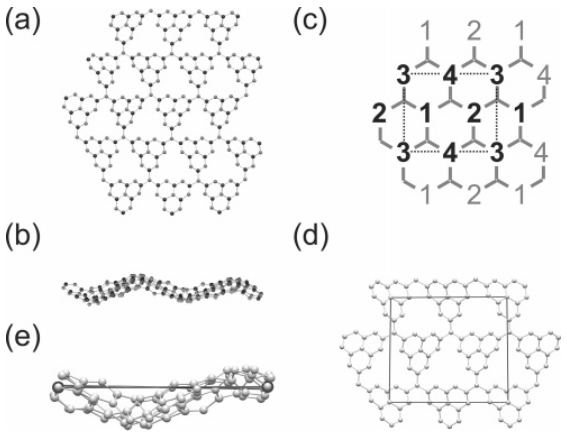

Figure 6. Parts a and b show the pseudosymmetric core region of the corrugated melem cluster depicted in Figure 5; part c shows the orientational periodicity of four distinguishable building blocks in part a; parts d and e depict the base of an orthorhombic unit cell.

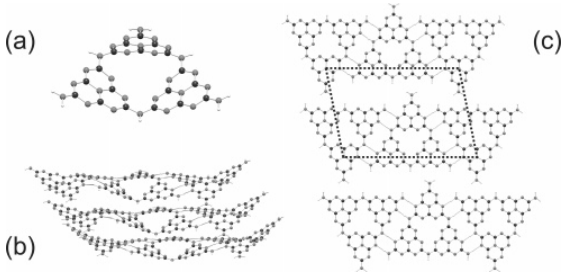

Figure 7. Planar and corrugated structures for cyclic melon: (a) isolated molecule; (b) corrugated mesh of cyclic melon (ABC... sequence); (c) periodic mesh of cyclic melon with the base of an oblique unit cell.

Cyclic Melon Systems. In contrast to the fully condensed species, the corrugation in a single melon unit leads to a C_s symmetric structure (see part a in Figure 7). Due to the simple assembly from three melem units, the evasion of close NN contacts through rotation about the NC bond of the NH nitrogen atoms exclusively leads to one distorted structure. Figure 7 shows the optimized structures of a cyclic melon mesh with an ABC... sequence (compare as well to Figure 3). The molecules tightly bind together through hydrogen bonding and form bands of melon (Figure 7, structures b and c). These bands loosely bind together, leading to an assembly of molecules in a densely packed layer. For both an ABC... and ABA... sequence, stable structures can be found. Furthermore, the C_s symmetry constraint of the single melon units transfers onto the melon mesh, leading to an intrinsically periodic layer (see structure b). For the ABC... sequence, the base of an oblique unit cell containing two melon molecules can be extracted. The cell parameters are 23.6 Å for the *a*-axis, 15.6 Å for the *b*-axis, and 104° for the angle γ. In the melon structure comprising the ABA... sequence, the base of an orthorhombic unit cell with four melon molecules can be extracted. Compared to the ABC... sequence, the *a*-axis remains 23.6 Å, whereas the *b*-axis elongates to 30.1 Å.

3.2. Energies. All of the above-presented CN(H) clusters exhibit close NN contacts. Due to the repulsion of the nitrogen lone pairs, corrugated layers are in general lower in energy in comparison to the respective planar system.[39] Figure 8 (top) presents a plot of the energy difference between corrugated and planar structures as a function of the number of NN contacts in all calculated layers. The gain in energy exhibits a linear relation to the close nitrogen contacts. It can be distinguished between triazine systems including orthorhombic and classical melamine based structures and heptazine systems which include the classical melem structures as well as the cyclic melon clusters. The only pronounced deviation from linear behavior is found for a triazine based structure (see inset in the left bottom part of Figure 8). This system is characterized by a large number of building units at the cluster boundary and only a small cluster core. Due to these features, it is more flexible than triazine systems of comparable size and can gain more energy from corrugation.

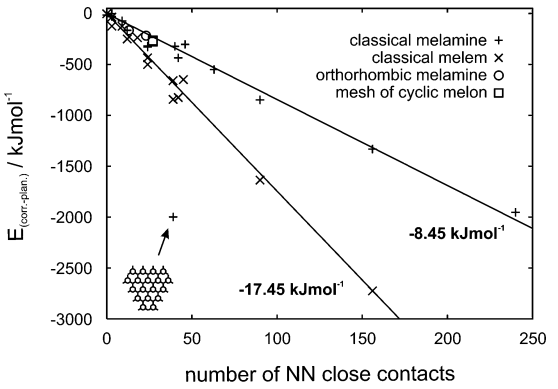

Figure 8. Plot of the energy difference between corrugated and planar layers as a function of the number of NN close contacts in the clusters; separate linear fits for melamine and melem based systems.

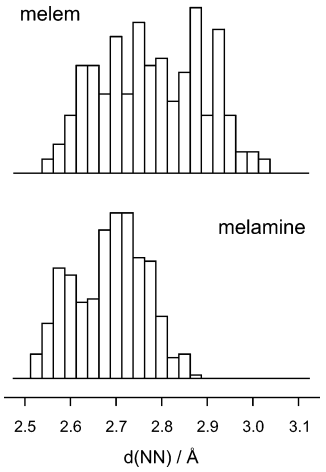

Figure 9. Distribution of NN distances in corrugated melamine and melem based systems; repulsive close contacts are found in a range of 2.525−2.875 Å for melamine and 2.550−3.025 Å for melem systems.

A general observation during geometry optimization was that building units close to the cluster boundary showed a larger distortion than those in the fully condensed core. We propose that the observed energy differences result from two opposite effects. On the one hand, the moieties distort to evade NN close contacts; on the other hand, the distortion causes structural stress. The observed geometry results from the interplay of both effects, and the more flexible the moiety in the condensed structure is, the more energy can be gained from corrugation. These flexible moieties can be found at the cluster boundary. As the calculated clusters vary in their structure (see Figure 2), the influence of the boundary on the energy gain varies as well. This can be

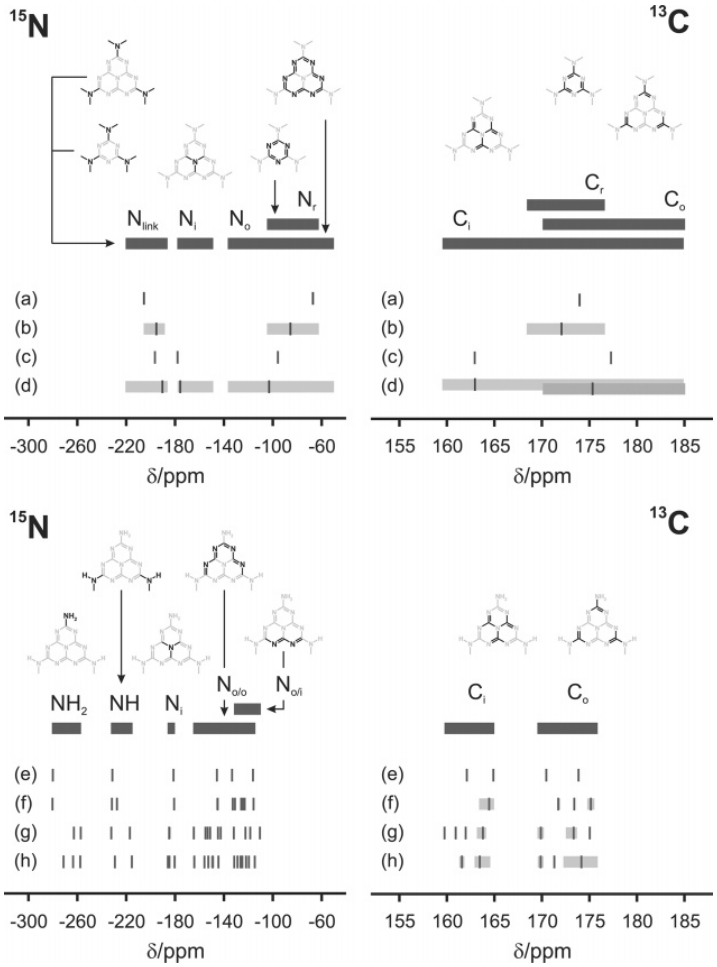

Figure 10. Signal assignment (depictions and dark bars indicating the maximum range of the respective shift) and distribution for planar (a, c, e, and g) and corrugated (b, d, f, and h) systems: melamine (a and b); melem (c and d); isolated melon (e and f); a hydrogen bonded melon system (g and h). Shifts closer than 1 ppm are grouped together described by the minimum to maximum spread of the distribution (gray areas) and the median value (dark markers).

seen in Figure 8 where for a few NN contacts (small cluster sizes) the energy values scatter around the linear trends, whereas the energy values for big clusters nicely match with the linear behavior. The energy gain per NN contact can be determined to be 8.45 kJ mol^{-1} for triazine systems and 17.45 kJ mol^{-1} for heptazine systems. This also originates in the different flexibilities of the structures. As mentioned above, corrugation takes place through a rotation of the mainly unchanged building blocks toward each other. The rotation of a melem unit leads to larger NN distances compared to the same rotation and resulting distances for a melamine building block. The larger the NN distance becomes, the more the repulsion of the nitrogen atoms can be evaded, resulting in a larger gain of energy. Figure 9 depicts the NN distance distribution for corrugated classical melamine and melem clusters in the range relevant for close nitrogen contacts. Compared to the NN distances in the melamine system which are found between 2.525 and 2.875 Å, the distances for the melem model indeed significantly shift to higher values (2.550−3.025 Å). This is a combined result of a shifted median value (2.700 Å for melamine and 2.775 Å for melem) and a broadening of the overall distribution as can be seen from the standard deviations (0.079 Å for melamine and 0.113 Å for melem).

3.3. NMR Parameters. The NMR isotropic shifts, δ_{iso}, the span, Ω, and the skew, κ, were calculated for the planar and corrugated melamine, melem, and melon based systems presented above (for details, see also section 2). Figure 10 gives an overview of the ^{15}N and ^{13}C signal assignment and the distribution of the chemical shifts in the respective systems. Shift differences of less than 1 ppm where grouped together and treated as a distribution. Figure 10 shows the overall spread of the distributions from their minimum to maximum value (gray areas) as well as the median value (dark bars). Tables 1 and 2 list the parameters δ_{iso}, Ω, and κ. For isolated signals, the exact values are given; distributions are described in terms of their median and the standard deviation (see parentheses in Tables 1 and 2).

Starting with the melamine based systems, two different nitrogen species and one carbon species can be differentiated (the ring nitrogen (N_r), the linking nitrogen (N_{link}), and the ring carbon (C_r) in Figure 10). The interconnecting nitrogen (N_{link}) exhibits a shift of about −205 ppm in the planar system. Upon corrugation, the median shifts by 10 ppm to lower field. In contrast, the median of the ring nitrogen (N_r) shifts by 19 ppm from about −67 ppm to higher field. The isotropic shift of N_r is more sensitive to the corrugation than δ_{iso} of N_{link}, as can be

TABLE 1: ^{15}N NMR Parameters δ_{iso}, Ω, and κ for Melamine, Melem, and Melon Based Systems (for Signal Assignment, See Figure 10); for Isolated Signals the Calculated Values Are Given, and Distributions Are Described in Terms of the Median and the Standard Deviation (in Parentheses)

	system		site	δ_{iso}/ppm	Ω/ppm	κ
(a)	melamine	planar	N_{link}	−205.5 (-)	94.1 (-)	−0.98 (-)
			N_r	−67.1 (-)	597.8 (-)	0.08 (-)
(b)	melamine	corrugated	N_{link}	−195.3 (4.5)	60.0 (9.8)	−0.84 (0.09)
			N_r	−85.6 (9.4)	509.8 (18.5)	−0.15 (0.03)
(c)	melem	planar	N_{link}	−196.6 (-)	127.6 (-)	−0.82 (-)
			N_i	−178.0 (-)	241.5 (-)	−1.00 (-)
			N_o	−95.8 (-)	449.7 (-)	−0.04 (-)
(d)	melem	corrugated	N_{link}	−190.4 (10.9)	76.4 (20.1)	−0.45 (0.24)
			N_i	−175.7 (9.9)	256.4 (23.7)	−0.92 (0.03)
			N_o	−103.1 (19.0)	424.0 (29.2)	−0.15 (0.12)
(e)	melon (isol.)	planar	NH_2	−280.1 (-)	114.1 (-)	0.19 (-)
			NH	−231.3 (-)	103.9 (-)	0.97 (-)
			N_i	−181.3 (-)	245.1 (-)	−0.94 (-)
			$N_{o/o}$	−145.7 (-)	319.8 (-)	−0.40 (-)
				−133.3 (-)	335.1 (-)	−0.28 (-)
			$N_{o/i}$	−116.3 (-)	417.2 (-)	−0.18 (-)
(f)	melon (isol.)	corrugated	NH_2	−280.5 (0.2)	114.2 (0.2)	0.18 (0.01)
			NH	−231.7 (0.0)	99.5 (0.0)	0.58 (0.00)
				−227.6 (-)	108.3 (-)	0.80 (-)
			N_i	−180.9 (0.1)	245.1 (2.3)	−0.95 (0.03)
			$N_{o/o}$	−145.2 (0.8)	320.9 (1.1)	−0.40 (0.00)
				−132.8 (0.1)	329.5 (0.1)	−0.33 (0.00)
				−131.0 (0.1)	345.4 (0.1)	−0.31 (0.00)
				−124.5 (0.0)	350.5 (0.0)	−0.33 (0.00)
			$N_{o/i}$	−125.9 (0.0)	376.1 (0.0)	−0.32 (0.00)
				−123.0 (0.1)	397.3 (0.2)	−0.25 (0.00)
				−115.8 (0.1)	398.2 (0.2)	−0.28 (0.00)
(g)	melon(network)	planar	NH_2	−262.8 (-)	124.1 (-)	0.32 (-)
				−257.3 (0.1)	111.5 (0.4)	0.82 (0.04)
			NH	−232.2 (-)	102.6 (-)	0.91 (-)
				−217.0 (1.0)	127.2 (1.4)	0.18 (0.03)
			N_i	−184.8 (0.8)	233.6 (1.6)	−0.94 (0.01)
			$N_{o/o}$	−164.7 (0.4)	257.3 (2.4)	−0.51 (0.01)
				−155.1 (-)	269.6 (-)	−0.46 (-)
				−153.3 (-)	275.5 (-)	−0.40 (-)
				−151.3 (0.4)	296.4 (8.5)	−0.43 (0.04)
				−144.9 (-)	295.4 (-)	−0.35 (-)
				−142.6 (-)	313.2 (-)	−0.35 (-)
				−131.9 (-)	337.0 (-)	−0.25 (-)
				−122.4 (1.0)	373.2 (0.1)	−0.19 (0.00)
			$N_{o/i}$	−118.5 (0.5)	409.7 (4.4)	−0.18 (0.01)
				−110.5 (0.7)	421.7 (1.4)	−0.15 (0.01)
(h)	melon(network)	corrugated	NH_2	−271.3 (-)	113.6 (-)	0.50 (-)
				−263.4 (-)	121.8 (-)	0.37 (-)
				−257.5 (-)	111.5 (-)	0.79 (-)
			NH	−229.2 (-)	106.8 (-)	0.62 (-)
				−215.4 (0.6)	104.6 (6.9)	0.31 (0.00)
			N_i	−185.9 (-)	228.4 (-)	−0.96 (-)
				−184.6 (-)	233.1 (-)	−0.95 (-)
				−180.4 (-)	239.2 (-)	−0.99 (-)
			$N_{o/o}$	−164.3 (-)	255.9 (-)	−0.52 (-)
				−156.0 (-)	270.0 (-)	−0.47 (-)
				−152.7 (0.6)	293.5 (1.3)	−0.45 (0.00)
				−149.2 (1.1)	285.7 (7.2)	−0.44 (0.02)
				−144.5 (-)	317.2 (-)	−0.36 (-)
				−126.3 (-)	335.4 (-)	−0.32 (-)
				−125.0 (-)	370.7 (-)	−0.24 (-)
				−114.5 (-)	373.6 (-)	−0.26 (-)
			$N_{o/i}$	−131.5 (-)	376.0 (-)	−0.29 (-)
				−128.9 (-)	361.8 (-)	−0.32 (-)
				−121.9 (-)	388.8 (-)	−0.26 (-)
				−119.6 (-)	391.3 (-)	−0.25 (-)
				−115.0 (0.2)	398.0 (15.7)	−0.27 (0.04)

seen from the standard deviations of the distributions which are 9.5 and 4.5 ppm, respectively (see part b in Table 1). Similar trends are found for the span, Ω, and the skew, κ. Ω decreases more significantly for N_r than for N_{link}. This change is accompanied by a larger distribution of the span of N_r. With about 0.2 and 0.1, the skew, κ, changes twice as much for N_r compared to N_{link} (compare parts a and b in Table 1). However, the change in κ is only minor. It is interesting to note that corrugation does not lead to a broad distribution of κ for N_r.

For melem based systems, three distinguishable nitrogen sites, the linking nitrogen (N_{link}), the inner nitrogen (N_i), and the outer nitrogen (N_o), as well as two carbon sites, the inner carbon (C_i) and the outer carbon (C_o), have to be distinguished (see Figure 10). Whereas in the melamine system corrugation influences

TABLE 2: ^{13}C NMR Parameters δ_{iso}, Ω, and κ for Melamine, Melem, and Melon Based Systems (for Signal Assignment, See Figure 10); for Isolated Signals, the Calculated Values Are Given, and Distributions Are Described in Terms of the Median and the Standard Deviation (in Parentheses)

system			site	δ_{iso}/ppm	Ω/ppm	κ
(a)	melamine	planar	C_r	174.0 (-)	167.5 (-)	0.33 (-)
(b)	melamine	corrugated	C_r	172.1 (1.3)	154.4 (2.9)	0.22 (0.07)
(c)	melem	planar	C_i	162.9 (-)	133.3 (-)	−0.04 (-)
			C_o	177.3 (-)	176.7 (-)	0.48 (-)
(d)	melem	corrugated	C_i	162.9 (8.3)	134.8 (8.1)	0.04 (0.09)
			C_o	175.3 (2.7)	175.7 (6.2)	0.35 (0.13)
(e)	melon (isol.)	planar	C_i	162.1 (-)	138.3 (-)	−0.06 (-)
				164.9 (-)	142.1 (-)	0.04 (-)
			C_o	170.5 (-)	154.7 (-)	−0.44 (-)
				173.9 (-)	172.5 (-)	0.14 (-)
(f)	melon (isol.)	corrugated	C_i	164.4 (0.5)	141.0 (1.7)	0.02 (0.03)
			C_o	171.7 (0.1)	155.8 (0.1)	−0.45 (0.01)
				173.4 (0.0)	170.3 (0.0)	0.12 (0.00)
				175.2 (0.4)	174.8 (2.1)	0.11 (0.05)
(g)	melon(network)	planar	C_i	159.8 (-)	135.9 (-)	0.02 (-)
				160.9 (-)	138.7 (-)	−0.01 (-)
				162.0 (-)	138.2 (-)	−0.04 (-)
				163.8 (0.3)	139.9 (1.6)	0.01 (0.05)
			C_o	169.9 (0.3)	134.3 (3.8)	−0.84 (0.08)
				173.3 (0.5)	164.2 (6.1)	0.05 (0.16)
				175.0 (0.0)	168.7 (1.6)	0.12 (0.07)
(h)	melon(network)	corrugated	C_i	161.6 (0.3)	137.1 (0.5)	0.05 (0.04)
				163.5 (0.7)	139.3 (1.0)	0.00 (0.03)
			C_o	169.9 (0.4)	138.3 (4.9)	−0.78 (0.10)
				171.3 (-)	144.6 (-)	−0.63 (-)
				174.2 (1.1)	165.4 (6.1)	0.01 (0.19)

the median values of all NMR parameters of the nitrogen atoms in the building block, for melem, mainly the tertiary nitrogen N_{link} is affected (compare parts c and d in Table 1). Large changes are found for the parameters Ω and κ. A general trend in the melem systems is that corrugation leads to a broader distribution of all NMR parameters compared to melamine systems. Upon structural distortion, the medians of the isotropic values, δ_{iso}, of N_{link} and N_o exhibit the same directional shifts compared to N_{link} and N_r in the melamine system (compare parts a and b to parts c and d in Figure 10). With values below 10 ppm, the magnitude of these shifts is smaller. The skew, κ, of the inner nitrogen (N_i) is least affected by corrugation, both in terms of the absolute change (compare parts c and d in Figure 10) and distribution of the value. The changes for the NMR parameter of the carbon sites mirror these findings, even though generally they are less sensitive to corrugation (see Figure 1 and Table 2). Upon corrugation, the values for δ_{iso}, Ω, and κ exhibit only small changes in their medians. However, the outstanding changes occur in the overall distribution of the chemical shifts (see Figure 10). Even though the standard deviations are small, δ_{iso} varies in a broad range from its minimum to maximum value. In the case of the melem system, this leads to the result that the strict separation of the chemical shifts of the inner and outer carbon sites (C_i and C_o) vanishes upon corrugation of the structure (see Figure 11). Even though the medians of the respective distributions do not significantly change in comparison to the planar structure, an overlap of both distributions is observed (see also Figure 10). A comparison of the nitrogen NMR values for the corrugated melamine and melem structures shows interesting differences in the skew, κ (see parts b and d in Table 1). Both the outer nitrogen site (N_o) and the linking nitrogen (N_{link}) are far more influenced by corrugation, as shown from the comparison to N_r and N_{link} in the melamine system. The standard deviations are much higher, indicating a significantly broader distribution of values. Furthermore, with −0.45, the κ value of the melem system is nearly half of the value found for the melamine system. These differences mirror the higher degree of structural distortion in the melem based structure as discussed above.

Turning to the melon based systems, the NMR parameters are prone to two different structural influences, the corrugation of the molecular moieties and hydrogen bonding between the molecules. To separately investigate these influences, the results for an isolated molecule and a hydrogen bonded system are shown (see parts e−h in Figure 10). It turned out that it is not possible to differentiate between the two different structures II-(a) and II(b) in Figure 3. For that reason, we exclusively present the results of isolated melon and the central melon in structure II(a).

In a planar single molecule, five well separated different isotropic shifts, δ_{iso}, are found for nitrogen. In the order from low to high field, these are NH_2, NH, and the inner nitrogen (N_i). Furthermore, we find two different shifts for the $N_{o/o}$ nitrogen which are located at the outside of the melon unit. The separation of the signals is caused by the different electronic influences of the NH_2 and NH neighbor groups. Finally, for

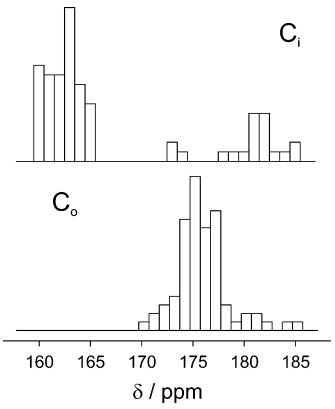

Figure 11. Distribution of the ^{13}C chemical shift, δ_{iso}, in corrugated melem based g-C_3N_4.

the $N_{o/i}$ atoms, which point to the inside of the melon structure, one shift is found. Upon corrugation, the NH, $N_{o/o}$, and $N_{o/i}$ shifts further split, whereas the nitrogen sites NH_2 and N_i remain unaffected by the structural change (compare parts e and f in Table 1). The change in the isotropic shifts is accompanied by overall changes of 10−20 ppm for the span, Ω, and about 0.1 in κ. With a variation of 0.4 in κ, the most significant change is found for the NH nitrogen.

The overall picture changes further including the influence of hydrogen bonding. Due to the different electronic environment, the NH_2 as well as the NH nitrogen involved in hydrogen bridges shift by about 15−23 ppm to lower field compared to the shifts found for planar systems (see parts e and g in Figure 10 and Table 1). As a general trend, the isotropic NMR values, δ_{iso}, of N_i and $N_{o/o}$ exhibit a shift to higher field compared to the isolated molecule. A pronounced change in the skew, κ, of the NH_2 and NH groups involved in the hydrogen bridge is found. For the corrugated hydrogen bonded structure, the shifts are further split up. The main effect is that the nitrogen species $N_{o/o}$ and $N_{o/i}$ do not exhibit separate ranges for the chemical shifts, δ_{iso}, any longer (compare to part h in Table 1).

The carbon spectrum of a planar isolated melon exhibits four different chemical shifts which can be divided into two groups, C_i and C_o. With a difference of about 0.6, the parameter κ of the C_o sites varies markedly (see part e in Table 2). The distortion of the structure leads to a distribution of the C_i and C_o chemical shifts in about the range found for the planar structure but does not change the overall picture (compare parts e and f in Table 2). Hydrogen bonding leads to a similar influence on the chemical shift. The values for δ_{iso} in general shift to higher field (compare parts e and g in Table 2). The difference in κ for the C_o sites increases to nearly 1.0 in its maximum.

4. Summary

We presented a comprehensive theoretical study of triazine and heptazine based structure proposals for g-C_3N_4. The systems range from layers with an orthorhombic and classical linkage of melamine building blocks over classically linked melem moieties to a hydrogen bonded mesh of cyclic melon molecules. For all of these systems, corrugated structures were found as the only minima on the energy surface. All planar systems pose saddlepoints on the hypersurface.

In general, the distortion of the cluster occurred in an amorphous-like manner, leading to single layers without periodic symmetry features. The source for corrugation is the repulsion of nitrogen lone pairs in close contacts. With a slope of about 9 kJ mol^{-1} for triazine based systems, the gained energy linearly depends on the number of these NN contacts in the clusters. The heptazine based systems gain about twice the energy per NN close contact in comparison with triazine based structures. The corrugation in both types of systems can be associated with a distortion about the NC bonds of the linking tertiary nitrogens, whereas the building units themselves remain basically rigid. It turned out that in such an arrangement melem as a building block establishes longer NN distances in the repulsive sites and therefore more energy through the formation of a corrugated structure.

It was found that the orthorhombic linkage of melamine moieties does not pose a promising proposal, as such systems did not yield stable structures for large clusters. A comparison of the classical corrugated melamine and melem layers indicated an overall trend of the heptazine systems to arrange more regularly. This was approved turning to the cyclic melon mesh where a tightly packed layer of hydrogen bonded molecules with translational periodicity represents the structural minimum. In both systems, the evasion from NN close contacts leads to regularly buckled layers. Furthermore, proposals for the periodicity of the layers in possible unit cells were extracted. For the classical melem system with axes of 12.1 and 13.4 Å and an angle of about 90°, the base of an orthorhombic cell was found. For cyclic melon, two different proposals were extracted, one for the base of an oblique cell (ABC... sequences with axes of 15.6 and 23.6 Å and an angle of 104°) and one for the base of an orthorhombic cell (ABA... sequences with axes of 15.6 and 23.6 Å). In a future project, these cutouts can be extended by stacking to build full unit cells and used as input structures for the geometry optimization under periodic boundary conditions.

A full study of the ^{15}N and ^{13}C chemical shift tensors was performed for all systems except for the orthorhombic melamine variant. The change in chemical shift upon corrugation and, in the case of the melon system, hydrogen bonding was investigated. The results clearly show the high potential of solid-state NMR for the characterization of layered C/N species even for amorphous systems. With the here presented overview (see Figure 10), the ^{15}N and ^{13}C spectra can directly be compared to the most prominent structure models, which is very valuable for the synthesis of g-C_3N_4. For the cyclic melon mesh, it was found that the ^{13}C as well as the ^{15}N skew, κ, reflects the hydrogen bonding in the system. The measurement of the anisotropy of the ^{13}C nucleus can therefore be used to locate hydrogen bonding in such systems.

References and Notes

(1) Kroke, E.; Schwarz, M. *Coord. Chem. Rev.* **2004**, *248*, 493−532.
(2) Kaner, R. B.; Gilman, J. J.; Tolbert, S. H. *Science* **2005**, *308*, 1268−1269.
(3) Matara, S. F. *Prog. Solid State Chem.* **2006**, *34*, 21−66.
(4) Horvath-Bordon, E.; Riedel, R.; Zerr, A.; McMillan, P. F.; Auffermann, G.; Prots, Y.; Bronger, W.; Kniep, R.; Kroll, P. *Chem. Soc. Rev.* **2006**, *35*, 987−1014.
(5) Liu, A. Y.; Cohen, M. L. *Science* **1989**, *245*, 841−842.
(6) Riedel, R. *Adv. Mater.* **1992**, *4*, 759−761.
(7) Schnick, W. *Angew. Chem., Int. Ed.* **1993**, *32*, 1580−1581.
(8) Li, C.; Cao, C.-B.; Zhu, H.-S. *Mater. Lett.* **2004**, *58*, 1903−1906.
(9) Lotsch, B. V.; Schnick, W. *Chem. Mater.* **2006**, *18*, 1891−1900.
(10) Lotsch, B. V.; Doeblinger, M.; Sehnert, J.; Seyfarth, L.; Senker, J.; Oeckler, O.; Schnick, W. *Chem. Eur. J.* **2007**, *13*, 4969−4980.
(11) Liu, A. Y.; Wentzcovitch, R. M. *Phys. Rev. B* **1994**, *50*, 10362−10363.
(12) Kouvetakis, J.; Bandari, A.; Todd, M.; Wilkens, B. *Chem. Mater.* **1994**, *6*, 811−814.
(13) Ortega, J.; Sankey, O. F. *Phys. Rev. B* **1995**, *51*, 2624−2627.
(14) Teter, D. M.; Hemley, R. J. *Science* **1996**, *271*, 53−55.
(15) Miyamoto, Y.; Cohen, M. L.; Louie, S. G. *Solid State Commun.* **1997**, *102*, 605−608.
(16) Yoon, Y.-G.; Pfrommer, B. G.; Mauri, F.; Louie, S. G. *Phys. Rev. Lett.* **1998**, *80*, 3388−3391.
(17) Molina, B.; Sansores, L. E. *Mod. Phys. Lett. B* **1999**, *13*, 193−201.
(18) Alves, I.; Demazeau, B.; Tanguy, B.; Weill, F. *Solid State Commun.* **1999**, *109*, 697−701. Zhang, Z.; Leinenweber, K.; Bauer, M.; Garvie, L. A. J.; McMillan, P. F.; Wolf, G. H. *J. Am. Chem. Soc.* **2001**, *123*, 7788−7796.
(19) Mattesini, M.; Matar, S. F.; Snis, A.; Etourneau, J.; Mavromaras, A. *J. Mater. Chem.* **1999**, *9*, 3151−3158.
(20) Lowther, J. E. *Phys. Rev. B* **1999**, *59*, 11683−11686.
(21) Snis, A.; Matar, S. F. *Phys. Rev. B* **1999**, *60*, 10855−10863.
(22) Courjault, S.; Tanguy, B.; Demazeau, G. *C. R. Acad. Sci., Ser. IIc* **1999**, *2*, 487−490.
(23) Montigaud, H.; Tanguy, B.; Demazeau, G.; Alves, I.; Birot, M.; Dunogues, J. *Diamond Relat. Mater.* **1999**, *8*, 1707−1710.
(24) Khabashesku, V. N.; Zimmerman, J. L.; Margrave, J. L. *Chem. Mater.* **2000**, *12*, 3264−3270.
(25) Zimmerman, J. L.; Wiliams, R.; Khabashesku, V. N.; Margrave, J. L. *Nano Lett.* **2001**, *1*, 731−734.

(26) Kroke, E.; Schwarz, M.; Horath-Bordon, E.; Kroll, P.; Noll, B.; Norman, A. D. *New J. Chem.* **2002**, *26*, 508−512.
(27) Rignanese, G.-M.; Charlier, J.-C.; Gonze, X. *Phys. Rev. B* **2002**, *66*, 205416.
(28) Mattesini, M.; Matar, S. F. *Phys. Rev. B* **2002**, *65*, 075110/1−075110/14.
(29) Vodak, D. T.; Kim, K.; Iordanidis, L.; Rasmussen, P. G.; Matzger, A. J.; Yaghi, O. M. *Chem. Eur. J.* **2003**, *9*, 4197−4201.
(30) Betranhandy, E.; Matar, S. F.; El-Kfoury, C.; Etourneau, J. *Z. Anorg. Allg. Chem.* **2004**, *630*, 2587−2598.
(31) Zhang, Y.; Sun, H.; Chen, C. *Phys. Rev. B* **2006**, *73*, 064109/1−064109/4.
(32) Komatsu, T. *J. Mater. Chem.* **2001**, *11*, 802−805.
(33) Komatsu, T.; Nakamura, T. *J. Mater. Chem.* **2001**, *11*, 474−478.
(34) Juergens, B.; Irran, E.; Senker, J.; Kroll, P.; Mller, H.; Schnick, W. *J. Am. Chem. Soc.* **2003**, *125*, 10288−10300.
(35) Horvath-Bordon, E.; Kroke, E.; Svoboda, I.; Fuess, H. *New. J. Chem.* **2005**, *29*, 693−699.
(36) Li, D.; Chung, Y.-W.; Yang, S.; Wong, M.-S.; Adibi, F.; Sproul, W. D. *J. Vac. Sci. Technol., A* **1994**, *12*, 1470−1477.
(37) LaManna, J.; Braddock-Wilking, J.; Lin, S.-H.; Feldman, B. J. *Solid State Commun.* **1999**, *109*, 573−576.
(38) Rovnyak, D.; Baldus, M.; Itin, B. A.; Bennati, M.; Stevens, A.; Griffin, R. G. *J. Phys. Chem. B* **2000**, *104*, 9817−9822.
(39) Hughbanks, T.; Tian, Y. *Solid State Commun.* **1995**, *96*, 321−325.
(40) dos Santos, M. C.; Alvarez, F. *Phys. Rev. B* **1998**, *58*, 13918−13924.
(41) Stafstroem, S. *Appl. Phys. Lett.* **2000**, *77*, 3941−3943.
(42) Meyer, J. C.; Geim, A. K.; Katsnelson, M. I.; Novoselov, K. S.; Booth, T. J.; Roth, S. *Nature* **2007**, *446*, 60−63.
(43) Frisch, M. J.; Trucks, G. W.; Schlegel, H. B.; Scuseria, G. E.; Robb, M. A.; Cheeseman, J. R.; Montgomery, J. A., Jr.; Vreven, T.; Kudin, K. N.; Burant, J. C.; Millam, J. M.; Iyengar, S. S.; Tomasi, J.; Barone, V.; Mennucci, B.; Cossi, M.; Scalmani, G.; Rega, N.; Petersson, G. A.; Nakatsuji, H.; Hada, M.; Ehara, M.; Toyota, K.; Fukuda, R.; Hasegawa, J.; Ishida, M.; Nakajima, T.; Honda, Y.; Kitao, O.; Nakai, H.; Klene, M.; Li, X.; Knox, J. E.; Hratchian, H. P.; Cross, J. B.; Bakken, V.; Adamo, C.; Jaramillo, J.; Gomperts, R.; Stratmann, R. E.; Yazyev, O.; Austin, A. J.; Cammi, R.; Pomelli, C.; Ochterski, J. W.; Ayala, P. Y.; Morokuma, K.; Voth, G. A.; Salvador, P.; Dannenberg, J. J.; Zakrzewski, V. G.; Dapprich, S.; Daniels, A. D.; Strain, M. C.; Farkas, O.; Malick, D. K.; Rabuck, A. D.; Raghavachari, K.; Foresman, J. B.; Ortiz, J. V.; Cui, Q.; Baboul, A. G.; Clifford, S.; Cioslowski, J.; Stefanov, B. B.; Liu, G.; Liashenko, A.; Piskorz, P.; Komaromi, I.; Martin, R. L.; Fox, D. J.; Keith, T.; Al-Laham, M. A.; Peng, C. Y.; Nanayakkara, A.; Challacombe, M.; Gill, P. M. W.; Johnson, B.; Chen, W.; Wong, M. W.; Gonzalez, C.; Pople, J. A. *Gaussian 03*, revision C.02; Gaussian, Inc.: Wallingford, CT, 2004.
(44) *MATLAB: the language of technical computing*; Math Works Inc.: Natick, MA.
(45) Sehnert, J.; Senker, J. *Chem. Eur. J.* **2007**, *13*, 6339−6350.
(46) Mason, J. *Solid State Nucl. Magn. Reson.* **1993**, *2*, 285−288.

Appendix B

The Gau2Sim library

The Gau2Sim program library was developed within the scope of this thesis and bridges the gap between the atomistic ab initio calculation of the NMR chemical shift tensor on the one hand and the simulation of NMR spectra from spin systems on the other hand. Figure B.1, table B.1 and table B.2 present an overview over the structure of the Gau2Sim library together with a list of the available modules and their capabilities. The ultimate goal was to provide a tool for the routine analysis of quantum chemical calculations which is why as many steps as possible where automatized throughout the work flow. All modules dealing with file input/output problems were written as Perl scripts. This programming language offers easy access to string manipulation and formatting. All mathematical analyses was carried out in MATLAB.[93] This language not only gives ready access to mathematical formalisms but also has a comfortable built-in GUI (graphical user interface) library which is convenient for the depiction of results. Furthermore, Perl scripts can be called up from any point in a MATLAB program which combines the advantages of both languages. For the automatizing of the simulation of MAS spectra with SIMPSON Tcl scripting was combined with Perl programming.[79] The calculation of wide-line spectra was carried out with C++.[78] All presented functions are implemented for an effective application of the tasks necessary in this work. However, due to the modular build up of the library it can easily be expended to include further applications. The already available scripts provide an ideal basis for the programming of such future tasks as the two principle kinds of NMR simulations, the calculation of wide-line as well

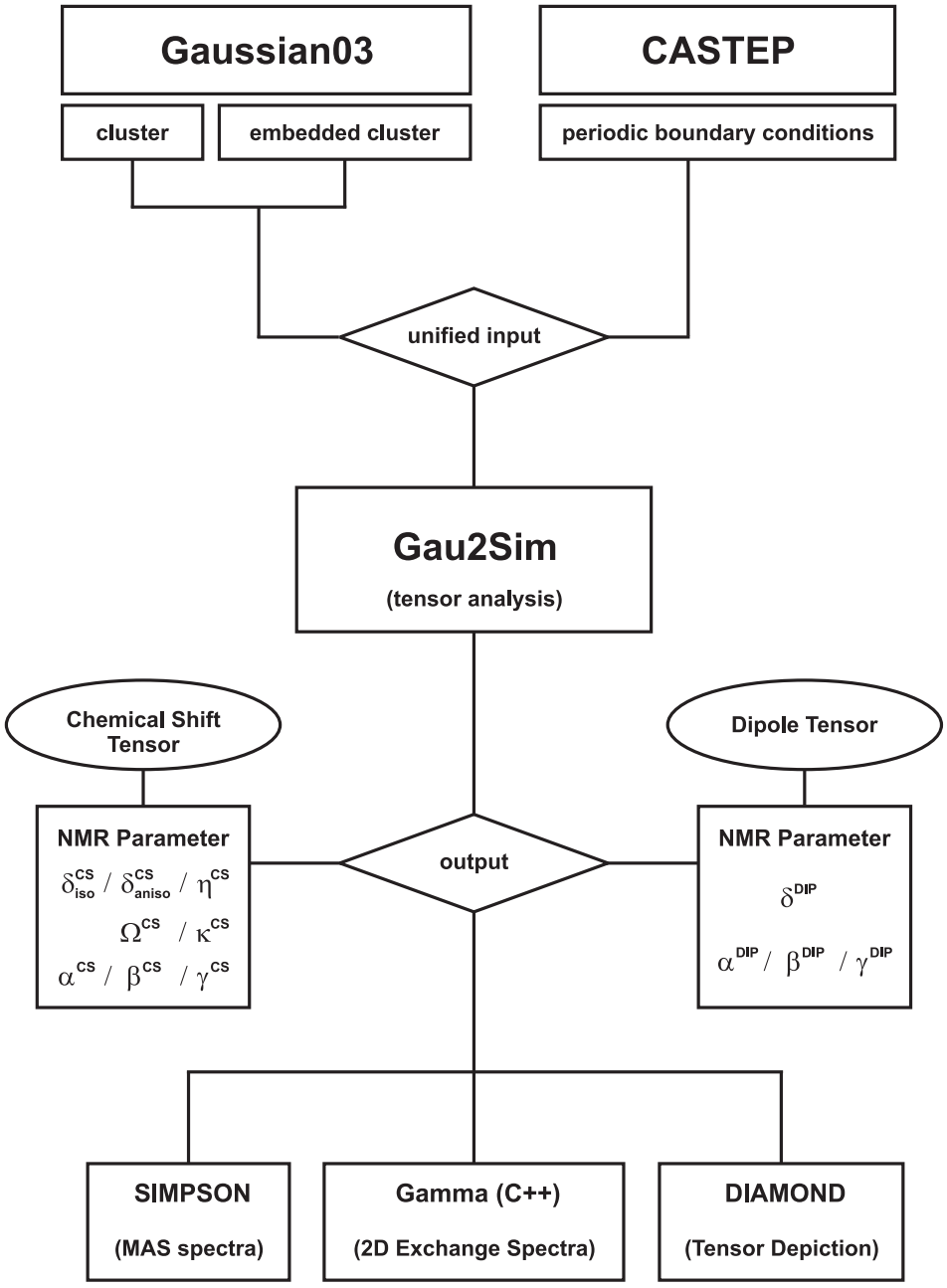

Figure B.1: The Gau2Sim library (see as well tables B.1 and B.2): output from Gaussian03[49] and CASTEP[50,51] NMR calculations can be unified into standard input for the tensor analysis; with the extraction tools the NMR tensor can fully be converted into arbitrary output; this includes the analysis of the chemical shift or the dipole tensor via the NMR parameters, the direct input into simulation tools for NMR spectra like SIMPSON[79] or GAMMA[78] and the depiction of the anisotropic symmetric part of the tensor with DIAMOND[92].

Tabelle B.1: Overview over module names and capabilities of the Gau2Sim program library (see as well figure B.1 and table B.2); Perl scripts are recognized by the *.pl*, MATLAB functions end with *.m* whereas GUI setups bear *.fig*; C++ programs do not exhibit any extension of the file name; the modules are grouped by common functionality.

(1)	*scan_2_movie.pl* *scan_2_NMR_relaxed.pl* *scan_2_NMR_rigid.pl*	extraction of energies and structure matrices from rigid or relaxed scans over the energy surface as well as automated input generation for the calculation of NMR surfaces
(2)	*gaussian_2_ten_n_mat.pl* *ONIOM_2_ten_n_mat.pl* *castep_2_ten_n_mat.pl*	extraction of Cartesian coordinates and tensor data from ab initio calculations
(3)	*KO_Rotate.m* *KO_Rotate.fig*	step-by-step GUI based manual Euler transformation between CAS and PAS, active and passive rotations can be performed
(4)	*Gau2Sim.m* *Gau2Sim.fig* *CSA_DIR_extractor.m* *CSA_extractor.m*	step-by-step GUI based as well as automated scripting analysis of spin systems on the base of the unified matrix and tensor file format created with modules (2)
(5)	*CSA_DIR_2_span_n_skew.m* *CSA_2_span_n_skew.m* *classical_2_span_n_skew.pl*	conversion between the Haeberlen-Mehring-Spiess and Herzfeld-Berger conventions
(6)	*simpsoner.pl*	simulation of MAS chemical shift spectra; automated creation of SIMPSON input for a system of uncoupled spins from the output created by modules listed under (4)
(7)	*1D_simul_Nspin*	simulation of one-dimensional wide-line spectra of systems comprising of N uncoupled spins
(8)	*2D_simul_Nspin*	simulation of two-dimensional rf-driven spin-diffusion wide-line spectra of systems with N spins for $t_m \rightarrow \infty$

Tabelle B.2: Overview over the auxiliary functions included the Gau2Sim library (see as well figure B.1 and table B.1); perl scripts are recognized by the *.pl* extension, MATLAB scripts end with *.m*.

mat_2_xyz.pl	conversion of the Gau2Sim matrix file into the Cartesian .xyz format
ppm2Hz.m	conversion from ppm to Hertz dependent from the spectrometer field given in terms of the ^{1}H Lamor frequency
gamma_nuc.m	returns the magnetogyric ratio of a given nucleus
molecule2.m	Depiction of the investigated structure including the tensor of a chosen spin plotted into the structure
extract_eigen1.m ... *extract_eigen4.m*	stepwise import of all data from the tensor file created by modules (2) into the MATLAB environment
calc_eigen.m	sorting of the PAS axes according to the Haeberlen-Mehring-Spiess convention; depiction of the PAS in the RAS
tensor_reduction.m	reduction of the full NMR tensor into its zero, first and second rank contributions
euler.m	(pseudo-)active Euler transformation of a vector in the Cartesian coordinate system according to the Euler angles α, β and γ
calc_euler.m	automated calculation of the Euler angles α, β and γ from the PAS in a given arrangement towards the RAS; the transformation can be visualized as an animated movie or as a depiction of the single steps involved

elliptic_tensor.m *elliptic_tensor_iso.m*	depiction of the ellipsoid representation of the symmetric part of the chemical shift tensor in the RAS; either the anisotropic part or the full shielding including the isotropic part is shown
contourer.m	depiction of 2D spectra as a combination of three distinct regions defined by the signal height: noise, spectrum and diagonal part

as MAS spectra, are already interconnected with the package and will only have to be modified.

The first task to be solved in the work flow from the ab initio calculation to the simulation of spectra is the extraction of the relevant information (positions of the nuclei and tensor data) from various output formats of the quantum mechanical programs (see figure B.1). These formats do not only vary between the here used Gaussian03 and CASTEP packages but for Gaussian03 are also dependent from the choice of calculation within the package itself. The tensor data is transferred to a unified format which can be analyzed with several extraction scripts. Here a GUI based variant exists where each step of the extraction is manually executed and displayed on the screen. For an analysis of extended spin systems an automated scripting alternative without graphical output can be chosen. The results of the tensor analysis includes all NMR parameters described in chapter 2 and comes in a format which can directly be used in the NMR simulation tools GAMMA and SIMPSON. Furthermore, the anisotropic symmetric part of the tensor is given such that it can be depicted in the DIAMOND program.

B.1 Unification of output from ab initio tensor calculations

The output of quantum mechanical calculations is converted into two distinct files called {*filename*}.*mat* and {*filename*}.*ten*. The matrix file {*filename*}.*mat* contains the Cartesian coordinates of the nuclei whereas the tensor file {*filename*}.*ten* comprises the results of the chemical shielding calculations. From a historical point of view the development of the packet started with the conversion of Gaussian03 text and it was convenient to

keep the given Gaussian03 data format and concentrate on the extraction of the necessary information. Therefore the format of the matrix file looks like:

```
1     7     0     12.512627 -9.723002 0.000000
2     6     0     13.249934 -8.565930 0.000000
3     7     0     12.579577 -7.298296 0.000000
4     6     0     11.159117 -7.248345 0.000000
...
```

From the left to the right the values represent the atomic label given by a consecutive number, the atom type given by the atomic number from the periodic table of elements, an arbitrary number which declares the atom type in the Gaussian output and the three Cartesian coordinates x, y and z.
In the tensor file the NMR data is given as follows:

```
1 N Isotropic = 30.5301 Anisotropy = 277.3923
  XX= -89.9535 YX= -51.6541 ZX=   0.0000
  XY= -52.8979 YY= -33.9144 ZY=   0.0000
  XZ=   0.0000 YZ=   0.0000 ZZ= 215.4583
  Eigenvalues: -121.2457 -2.6223 215.4583
  Eigenvectors:
    (1)    0.858024   0.513609    0.000000
    (2)   -0.513609   0.858024    0.000000
    (3)    0.000000   0.000000    1.000000
...
```

The output is subdivided into three kinds of information. In the first part the nucleus is identified by the same consecutive number as in the matrix file and its atomic symbol followed by two NMR parameters extracted from the tensor. The isotropic chemical shift is given for the shielding convention (see chapter 2). The anisotropy is the shielding anisotropy Δ as defined in equation 2.12 but with the axes sorted after their absolute shielding values according to $\sigma_{zz} > \sigma_{yy} > \sigma_{xx}$ from the Herzfeld-Berger convention rather than the Haeberlen-Mehring-Spiess.[48] The following part lists the full shielding tensor as given in equation 2.5. The last part is only available with the Gaussian keyword *'nmr=(PrintEigenvectors)'* and lists the Eigenvalues as well as the axes of the PAS, each represented by a Cartesian vector.

B.1.1 Extraction of tensor data from Gaussian03 output

The Gaussian03 output file {*filename*}.*log* can be converted with the scripts *gaussian_2_ten_n_mat.pl* or *ONIOM_2_ten_n_mat.pl* for standard or ONIOM NMR calculations, respectively. In both cases a file {*filename*}.*log.mat* is created which contains the atomistic structure of the system. Note that the matrix is given in standard coordinates which is the input orientation transformed into a mass weighted internal coordinate of the Gaussian03 calculation. It is this coordinate system which serves as RAS for the description of the spin system. The tensor information is found in a file called {*filename*}.*log.ten*.

B.1.2 Extraction of tensor data from CASTEP output

The results of a CASTEP NMR calculation are given in two separate files, {*filename*}.*castep* and {*filename*}.*magres*. With *castep_2_ ten_n_mat.pl* they can be converted into the Gau2Sim format. However, the procedure is less straightforward than with the Gaussian03 output.

In the *.castep* file the atomic positions are given as fractional coordinates of a unit cell whereas the *.magres* file contains the absolute Cartesian coordinates together with the NMR shielding data. When depicted the given coordinates do not make up for a meaningful structure because the fractional coordinates u, v and w take arbitrary positive or negative values lower or greater than 1 indicating that they do not result from a single unit cell. Probably they represent the Cartesian positions of the atoms of one Brillouin zone in reciprocal space which is used for the NMR calculation under periodic boundary conditions.

This shortcome is solved by a stepwise change of u, v and w until all take positive values between 0 and 1 and thus describe a single unit cell. From these data a file named {*filename*}.*castep.res* is written which contains the structure in the ShellX format. It serves for the depiction of the calculated system with DIAMOND. In a following step the fractional coordinates are used together with the cell axes to calculate the atomic positions in Cartesian space. The Cartesian representation of the respective axis is given in the *.castep* file. The script further allows to choose multiples of the cell axes for the output and therefore to translate the unit cell in space. This proves useful as the Gau2Sim format describes the system as a cluster whereas the CASTEP calculation defines the system via a unit cell which does not necessarily present a meaning-

ful structural cutout when depicted by itself. The cluster of arbitrary size is written to {*filename*}.*castep.mat* in Gau2Sim and to {*filename*}.*castep.xyz* in xyz file format. The tensor data is taken from {*filename*}.*magres* and written to {*filename*}.*castep.ten* for all nuclei given in {*filename*}.*castep.mat*. Furthermore, a file called {*filename*}.*magres.ten* is put out which contains the tensor data of an isolated unit cell.

B.2 Analysis of NMR tensors

The abovementioned unified format of the *.mat* and *.ten* file can be read in with all Gau2Sim scripts (compare to modules (4) in table B.1). These programs differ in their approach to the analysis. The core is a GUI based variant of Gau2Sim (*Gau_2_Sim.m*) which tackles the analysis of the tensor step-by-step. Each step is visualized and both, chemical shift as well as dipole tensors can be treated. For a routine analysis of spin systems containing more than a few nuclei of interest this approach is too labor costly which is why a fully automated variant for the extraction of chemical shift tensor was written.

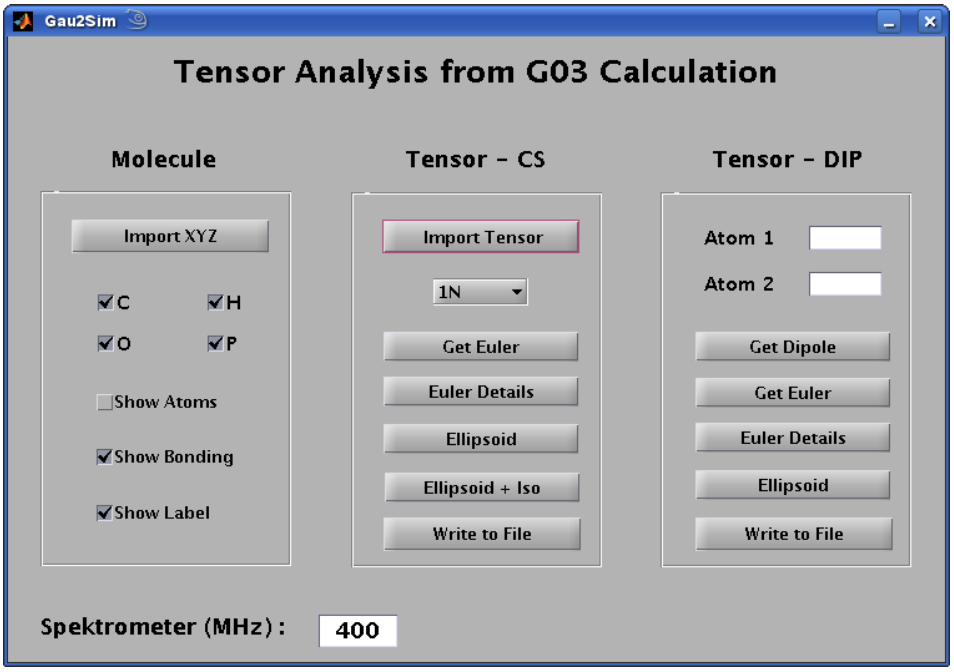

Figure B.2: Gau2Sim GUI for the stepwise analysis of chemical shielding tensors and the direct dipole coupling tensor.

B.2.1 GUI based tensor analysis with Gau2Sim

Figure B.2 shows the graphical user interface of Gau2Sim which serves as a step-by-step tool for the depiction and analysis of arbitrary spin systems from results of quantum mechanical calculations. Two principle modi are available, both are combined with depictions of the currently analyzed tensor in the model system and in the reference axis system. In either case the analysis starts with the import of the matrix file in the above described format.

For the analysis of chemical shielding the tensor file has to be imported. The calculated nuclei can then be chosen from a dropdown menu, the current tensor is immediately depicted via its principle axes scaled by η according to the anisotropic part of σ_{CS} in equation 2.11 (see left side of figure B.5).

The first step of the tensor analysis is the extraction of its orientation towards a common reference axis system. For this reference the internal mass weighted coordinate system of the quantum mechanical calculation was taken and will further be referred to as CAS. For an analysis of the tensor arrangement the Euler transformation in Cartesian coordinates had to be implemented which was done in two steps (compare to section 2.3.1).

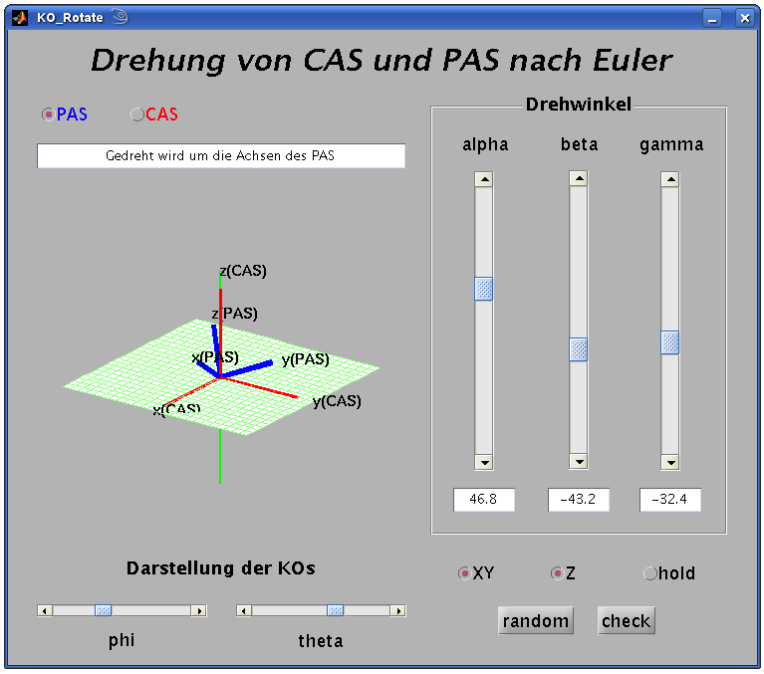

Figure B.3: Screenshot of the KO_Rotate GUI; the Euler transformation between PAS and CAS can be investigated in terms of active or passive rotations.

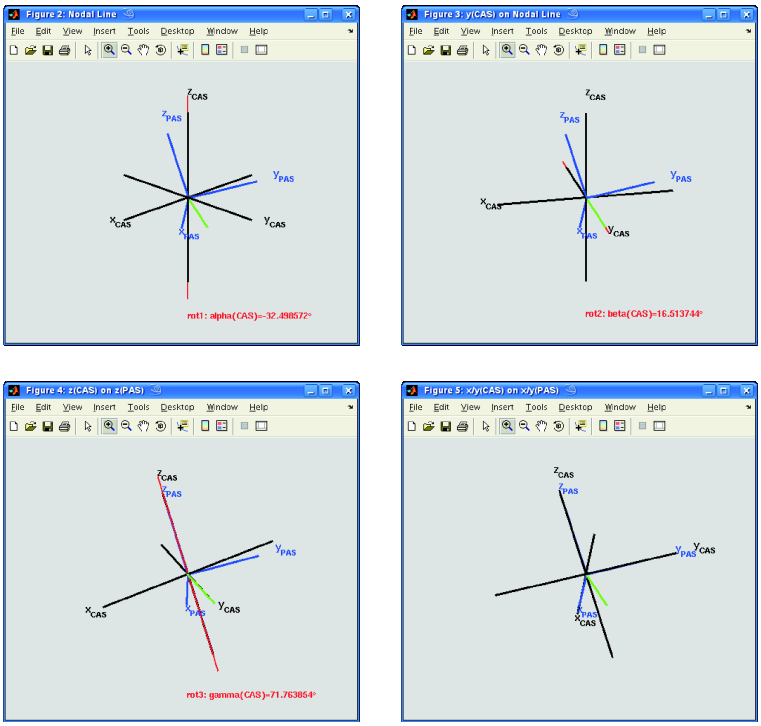

Figure B.4: Euler transformation from CAS into PAS as implemented in the Gau2Sim library; the single steps of rotations about z(CAS), y(CAS) and z(CAS) are performed until both coordinate systems match (compare as well to figure 2.1).

At first a graphical tool for the Euler transformation of two coordinate systems was developed which helps in understanding the crucial point of active and passive rotations. Figure B.3 shows a screenshot of this GUI based MATLAB interface *KO_Rotate*. The starting point is a situation with two matching coordinate systems. One of the systems can be distorted with respect to the other by choosing values for α, β and γ (see CAS and PAS in figure B.3). As the main application of the program was for educational purposes another feature was build in. The program is capable of creating a random orientation of the coordinate systems. The Euler angles for this random orientation is unknown and has to be searched by the user. Chosen angles can be checked with the correct values stored by the program.

The second step of implementation required an automated calculation of the Euler angles α, β and γ from a given tensor orientation. Figure B.4 shows the single steps of this procedure as implemented in the Gau2Sim library (GUI button 'Euler Details'). For the reasons outlined in section 2.3.1 the CAS is actively rotated into the PAS (rotation axes are marked with a red line). The Euler transformation is not unique and always carried

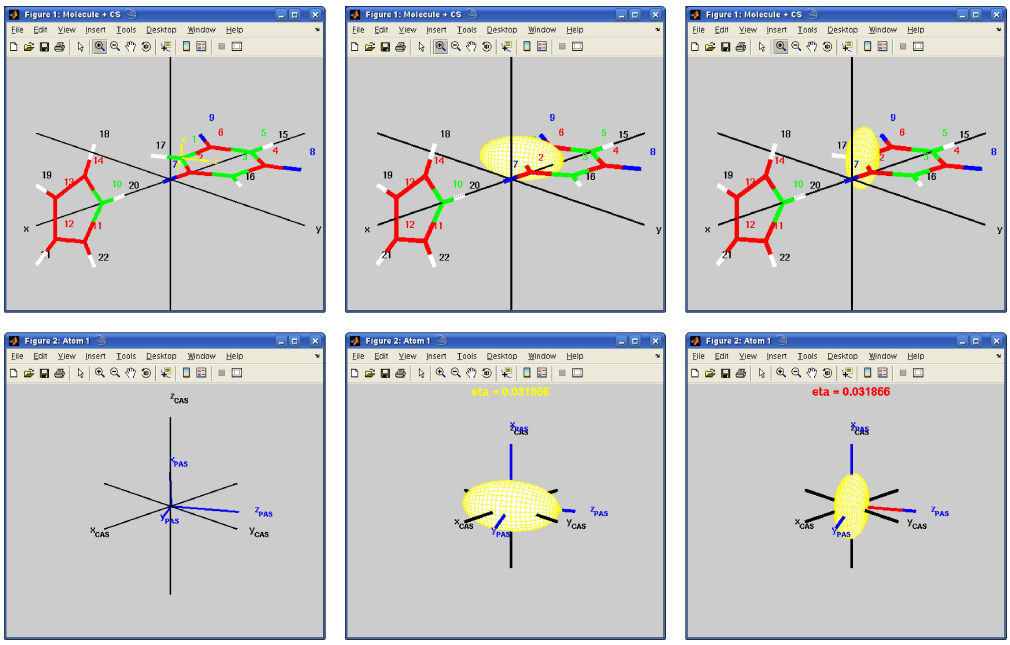

Figure B.5: Depiction of the symmetric part of the ab initio calculated chemical shielding tensor with respect to the atomistic model (top) and in the more abstract reference to the CAS (bottom, the mass weighted internal coordinate system of the calculation is chosen for the CAS); the anisotropic part of the tensor can be viewed in two ways, either via the axes of its PAS or in the classical ellipsoid representation; additionally the full tensor including the isotropic contribution can be visualized as an ellipsoid which gives an impression of the shielding of the nucleus.

out according to the following scheme. First the intersection between the xy planes is determined and the nodal line defined such that an acute angle with y(CAS) is given (see green line figure B.4 and also compare to 2.1). The angle α between the nodal line and y(CAS) is determined and the CAS rotated about z(CAS) until y(CAS) and the nodal line match. Then the angle between z(CAS) and z(PAS) is calculated and the CAS rotated about its y axis until both match. In the last step the angle between x(CAS) and x(PAS) yields the information to superpose both coordinate systems by a rotation about z(CAS). Based on the such extracted angles the active rotation of the PAS into the CAS can also be visualized via an animated movie (GUI button 'Get Euler').

With the known Euler angles the symmetric part of the chemical shift tensor can be depicted in various ways (figure B.5). Either the atomistic model system can be taken as a

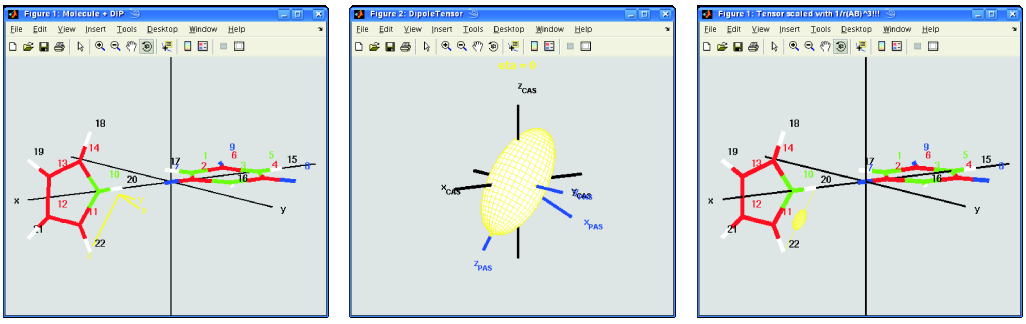

Figure B.6: Depiction of the tensor of the direct dipole coupling between H20 and H22 (from left to right): construction of the PAS between the atoms with z(PAS) interconnecting the nuclei and y(PAS) parallel to the xy plane of the RAS; ellipsoid representation of the tensor in the RAS; ellipsoid representation of the tensor in the molecule scaled by the size of the dipole coupling constant.

reference or the CAS, this mode being closer to the classical conception used in NMR spectroscopy. The anisotropic part of the CS tensor can be depicted via its principle axes or via an ellipsoid representation (left and middle of figure B.5). In both cases the z-axis is normed to a value of 1 whereas the remaining axes are scaled by η (this corresponds to the last matrix of equation 2.11). Finally the isotropic part of the tensor can be included in the ellipsoid representation (right side of figure B.5). This depiction gives an impression of the overall shielding of the investigated nucleus.

As another important feature for the construction of coupled spin systems the tensor of the direct dipole interaction can be build from the structural data of two chosen nuclei (menu 'Tensor - DIP' in the Gau2Sim GUI in figure B.2). The z axis of the tensor interconnects these atoms and y is chosen such that it is oriented parallel to the xy plane of the RAS (see figure B.6). Due to $\eta = 0$ this alignment of the y axis is not imperative but chosen by the program. The x axis is fixed through the constraint of a right handed coordinate system for the PAS. On the base of this coordinate system the Euler angles are evaluated and the dipole tensor can be depicted in an ellipsoid representation like the chemical shift tensor. In the depiction of the tensor in the molecule the size of the ellipsoid is scaled by the dipole coupling constant which is calculated from the distance between the chosen nuclei and their magnetogyric ratios (compare to equation 2.29).

Through the Gau2Sim GUI arbitrary spin systems can be evaluated and understood. The depiction of the chemical shielding tensor in the atomistic structure is a particular inte-

resting feature. It leads to an understanding of the orientation of the PAS in dependency from the symmetry of the local structure. Here the change of the tensor alignment with respect to a change in structure can systematically be investigated. Furthermore the difference in the anisotropy of the chemical shift with respect to the absolute shielding becomes obvious (compare to figure B.5: the z axis of the anisotropic part points along the CH bond whereas the largest shielding occurs perpendicular to the molecular plane; however, both tensorial representations obey the constraints introduced through the local symmetry of the molecule).

B.2.2 Depiction of the anisotropic symmetric part of the NMR tensor with DIAMOND

For the depiction of the NMR tensors in publications the quality of the illustrations as produced with MATLAB is not sufficient. For this purpose the program DIAMOND can be used which is capable of depicting crystal structures including the thermal ellipsoids from the structure solution. These ellipsoids as well base on a tensorial formalism and can be used for the depiction of the NMR data. The standard output of Gau2Sim contains a line with the tensor ellipsoid given in DIAMOND format which can be introduced as a thermal ellipsoid as follows.
The matrix file is converted into standard XYZ format using the script *mat_2_xyz.pl*. The output can be imported in DIAMOND and saved as ShellX file (for CASTEP calculations the ShellX file is already produced by *castep_2_ ten_n_mat.pl*). This file contains entries for the atoms in fractional coordinates:

```
C    1   0.58395   0.14187   0.34867
C    1   0.63225   0.08108   0.49754
C    1   0.72155   0.04712   0.46627
 ...
```

The lines can be extended for isotropic thermal ellipsoids the size of the atoms:

```
C    1   0.58395   0.14187   0.34867     1.000 0.02
C    1   0.63225   0.08108   0.49754     1.000 0.02
C    1   0.72155   0.04712   0.46627     1.000 0.02
 ...
```

For chosen nuclei the anisotropic ellipsoid of the NMR tensor is introduced via the in-

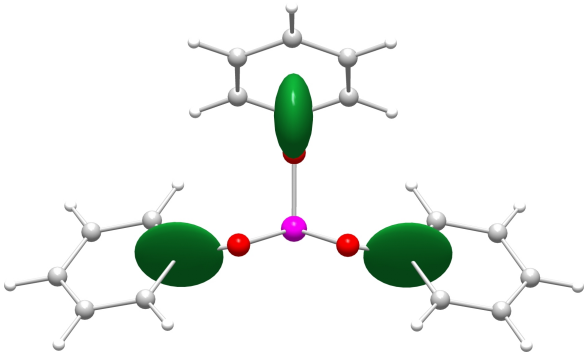

Figure B.7: Example for the depiction of chemical shift tensors via thermal ellipsoids in DIAMOND - high quality pictures for publications.

sertion of the line from the Gau2Sim output:

```
C    1   0.58395   0.14187   0.34867      1.000 =
   0.400000 0.344962 0.062542 0.117704 -0.029421 0.005447
C    1   0.63225   0.08108   0.49754      1.000 0.02
C    1   0.72155   0.04712   0.46627      1.000 0.02
 ...
```

The such manipulated file can be imported in DIAMOND. Now the NMR tensors can be introduced into the structure by activating the thermal ellipsoids and the whole system is available to graphical processing. Figure B.7 shows the result of the depiction of three chemical shift tensors in triphenyl phosphite as an example.

B.2.3 Automated tensor analysis with Gau2Sim

However instructive, the use of the Gau2Sim GUI is an impracticable way of routinely analyzing large spin systems. For this reasons the single steps of the analysis of the chemical shift tensor were compiled in the automated variants *CSA_extractor.m* and *CSA_DIR_extractor.m* of Gau2Sim. Given the index of the nucleus to investigate *CSA_extractor.m* returns the full tensor analysis written into a file called {*filename*}.*log.ten.Xi*. X denotes the name of the atom itself and i stands for the index of the nucleus. Through looping over the index in the MATLAB environment even large systems can be analyzed in very short time.

Instead of varying the investigated nucleus *CSA_DIR_extractor.m* extracts NMR data for

different structures given in a common directory. It automatically searches for the *.mat* and *.ten* files and extracts the NMR data for a desired site i. The output is written to a directory called *EXTRACTED*. This allows for the investigation of whole NMR hypersurfaces over a large number of structural variations (in the context of this work up to 800 variations have been performed on a single systems).
Furthermore, the conversion between the Haeberlen-Mehring-Spiess and the Herzfeld-Berger conventions can be carried out with the script *CSA_2_span_n_skew.m* which reads the {*filename*}*.log.ten.Xi* as given by *CSA_extractor.m*. Besides the file {*filename*}*.log.ten.Xi.NMRvalues* which contains the NMR parameters of both conventions an additional file called {*filename*}*.log.ten.Xi.data* is created in the format of the following example:

```
1    -53.7584     77.2663  0.36184756 179.977 -90.008 -90.000
1    -0.89203    -0.00007    -0.00049

1    -78.4122      0.0008      -0.013
1     -0.0003     23.5079     -0.0179
1     -0.0091      -0.017   -106.3708
```

All lines of this file start with a number for the spin in the output followed by different kind of information. The first line contains the tensor in the format of a SIMPSON input (isotropic shift σ_{iso}, anisotropy δ, asymmetry parameter η and the Euler angles α, β and γ). The second line exhibits the Cartesian coordinates of the nucleus and the following lines bear the symmetric part of the chemical shift tensor. This format is read in by the self-written programs for the calculation of wide-line spectra.
Through this step the conversion of the output of quantum chemical calculations became a routine task yielding a base for the simulation of NMR spectra of arbitrary spin systems. In this work these simulations were restricted to MAS spectra as well as wide-line 1D and 2D spectra of uncoupled spins but in principle the ab initio description of any arbitrary NMR experiment is available.

B.3 Simulation of MAS spectra with SIMPSON

In MAS experiments the overlap of signals can hinder the analysis of the spectral lineshape. For high rotational frequencies such an overlap results from the natural linewidth of

the recorded sample causing signals with similar chemical shifts to merge. At low rotational frequencies additionally spinning sidebands come into play. The lower the spinning frequency, the more the sidebands overlap with each other or the central signals. Furthermore the anisotropy of the observed nucleus alters the NMR spectrum. Even though all of these factors can complicate the assignment of a MAS spectrum they are, however, included when calculating the MAS spectrum from ab initio results. Such a simulation yields the full theoretical lineshape of the MAS spectrum which can directly be compared to an experimental spectrum and taken as a good starting point for a fit of the experimental data.

The script *simpsoner.pl* allows for the automated calculation of spin systems with arbitrary numbers and types of spins. Figure B.8 shows the organization and mode of operation of the program. In the directory *simpsondir* the extracted tensor data of the full system is given in the Gau2Sim output format. It contains spins of arbitrary type and number. For each type of spin that is to be calculated a directory *spindir* has to be available which

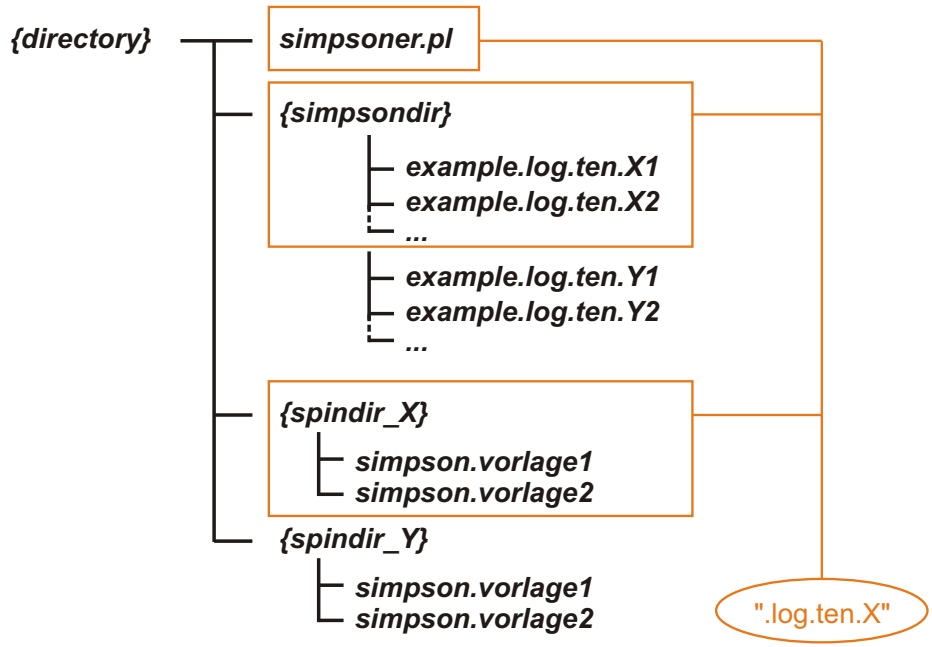

Figure B.8: File structure for the automated calculation of MAS spectra with *simpsoner.pl*: the directory *simpsondir* contains the Gau2Sim output of the whole system and *spindir* SIMPSON input templates for the nuclei X, Y, ...; *simpsoner.pl* uses a search pattern to pick out the specific nuclei (here all spins of type X), automatically creates the input file, calculates the MAS spectra and stores them in *simpsondir*.

contains two SIMPSON templates, one for the head of the input script and one for the tail. Here the parameters of the NMR experiment are set as for example the rotational frequency. *simpsoner.pl* takes a search pattern to pick out specific spin types from *simpsondir*, collects the tensor data in a spin system and embeds it between the head and tail as given in the templates. The such produced SIMPSON input file is calculated and the resulting spectra stored in *simpsondir*.
For example, in the workflow as given in figure B.8 the search pattern '.log.ten.X' collects all X nuclei from *simpsondir* and combines them with the templates taken from *spindir_X*. On the base of a finished quantum mechanical calculation the overall procedure of the extraction of the tensor data with the above described script including the simulation of MAS spectra with SIMPSON only takes roughly half an hour. The most time consuming step therefore remains the calculation of the chemical shift tensor itself.

B.4 Simulation of wide-line spectra with GAMMA

The calculation of wide-line spectra was carried out with self written programs using the GAMMA C++ library and follows the steps described in chapter 2. For the information on the spin system the Gau2Sim output is read in. This makes the chemical shift parameters σ_{iso}, δ, η and the Euler angles α, β and γ as well as the symmetric part of the shielding tensor accessible for the simulation (compare to B.2.3).

B.4.1 1D wide-line spectra

Figure B.9 summarized all essential steps towards a theoretical 1D spectrum. First a sweep width (SW) is defined which includes the full frequency axis of the spectrum. Via the grid size the SW is subdivided into a grid specifying separate sections of the frequency axis. In a next step a powder average is read in from an external file. It was created by an equal distribution of a number of vectors on a sphere (in this work 12000 orientations were taken). Each vector is defined by the polar angles θ and ϕ and bears a weighting which represents the contribution of the single orientation to the spectral intensity. The weighting roots in the fact that each vector defines a cutout of the surface of the sphere and therefore a subensemble of orientations.
The value for the weighting is the area of the cutout and the overall powder average is

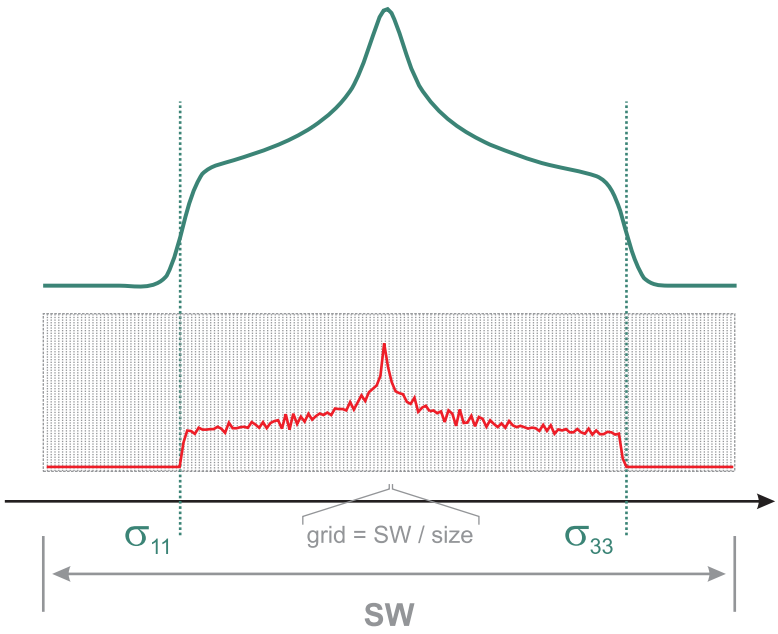

Figure B.9: Simulation of 1D wide-line chemical shift spectra: the sweep width (SW) is subdivided into a grid; each orientation from the powder average contributes to a special interval of the grid and the calculation of all contributions gives the theoretical spectrum (bottom); this spectrum has further to be convoluted to eliminate the theoretical noise (top).

created such that in an idealized case the weighting takes the same value for each vector (and therefore the areas are equally large). The sum over all weighing results in the entire surface of the sphere which is unified to 1. The chemical shift tensor is transformed into its spherical parts which can be easily rotated from the PAS over the CAS into the LAS. Resulting from quantum mechanical calculations it is already given in its representation in the CAS. Therefore the usually first rotation from the PAS into the CAS is omitted and only the transformation into the PAS treated in the further proceeding. For each orientation of the powder average the resonance frequency is calculated and the weighting of the powder average added to the respective interval of the grid on the frequency axis of the spectrum. The result of this procedure is shown in figure B.9. Due to the finite number of vectors in the powder distributions and the finite size of the grid an artificial noise appears on the spectrum. Therefore it has to be convoluted with a broadening function to be compared to experimental spectra. For crystalline phases a Lorentzian lineshape can be used whereas in disordered phases a Gaussian function is common.

B.4.2 2D wide-line spectra

The principle procedure for the simulation of spectra for 2D rf-driven spin-diffusion spectroscopy matches the approach described in B.4.1. Again a grid is defined, this time over the 2D plane included by the frequency axes ω_1 and ω_2 (compare to figure ref_FIG_2D (d)). In the here presented work exclusively mixing times of $t_m \rightarrow \infty$ were simulated. In this situation the spin-diffusion leads to a homogeneous exchange between all nuclei and the spectral intensity is distributed over the 2D plane. Figure B.4.2 shows the example for an exchange between three spins in a fixed arrangement towards each

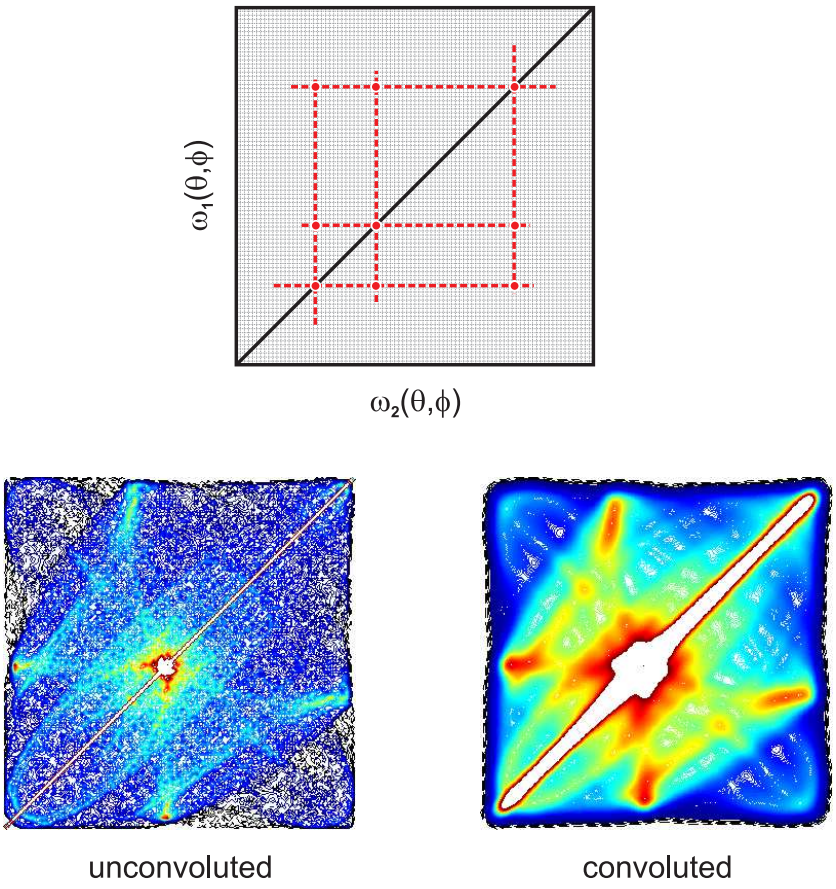

Figure B.10: Simulation of 2D rf-driven spin-diffusion wide-line spectra for three spins and $t_m \rightarrow \infty$: the intensity is distributed over a 2D grid; signals appear for all possible combinations of the three frequencies $\omega(\theta_1, \phi_1)$, $\omega(\theta_2, \phi_2)$ and $\omega(\theta_3, \phi_3)$ leading to characteristic ridges; the artificial noise is eliminated through a 2D convolution with a Gaussian function.

other (compare as well to figure B.7). For $t_m \rightarrow \infty$ the spectral intensity is distributed between all possible combinations of the three frequencies $\omega(\theta_1, \phi_1)$, $\omega(\theta_2, \phi_2)$ and $\omega(\theta_3, \phi_3)$. The powder average weighting is assigned to the respective area in the grid. The procedure is carried out over all possible orientations of the CAS described by the powder average. As the spin system is fixed to the CAS only chosen off-diagonal signals appear in the 2D spectrum (compare to section 2.5) causing ridges in the spectrum which are characteristic for the simulated tensor arrangement ('unconvoluted' in figure B.10). For the same reason as in the one-dimensional case artificial noise covers the ridges. It can be eliminated by the convolution with a 2D gaussian function leading to a spectrum which can directly be compared to the experiment ('convoluted' in figure B.10).

Bibliography

[1] Kroke, E.; Schwarz, M. *Coord. Chem. Rev.*, **2004**, *248*, 493 – 532.

[2] Kaner, R. B.; Gilman, J. J.; Tolbert, S. H. *Science*, **2005**, *308*, 1268 – 1269.

[3] Horvath-Bordon, E.; Ralf Riedel, R.; Zerr, A.; McMillan, P. F.; Auffermann, G.; Prots, Y.; Bronger, W.; Kniep, R.; Kroll, P. *Chem. Soc. Rev.*, **2006**, *35*, 987 – 1014.

[4] Bernstein, J.; Davey, R.; Henck, O. *Angew. Chem.*, **1999**, *111*, 3646–3669.

[5] Chemburkar, S. R.; Bauer, J.; Deming, K.; Spiwek, H.; Patel, K.; Morris, J.; Henry, R.; Spanton, S.; Dziki, W.; Porter, W.; Quick, J.; Bauer, P.; Donaubauer, J.; Narayanan, B. A.; Soldani, M.; Riley, D.; McFarland, K. *Org. Proc. Res. Dev.*, **2000**, *4*, 413–417.

[6] Dunitz, J. D.; Bernstein, J. *Acc. Chem. Res.*, **1995**, *28*, 193–200.

[7] Bernstein, J. *Polymorphism in Molecular Crystals*, **2002**, *Clarendon Press, Oxford*.

[8] Bernstein, J. *Organic Solid State Chemistry: Conformational Polymorphism*, **1987**, *Elsevier, Amsterdam*, 471.

[9] Thallapally, P. K.; Jetti, R. K. R.; Katz, A. K.; Carell, H. L.; Singh, K.; Lahiri, K.; Kotha, S.; Boese, R.; Desiraju, G. R. *Angew. Chem.*, **2004**, *116*, 1169–1175.

[10] Wang, Y.; Fu, H.; Peng, A.; Zhao, Y.; Ma, J.; Maa, Y.; Yao, J. *Chem. Commun.*, **2007**, pp 1623–1625.

[11] Henck, J.-O.; Bernstein, J.; Ellern, A.; Boese, R. *J. Am Chem. Soc.*, **2001**, *123*, 1834–1841.

[12] Desiraju, G. R. *Crystal Engineering*, **1989**, *Elsevier, Amsterdam*.

[13] Vishweshwar, P.; McMahon, J. A.; Zaworotko, M. J. *Frontiers in Crystal Engineering*, **2006**, *John Wiley & Sons Ltd.*, 25–49.

[14] Bernstein, J.; Henck, J.-O. *Cryst. Engin.*, **1998**, *1*, 119–128.

[15] Blagden, N. *Powder Techn.*, **2001**, *121*, 46–52.

[16] Hiremath, R.; Basile, J. A.; Varney, S. W.; Swift, J. A. *J. Am. Chem. Soc.*, **2005**, *127*, 18321–18327.

[17] Richet, P.; Gillet, P. *Eur. J. Mineral.*, **1997**, *9*, 907–933.

[18] Mishima, O.; Stanley, H. *Nature*, **1998**, *396*, 329–335.

[19] Jansen, M.; Jäschke, B.; Jäschke, T. *Struct. Bond.*, **2002**, *101*, 137–191.

[20] Yarger, J. L.; Wolf, G. H. *Science*, **2004**, *306*, 820–821.

[21] Senker, J.; Rössler, E. *Chem. Geol.*, **2001**, *174*, 143–156.

[22] Tarjus, G.; Kivelson, S. A.; Nussinov, Z.; Viot, P. *J. Phys.: Condens. Matter*, **2005**, *17*, R1143–R1182.

[23] Tarjus, G.; Alba-Simionesco, C.; Grousson, M.; Viot, P.; Kivelson, D. *J. Phys.: Condens. Matter*, **2003**, *15*, S1077–S1084.

[24] Sinha, I.; Mandal, R. K. *J. Non-Cryst. Solids*, **2003**, *324*, 36–49.

[25] Levi, C. G. *Acta mater.*, **1998**, *46*, 787–800.

[26] Baldus, M. *Angew. Chem.*, **2006**, *118*, 1204–1207.

[27] Harris, K. D. M.; Cheung, E. Y. *Chem. Soc. Rev.*, **2004**, *33*, 526–538.

[28] Harris, K. D. M. *Cryst. Growth Des.*, **2003**, *3*, 887–895.

[29] Tremayne, M. *Phil. Trans. R. Soc. Lond. A*, **2004**, *362*, 2691–2707.

[30] Elena, B.; Pintacuda, G.; Mifsud, N.; Emsley, L. *J. Am. Chem. Soc.*, **2006**, *128*, 9555–9560.

[31] Emsley, J. W.; Feeney, J. *Prog. Nuc. Magn. Res. Spectrosc.*, **2007**, *50*, 179–198.

[32] Taulelle, F. *Solid State Sci.*, **2004**, *6*, 1053–1057.

[33] Harris, R. K. *Solid State Sci.*, **2004**, *6*, 1025–1037.

[34] Senker, J.; Seyfarth, L.; Voll, J. *Solid State Sci.*, **2004**, *6*, 1039–1052.

[35] Schulz-Dobrick, M.; Metzroth, T.; Spiess, H. W.; Gauss, J.; Schnell, I. *Chem. Phys. Chem.*, **2005**, *6*, 315–327.

[36] Brouwer, D. H.; Darton, R. J.; Morris, R. E.; Levitt, M. H. *J. Am. Chem. Soc.*, **2005**, *127*, 10365–10370.

[37] Beitone, L.; Huguenard, C.; Gansmüller, A.; Henry, M.; Taulelle, F.; Loiseau, T.; Férey, G. *J. Am. Chem. Soc.*, **2003**, *125*, 9102–9110.

[38] Matara, S. F. *Prog. Solid State Chem.*, **2006**, *34*, 21 – 66.

[39] Ouvrard, C.; Price, S. L. *Cryst. Growth Des.*, **2004**, *4*, 1119–1127.

[40] Davey, R. J. *Chem. Comm.*, **2003**, pp 1463–1467.

[41] Day, G. M.; Motherwell, W. D. S.; Jones, W. *Phys. Chem. Chem. Phys.*, **2007**, *9*, 1693–1704.

[42] Stevens, R.; Pitzer, R. M.; Lipscomb, W. N. *J. Chem. Phys.*, **1963**, *38*, 550–560.

[43] Fleischer, U.; van Wüllen, C.; Kutzelnigg, W. *NMR Chemical Shift Computation: Ab Initio*. Wiley, New York, 1998. in: Encyclopedia of Computational Chemistry.

[44] Kutzelnigg, W. *Isr. J. Chem.*, **1980**, *19*, 193–201.

[45] Schindler, M.; Kutzelnigg, W. *J. Chem. Phys.*, **1982**, *76*, 1919–1925.

[46] Schindler, M.; Kutzelnigg, W. *J. Am. Chem. Soc.*, **1983**, *105*, 1360–1371.

[47] Schindler, M.; Kutzelnigg, W. *Mol. Phys.*, **1983**, *48*, 781–789.

[48] Wolinski, K.; Hinton, J. F.; Pulay, P. *J. Am. Chem. Soc.*, **1990**, *112*, 8251–8260.

[49] Pople et al. *Gaussian 03, Revision D.01*. Gaussian, Inc., Wallingford, CT, 2004.

[50] Segall, M. D.; Lindan, P. J. D.; Probert, M. J.; Pickard, C. J.; Hasnip, P. J.; Clark, S. J.; Payne, M. C. *Phys. Rev. B*, **2001**, *63*, 245101/1–245101/13.

[51] Yates, J. R.; Pickard, C. J.; Payne, M. C.; Mauri, F. *J. Chem. Phys.*, **2003**, *118*, 5746–5753.

[52] Facelli, J. C.; Grant, D. M. *Nature*, **1993**, *365*, 325–327.

[53] Salzmann, R.; Ziegler, C. J.; Godbout, N.; McMahon, M. T.; Suslick, K. S.; Oldfield, E. *J. Am. Chem. Soc.*, **1998**, *120*, 11323–11334.

[54] Eichele, K.; Wasylishen, R. E.; Corrigan, J. F.; Taylor, N. J.; Carty, A. J.; Feindel, K.; Bernard, G. M. *J. Am. Chem. Soc.*, **2002**, *124*, 1541–1552.

[55] Stueber, D.; Grant, D. M. *J. Am. Chem. Soc.*, **2002**, *124*, 10539–10551.

[56] Poon, A.; Birn, J.; Ramamoorthy, A. *J. Phys. Chem. B*, **2004**, *108*, 16577–16585.

[57] Birn, J.; Poon, A.; Mao, Y.; Ramamoorthy, A. *J. Am. Chem. Soc.*, **2004**, *126*, 8529–8534.

[58] Wang, W.; Phung, C. G.; Alderman, D. W.; Pugmire, J.; Grant, D. M. *J. Am. Chem. Soc.*, **1995**, *117*, 11984–11988.

[59] Heller, J.; Laws, D. D.; Tomaselli, M.; King, D. S.; Wemmer, D. E.; Pines, A.; Oldfield, E. *J. Am. Chem. Soc.*, **1997**, *119*, 7827–7831.

[60] Aimi, K.; Yamane, A.; Ando, S. *J. Mol. Struct.*, **2002**, *602-603*, 417–428.

[61] Colombo, D.; Ferraboschi, P.; Ronchetti, F.; Toma, L. *Magn. Reson. Chem.*, **2002**, *40*, 581–588.

[62] Harper, J. K.; Facelli, J. C.; Barich, D. H.; McGeorge, G.; Mulgrew, A. E.; Grant, D. M. *J. Am. Chem. Soc.*, **2002**, *124*, 10589–10595.

[63] Potrebowski, M. J.; Assfeld, X.; Ganicz, K.; Olejniczak, S.; Cartier, A.; Gardiennet, C.; Tekely, P. *J. Am. Chem. Soc.*, **2003**, *125*, 4223–4232.

[64] Zheng, A.; Yang, M.; Yue, Y.; Ye, C.; Deng, F. *Chem. Phys. Let.*, **2004**, *399*, 172–176.

[65] Ochsenfeld, C.; Brown, S. P.; Schnell, I.; Gauss, J.; Spiess, H. W. *J. Am. Chem. Soc.*, **2001**, *123*, 2597–2606.

[66] Benzi, C.; Crescenzi, O.; Pavone, M.; Barone, V. *Magn. Res. Chem.*, **2004**, *42*, S57–S67.

[67] Benzi, C.; Cossi, M.; Barone, V.; Tarroni, R.; Zannoni, C. *J. Phys. Chem. B*, **2005**, *109*, 2584–2590.

[68] Charpentier, T.; Ispas, S.; Profeta, M.; Mauri, F.; Pickard, C. J. *J. Phys. Chem. B*, **2004**, *108*, 4147–4161.

[69] Gervais, C.; Profeta, M.; Lafond, V.; Bonhomme, C.; Azais, T.; Mutin, H.; Pickard, C. J.; Mauri, F.; Babonneau, F. *Magn. Res. Chem.*, **2004**, *42*, 445–452.

[70] Gervais, C.; Dupree, R.; Pike, K. J.; Bonhomme, C.; Profeta, M.; Pickard, C. J.; Mauri, F. *J. Phys. Chem. A*, **2005**, *109*, 6960–6969.

[71] Harris, R. K.; Joyce, S. A.; Pickard, C. J.; Cadars, S.; Emsley, L. *Phys. Chem. Chem. Phys.*, **2006**, *8*, 137–143.

[72] Baldus, M. *Angew. Chem.*, **2006**, *118*, 1204–1207.

[73] Facelli, J. C.; Orendt, A. M.; Jiang, Y. J.; Pugmire, R. J.; Grant, D. M. *J. Phys. Chem.*, **1996**, *100*, 8268–8272.

[74] Walker, O.; Mutzenhardt, P.; Tekely, P.; Canet, D. *J. Am. Chem. Soc.*, **2002**, *124*, 865–873.

[75] Kaji, H.; Yamada, T.; Tsukamoto, N.; Horii, F. *Chem. Phys. Let.*, **2005**, *401*, 246–253.

[76] Bühl, M. *NMR Chemical Shift Computation: Structural Applications*. Wiley, New York, 1998. in: Encyclopedia of Computational Chemistry.

[77] Hodgkinson, P.; Emsley, L. *Prog. Nucl. Magn. Reson. Spectrosc.*, **2000**, *36*, 201–239.

[78] Smith, S. A.; Levante, T. O.; Meier, B. H.; Ernst, R. R. *J. Magn. Reson.*, **1994**, *106a*, 75–105.

[79] Bak, M.; Rasmussen, J. T.; Nielsen, N. C. *J. Magn. Res.*, **2000**, *147*, 296 – 330.

[80] Schmidt-Rohr, K.; Spiess, H. W. *Multidimensional Solid-State NMR and Polymers*. Harcourt Brace and Company, 1994.

[81] Günther, H. *NMR-Spektroskopie*. Georg Thieme Verlag, 1992.

[82] Smith, S. A.; Palke, W. E.; Gerig, J. T. *Concepts Magn. Res.*, **1992**, *4*, 107 – 144.

[83] Levitt, M. H. *J. Magn. Res.*, **1997**, *126*, 164 – 182.

[84] Mason, J. *Solid State Nucl. Magn. Reson.*, **1993**, *2*, 285 – 288.

[85] Smith, S. A.; Levante, T. O.; Meier, B. H.; Ernst, R. R. *Chem. Rev.*, **1999**, *99*, 293–352.

[86] Koch, W.; Holthausen, M. C. *A Chemist's Guide to Density Functional Theory*. WILEY-VCH, 2002.

[87] Haeberlen, U. *High Resolution NMR in Solids. Selective Averaging*. Academic Press, 1976.

[88] Harris, R. K.; Kowalewski, J.; de Menezes, S. C. *Pure & Appl. Chem.*, **1997**, *69*, 2489 – 2495.

[89] Herzfeld, J.; Berger, A. E. *J. Chem. Phys*, **1980**, *73*, 6021 – 6030.

[90] Senker, J.; Sehnert, J.; Correll, S. *J. Am. Chem. Soc.*, **2005**, *127*, 337–349.

[91] Robyr, P.; Tomaselli, M.; Straka, J.; Grob-Pisano, C.; Suter, U. W.; Meie, B. H.; Ernst, R. R. *Mol. Phys.*, **1995**, *84*, 995–1020.

[92] *Scientific Computing World*, **2002**, *63*, 19–21.

[93] MATLAB. *The language of technical computing*. Math Works Inc., 24 Prime Park Way, Natick, MA 01760-1500. Copyright 1984-2004.